Respiratory Motion Modelling and Predictive Tracking for Adaptive Radiotherapy

Sahih, Abdelhamid

Award date:
2010

Respiratory Motion Modelling and Predictive Tracking for Adaptive Radiotherapy

Abdelhamid Sahih

DEUG (Ma), Licence (Ma), Maîtrise (Fr), Msc (Fr).

April 2010

Respiratory Motion Modelling and Predictive Tracking for Adaptive Radiotherapy

Abdelhamid Sahih

DEUG (Ma), Licence (Ma), Maîtrise (Fr), Msc (Fr).

April 2010

A Thesis submitted in partial fulfilment of the University's requirement for the degree of Doctor of Philosophy.

Control Theory and Applications Centre (CTAC), Coventry University

in collaboration with University Hospitals Coventry and Warwickshire (UHCW), NHS Trust.

This work was sponsored by the Framework 6 European integrated project Methods and Advanced Equipment for Simulation and Treatment in Radiation Oncology (MAESTRO).

Summary

External beam radiation therapy (EBRT) is the most common form of radiation therapy (RT) that uses controlled energy sources to eradicate a predefined tumour volume, known as the planning target volume (PTV), whilst at the same time attempting to minimise the dose delivered to the surrounding healthy tissues. Tumours in the thoracic and abdomen regions are susceptible to motion caused mainly by the patient respiration and movement that may occur during the treatment preparation and delivery. Usually, an adaptive approach termed adaptive radiation therapy (ART), which involves feedback from imaging devices to detect organ/surrogate motion, is considered. The feasibility of such techniques is subject to two main problems. First, the exact position of the tumour has to be estimated/detected in real-time and second, the delay that can arise from the tumour position acquisition and the motion tracking compensation. The research work described in this thesis is part of the European project entitled 'Methods and advanced equipment for simulation and treatment in radiation oncology' (MAESTRO), see Appendix A. The thesis presents both theoretical and experimental work to model and predict the respiratory surrogate motion. Based on a widely investigated clinical internal and external respiratory surrogate motion data, two new approaches to model respiratory surrogate motion were developed. The first considers the lung as a bilinear model that replicates the motion in response to a virtual input signal that can be seen as a signal generated by the nervous system. This model and a statistical model of the respiratory period and duty cycle were used to generate a set of realistic respiratory data of varying difficulties. The aim of the latter was to overcome the lack of test data for a researcher to evaluate their algorithms. The second approach was based on an online polynomial function that was found to adequately replicate the breathing cycles of regular and irregular data, using the same number of parameters as a benchmark sinusoidal model. The two developed models were extended to predict the surrogate motion by means of a sliding window polynomial function and an adaptive mode of the bilinear model. The new prediction algorithms for long and short time motion prediction developed by the author were compared to some predictors based neural network (NN) and Kalman Filter (KF), both established by MAESTRO co-workers, and using the same data. It was found that while the sliding polynomial model performs well over a short-time prediction (0.2s), the adaptive approach of the bilinear model performs better over a long-time prediction (up to 0.6s). The modelling and prediction of the respiratory surrogate motion were also performed by considering input-output measurement. For this purpose, a novel experiment designed by the author involving Spirometry and external surrogate markers has been carried out. A comparison between the performance of a set candidate linear and bilinear models has shown that a second order linear model gives the best results. The impact of using a virtual input signal instead of physical input has revealed that using a virtual input gives better results than using a physical input. A new approach was applied

to the predictive tracking of respiratory surrogate motion. The work was carried out by building a non-linear model of the patient support system (PSS) to achieve a good simulation model for the latter. The combination of the prediction and control to compensate for respiratory motion during the radiotherapy treatment was also considered. Finally, the overall MAESTRO aim was achieved by introducing a new strategy to accommodate for tumour/organ motion. The latter was assessed in clinical environment at the University Hospitals Coventry and Warwickshire (UHCW).

Acknowledgement

Writing acknowledgements, such as this, is always a treacherous task, because it is too easy to forget someone. In case I have done, I hope you will accept my deepest apologies and my reassurance that no malice was intended.

First of all, I would like to express my sincerest gratitude to my supervisors Prof. Keith Burnham and Dr Olivier Haas of the CTAC at Coventry University for the opportunity to pursue this research project and their academic as well as financial support of my studies. They have always encouraged me and given me complete freedom to explore new ideas. Additionally thanks to my third supervisor Dr John Mills of the UHCW for his guidance and help throughout my thesis work. I would like also to thank Dr Peter Reeve and Dr Benoit Vinsonneau for their valuable academic discussion.

This research has been supported and funded by the Framework 6 European integrated project MAESTRO. I would like to thank Dr Oliver Haas, Professor Keith Burnham, Dr John Mills, Dr Imke Land, Dr Piotr Skworcow, Dr Devi Putra, Dr John Goodband, Mr Amir Mekherbeche, Mr Hugues Komi Kode, Mr George Koustoumpardis, Miss Audrey Rizzo, Miss Myriam Clesse, Daniel Paluszczyszyn, Dave and the Physics staff at the UHCW for an enjoyable collaboration and for their many helpful suggestions.

I am thankful to Virginia Commonwealth University (VCU) (USA) and Hokkaido University (Japan) for providing precious tumour motion data. Special acknowledgements to Dr Paul Keall and Dr Gregory Sharp for their precious conversations and academic support.

I would like to thank all my friends who supported and motivated me, especially in the last period of my PhD. Warm thanks go particularly Tarik, Dr Imke land, Janice, Michael, Daniel, Sami, Mousa, Khalid, Imad, Moumen, Youssef, Amine, my colleagues from CTAC and all friends from Coventry.

Special thanks directed to my family, I would like to express my most profound thanks. They were a constant source of support and encouragement and I couldn’t have done it without their help. This thesis is dedicated to them.

Finally, special dedication to my two grandmothers who passed away.

Contents

Glossary of Symbols and Abbreviations

In this section the notational conventions used for mathematical symbols, operators and abbreviations are presented.

Notations, Symbols and Operators

$y(t)$	Output variable at time t
$u(t)$	Input variable at time t
h_p	Prediction horizon
$\widehat{y}(t+h_p\|t)$	Predicted value of $y(t)$ at time $t+h_p$ given the information at time t
$y(t-\kappa\|t)$	Delayed value of $y(t)$ by κ given at time t
t	Integer time step (for convenience, two notations are used, e.g. y_t and $y(t)$)
κ	Integer time delay
q^{-1}	Backward shift operator
$P(q^{-1})$	Polynomial in q^{-1}, e.g. $P(q^{-1}) = 1 + p_1 q^{-1} + ... + p_n q^{-n}$
$det[A]$	Determinant of the matrix A
$\varphi(t)$	Observation vector at time t
$\theta(t)$	Parameter vector at time t
δ_{ij}	Kronecker δ-function
$\widehat{\bullet}$	Estimate
$\overline{\bullet}$	Mean value
N	Number of observations
λ	Forgetting factor
f_s	Sampling frequency
$\mathbf{Y}^N$	Vector of N observations
$\|.\|_2$	Euclidean $l_2 - norm$

$\underset{\theta \in \mathcal{D}}{\operatorname{argmin}}$	A value of θ in the parameter space $\mathcal{D}$, that minimizes a given cost function

Abbreviations and Acronyms

2D	Two-Dimensional
3D	Three-Dimensional
3DCRT	Three-Dimensional Conformal Radiation Therapy
4D	Four-Dimensional
4DCRT	Four-Dimensional Conformal Radiation Therapy
4DCT	Four-Dimensional Computerised Tomography
ABC	Active Breathing Control
AI	Audio Instruction
AP	Anterior-Posterior
AR	Autoregressive
ARMA	Autoregressive Moving Average
ART	Adaptive Radiation Therapy
ARX	Autoregressive with eXogenous Variables
ATT	Average Tumour Trajectory
AVB	Audio-Visual Biofeedback
BARX	Bilinear Autoregressive with eXogenous Variables
BLS	Bilinear System
BM	Bilinear Model
BP	Bayesian Regularisation
BTI	Bilinear Time-Invarying
BTV	Bilinear Time-Varying

CA	Constant Acceleration
CC	Cranial-Caudal
CG	Conjugate Gradient
CGBP	Conjugate Gradient Back-Propagation
CI	Confidence Interval
CRT	Conformal Radiation Therapy
CT	Computerized Tomography
CTAC	Control Theory And Application Centre
CTV	Clinical Target Volume
CV	Constant Velocity
DIBH	Deep Inspiration Breath-Hold
DMLC	Dynamic Multileaf Collimator
DRR	Digitally Reconstructed Radiograph
DVH	Dose Volume Histogram
EBRT	External Beam Radiation Therapy
ECG	Electrocardiogram
EM	External Markers
EOE	End-Of-Exhale
EPID	Electronic Portal Imaging Devices
EX	Exhalation
FB	Free Breathing
FFT	Fast Fourier Transform
GEV	Generalized Extreme Value
GRNN	Generalised Regression Neural Network

GTV	Gross Tumor Volume
ICRU	International Commission on Radiation Units and Measurements
IFM	Internal Fiducial Markers
IGRT	Image Guided Radiation Therapy
IM	Internal Margin
IMM	Interacting Multiple Model
IMRT	Intensity Modulated Radiation Therapy
IN	Inhalation
IRIS	Integrated Radiotherapy Imaging System
ITV	Internal Target Volume
KF	Kalman Filter
KV	Kilovoltage
LINAC	Linear Accelerator
LLS	Linear Least squares
LM	Levenberg-Marquardt
LMS	Least-mean-square
LS	Least squares
LTV	Time-Varying Linear
MAE	Mean Absolute Error
MAESTRO	Methods And Advanced Equipment For Simulation And Treatment In Radiation Oncology
MASE	Mean Absolute Simulation Error
MaxAE	Maximum Absolute Error
MGH	Massachusetts General Hospital

ML	Medial-Lateral
MLC	Multileaf Collimator
MLP	Multi-Layer Perceptron
MPC	Model Predictive Controller
MRI	Magnetic Resonance Imaging
MRS	Magnetic Resonance Spectroscopy
MSE	Mean Squared Error
MSPE	Mean Squared Prediction Error
MSSE	Mean Squared Simulation Error
MV	Megavoltage
NARX	Nonlinear Autoregressive with eXogenous Variables
NN	Neural Network
nRMSE	Normalized Root Mean Squared Error
NTCP	Normal Tissue Complication Probability
OAR	Organ At Risk
OE	Output Error
PC	Personal Computer
PDF	Probability Distribution Function
PEM	Prediction Error Method
PET	Positron Emission Tomography
PRBS	Pseudo Random Binary Signal
PRV	Planning Organ At Risk
PSS	Patient Support System
PTP	Peak-To-Peak

PTV	Planning Target Volume
QA	Quality Assurance
RBS	Random Binary Signal
RF	Radio-Frequency
RLS	Recursive Least Squares
RMS	Root Mean Square
RMSE	Root Mean Squared Error
RMSSE	Root Mean Squared Simulation Error
ROI	Regions Of Interest
RPM	Real Time Position Management
RT	Radiation Therapy
RTRT	Real-Time Tumour Tracking Radiotherapy
RTTT	Real Time Tumour Tracking
SD	Standard Deviation
SHL	Signal History Lengths
SI	Superior-Inferior
SISO	Single-Input Single-Output
SM	Setup Margin
SMART	Synchronized Moving Aperture Radiation Therapy
SNR	Signal to Noise Ratio
SPECT	Single Photon Emission Computed Tomography
TC	Target Coverage
TCP	Tumour Control Probability
Tp	Prediction Time

TSP	Time-Series Prediction
UHCW	University Hospitals Coventry and Warwickshire
US	Ultrasound
UTCP	Uncomplicated Tumour Control Probability
VCU	Virginia Commonwealth University

List of Figures

List of Tables

Chapter 1

General introduction

1.1 Background

RT, also called *radiotherapy*, is an efficient treatment technique that consists in the delivery of a precisely controlled and monitored dose of electromagnetic and particle radiations to eradicate a predefined volume of abnormal cells, known as a *tumour*. The radiations aim to destroy these malignant cells making them unable to divide, reproduce and supplant the surrounding healthy cells. Over time, the abnormal cells die and the tumour shrinks. Although healthy cells can also be damaged by radiation, they can repair themselves more effectively than radio-sensitive cancer cells. Therefore, the main goal of RT is to maximise the dose delivery to abnormal cells while sparing exposure to the surrounding normal cells [Jeremić and Aaronson 2005].

There are three common ways to apply radiation to a cancerous tumour in current day RT. The first method called *brachytherapy*, which consists in placing radioactive material, sealed in catheters or seeds, directly in the tumour region for a prescribed period of time. The second, known as *unsealed source* radiotherapy, is based on injecting or ingesting a soluble radioactive substance. The most common form of RT is external beam radiotherapy (EBRT) that operates by applying an external source (usually called a linear accelerator (LINAC)) of high or low energy rays.

Radiation treatment involves two major procedures, which are *treatment preparation* and *treatment delivery*. The former consists of treatment simulation and planning, whereas the latter is usually done in multiple treatment fractions. Each fraction consisting of two stages i.e. patient positioning (set-up) and treatment delivery. At the treatment simulation stage, patient and tumour geometrical information are acquired. This is often performed through advanced diagnosis scans such as computerised tomography (CT), magnetic resonance imaging (MRI), or radiography with and without contrast media. A three-

dimensional (3D) patient model, which includes models for the target (often called *target delineation*) and organs at risk (OAR), is then built using computer software. The choice of the imaging modality to be used depends on the area of the body to be investigated.

Treatment planning is referred to the process of designing a particular treatment for each patient. This takes into account the patient's model, built in simulation stage and treatment machine data [1] in the computer, to find an adequate treatment plan, by trying various treatment parameters such as beam characteristics and directions. This process can be viewed as performing a 'virtual' treatments using a 'virtual' machines on the 'virtual' patient (both modelled in the computer). During each fraction of treatment execution, the patient is first positioned under the LINAC, attempting to duplicate the reference patient geometry acquired in the machine coordinate system during the treatment simulation (or the 'virtual' patient model used for treatment planning), and then the treatment plan is delivered to the patient.

In addition to geographical position of the tumour, factors such as patient positioning, beam arrangement, appropriate dose, shielding and instructions for proper implementation of the treatment procedure should be taken into consideration for a good RT treatment plan. The patient's body should remain as still as possible to accurately aim the radiation only at the target while avoiding healthy tissues. This is especially difficult in areas that are normally moving, such as the lungs and abdominal organs. In such sites, a slight shift in position could move the target out of the radiation beam's path. How to keep the patient geometry close to the reference model in the machine coordinate system or how to update the model to accommodate the changing patient geometry are the current research topics of the image guided radiation therapy (IGRT).

In order to focus, accurately, the radiation beam on a central point, referred to as the 'isocentre' within the target, the patient and treatment machine must be correctly aligned. Depending on the body area to be treated, different techniques may be used for patient body positioning, including: skin markers, laser lights, field lights, infra-red cameras and x-ray positioners. Laser lights are used to make sure the patient is level and straight on the table or couch. Field lights correspond to the skin marks. Infra-red cameras use body markers or tattoo to detect patient position and match the markers to the position in the treatment plan. X-ray positioners take stereoscopic x-rays of the patient anatomy and match them to the position in the treatment plan images.

[1] The treatment machine data includes for example beams characteristics, linear accelerator angles and X, Y, Z position of the patient support system.

1.2 Problem statement

Various errors may occur during each step of the RT process, which cause a significant deterioration in the treatment accuracy [Booth 2002, Herk 2004, Engelsman et al. 2001]. These errors are divided into *systematic errors*, i.e. the ones that occur in the course of the treatment preparation, and *random errors*, i.e. errors that take place during the delivery stage. The systematic errors include a patient positioning errors during simulation, organ motion, delineation error, dose calculation, and mechanical inaccuracy of the LINAC, such as field size, gantry angle, system calibration. Patient positioning, organ motion, and mechanical inaccuracy errors can also happen during the treatment delivery, resulting in random errors.

Tumours in the thoracic and abdomen regions are susceptible to motion caused mainly by the patient respiration, the patient motion and sometimes by skeletal muscular, cardiac, or gastrointestinal systems. A great deal of effort has been devoted to limit tumour motion due to the respiration. The most invasive method uses some immobilisation device where the patient's motion is restricted. The conventional non-invasive way to account for organ motion is to expand the tumour margins to ensure that the entire tumour will receive the prescribed dose [Herk 2004]. Alternatively, tumour motion control can be achieved by monitoring breathing either passively [Hanley et al. 1999] or actively [Wong et al. 1999]. Another category of methods allow patient's free breathing (FB) while adapting the radiation beam to the tumour position.

Respiratory gating is a technique that synchronises radiation treatment to the patient's respiratory cycles. It operates such that the radiation beam is on only within a specific phase or portion of patient's breathing cycle [Jiang 2006b]. Real-time tumour tracking (RTTT) technique [Murphy 2004], can be realised by using dynamic multi-leaf collimator (DMLC) [Webb 2006] or LINAC based robotic arm [Schweikard et al. 2004] or, alternatively, by keeping the tumour under the beam path via PSS control [D'Souza et al. 2005, Skworcow et al. 2007]. Organ motion has also been included in the calculation of the dose distribution [Lujan et al. 1999], and various schemes to investigate the relationship between organ motion and motion management techniques has been carried out in [Land 2009].

Except for the breath-holding technique, the remaining respiration motion compensation methods mentioned above demand a good understanding of the motion characteristics. During the treatment simulation stage, tumour motion is measured and a model can be derived. With the help of this model, parameters of the motion can be estimated and utilised in treatment planning. Moreover, an online monitoring of the tumour position can be applied with either gating or RTTT techniques.

The used adaptive approaches to compensate for tumour motion require the exact position of the latter to be estimated/detected in real-time. Tumour detection has been carried out by tracking the tumour itself

[Sixel et al. 2003], host organ [Davies et al. 1994], radiographic fiducial markers [2] implemented near or in tumour [Seppenwoolde et al. 2002b], radioactive tracers targeting [Weiss et al. 1972], and surrogate organ such as diaphragm [Vedam et al. 2003b, Ford et al. 2002]. This was achieved by different imaging modalities such as Ultrasound (US) [Davies et al. 1994], CT [Shimizu et al. 2000b], MRI [Korin et al. 1992] and more commonly fluoroscopy [Shirato et al. 2000b, Shimizu et al. 2001, Ozhasoglu and Murphy 2002, Seppenwoolde et al. 2002b]. However, the utilisation of such imaging systems necessitates time to process the data and transmit the position of the tumour. On the other hand, both the multi-leaf collimator (MLC) and PSS are electromechanical devices with limited response time. The combination of the above effect means that by the time the MLC/PSS reaches the desired position, the organs may have moved. There is therefore a need to predict in advance the motion of the organ to be tracked [Sahih et al. 2006; 2005].

1.3 Aims and objectives

According to the problem statement, respiratory motion modelling and prediction are the two main issues for an accurate radiotherapy treatment. This research aims to investigating new modelling and prediction techniques as well as the application of the former to simulate realistic respiratory motion. To achieve these aims the following objectives were considered:

- To model the respiratory surrogate motion. In order to realise this objective the following tasks were carried out:
  - Identify benefits and limitation of the existing models.
  - Perform a pre-processing and a statistical analysis of published data.
  - Investigate system engineering and identification approaches to model respiratory surrogate motion.
  - Extract the respiratory surrogate motion drift.
  - Validate the modelling approaches using clinical data.
  - Acquire additional breathing signals.
- To develop more realistic respiratory trajectories to be used as a benchmark. This has involved the following issues:

[2] Fiducial markers are implantable markers used in radiotherapy treatment to provide real-time accurate localisation of the tumour volume.

  - Use the developed respiratory surrogate motion model.
  - Build statistical models of period and duty cycle parameters of the respiratory surrogate motion.
  - Involve a model of different drift signals.

- To design, develop and implement new motion prediction strategies. The achievement of this objective the following tasks were carried out:
  - Design a new breathing experiment.
  - Assess the prediction strategy in real-time.
  - Compare the performance of the developed prediction algorithms to those introduced in the published work.

1.4 Thesis outline

The thesis is organised as follow:

Chapter 2 presents a review of the principles of the RT process in practice, the equipments and imaging modalities currently in use as well as the main treatment techniques/approaches. Thereafter, the problem of treatment inaccuracy caused by uncertainties, such as patient/tumour motion, and treatment machines inaccuracy, is raised. The research has been focused mainly on the organ/tumour uncertainties and more exactly those caused by the breathing process. The source of breathing process was studied by investigating the respiratory system function. The main characteristics of the respiratory surrogate motion such as frequency, range and speed were identified from the literature. A number of solutions have been proposed to compensate for the tumour motion. However, some of these methods are limited by the necessity to determine tumour position in real-time and the existence of a systematic time delay.

Chapter 3 reviews the most significant published papers on organ/tumour motion modelling and prediction to overcome the organ/tumour motion problems in RT as well as various assessment criteria that have been used to evaluate these techniques. While the motion model is necessary for motion simulation in order to assess, for example, the radiotherapy machines and treatment strategy, and motion tracking in real-time, the prediction is essential to overcome the problem of time delay during the beam delivery. The review of the few developed modelling approaches has revealed that there are three different types of models: (i) periodic models, (ii) phase based models, and geometrical model. The prediction algorithms developed includes linear predictors, neural network (NN) and KF techniques. The last part of the Chapter reviews existing assessment criteria in order to establish a ground for comparison.

Chapter 4 describes the pre-processing, characteristics and statistical analysis of the clinical data investigated in both anterior-posterior (AP) and superior-inferior (SI) directions. The data were provided by Virginia Commonwealth University (VCU) (USA) and Hokkaido University-School of Medicine (Japan). The data was grouped in four sets, namely free-breathing (FB), audio-instruction (AI), audio-visual biofeedback (AVB) and internal fiducial markers (IFM). The time and frequency analysis of each data set have highlighted the presence of breathing abnormalities, baseline drift, measurement noise and heart beat in the internal data. The overall drift signal, measurement noise and respiratory data for each data set were found to be approximated by a Gaussian distribution with different parameters. A new parametrisation of the respiratory surrogate motion was adopted which considers the breathing as a succession of exhalation and inhalation. Different breathing parameters were estimated and the statistical distribution of the period and duty cycle obtained. This analysis enabled the modelling work described in Chapter 5 and 6 to be based on the knowledge gained on the respiratory data.

Chapter 5 introduces a new modelling approach which was deduced from the analysis of the respiratory motion performed in Chapter 4. It consists in considering the lung as a bilinear system, which responds to a square wave signal, assumed to be generated by the nervous system. The disturbances such as drift, measurement noise and heartbeat were considered as external signals that were not included in the breathing motion modelling. Two approaches to deal with the drift signal were considered. The first models the drift by a polynomial function with different orders, the second filters the surrogate motion signal to remove the drift. For both drift removal techniques, models of each patient from the different clinical data set were estimated and validated. The model parameters were estimated using nonlinear constrained optimisation technique and nonlinear non-constrained optimisation technique. The resulting model was used to generate a set of benchmarks respiratory motion trajectories that summarise typical behaviour in sets of 4 mins durations. In addition to the average model, an adaptive approach of the bilinear model was developed. The latter was found to be able to follow accurately the changes in the respiratory patterns. A second modelling approach to model the respiratory cycles was also introduced which is based on the polynomial fitting. This was performed online and compared to the widely used Lujan model [Lujan et al. 1999], which was also implemented online.

Chapter 6 describes a new experiment designed and carried out by the author. It exploits both Spirometry signals and external chest markers. The data collected from the experiment was then pre-processed and analysed prior to their use in modelling and prediction. The system identification procedure that consist in finding the appropriate model of the lung system among different linear and bilinear model structures was carried out and a second order linear model was found to give the best performance. In addition, this model structure was assessed using a virtual input signal instead of the physical one. It was found that the

virtual input gives better results than the physical input. A new predictive tracking approach based on the Spirometry measurement and external chest markers was introduced. A demonstration of such approach shows that the latter can predict 0.2s ahead with a root mean squared error (RMSE) of 0.42 mm.

Chapter 7 presents an adaptive bilinear model and a sliding polynomial function as a new prediction algorithms which were compared to a set of prediction algorithms based on KF and NNs. The outcome of this comparison was that the sliding polynomial model perform better for a short time prediction (0.2s) and the adaptive bilinear model gives a better prediction results for a long time prediction (0.4, 0.5 and 0.6s). Having completed the work on motion prediction, a simulation model of the PSS was built using some measurements at the UHCW. The parameter estimation strategy developed by the author is presented. Finally, a demonstration of the overall motion compensation strategy developed within the MAESTRO project was presented.

Chapter 8 discusses the final conclusions made in this thesis and future research stemming from this work.

1.5 Contributions

The main contributions in this thesis are :

- Performed a thorough survey of relevant literature in Chapter 2 and 3.
- Developed two new approaches for modelling, simulation and tracking of the respiratory surrogate motion based on the bilinear modelling framework and a polynomial function. Details are given in Chapter 5.
- Exploited the bilinear model to generate a set of realistic respiratory surrogate motion to overcome the lack of benchmark data and allow researcher in the field to assess and compare different algorithms and motion strategies (see Chapter 5).
- Designed a new experiment to evaluate the benefit of combining flow measurement and external chest markers for modelling and predictive. Details are in Chapter 6.
- Introduced two new prediction algorithms based on a sliding polynomial model and an adaptive bilinear model (see Chapter 7).

A summary of the main contributions and where can be found in the Thesis are shown in the following diagram:

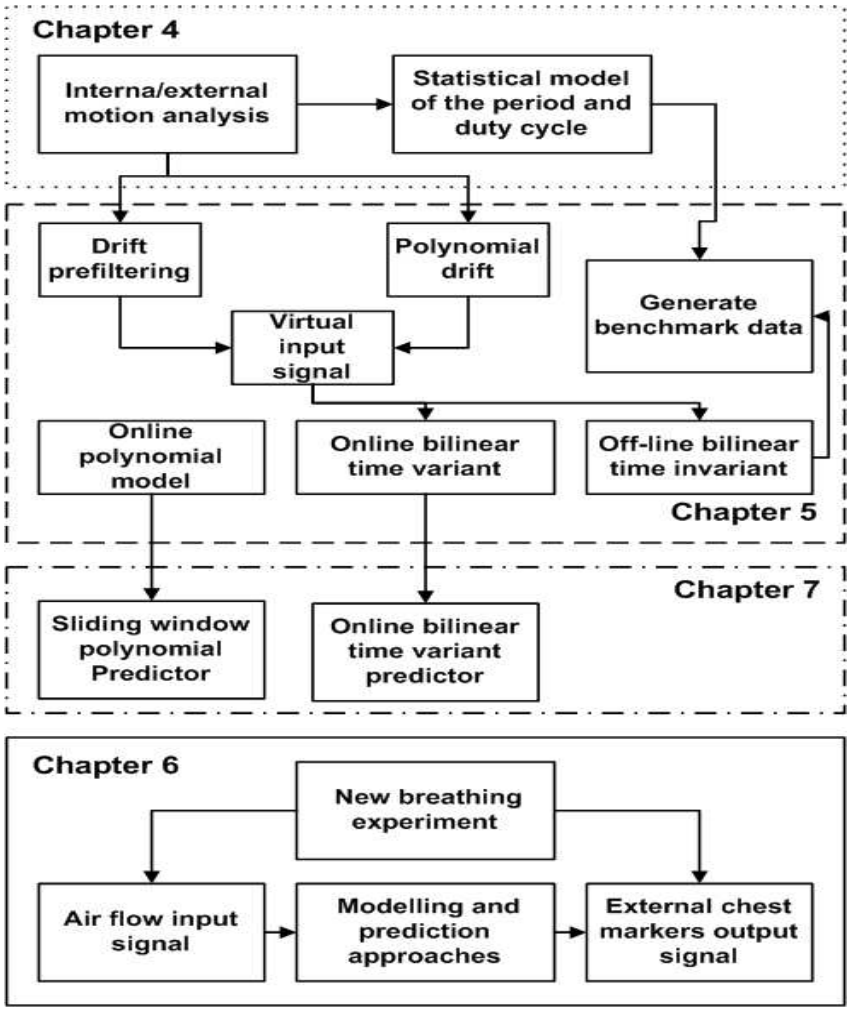

Fig. 1.1: Illustrating the flow chart of the different contributions.

1.6 Publications

During the period of this research, some contributions have been made to the field of system/control engineering and medical physics, through the publication of one journal paper and ten papers in conference proceedings:

Conference and journal papers

- Haas O.C.L., Skworcow P., Sahih A., Land I., Paluszcyszyn D., Mills J., Bueno G., and Fisher M. (2008). New couch based control system for automatic inter and intrafraction motion compensation for IGRT. *Radiotherapy & Oncology*, 88 (Suppl. 2):S124 (2008). ESTRO 27 European Society for

Therapeutic Radiology and Oncology Conference, Gothenburg (Sweden), 2008

- Mills J.A., Haas O.C.L., Bueno G., Fisher M., Sahih A., Skworkow P., Putra D., Burnham K.J., Land I., Young K., Sage J., Wilson A.J. and Martinez-Albala A., Torres M., Delgado J.M., Carrascosa C., and Yu S. (2007). Target motion detection and the adaptation of radiotherapy delivery systems for high-precision radiotherapy treatment. *Strahlentherapie und Onkologie*, 183(Suppl. 1):152 (2007). DEGRO German Society of Therapeutic Radiology and Oncology Conference, Hanover (Germany).

- Sahih, A., Haas O.C.L., Mills, J.A., and Burnham, K.J. (2007). A new bilinear model for respiratory motion. Jean-Pierre Bissonnette, ed., In *XVth International Conference on the Use of Computers in Radiation Therapy*, Volume 1, pages 133-137, Toronto, Canada.

- Skworcow, P., D. Putra, A. Sahih, J. Goodband, O.C.L. Haas, K.J. Burnham and J.A. Mills (2007). Predictive tracking for respiratory induced motion compensation in adaptive radiotherapy. *Measurement + Control* 40(1) 16-19.

- Sahih, A., Haas, O.C.L., Goodband, G.H., Putra, D., Mills, J.A., and Burnham, K.J. (2006). Respiratory motion prediction for adaptive radiotherapy. In *Proc. CD-ROM of IAR & ACD Annual Meeting*, Nancy, France.

- Sahih, A., Haas, O.C.L., Burnham, K.J., and Mills, J.A. (2006). Bilinear filter approach for internal and external respiratory motion modelling and prediction. In *Int. Conf. on Systems Engineering*, pages 425-430, Coventry, UK.

- Skworcow, P., D. Putra, A. Sahih, J. Goodband, O.C.L. Haas, K.J. Burnham, J.A. Mills (2006). Predictive tracking for respiratory induced motion compensation in adaptive radiotherapy. *UKACC Control 2006 Mini Symposia*, pages 203-210, Glasgow, UK.

- Skworcow, P., A. Sahih, O.C.L. Haas, J.A. Mills, and Burnham, K.J. (2006). Towards effective organ immobilization via a predictive bilinear feedforward model based approach to control a radiotherapy patient support system. *Proc. CDROM. International Conference: Control 2006*, Glasgow, UK.

- Sahih, A., O C L Haas, O.C.L., Mills, J.A., and Burnham, K.J. (2005). Organ motion modelling and prediction for adaptive radiotherapy. In *Proc. CD-ROM of IAR & ACD Annual Meeting*, pages 211-216, Mulhouse, France.

- Sahih, A., Haas, O.C.L., Burnham, K.J., and Mills, J.A. (2005). Organ motion modelling and prediction. In Proc. *6th Polish-British Workshop, Computer Systems Engineering*. IEE Control and Automation Professional Network, pages 9-20, Wroclaw, Poland.

- Skworcow, P., A. Sahih, O.C.L. Haas, K.J. Burnham, Mills, J.A. (2005). Assessing the mechanical accuracy of radiotherapy treatment equipment: A precursor to control system design. *6th Polish-British Workshop, Computer Systems Engineering*. IEE Control and Automation Professional Network, pages 145-156, Wroclaw, Poland.

Abstracts and Posters

- Sahih, A., Haas, O.C.L, Mills, J.A. and Burnham, K.J. (2006). Respiration cycles modelling using a bilinear filter approach. *Biennial radiotherapy meeting*, University of East Anglia, Norwich.

Awards

- Winner of the poster award in *biennial radiotherapy meeting*, University of East Anglia, Norwich 2006.

Citations of My Research

- Ernst F., Schlaefer, A. and Dieterich, S. and Schweikard, A. (2008). A Fast Lane Approach to LMS prediction of respiratory motion signals. Biomedical Signal Processing and Control, 3(4): 291–299.

The author has also contributed to three MAESTRO project deliverables in the form of reports and/or softwares. The softwares consisted in Real-time implementation of some predictors and $LabVIEW^{TM}$ based video tracking system.

Chapter 2

An overview of external beam radiation therapy (EBRT)

2.1 Introduction

A number of uncertainties may occur during/prior to the RT treatment resulting in a degradation of the accuracy for the whole RT process. The most dominant uncertainties are tumour/organ and patient motion [Langen et al. 2001, Di Yan 2001]. Research has been conducted towards the investigation of moving tumours, especially those generated by the respiration [Hoisak et al. 2004, Jiang 2006b, Kubo and Hill 1996]. Note that patient's motion can also induce tumour motion. Several methods to compensate for tumour and patient motion have been introduced [Hanley et al. 1999, Di Yan 2001, Herk 2004, Mageras and Yorke 2004, Shirato et al. 2007].

Modern advances in computers have fuelled both development in RT treatment equipment and imaging techniques for diagnosis and cancer localisation. The next direction in RT was to account for organ/patient movement and changes, which is being called ART. The latter considers the treatment delivery as a closed-loop feedback system, where dynamic variation of patient position and tumour geometry/location is exploited to adapt the radiation delivery. The implementation of ART requires radiation delivery system modification for hardware components including LINAC, MLC and on-line imaging devices/software.

This chapter aims at giving an overview concerning the current state of EBRT practice and the uncertainties that can be faced, particularly organ/tumour motion due to the natural respiration. Section 2.2 highlights the clinical practice of the EBRT and the up to date techniques/tools that contributed to the progress of the latter. Section 2.3 reviews different uncertainties that might occur during or between patient irradiation and describes current solutions to compensate for some of them. An understanding of

respiratory system function and description of respiratory motion characteristics are discussed in Section 2.4. Section 2.5 reviews the compensation methods that explicitly manage respiratory motion during RT. A discussion of the main outcomes of the chapter is presented in the last section.

2.2 Outline of clinical radiotherapy treatment

2.2.1 Imaging modalities for radiotherapy

The evolution of RT has been strongly linked with the development of imaging techniques. They are involved in every key step of the RT process, ranging from patient staging, simulation, treatment planning, and radiation delivery, to patient follow-up. One of the most important issues in RT is to provide information about the tumour target and critical structure relative to the patient anatomy.

The emergence of CT techniques revolutionised RT and allowed the use of image data to build a 3D patient model and 3DCRT design. This imaging modality evolves many advantages, including high spatial integrity, high spatial resolution, excellent bony structure depiction, and the ability to provide relative electron density information used for radiation dose calculation. In addition, it can be done in either axial, spiral, or cone-beam mode. Recent advances in CT technology has led to the development of four-dimensional computerised tomography (4DCT) which is based on 3D images with the additional dimension being time. With this dynamic imaging technique, one can carry out not only new diagnoses but also provide new interventional therapy through real-time observation [Mageras et al. 2004]. In practice, 4DCRT is a very difficult problem, with many levels of complexity [Keall 2004].

A second type of imaging modality used for RT is MRI. It provides superior soft tissue discrimination and is used as primary image modality for central nervous system structures and within the abdomen and pelvis. It has also been widely used in the diagnosis and tumour delineation. It is also utilised for virtual simulation of radiation treatment for some specific disease sites. In a clinical setting, MRI is typically employed together with CT images with the help of image fusion software to delineate the extent of the malignancy. An example of the use of MRI technique to obtain the four-dimensional (4D) information of the lung can be found in [Shimizu et al. 2000a].

Another useful imaging modality for RT is known as ultrasound (US). It utilises high-frequency (1$\sim$10MHz) sound waves to generate anatomical images that have high spatial resolution and tissue characterisation discrimination power through image texture analysis. This imaging modality has been particularly useful in prostate imaging. Trans-rectal US is an imaging modality which permits an examination/ localisation of the prostate gland [Sawada et al. 2004, Yu et al. 1999] and it is an imaging modality of choice in

guiding the prostate seed implant procedure.

Fluoroscopy is an imaging technique in which x-rays continually strike a fluorescent plate that is coupled to a video monitor. In a fluoroscopic images, tumours lack sufficient contrast with the surrounding tissue. Therefore, in treatment preparation metal clips are often implanted around the tumour [Shirato et al. 1999]. Since these clips are radio opaque making them highly visible in fluoroscopy images and CT scans.

The imaging modalities mentioned above are anatomic in nature, i.e. they provide snapshot of a patient's anatomy without biological information of various organs or structures. Functional imaging techniques such as magnetic resonance spectroscopy (MRS), PET, and SPECT provide metabolic, or other functional data indicating the location, size, and aggressiveness of disease. These techniques may help clinicians to observe functional changes so that they can create targeted treatment plans that deliver escalated doses to the most metabolically active parts of a tumour. PET is widely used for lung [Caldwell et al. 2001] little for nasopharynx and neck [Daisne et al. 2004]. SPECT was used for lung perfusion measurement for planing and during follow-up [Seppenwoolde et al. 2002a].

The patient's anatomy is changing during the radiation delivery, which makes the patient's model created prior to the treatment outdated. Therefore, techniques for image guidance have been developed. The classical example is the electronic portal imaging which allows correction of the set-up of the bony anatomy and/or markers. Diagnostic x-ray imaging provides better contrast over shorter exposure intervals than portal imaging and it was adopted as an improvement for patient's set-up and tracking during treatment.

The usual implementation of image guidance involves either dual kilovoltage (KV) x-ray sources and solid-state flat-panel detectors mounted permanently to the floor and ceiling of the treatment room or a source/detector system mounted to the gantry arm for rotation around the patient. The x-ray images have been used for bony anatomy and marker based set-up when the x-ray imaging set is integrated with the LINAC [Balter et al. 1995b;a], and for determining tumour motion in lung [Shimizu et al. 2001]. The megavoltage (MV) images are widely used for set-up based on the bony anatomy and on markers, see for example [Nederveen et al. 2003]. However, they are rather time consuming and not necessarily accurate all the time.

The precise localisation of the target volume is the key issue for organ motion tracking. There are two approaches to realise such detection which are 'on-line' or 'real time'. The 'on-line' or inter-fraction method, also referred to as IGRT, images the patient before the delivery of radiation and then modifies the machine set-up accordingly. In terms of imaging technologies the current on-line target localisation techniques for EBRT include two-dimensional (2D) KV and MV radiographic imaging (Electronic portal

imaging). Portal imaging is currently the most widely used technique to routinely obtain the appropriate anatomical information and adjust to the patient's position if the displacement exceeds agreed tolerances. The main issue with MV imaging is the lack of contrast which limits its use for adjustment based on the bony anatomy as opposed to the actual planning target volume (PTV) position.

The 'real time' approach also referred to as ART, images the patient whilst the treatment is taking place. There is currently no method able to provide detailed 2D and 3D anatomy of the cancerous tissues whilst the patient is being irradiated. However, it is possible to infer the location of the PTV during treatment when the PTV is enclosed in bony anatomy (e.g. brain tumour) or from surgically implanted markers that can be tracked with a KV imager. These two techniques are now described.

External markers are used in combination with video imaging systems based on standard or infra-red devices such as the $Polaris^{\textcircled{R}}$ system. External markers are usually made of a number of geometrical shapes (usually spheres) that are combined together to form a predefined object. The positions of the individual markers within that 'object' need to remain constant to minimise measurement errors. The 'object' made of this set of individual spheres can then be tracked using a stereoscopic vision system. The use of several spheres to form a single 'object' increases the accuracy of the tracking system. Note, however, that some commercial systems rely on the use of individual markers as opposed to groups of markers. The advantage of such a system is the speed at which the position of the sphere can be detected. For example the Polaris system is able to obtain a position in 34 ms and thus feedback control of the PSS, gantry or MLC positioning is feasible. However, the drawback is the uncertainty that exists and the need to correlate external patient motion with internal motion.

Internal markers, namely fiducial markers, are implanted surgically into the PTV and, therefore, their position is directly related to the position of the PTV. They are usually made of a high density inert material and shaped such that they do not move too much during the course of the treatment. The marker material ensures that they can be easily detected using KV imaging where they appear as pixels with whiter color than bones (i.e. at one extreme of the range of pixel grey level) within a PTV usually located in the middle of the range of grey levels. Fiducial marker detection and tracking is therefore a relatively simple task from the image processing perspective. This means that tracking of fiducial marker can also be fast e.g. 90 ms (see for example [Shirato et al. 2000a]).

2.2.2 Radiotherapy treatment delivery machines

Several types of irradiation technologies can be used to produce the shape and the aim of the radiation beam directed to the volume target. Each machine offers a different level of accuracy and ability to deliver

various radiation techniques to treat the tumour.

Linear accelerator system

Medical LINAC system is the standard technology for delivering conventional radiotherapy which uses a gantry construction for moving the linear accelerator (see Figure 2.1). However, this mechanical construction can deliver radiation from a limited number of directions during a single treatment. Meanwhile, its ability to compensate for target motion during treatment is inherently very limited. Several additional factors limit the accuracy of gantry-based systems, most notably mechanical flex and lack of fully computerised position/motion control. Conventional LINAC systems has six motion axes, which are sufficient to target any point within a given workspace from any angle. However, four out the six axes of the LINAC gantry are built into the patient table, or so called PSS. The latter is a moving table (or couch) on which the patient is laid down during the treatment.

Fig. 2.1: Standard radiotherapy treatment machine and coordinate system according to the IEC61217 standard. Machine illustration courtesy of Elekta Ltd

The PSS has four degrees of freedom: Forward-backward (Y-axis or longitudinal axis), left-right (X-axis or lateral axis), up-down (Z-axis or height axis), and one rotational (around the vertical Z-axis referred to the iso-center). Note that manufacturers also have their own coordinate systems. It is essentially used to position the patient's under the radiation beam. The radiation beam produced by a LINAC gantry can be shaped and aimed at the target from various directions by rotating the gantry and moving the PSS

simultaneously.

CyberKnife system

Tumour induced organ motion is difficult to track with conventional LINAC based systems, and the accuracy of such an approach would inherently be very limited. In contrast, modern robotic manufacturing relies on highly accurate motion control and high unit numbers. The CyberKnife is frameless radiation treatment system that incorporates a six degree of freedom robotic arm to precisely position a linear accelerator as well as imaging system [Schweikard et al. 2000, Wilson 2006]. Similarity to LINAC system, CyberKnife system contains a couch and positioning system (see Figure 2.2).

Fig. 2.2: Components of a CyberKnife Suite.

The imaging system consists of a stereo low-energy x-ray source mounted on the ceiling that generates two perpendicular diagnostic x-rays. Coupled with a pair of x-ray detectors mounted orthogonally in a 'V' shaped frame and fixed to the floor directly below the robot isocenter. This system determines the location of bony landmarks or implanted radio-opaque fiducials. A control system compares periodically acquired images from the x-ray detectors with preoperative CT images, providing feedback to realign the LINAC to compensate for patient movements [Wilson 2006]. Although such system can follow the slow rate motion such as the brain tumour, a high rate motion (lung tumour for example) is hard to follow without any prediction.

2.2.3 Intensity modulated radiotherapy (IMRT)

As the shape of tumour is irregular and may change during treatment process because of different factors such as respiratory motion, then, the beam field must be shaped to reduce the irradiation of adjacent normal tissues. The conformal radiation therapy (CRT) offers the greatest advantage at sites where existing local control is limited by the collateral dose to normal structures. As its name implies, IMRT allows to modulate the intensity of each radiation beam, so each field may have one or many areas of high intensity radiation and any number of lower intensity areas within the same field, thus allowing for greater control of the dose distribution with the target. The introduction of IMRT has further improved outcomes by increasing organ sparing, providing better local control of disease, enhancing quality of life and reducing treatment associated morbidity.

In contrast to CRT, in which the shaping was achieved using two pairs of metal blocks called ‘jaws’, the IMRT employ multiple opposing metal slats [Bortfeld et al. 2006, Webb 2001, Meyer 2001, Goodband 2006]. Collimator devices (see Figure 2.3) are the most used tools to shape the radiation fields to match the geometry of the tumour. Initially developed for CRT, MLC are the most versatile device to focus and shape the beam. They are located in the head of LINAC perpendicular to the central axis and consist of a set of parallel opposed mobile tungsten leaves [Meyer 2001]. Each leaf can be controlled independently in the forward or in reverse direction. Beam modulation can be achieved by varying the position of the leaves over time during irradiation. This can be done dynamically (DMLC), referred to as dynamic-leaf-sweep or sliding window technique, which is addressed in [Boyer and Strait 1997], with the leaves in motion during irradiation. It can also be achieved statically by delivering multiple static fields, also denoted the step-and-shoot technique, in which the MLC are positioned in different position for each sub-field.

Fig. 2.3: An illustration of an industrial MLC. Photo courtesy of Varian Medical Systems of Palo Alto, California. Copyright 2003, Varian Medical Systems.

IMRT involves an advanced concept to deliver 3DCRT known as inverse treatment planning with optimisation by computer. As distinct from the forward planning process, where only the best beam configuration is taken after different tries, the inverse process starts with the required dose distribution and constraints imposed on the problem, then uses a computer to calculate the optimal beam weight and directions [Goodband 2006]. There are several techniques to deliver IMRT, including metal compensator, MLC operation in multiple static-field mode, DMLC, intensity modulated arc therapy (IMAT), slice-based tomotherapy with a multi-vane intensity modulating collimator (MIMiC), spiral tomotherapy, CyberKnife and Non-MLC-based techniques (concepts) [Bortfeld et al. 2006].

2.2.4 Adaptive and image guided radiotherapy

The IMRT technique provides the capability of delivering a highly conformal radiation dose distribution to a complex static target volume. However, treatment errors related to internal organ motion may greatly degrade the effectiveness of conformal radiotherapy for tumours located in the thoracic and abdominal regions, especially when the treatment is done in a hypo-fraction or single fraction manner. This has become a pressing issue in the emerging era of IGRT. This latter makes use of many different imaging techniques ranging from portal imaging and fluoroscopy to MV cone-beam CT and following regimens as simple as a single set-up image or as complex as intrafraction tumour tracking [Murphy 2004, Mageras 2005, Jaffray 2005, Xing et al. 2006, Huntzinger 2004].

The process of IGRT involves all steps in the treatment including patient immobilisation, CT simulation, treatment planning, plan verification, patient set-up verification and correction, delivery, and quality assurance (QA). Many IGRT solutions have been proposed to resolve the problem of target definition and beam targeting. Briefly, IGRT developments are focused in four major areas: (1) biological imaging tools for better definition of tumour volume; (2) time-resolved 4D imaging techniques for modelling the intra-fraction organ motion; (3) on-board imaging system or imaging devices registered to the treatment machines for inter-fraction patient localisation; and (4) new radiation treatment planning and delivery schemes incorporating the information derived from the new imaging techniques.

A full implementation of IGRT will lead to the concept of ART [Yan et al. 1997a, Yan 2004]. In this process the dose delivery for subsequent treatment fractions of a course of radiotherapy can be modified to compensate for inaccuracies in dose delivery that cannot be corrected for by simply adjusting the patient's positioning. The causes of these inaccuracies may include tumour shrinkage, patient loss of weight and increased hypoxia resulting during the course of fractionated treatment. This promising procedure is developed in order to track and compensate for tumour and patient motion.

The motivation for the development of such a technique is that if the cancerous cells can be targeted more effectively, then it will be possible to reduce the treatment margins, hence to a reduction of dose absorbed by the healthy tissues. Usually, the treatment planning uses imaging techniques to define a static parameters such as patient position, organ and beam deviation and dose distribution. These parameters can be estimated during the treatment by using a new observation and measurement. For example tumour in abdominal site, parameters such as frequency and magnitude of breathing must be monitored online during the treatment.

2.2.5 Quality assurance (QA) in radiotherapy

The designed treatment may be different from the delivered one, due to various reasons including the inaccuracy of the treatment machines and staff errors. This has came out with a procedure called QA [Kutcher et al. 1994]. In this protocol, the performance of the equipments used for radiotherapy have to be checked regularly in order to ensure that the therapy unit performs according to specifications, and that the unit is safe to use for patients and staff. It can also be referred to the assessment of a new radiotherapy treatment system or strategy. Usually, physical objects called phantoms are used during quality checks. Several phantoms to simulate the motion of lung have been proposed [Hugo et al. 2002, Zhou et al. 2004, Nioutsikou et al. 2006].

2.3 Radiotherapy uncertainties

RT uncertainties are a (possibly large) source of unknowns (or errors) that act during treatment preparation and delivery. The main ones are organ motion and patient positioning (set-up) [Hurkmans et al. 2001, Langen et al. 2001, Booth 2002, Herk 2004, Goitein 2004]. Understanding these uncertainties, their characteristics and causes, and techniques to control or reduce them are very important for comprehensive health care. A thorough understanding of the treatment uncertainties is also required if these latter or part of it, is to be modelled, which is one task of this thesis. Uncertainties in radiotherapy process have been classified into systematic and random. *Systematic errors* act during treatment preparation and *random errors* during the delivery execution. Both errors have an impact on the entire treatment. As consequence, a safety margin is required to ensure that the prescribed dose is delivered to the target volume.

The international commission on radiation units and measurements (ICRU) report 50 and supplement report 62 [ICRU 1994; 2000], provide general guidelines to accommodate for uncertainties in planning of EBRT treatments. In the latter, several target and critical structure volumes and margins that help in

the treatment planning process and that provide a basis of comparison of treatment outcomes have been defined and described.

The gross tumour volume (GTV) is defined as the obvious tumour volume which has been delineated using imaging modalities, reference frame of the bony anatomy and clinical examinations, by the clinician, and must be eradicated. Usually, the treatment can take several days which is accompanied with microscopic extent of the tumour or growth. This clinical growth is also involved by adding a fixe or variable margin to the GTV to obtain what it is called clinical target volume (CTV). The planning target volume (PTV) includes both internal margin (IM) to account for uncertainties in organ shape, size, and motion, and setup margin (SM) to account for beam geometry and patient set-up. Internal target volume (ITV) is defined as the Clinical target volume (CTV) plus IM.

Important organs around the tumour and their movement are also involved in the planning by introducing the quantities organ at risk (OAR) and planning organ at risk (PRV). In Figure 2.4 a graphical representation of the volumes of interest are depicted. The size of treatment margin depends on the site to be treated and clinical experience of the clinician. More details about designing margins can be found in [Herk 2004, Booth 2002, Ekberg et al. 1998].

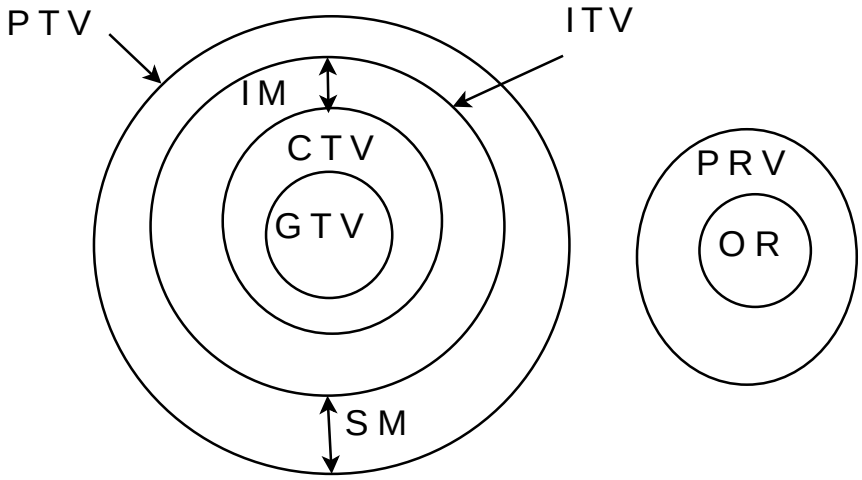

Fig. 2.4: Volumes and margins definitions.

2.3.1 Patient positioning

During the treatment delivery, the position of the PTV with respect to the beam, may differ from the intended or reference position, done at planning stage. Consequently, systematic differences between the planned patient position and its average position over a course of fractionated therapy may exist. This is due to many factors including inaccurate alignment of positioning devices and differences in cushioning capacity of couch material between CT and treatment [Booth 2002, Hurkmans et al. 2001]. Random error

can also exist between the daily patient positions and the desired patient position, due to factors such as the width of positioning laser beams and human error. The patient positioning errors then can be defined as consisting of systematic and random components [Herk et al. 2000, Hurkmans et al. 2001, Bortfeld et al. 2002, Booth 2002].

The reference patient position is recorded on a reference image, being either a simulator image or a digitally reconstructed radiograph (DRR) in which anatomical structures (e.g. bone, lung, body contour), radio-opaque markers (if any) and the outline of the field which is used to generate the image are seen [Hurkmans et al. 2001]. It is more common to use EPID rather than MV films because of time consuming and less accuracy of these latter [Hurkmans et al. 2001].

Generally the coordinate system that is adopted is based on the patient coordinate system. It is defines by X in the medial-lateral (ML) direction, Y in the anterior-posterior (AP) (or ventral-dorsal) direction and Z in the superior-inferior (SI) (or Cranial-Caudal (CC)) direction [Booth 2002, ICRU 1987]. Figure 2.5 illustrates this defined motion directions. The positive and negative directions do differ in the literature. In practise, the orientation and direction of X, Y, Z is based on the linear accelerators software specifications and may differ between corporations.

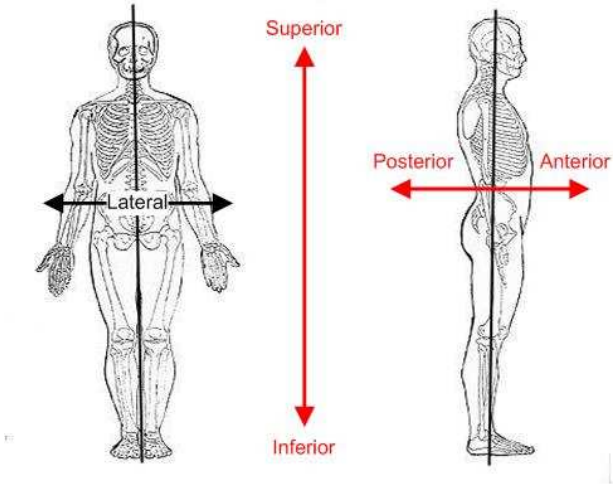

Fig. 2.5: Motion directions.

A selection of the studies investigating set-up measurement errors in the thoracic region is presented in Table 2.1. For the lung, set-up errors in the order of 2 to 4 mm have been reported in [De Boer et al. 2001]. In [Hurkmans et al. 2001], it has been reported that the range of standard deviation of *systematic error* is 1.8-5.1 mm and 2.2-5.4 mm for *random error*. A small predominance of set-up errors in ML and CC directions, comparing to AP direction was showed in [Vijlbrief et al. 1998]. The set-up errors for lung cancer irradiations are generally larger than set-up errors for prostate and head and neck treatments. This is mainly caused by the lack of rigid structures like the skull or hipbones, which can be used to

immobilise the patient, and breathing motion [Hurkmans et al. 2001].

To reduce the set-up errors different methods have been investigated. For example, DeSteene *etal.* [DeSteene et al. 1998] has introduced an on-line correction protocol. After correction using a computer controlled treatment couch, the overall set-up errors in the ML and CC direction were reduced from 5.7 mm and 4.5 mm ($\pm$1 mm standard deviation (SD)) to 1.2 mm and 1.0 mm ($\pm$1 mm SD), respectively. In [Bortfeld et al. 2002] methods based on single set-up correction of the $(N+1)^{th}$ treatment fraction by using the set-up measurements of the previous N fractions. It is argued in [Bortfeld et al. 2002] that in many cases it might be sufficient to correct the systematic errors and accept the random errors. The set-up position is achieved by the mean of the landmarks clearly visible like bone, on the EPID or portal film. This involves both random and systematic error.

Although many mechanisms exist to monitor and manage target positioning, the application of EPIDs is becoming a standard tool for this purpose [Herman 2005]. EPIDs image quality has rivalled or exceeded that of film almost since its inception in the 1980s, [Kruse et al. 2002]. These devices have sub-millimeter spatial resolution and sufficient contrast resolution (superior to film) [Munro 1995] to image most bony anatomy or a small metallic marker implanted in 30 or 40 cm of tissue.

Tab. 2.1: A summary of few patient set-up errors studies.

Authors, year.	Type of measurement	Direction	No. of patients	No. of images	$\sigma_{systematic}$ (mm)		σ_{random} (mm)	
					Immobilisation	No Immobilisation	Immobilisation	No Immobilisation
[Yan et al. 1997b]	EPID	AP	27	431	-	-	-	-
		ML			-	2.5	-	2.3
		SI			-	3.5	-	2.7
[Vijlbrief et al. 1998]	EPID	AP	35	375	-	1.8	-	2.2
		ML			-	2.1	-	2.9
		SI				2.5		2.9
[DeSteene et al. 1998]	EPID	AP	16	98	0.8 deg	-	1.1 deg	
		ML			5.1	-	2.5	-
		SI			2.8	-	3.5	-
[Samson et al. 1999]	EPID	AP	8	53	-	-	-	-
		ML			2.5	-	2.0	
		SI			2.0	-	2.8	
[Halperin 1999]	Film	AP	11	170	-	-	5.1	-
		ML			-	-	3.7	-
		SI					5.1	
[Halperin 1999]	Film	AP	11	17			3.6	
		ML					5.3	
		SI					5.4	
[Di Yan 2001]		AP			-	-	-	-
		ML					2.5	
		SI					3.5	

2.3.2 Organ motion

The effects of tumour/organ motion in RT can occur in both the imaging and treatment delivery stages. In the imaging stage, tumour/organ motion can generate two effects. First, imaging of moving tumours during CT scanning can causes artifacts and hence distortion of the target volume and incorrect positional and volumetric information [Chen et al. 2004]. One reason of these motion artifacts is that different parts of the object move in and out of the CT slice window during image acquisition [Keall et al. 2006b]. Second, the image is distorted because of the relative speed of motion and scanning.

Three different scenarios of scanning moving tumours have been given in [Chen et al. 2004, Jiang 2006a]: i) If the scanning speed is much slower compared with the tumour motion speed, the images are smeared. ii) If the CT-scanning speed is much faster than the tumour motion speed, then the target position and shape are captured at an arbitrary breathing phase. iii) If the scanning speed is comparable with the tumour motion speed, which is the case of most currently available helical CT scanners, the captured tumour position and shape can be heavily distorted.

Radiation delivery in the presence of intrafraction organ motion causes an averaging or blurring of the static dose distribution over the path of the motion. This displacement results in a deviation between the intended and delivered dose distributions. Assuming a static beam, the total positional error affecting the dose is the composite vector of internal (e.g., tumour-bone) and external (bone-treatment room) displacements. Thus, for conventional (non-IMRT) treatments, in which the dose gradient in the center of each field can be assumed to be fairly small, the effect is manifested by a blurring of the dose distribution by the anatomy moving near the beam edges, in effect increasing the beam penumbra. This effect is thought to be exacerbated during IMRT delivery, causing motion artifacts in dose distribution due to the interplay between motion of the leaves of a MLC and the component of target motion perpendicular to the beam [Keall et al. 2006b]. However, it was found in [Herk 2004, Engelsman et al. 2001] that respiration motion with clinical relevant amplitude has a small impact on the dose compared with other errors that may occur in clinical practice.

2.3.3 Other uncertainties

Set-up errors and tumour motion are not the only factors causing uncertainty in the position of the CTV. The predominant error after set-up and tumour motion is tumour delineation. Several geometrical uncertainties are involved in the delineation process. The limited resolution of imaging modalities causes a partial volume effect [Links et al. 1998]. The type of imaging modality to define the target volumes can also generate a geometrical error. For example, prostate GTV's defined using MRI have been found to be

30% smaller than those same tumours defined by means of conventional CT scans [Rasch et al. 1999].

The observer or inter-observer can also generate a delineation uncertainty. A comparison among clinicians show a factor of 1.8 variation in the CTV definitions for the same tumour from the same set of images [Ketting et al. 1997]. Tumour delineation is discussed in the [ICRU 2000] document, and should be considered in the definition of a PTV, but is not explicitly described as belonging to either the IM or setup margin (SM). Delineation uncertainty is a purely systematic error; it will influence all treatment fractions in an identical way through the treatment planning process.

Approximations of algorithms used in the treatment planning software do exist. The DRR can introduce errors due to sampling and digitisation resolution [Hurkmans et al. 2001]. The inter-observer variation introduced by the manual matching of a reference image and a portal image could also introduce substantial measurement errors [Bissett et al. 1995]. Today's computer aided delineation tool provided with EPID software facilitate this registration process and make it more consistent .

The source of setup errors can be mechanical due to the equipment accuracy or technique used for patient positioning and immobilising. Motions of the patient table (especially lateral table tilting) are likely to cause involuntary counter-motion of the patient. Such involuntary motions lead to muscle contraction, changes in breathing patterns, and may cause substantial additional inaccuracy. Given the kinematic and size limitations of such systems, most researchers have investigated methods for motion detection rather than active motion tracking.

2.4 Respiratory motion characteristics

Tumour motion is becoming an important issue in IGRT, that can be caused by respiratory, skeletal muscular, cardiac and gastrointestinal systems. However, more research and development has been directed towards accounting for respiratory motion. This includes respiratory system function, breathing motion characteristics and respiratory motion management for radiotherapy.

2.4.1 Respiratory system function

Patient breathing during or within fractions can cause motion of tumours, especially those located in the thorax and abdomen. Therefore, a good understanding of respiratory system function is valuable to identify the component that are responsible of respiration and then motion of tumours. The human body is composed of tissues that require oxygen continually for their normal function, hence, the respiratory system aims to obtain oxygen from the atmosphere, through the nose or mouth, and supply it to the cells,

while excreting the carbon dioxide produced by cellular metabolism, through nose and mouth as well.

The respiratory system is composed of lung, conducting airways, parts of the central nervous system concerned with the control of the muscles of the respiration and the chest wall [Levitzky 2002]. The muscles of respiration consists of diaphragm, intercostal muscles, scalene muscles, Sternocleidomastoid muscles, Pectoralis major, and abdominal muscles. These respiratory muscles, as well as their use in inspiration and expiration, are described in [George 2005].

Fig. 2.6: Right and left lung.

The main function of respiratory system is to exchange the carbon dioxide by oxygen along inspiration and expiration phases, which take place in the lungs [Levitzky 2002, Bronzino 2000]. The lung is the essential organ of the respiration process which consists of two irregular conical-shaped right and left lungs, that occupy the thoracic cavity and separated from each other by the mediastinum and heart. This latter is extends out into the left thoracic space [Cotes 1993], therefore the left lung is smaller than the right lung. The right lung is subdivided into upper, middle and lower lobes. The left lung is subdivided into upper and lower lobes (see Figure 2.6).

During inspiration phase, fresh air, containing oxygen, is inspired into the lungs through the conducting airways. The force needed to cause the air to flow are generated by the respiratory muscles, acting on command initiated by the central nervous system. At the same time, venous blood returning from the various body tissues is pumped into the lungs by the right ventricle of the heart. This mixed venous blood has a high carbon dioxide content and low oxygen content. In the pulmonary capillaries, carbon dioxide is exchanged for oxygen. The blood leaving the lungs, which now has high oxygen content, is distributed to the tissues of the body by the left side of the heart. During expiration phase, gas with a high concentration of carbon dioxide is expelled from the body.

The compression and expansion of the lungs are due to the muscles of respiration which supply a force that induced a rhythmic pattern of neuron-induced action to cause lungs air inspiration and expiration. Hence, respiratory muscles are divided into inspiration and expiration muscles. The muscles of inspiration include the diaphragm, the external intercostal, and the accessory muscles of inspiration. The primary muscle of inspiration is the diaphragm, which is a large dome-shaped muscle that separates the thorax from the abdominal cavity [George 2005].

Inspiration primarily requires contraction of the diaphragm and the external intercostal muscles located between the ribs. Contraction of the diaphragm causes it to move downward and increases the vertical dimension of the thoracic cavity, resulting in pulmonary expansion. Contraction of the diaphragm produces a 75% change in intra-thoracic volume during resting inspiration [Mead and Loring 1982]. The external intercostals contract to elevate the lower ribs and push the sternum outward, increasing the anteroposterior dimension of the thoracic cavity [Kenyon et al. 1997]. Expiration is normally passive because of the elastic recoil.

There is hysteresis in the relationship between pressure and lung volume; lung volume is different between inspiration and expiration at the same pressure [Tiddens et al. 1999]. In voluntary active expiration, the internal intercostal muscles contract and pull the rib cage downward, and the abdominal muscles assist by pulling the rib cage down and increasing abdominal pressure which forces the diaphragm up. Attempts to perform tidal inspiration with the diaphragm alone markedly reduces rib cage expansion and the upper rib cage moves paradoxically. In supine position and during normal quit breathing about two third of the air entering the lungs due to the diaphragm [Levitzky 2002].

Several studies have been carried out to investigate the range of tumours motion (see Table 2.2). Motion of organs has traditionally been studied for cardiac surgery applications and tele-operations [Ginhoux et al. 2003]. It has been classified to voluntary, e.g. patient moving, involuntary, part of his body, e.g. unforced breathing [Shirato et al. 2004b]. Other authors have classified motion as periodic, e.g. due to breathing or heart motion, irregular, e.g. due to difficulties in breathing, and random, e.g. gas in rectum. Understanding the tumour or host organ motion characteristics is necessary for accurate RT. This prior knowledge is also required for appropriate modelling process which is one of the objectives in this thesis. In this paragraph, a brief review of different studies that investigate tumour or respiratory motion is presented.

Several studies have been undertaken on different class of patients including, normal, diseased, young and old, for the purpose of investigating the variability in breathing patterns. Most of the studies attempted to quantify magnitude, direction, period, phase and rate of motions as well as factors that have direct impact on breathing motion. The correlation between these variables has also been investigated. In this section,

a review of different contributions related to the characteristics of breathing are presented.

In the early 1960s, Priban et *al.* [Priban 1963] demonstrated statistically that breath-to-breath fluctuations in respiratory cycle variables, like frequency and tidal volume, were not purely random. In fact, breath-to-breath variations in the breathing pattern can occur as uncorrelated random variations, correlated random variations, or any of the two types of non-random changes: periodic oscillations and non-periodic fluctuations [Bruce 1996]. This breath-to-breath variability and person-to-person and, in general, respiratory motion variability may be attributed to various causes such as central neural mechanisms, anatomic variabilities, genetic variation, pulmonary afferent activities and/or chemoreflex mechanisms [Bruce 1996, Shea and Guz 1992]. Tobin et *al.* [Tobin 1983] have also shown that breathing changes with age and is more regular in young rather than old normal adults.

Samson et *al.* showed that the error in the measurement of the intrafractional motion was reduced if a combination of two match structures was used, compared to using only one structure [Samson et al. 1999]. The spread in ML and CC translations was limited for the clavicle and thoracic wall (<1 mm, 1 mm SD), while the carina exhibited a somewhat greater movement (SD >1 mm). De Boer et *al.* used this combination of two or three match structures to measure the difference in patient position between CT scanning and simulation for a group of 16 patients [De Boer and Heijmen 2001]. If the CT data are used for treatment planning, these differences lead to systematic treatment set-up errors. They found errors of 4, 1 and 3 mm (1 mm SD) in the ML, CC and AP direction, respectively. In the same individual, the tidal volume and frequency can change with the biochemical condition (eg, CO2 concentration, exercise), body position (standing, supine, or prone), abdominal contents (food intake, time elapsed since eating), and emotional condition (anxiety). Respiratory motion of the internal organs depends on the body position, the position of the arms, and the type of immobilisation devices used [Giraud et al. 2001].

2.4.2 Range of motion

Organ motion caused by respiration may result in a large displacement of treatment sites from their planned positions for tumours in the lung, pancreas, thorax and abdomen [Langen et al. 2001, Vedam et al. 2001]. The diaphragm motion creates organ displacement around 50 mm in SI direction and 20 mm in AP direction. The movement was shown in [Langen et al. 2001, Ross et al. 1990, Korin et al. 1992] to be largest in the CC direction for the diaphragm and the carina; with maximum deviations of 22 and 12.5 mm, respectively. For the right and left lung tops and the lateral position of the carina, maximum deviations of 4, 2 and 5 mm were observed, respectively.

In an early study, Wade [Wade 1954] measured diaphragm motion using fluoroscopy on 10 males. It was

found that in the supine patients, the average diaphragm motion was 17 mm and 99 mm for normal and deep breathing, respectively. The right hemi-diaphragm motion was investigated in [Weiss et al. 1972] involving 30 patients using fluoroscopy images. During quiet breathing, the diaphragm moved 13 ± 5 mm in supine patients. Under deep breathing conditions, the movement ranged from 12 to 75 mm. A tumour motion of 10-25 mm in 7 FB patients was reported in [Ohara et al. 1989]. Intra-thoracic tumour movement with respiratory and cardiac motion using ultrafast computerized tomography (UFCT) scanner was investigated in [Ross et al. 1990]. It was noticed in the latter a minimal movement for tumours of the upper lobe or those attached to the chest wall in 20 patients, but observed motion of the order of 10 mm for hilar and lower lobe tumours. Kubo et *al.* [Kubo and Hill 1996], using fluoroscopic movies, observed tumour motion of approximately 15 mm in 1 of 3 patients.

The MRI techniques was employed in [Korin et al. 1992] to study motion of the upper abdominal organs in 15 volunteers. The average peak-to-trough (PTT) diaphragm movement was 13 mm during normal breathing and 39 mm during deep breathing. Ultrasound was employed in [Davies et al. 1994] to study motion of kidney, liver, and diaphragm with respiration in 9 supine patients. Under normal respiration, the mean peak-to-trough (PTT) liver motion was 10 ± 8 mm, with a range of 5-17 mm. Under deep breathing, the mean liver motion was 37 ± 8 mm (range 25-57 mm). The above values refer to the SI direction of motion. For the AP and lateral directions, motions were less than 2 mm under both respiration conditions. Typical variations in the respiratory motion patterns of 10 to 20 mm for the same patient (in pediatrics) is reported in [Sontag et al. 1996].

Using fluoroscopic images, Kubo and Hill [Kubo and Hill 1996], studied the motion of the chest wall for three lung patients and one breast patient. It has been found that the right chest wall moved laterally by 5-7 mm and the anterior chest wall moved vertically 2-8 mm. To evaluate the motion of CTV due to respiration and other internal organ motions, fluoroscopy at simulator was performed for 20 patients in [Ekberg et al. 1998]. All patients were immobilized in the treatment position using an individual polyurethane foam cast. They found an average CTV movement with quiet respiration was about 2.4 mm (range: 0-5 mm) in the ML and AP directions. Movement in the CC direction was on average 3.9 mm with a range of 0-12 mm (range: 0-12 mm).

The SI excursion of the right diaphragm using fluoroscopic movies was investigated in [Balter et al. 1998]. Twelve patients participated in the study that was performed under normal breathing conditions. The average excursion movement was 9.1 mm and had a SD of 2.4 mm. In [Hanley et al. 1999], the tumour motion due to respiration was assumed to be 10-20 mm in the PTV design. In the latter, fluoroscopy images were used to measure the movement of the diaphragm under deep inspiration breath hold and normal breathing conditions in five supine lung cancer patients. During FB, the mean diaphragm

movement was 26.4 mm, during a single breath hold 1 mm, and between different breath holds 2.5 mm.

CT scans of 13 patients with a total of 16 lung tumours during normal breathing were investigated in [Shimizu et al. 2000b]. These CT scans were taken at the same position over a time interval and thus the AP movement of a tumour could be found. Estimates of the CC motion of the tumours were made assuming the tumours were spherical using simple trigonometry. Where a tumour's motion caused it to completely disappear from the CT scan it was assumed that it had a displacement equal to the radius of the tumour. Tumours in the upper and lower lobes of the lung were differentiated. It has been found that the movement in AP direction was less than 10 mm in 80% of the cases but could be as much as 24 mm for a tumour in the lower lobe. The estimated mean amount of CC movement for tumours at the upper/middle lobe was 6.2 mm, and ranged from 2.4 to 11.3 mm; the mean value for tumours of the lower lobe was 9.1 mm and ranged from 3.4 to 24.0 mm.

Twenty patients were involved in a study done by Seppenwoolde et *al.* [Seppenwoolde et al. 2002b]. Seventeen of them had non-small cell primary lung cancer and 3 had metastatic tumours. A 2 mm gold marker was implanted in or near the tumour and its position was recorded 30 times per second using fluoroscopy during treatment. The average amplitude of the tumour motion was greatest (12 ± 2 mm) in the CC direction for tumours situated in the lower lobes and not attached to rigid structures such as the chest wall or vertebrae. For the lateral and AP directions, tumour motion was small both for upper- and lower-lobe tumours (2 ± 1 mm). Chen et *al.* [Chen et al. 2001], have assessed the tumour motion of 20 patients, with help of simulation fluoroscopy. Tumour motion varies in a range of 0 to 50 mm. From the 20 patient, only 10 where the diaphragm was reliably detectable. The range and the average of the diaphragm motion for 10 patients were 60 mm and 26 mm, respectively.

Neicu et *al.* [Neicu et al. 2003], have carried out an analysis of breathing pattern regularity of 11 data-sets. These breathing data were selected from 41 lung tumour measurement in CC with maximum peak-to-peak motion greater than 10 mm. The average amplitude (for every data-set) was 7.6-22.5 mm, with relative standard deviations of amplitude (σ/A_{avg} $\%$) 6%-49%. Murphy et *al.* [Murphy et al. 2002a], reported that lung tumours can move by 5 mm to 25 mm during regular breathing.

Shimizu et *al.* [Shimizu et al. 2000c; 2001] have used the same system as Kitamura et *al.* [Kitamura et al. 2002] to record the movement of implanted lung-tumour markers at 30 Hz showing that, with free breathing, markers moved up to 16 mm. Onimaru et *al.* [Onimaru et al. 2005], have used data collected by a real-time tumour tracking radiotherapy (RTRT) system on 39 patients, to evaluate The effects of tumour location and pulmonary function on the motion of fiducial markers near lung tumours. They found a median tumour movements in the ML, AP, and CC directions were 1.1 mm, 2.3 mm, and 5.4 mm, respectively. There was no significant correlation between respiratory function and magnitude of

marker movement in any direction. Gierga et *al.* [Gierga et al. 2005], examined the correlation of external markers and abdominal tumour using fluoroscopy sessions for 4 patients. The maximum amount of peak-to-peak SI tumour motion was 25 mm. The most comprehensive publication on organ motion and its management by Langen and Jones [Langen et al. 2001] collated tables of studies for liver, diaphragm, kidneys, pancreas, lung, bladder, rectum and prostate from 66 studies.

Depending on the survey, organs considered and direction, typical movements for normal breathing are in the order of 30 mm. The largest displacement occurs in the chest for deep breathing. Normal or quiet breathing motion tends to be limited to 20 or 30 mm although this differs depending on the organ and the direction of motion.

Tab. 2.2: A summary of different motion studies. Negative values represents displacements in the opposite direction to the measurements

Authors, year.	Site	Technique	No. of patients	Immobilization	Displacement [mm]								
					SI			AP			ML		
					$\overline{z}$	σ_z	Range	$\overline{y}$	σ_y	Range	$\overline{x}$	σ_x	Range
[Ross et al. 1990]	ULB	CT	20	NO	NA	NA	NA	1.4	NA	NA	1	NA	NA
–	MLB	–	–	NO	NA	NA	NA	0	NA	NA	9	NA	NA
–	LLB	–	–	NO	NA	NA	NA	9.8	NA	NA	10.5	NA	NA
[Ekberg et al. 1998]	Lung	Fluoroscpy	20	Yes	3.9	2.6	0-12	2.4	1.3	0-5	2.4	1.4	0-5
[Balter et al. 1998]	Diaphragm-Right side	–	12	NO	9.1	2.4	NA	NA	NA	NA	NA	NA	NA
[Hanley et al. 1999]	Diaphragm	–	5	YES	12	NA	1-20	5	NA	0-13	1	NA	0-1
[Shimizu et al. 2000b]	LLB	–	13	NO	9.1	NA	3.4 to 24	<10	NA	NA	NA	NA	NA
–	ULB/MLB	–	–	–	6.2	NA	2.4 to 11.3	NA	NA	NA	NA	NA	NA
[Barnes et al. 2001]	LLB	–	–	-	18.5		9-32	NA	NA	NA	NA	NA	NA
–	MLB,ULB	–	–	-	7.5		2-11	NA	NA	NA	NA	NA	NA
[Chen et al. 2001]		Fluoroscpy					0-50	NA	NA	NA	NA	NA	NA
[Engelsman et al. 2001]	MLB,ULB	–					2-6	NA	NA	NA	NA	NA	NA
–	LLB	–					2-9	NA	NA	NA	NA	NA	NA
[Shimizu et al. 2001]		–			–	–	–	6.4		2-24	–	–	–
[Stevens et al. 2001]		CT			4.5		0-22						
[Giraud et al. 2001]	Diaphragm-Right side	–	10/20	Alpha cradle	34.25	20.51	6.7-63.4	NA	NA	NA	NA	NA	NA
–	–	–	–	Posirest device	29.7	18.09	3.1-54.0	NA	NA	NA	NA	NA	NA
–	Diaphragm-Left side	–	–	Alpha cradle	42.1	22.59	13.2-95.0	NA	NA	NA	NA	NA	NA
–	–	–	–	Posirest device	30.6	14.94	3.8-58.8	NA	NA	NA	NA	NA	NA
–	Lung apices-Right side	–	–	Alpha cradle	2.9	3.19	0.8-11.2	4.9	2.95	1.1-9.1	6.8	4.25	1.9-15.4
–	–	–	–	Posirest device	11.6	8.14	3.6-28.2	10.7	5.02	3.6-18.7	8.2	3.10	3.5-12.9
–	Lung apices-Left side	–	–	Alpha cradle	4.0	5.17	0.1-17.6	7.3	4.15	2.3-12.1	4.0	1.80	1.6-7.3
–	–	–	–	Posirest device	13.6	6.71	3.6-24.7	8.8	5.37	1.9-15.8	6.3	8.99	-16.1-17.6
–	Carnia	–	–	Alpha cradle	-9.8	6.28	-18.0-1.5	5.5	3.69	0.6-9.8	1.0	2.39	-2.3-4.8
	–	–	–	Posirest device	-11.1	8.22	-29.3-(-5.3)	8.9	6.44	0.5-18.8	-3.7	3.81	-10.2-2.3
–	Thorax-ULB	–	–	Alpha cradle	NA	NA	NA	10.7	8.58	2.0-28.5	7.8	5.37	2.2-17.6
	Thorax-MLB	–	–	–	–	–	–	9.7	7.18	0.7-19.5	2.70	1.58	1.5-6.4
	Thorax-LLB	–	–	–	–	–	–	9.8	6.94	1.0-18.4	4.0	2.45	1.3-8.1
	Thorax-ULB	–	–	Posirest device	–	–	–	21.7	9.33	7.6-37.3	12.2	5.87	7.7-28.4
	Thorax-MLB	–	–	–	–	–	–	16.9	9.90	2.9-30.7	18.6	18.91	0.5-50.5
	Thorax-LLB	–	–	–	–	–	–	15.4	9.28	2.6-29.7	25.1	25.22	2.9-64.1
[Murphy et al. 2002b]		Fluoroscopy			7	–	2-15	–	–	–	–	–	–
[Seppenwoolde et al. 2002b]	ULB	–	11	NO	2.0	2.2	0.2-8.7	2.2	1.9	0.2-8.2	1.2	0.9	0.4-2.8
	MLB	–	2	–	5.9	1.05	0.7-11.1	3.5	0.4	1.2-5.8	0.65	0.2	0.2-1.1
	LLB	–	8	–	12	6	5.4-24.6	2.2	1.9	0.2-8.2	1.2	0.9	0.4-2.8
[Erridge et al. 2003]	13ULB, 12 LLB, MLB	EPID	25	–	12.5	7.3	5-34	9.4	5.2	5-21	7.3	2.7	3-13
[Grills et al. 2003]		CT					2-30			0-10			0-6
[Sixel et al. 2003]		–					0-13			0-5			0-4
[Plathow et al. 2004]	LLB	MRI			9.5		4.5-16.4	6.1		2.5-9.8	6.0		2.9-9.8
–	MLB	–			7.2		4.3-10.2	4.3		1.9-7.5	4.3		1.5-7.1
–	ULB	–			4.3		2.6-7.1	2.8		1.2-5.1	3.4		1.3-5.3

2.4.3 Frequency of motion

Some of the earliest data collected on the range in frequency of breathing observed in adults shows that they can be anywhere between 0.1 to 0.5 Hz [Quetelet 1842]. According to Shirato et *al.* [Shirato et al. 2004b], the breathing frequency of a healthy person at rest can be between 0.2 and 0.25 Hz. The inspiratory and expiratory durations also showed that there could be several combinations of the inspiration time and the expiration time. Golla et *al.* [Golla and Antonovitch 1929], found that some normal subjects have regular breathing while others have habitually irregular breathing. According to [Benchetrit 2000a], individuals have different traits that make it possible to recognise them amongst others.

Seppenwoolde et *al.* [Seppenwoolde et al. 2002b], found a typical breathing has a frequency 0.2-0.3Hz. Typical variations in the frequency of a single respiratory cycle of 0.2-0.5 Hz, for the same patient (in pediatrics) is reported in [Sontag et al. 1996]. In [Neicu et al. 2003], it was found that the average frequency (for every data set) changes from 0.25 Hz to 0.4 Hz with a mean value around 0.3 Hz and relative standard deviations of period (σ/T_{avg} %) in percentage 7%-25%. In the latter contribution [Neicu et al. 2006], analysis frequency of breathing for 60 volunteer data sets with duration of 240 s. They reported an average breathing frequency ranges from 0.2 to 0.3 Hz with a mean value of 0.2 Hz.

Chen et *al.* [Chen et al. 2001] calculated frequencies between 0.3 Hz and 0.7 Hz for 20 patients. These were strictly measured during quiet respiration and did not take into account the effects of sighing and deep inhalation. By analysing the spectrum of obtained videos, they found a peak location at 0.36 Hz. Gierga et *al.* [Gierga et al. 2005], examined the correlation of external markers and abdominal tumour using fluoroscopy sessions for 4 patients. It was found that the period of the breathing cycle ranged from 0.2 Hz to 0.4 Hz. Moreover, a frequency analysis of fluoroscopic image sets has shown similar frequency components in the motion of abdominal wall and the motion of liver tumours in both the AP and SI direction.

To assess the frequency and amplitude of the periodic physiological organ motion during radiotherapy treatment Diez et *al.* proposed a new method based on cross-correlations with matched filters [Díez et al. 2004]. Once the acquisition of fluoroscopic sequences has been collected, a reference image is cross-correlated with the image sequence using matched filters. The correlation values grow and decrease following the periodic movement of the respiration, building a correlation wave. The correlation value is maximal when the reference image is correlated with itself (autocorrelation). The respiration frequency can be detected by applying a Fourier analysis of the correlation wave.

2.4.4 Motion speed and acceleration

The speed of breathing motion depends on patient. However, according to [Schweikard et al. 2000] typical respiratory velocity is of the order 2-4 mm$\cdot s^{-1}$. Note that when the patient is stressed the velocity of motion could be significantly greater. The only study that contains data regarding velocity and acceleration of organs due to respiration was done in [Davies et al. 1994]. Velocities in the range of 5-15 mm$\cdot s^{-1}$ and accelerations between 10 and 25 mm$\cdot s^{-2}$. Seppenwoolde et *al.* [Seppenwoolde et al. 2002b], found that the average speed of lung and liver tumours is on the order of 10 mm$\cdot s^{-1}$ (assuming the peak-to-peak motion amplitude is about 20 mm and the period is about 4s).

The phantom used in [Shirato et al. 2000b] possessed only one axis of rotation and was capable of speed of about 40 mm$\cdot s^{-1}$. Note, however, that the speed of the markers on the four patients included in the study was in the range 0.5-30.3 mm$\cdot s^{-1}$. In [Fitzpatrick et al. 2005] the speed of the signal obtained from a real time position management (RPM) respiratory monitoring device from Varian Medical Systems, Palo Alto CA, was found to range from 0.4 mm$\cdot s^{-1}$ to 20 mm$\cdot s^{-1}$ with an average speed of 8 mm$\cdot s^{-1}$.

2.5 Respiratory motion management

Significant amount of work has been devoted to limit tumour motion due to the respiration. Investigators are pursuing several strategies that range from simple and unobtrusive to complicated, quasi-invasive, and quite costly. The aim is to reduce the dose margins and dose targeting error associated with respiratory motion. The traditional way to account for organ motion is to add a safety margin to the CTV to get the PTV [Herk 2004]. Control of breathing motion has also been introduced, using techniques such as breath holding, forced shallow breathing (such as jet ventilation) and abdominal compression [Hanley et al. 1999, Mah et al. 2000, Rosenzweig et al. 2000, Wong et al. 1999, Stromberg et al. 2000, Remouchamps et al. 2003a;b]. Another category of methods allow free tumour motion while adapting the radiation beam to the tumour position by either respiratory gating, beam tracking, or couch-based and MLC-based motion compensation [D'Souza et al. 2005]. Organ motion has also been included in the calculation of the dose distribution [Lujan et al. 1999].

2.5.1 Margin expanding

This is the traditional approach to account for organ motion and setup uncertainties. The extent of these latter are measured or estimated, and margins are added around the CTV to form the PTV, to ensure that the entire CTV will receive the prescribed dose [ICRU 1994; 2000, Herk 2004]. The size of the

margin has to be large enough to ensure the delivery of the prescribed dose to a moving target and small enough to keep the normal tissue complications to an acceptable level. The size of the margins needed to compensate for the different variations and uncertainties varies from one anatomical region to another and is dependent on the treatment technique, fixation, etc.

Several margin designing techniques have been proposed. For example, in the Northern Association of Clinical Physics recommendation [Aaltonen et al. 1997], separate margins were proposed for positioning uncertainty and for organ motion, called the setup margin and the internal margin, respectively. This concept of separate margins suggests that a linear separation of the internal errors (organ motion) and setup errors can be made. However, because external error sources and internal error sources are generally not correlated, a linear addition of their standard deviations is, in general, not correct [Herk et al. 2000]. An overview of different margin recipes can be found in [Herk 2004].

The main difficulties with this margin enlarging is that the motion must be measured accurately and applying additional margins may lead to increased dose to normal tissues. In addition, it does not describe the effects of the uncertainties on the normal tissues near the CTV. Therefore, this approach has been extended by incorporating the uncertainties on the dose calculation, thereby giving more complete and accurate information on the dose delivered to both the target volume and the nearby normal tissues [Lujan et al. 1999]. This is based on a convolution of static dose distribution with a function (generally Gaussian) representing the distribution of uncertainties from setup and intrafraction organ motion.

2.5.2 Breath-holding

The obvious approach to reduce healthy tissues overdosing is to minimise the motion itself, and the simplest way to do that is via breath holding. This can be done passively [Hanley et al. 1999, Mah et al. 2000, Rosenzweig et al. 2000, Kim et al. 2001, Barnes et al. 2001] or actively [Wong et al. 1999, Stromberg et al. 2000].

A voluntary breath holding technique was investigated in [Suramo et al. 1984]. In this study, a bar was placed above the abdomen that touched the patient's skin at the end of their normal inspiration. Patients were asked to hold their breath at this stage. The measured mean motion, relative to that observed during normal breathing, of the liver, pancreas, and kidneys was reduced from 25 to 2 mm, 20 to 1 mm, and 19 to 1 mm, respectively.

Schwartz et *al.* examined kidney movement in patients who held their breath at deep inspiration and expiration [Schwartz et al. 1994]. Alternatively, Blomgren et *al.* investigated the application of abdominal pressure and reported movements of the diaphragm of 10 mm or less during normal breathing [Blomgren

et al. 1995]. For both cases, a mean mobility of less than 3 mm was observed. Balter et *al.* found an average of a 12% difference in liver volumes between breath-hold CT scanning and free breathing (FB) CT scanning [Balter et al. 1996].

Forced breath holding, or active breathing control (ABC), was investigated in [Wong et al. 1999]. The patient breathes through an apparatus that allows the immobilisation of breathing at preselected phases of the breathing cycle. Breathing is suspended for an amount of time that is tolerated by the patient. The acceptance of this technique was tested on 12 patients, 4 of which were lung cancer patients. If breathing was suspended at the end of the normal breathing cycle, all but one lung cancer patient were able to tolerate a breath-holding period of 20 s or longer. This patient tolerated a breath holding period of 15s.

Five of the 12 patients participated in a study where CT scans were obtained using the ABC method and during FB conditions. Two repeat ABC scans of one patient, taken 30 min apart, were used to assess the reproducibility of the diaphragm location. Relative to bony landmarks, the edge of the diaphragm moved, on average, by 1.5 mm. The movement of the liver between 2 ABC scans was examined for 2 patients and was found to be less than 1 mm. This compares with an observed motion of the liver of 4 mm between the 2 opposite extremes of the breathing cycle.

A study accomplished by Giraud et *al.* at two different centers, the Institute Curie and Tenon hospital [Blomgren et al. 1995]. This involved ten patient from each center, all of a similar age (early 60s), weight ($\approx\ 70kg$), height ($\approx\ 167\ cm$), tumour size and tumour stage. The method used was the same at each center; three CT scans were taken, one during FB and two during deep breath-hold. However, at the Institute Curie an alpha cradle was used to immobilise the patient while at the Tenon hospital a posirest device was used to hold patients' arms above their heads. It has found that, the greatest displacements were observed for the diaphragm, and the smallest displacements were observed for the lung apices and carina. The relative amplitude of motion was comparable between the two centers. Also the use of a personalised immobilisation device reduced lateral thoracic movements.

According to a study done by Barnes et *al.* , on 8 patient over 10 after excluding 2 patient because of their incapability to reproduce the deep inspiration breath-hold (DIBH), an extraordinary range of breath-hold periods up to 52s has been achieved [Blomgren et al. 1995]. Kim et *al.* experimented with four different parts of the breathing cycle for breath-hold [Kim et al. 2001]. Murphy et *al.* in a study involving 13 patient, showed that breath-holding can allow the reduction of tumour motion dosimetry margins to 2 mm or less for lung cancer treatments [Murphy et al. 2002b].

Butler et *al.* conducted a study to determine whether more normal lung tissue was excluded from high dose when treating a lung tumour if the radiation were gated [Butler et al. 2004]. They studied gating

on deep-inspiration breath-hold (DIBH; generally 60% of vital capacity), or on 0% (full expiration) and 100% (full inspiration) of tidal volume. Mageras and York pointed out that 60% of patients at Memorial Sloan-Kettering Cancer Center (MSKCC) cannot comply with DIBH [Mageras and Yorke 2004].

Della Biancia et *al.* showed improved normal lung sparing at end inspiration compared with end expiration [Della Biancia et al. 2005]. Gagel et *al.* have found after a study involving 36 patient that using ABC to modify regularity of the respiratory cycle through reduction of breath volume, a significant and reproducible reduction of chest and diaphragm motion is possible, enabling reduction of treatment planning margins [Blomgren et al. 1995].

Breathing hold techniques offer the advantage of being relatively simple to implement. However, they suffer from some disadvantage such as excessive treatment time, extra therapist requirement and limited patient compliance because they require momentary cessation or constraint of breathing by patients who typically already have limited respiratory capacity [Huntzinger 2004, Kubo et al. 2000].

2.5.3 Respiratory gating

Respiratory gating is one of the promising techniques to account for respiratory motion, and which allows patient's FB while adapting the radiation beam to tumour position [Mageras and Yorke 2004, Jiang 2006b]. It operates such that radiation beam is only on within a pre-selected phase or portion of patient's breathing cycle that is detected either directly or indirectly. Usually, a predefined physical window commonly referred to "gate", which its position and width are determined within respiratory cycle, is adopted.

Currently a large proportion of respiratory-gated radiotherapy is performed using either internal gating by fluoroscopic or magnetic tracking of implanted radio-opaque markers [Shirato et al. 1999; 2000a;b, Shimizu et al. 2000b, Seiler et al. 2000, Shimizu et al. 2001, Harada et al. 2002, Hummel et al. 2002, Berbeco et al. 2005], or external gating such as video camera, Spirometer, or strain gauge based systems, relies on the correlation between external and internal motion [Ohara et al. 1989, Kubo and Hill 1996, Ramsey et al. 1999, Kubo et al. 2000, Minohara et al. 2000, Vedam et al. 2001, Keall et al. 2002, Kini et al. 2003, Zhang et al. 2003, Jiang 2006b].

For greater accuracy, the respiratory gating methods require the exact tumour location in real-time. Continuous radiographic and fluoroscopic observation of the tumour during treatment has been employed [Shirato et al. 2000b]. Internal gold markers have been used, to gate the radiation treatment [Shimizu et al. 2001, Harada et al. 2002, Neicu et al. 2003, Shirato et al. 2000b]. However, this approach is often difficult and the skin dose to the patient can be quite high during longer procedures. Instead, the use of ex-

ternal anatomical markers or so-called surrogate motion is being investigated as a method of non-invasive tumour tracking [Keall et al. 2001, Chen et al. 2001, Mageras et al. 2001, Vedam et al. 2003b, Schweikard et al. 2004, Tsunashima et al. 2004, Hoisak et al. 2004, Ahn et al. 2004a, Ionascu et al. 2007]. If the tumour motion and surrogate signal are spatially and temporally correlated, then the tumour position can be deduced.

Research has been carried out to check correlation between external and internal organ motion. Vedam et *al.* [Vedam et al. 2003b] reported a mean correlation coefficient of 0.94, between diaphragm and abdominal motions. Hoisak et *al.* [Hoisak et al. 2004], found a correlation coefficients ranging from 0.51 to 0.98 between abdominal motion and lung tumour motion. Ahn et *al.* [Ahn et al. 2004a] achieved an average correlation of 0.77 between skin and tumour movements with a range between 0.41 and 0.97. Schweikard et *al.* [Schweikard et al. 2004] have also confirmed the hypothesis that external motion is related to internal motion. An evident correlation between 3D tumour motion and external respiratory motion obtained from laser displacement sensors has been found by Tsunashima et *al.* [Tsunashima et al. 2004].

Berbeco et *al.* [Berbeco et al. 2005] have proposed that the fluoroscopically observed change in density of lung can be used to gate to specific breathing phases. Solberg [Solberg 2000] and Kini et *al.* [Kini et al. 2000] have gated therapy using the information from infrared surface markers. Since the emergence of the RPM system (Varian Medical Systems, Palo Alto, CA 94304), there has been an increase in the use of external signals clinically for gating.

Another type of gating based on patient feedback, either auditory or visual has been implemented and evaluated [Kubo and Wang 2002, George et al. 2006, George 2005, Kini et al. 2003]. Kini et *al.* [Kini et al. 2003] used RPM system (Varian Medical Systems, Palo Alto, CA), to evaluated the feasibility of using patient training tools and their effect on the breathing cycle regularity and reproducibility during respiratory-gated radiotherapy. They concluded that audio prompts improves the stability of respiration frequency of the patient but does not maintain the range of respiratory motion, whereas visual prompts control only the regularity of the displacement and the frequency is not reproducible.

Based on this results, combined audio-visual biofeedback was devised to improve the reproducibility of audio-visual biofeedback. Recently Neicu et *al.* [Neicu et al. 2006] described results of audio and visual prompting and demonstrated improvement in the efficacy of so-called synchronized moving aperture radiation therapy, using respiratory traces from single-patient and volunteer sessions.

Several studies [Ford et al. 2002, Minohara et al. 2000, Keall et al. 2002, Mageras et al. 2001, Hugo et al. 2002; 2003, Mageras and Yorke 2004, Keall et al. 2004b] have investigated the effects of respiratory gat-

ing on margin reduction, imaging and delivery. It has been seen that with respiratory-gated radiotherapy, there is better target delineation and therefore a potential margin reduction.

The use of respiratory gating has many advantages over breath-holding techniques, but advanced gating equipment at both imaging and radiation delivery are mandatory. Unlike the conventional radiotherapy in which the beam is delivered continuously, the implementation of gated radiotherapy can achieve up to maximum of twice the time required for conventional radiation delivery as found in [Tada 1998].

Another disadvantage of respiratory gating is baseline shift, i.e. variation of the mean value over time. Based on the analysis by Vedam et *al.* [Vedam et al. 2003b] that external motion is correlated to internal motion, it can be assumed that a baseline shift of the external signal indicates baseline shift of internal organ motion. A baseline shift may cause several problems. The beam may be triggered at the wrong phase of the breathing position or may not be triggered at all. The use of external signals for gating can be subject to a delay which must be taken into account. Finally, it is important to note that respiratory gating reduces but does not eliminate respiratory tumour motion during radiotherapy.

2.5.4 Real-time tumour tracking

Another option to compensate for respiratory motion is to continuously adapt the radiation beam delivery to the changes of tumour position, known as RTTT [Keall et al. 2006b, Murphy 2004, Shirato et al. 2007]. This method can be realised by using a DMLC [Keall et al. 2006a, Webb 2006] or LINAC based robotic arm [Schweikard et al. 2004] or, alternatively, by keeping the tumour under the beam path via couch control [D'Souza et al. 2005]. The effectiveness of real-time tumour tracking system depends on its ability to track tumour position location in real-time, accommodate for system latency, reposition the beam delivery and adapt dosimetry in order to allow for tumour changing and critical structure configurations [Murphy 2004].

Currently, the continuous location of tumour position during the treatment is clinically in use and still under development. A RTRT system is the most advanced technology developed by Mitsubishi Electronics Co, Ltd. (Tokyo, Japan), in collaboration with the Hokkaido University Hospital [Shirato et al. 1999, Shimizu et al. 2000d; 2001, Shirato et al. 2000a;b, Seppenwoolde et al. 2002b, Shirato et al. 2003, Harada et al. 2002].

Using this system, the fiducial markers implanted at the tumour site prior to treatment, can be directly tracked fluoroscopically at a video frame rate of 30Hz [Shirato et al. 2000b]. The LINAC is gated to irradiate the tumour only when the marker is within a given tolerance (gating window) from its planned coordinates relative to the isocenter. The tolerance value was set at ± 1 to ± 3 mm according to the

patient's characteristics and the margin used in treatment planning [Shimizu et al. 2001]. The phantom experiment demonstrated that the geometric accuracy of the tumour-tracking system is better than 1.5 mm for moving targets up to a speed of 40 mm$\cdot s^{-1}$ [Shirato et al. 2000b].

This system, as well as its application in radiotherapy, has been published by the Hokkaido group [Shirato et al. 1999, Shimizu et al. 2000d; 2001, Shirato et al. 2000a;b, Seppenwoolde et al. 2002b, Shirato et al. 2003, Harada et al. 2002, Seppenwoolde et al. 2002b, Shirato et al. 2004b;a, Ahn et al. 2004b, Shirato et al. 2003]. Studies of 3D internal lung tumour movement involving gold markers have been performed on 20 patients in [Seppenwoolde et al. 2002b]. Three-dimensional 3D position of 2.0 mm gold marker inserted into or near the lung tumour mass were recorded at a sampling frequency of 30Hz for more than 10 continuous minutes.

In [Brewer et al. 2004], 3D tracking of surgical clips implanted in 5 patients by means of online two orthogonal fluoroscopic imaging (In CC and ML direction) has been done. The root mean squared error in estimating 2D marker position was 0.47 mm on average. To correct for the rotational error of the CTV, Shirato et *al.* [Shirato et al. 2004a] have used static cubic phantom. The accuracy of the system and the additional dose due to the diagnostic X-ray, and its performance during clinical use have been determined in [Shirato et al. 2000b].

Jiang et *al.* [Jiang 2006b], have reviewed different technical aspect of image-guided respiration-gated RT and explained the implementation of internal gating technique developed by Hokkaido University and external gating from MGH. They pointed out that RTRT is the only system which can monitor the internal position of a tumour during irradiation.

Real-time imaging system such as fluoroscopy has been adopted to directly locate tumour volume at sufficient high frequency. For example, at MGH, a technique has been explored to detect the lung tumour position directly based on the fluoroscopic images [Berbeco et al. 2005]. The idea is to calculate the correlation score between the motion-enhanced reference template and each frame of fluoroscopic images and to generate gating signal based on the score. Preliminary work shows this approach is promising, but still needs further development. Sometimes, the tumour can not be visible on the images due, for example, to its low contrast. Therefore, fiducial markers or an active/passive signaling device implanted around or into the tumour can be applied with fluoroscopy or non-radiographic images. For more details about real-time tumour tracking, the reader can see these contributions [Shirato et al. 2007, Murphy 2004].

Research is being directed toward the use of radio-frequency (RF) devices that can magnetically tracked from outside the patient. Seiler et *al.* . [Seiler et al. 2000] have described a miniature, implantable powered RF coil sensor which can either implanted or otherwise attached to the patient such that it moves

with the tumour or organ of interest. An array of coils is used to create an alternating magnetic field and the induced voltages in the sensor coil are measured. The position of the sensor could be determined by the authors with a accuracy of 1-2 mm. Using a phantom containing an x-ray film, the feasibility of the tracking method was demonstrated. While the phantom was moved along a 2 cm diameter circle at a frequency of 0.25 Hz, the system was used to gate a proton beam on when the sensor was within a 3 mm diameter sphere of a given point. Evaluation of the x-ray film showed that the absorbed dose distribution compared well with that measured on a stationary x-ray film.

In some cases, continuous fluoroscopy imaging of the tumour position is not feasible, hence, it is necessary to infer the tumour position from external respiration signals. However, this concept requires a robust 3D spacial and temporal correlation between the measured respiratory signal and tumour position. The correlation is verified before the treatment and used to predict the tumour position during the delivery. Due to the breathing irregularity, this correlation can be non-stationary. To overcome this problem, the correlation must be updated continuously, during the treatment by using both images and respiratory signals, acquired simultaneously [Schweikard et al. 2000].

Because of the hysteresis nature of the breathing, the 3D relationship between the motion of the external and internal anatomy requires complex models. However, simple linear correlation equations have been found between the relative positions of the diaphragm and the one-dimensional motion of external markers placed at the upper abdomen [Kini et al. 2003, Vedam et al. 2003b]. These correlation equations are patient specific and depend on the breathing method. Fourier analysis of fluoroscopic image sets has shown similar frequency components in the motion of abdominal wall and the motion of liver tumours in both the AP and SI direction [Gierga et al. 2005].

Studies found the respiration motion of the upper abdomen to be in-phase with the diaphragm, and liver, pancreatic and some lung tumours. However, others have shown a time lag for the motion of markers on the chest wall [Ahn et al. 2004a] and lung tumours. Minohara et al [Minohara et al. 2000] found a phase difference of about 0.2s between the position of the diaphragm and the respiratory signal from the light-emitting diode camera system placed under the left rib.

Studies attested to the correlation of external marker motion with the 2D internal motion of the diaphragm [Vedam et al. 2003b, Mageras et al. 2001] or internal markers [Gierga et al. 2005]. However, for a given external marker, the ratio of internal to external marker motion can be relatively large [Gierga et al. 2005]. It has been found in [Ahn et al. 2004a] that skin and tumour experience the same motion and remained correlated for some axes of motion.

Beam tracking radiation therapy seeks to address the problems of gating by moving the radiation beam

dynamically to follow the target volume [Murphy 2004]. This was first introduced in robotic radiosurgery system (CyberKnife) [Ozhasoglu et al. 2000, Schweikard et al. 2000, Murphy et al. 2003, Murphy 2002], and later adopted for motion-adaptive radiotherapy [Shirato et al. 2000a, Keall et al. 2001, Neicu et al. 2003].

For linac-based radiotherapy, tumour motion can be compensated for using a DMLC [Keall et al. 2001, Neicu et al. 2003, Keall et al. 2005, Wijesooriya et al. 2005, Webb 2005b;a]. Linac-based beam tracking is still under development. Much effort is needed to overcome the technical difficulties and to solve quality assurance issues associated with this technique before it can be applied to patient treatment.

At MGH a new beam tracking technique called synchronised moving aperture radiation therapy (SMART), was proposed to account for tumour motion during the treatment [Neicu et al. 2003; 2006]. This technique is based on synchronising the moving radiation beam aperture formed by a DMLC with the tumour motion induced by respiration. The success of this method depends on the precise and fast detection of tumour simulation/treatment and the reproducibility of tumour motion patterns.

The former requirement is performed by a special imaging system integrated radiotherapy imaging system (IRIS) developed at MGH [Berbeco et al. 2004] and the latter one was achieved by an average model of tumour trajectory called average tumour trajectory (ATT), which is derived during treatment simulation stage. During the treatment delivery, respiratory surrogates or implemented markers are monitored and the beam is turned on only when the tumour is within ATT and off if it drift away. Therefore, the radiation beam aperture formed by a DMLC is synchronised with the ATT.

Another approach involving a control of the patient couch to automatically reposition the patient in order to keep the moving tumour in the path of the radiation beams was considered. A feasibility study for such an approach has been reported in [D'Souza et al. 2005]. The couch-based approach has an advantage in that it is potentially able to compensate 3D motion of the tumour, whilst a MLC-based approach is only able to compensate 2D motion. Furthermore, the approach only requires basic modification of the currently available PSS technology and retains the existing gantry-based treatment machine, which is a less expensive and more efficient option compared to the robotic-arm-based approach that needs a new machine configuration.

It was shown that this method is feasible and effective for moving tumours treatment. However, it is very sophisticated and expensive to be use in every hospital. The imaging system used in this approach can introduce more radiation to the patient, and can affect the accuracy of tracking if the imaging system is in poor conditions. Finally, a delay is introduced, and which should be compensated by means of a predictor.

2.6 Discussion

The development of RT was motivated by the existence of treatment uncertainties, which degrade the treatment accuracy. The introduction of techniques such as IMRT, IGRT, and recently ART have improved precision and accuracy to the treatment. To fulfil the expected benefits of the new techniques, organ motion, patient and machine inaccuracy uncertainties have to be reduced. A number of studies have been conducted to understand, quantify, and propose solutions to reduce errors and uncertainties in RT. A range of QA procedures takes place to reduce machines inaccuracy and uncertainties and evaluate the performance of new treatment technique.

The main concern in RT was the problem of organ/tumour motion, and particularly motion due to the natural respiration. Several studies have been undertaken to understand the breathing process and quantify its parameters such as magnitude, frequency and rate of motion. One of the outcomes of these studies was that the respiratory motion patterns exhibit variability from patient to patient and even within the same patient. The respiratory motion was found to be larger in the SI direction and can achieve a maximum displacement of 34 mm. The range in frequency of breathing was reported to be between 0.1 and 0.5 Hz, which means that the length of one breathing cycle can range from 2 to 10s. The speed of breathing depends on the patient and its value can be up to 15 mm$\cdot s^{-1}$.

The traditional approach to account for the organ/tumour motion is to expand the margins to make sure that the whole tumour volume is eradicated, or consider the motion during the dose calculation. Immobilisation techniques are routinely used to reduce the patients' motion. However, the 'best' immobilisation devices, in the sense of maintaining the treatment site virtually immobile, can not be used with every patient. Another way to manage respiratory motion is allow patient's FB and adapt the radiation beam to tumour position, through respiratory gating and RTTT techniques. For the latter, the exact tumour position has to be measured/estimated in real-time. A model of the respiratory motion can be used in this case to replicate the tumour motion during the treatment or in order to assess a new treatment strategy for tumour motion. The IGRT tools have been introduced within the ART approach to improve the treatment of the moving tumours. However, using such approach generates a systematic delay, which can lead to a mismatch of the radiation and tumour position. The last two issues have motivated different research groups to work toward respiratory motion modelling and prediction, in order to achieve a better performance of tumour motion tracking based methods. The next Chapter reviews theses studies to provide a platform against which the work presented in this Thesis can be evaluated.

Chapter 3

Critical review of organ/tumour motion modelling and prediction

3.1 Introduction

The aim of this Chapter is to present a critical review of current radiotherapy treatment techniques to identify shortcomings of current methods and algorithms in view to justify the selection of algorithms presented in the subsequent Chapters. A variety of tumour/patient motion compensation techniques have been developed or are under development. These techniques comprise margin expansion, breath holding, respiratory gating, beam tracking, PSS/MLC based tracking and robotic beam re-alignment (see Chapter 2). Excluding breath holding, all other compensation methods require an adequate understanding of the tumour motion characteristics and its reproducibility. As a consequence, an accurate description of tumour motion by means of a model is highly desirable to derive the appropriate treatment strategy [Land 2006]. For example, such a model could be used to determine the amplitude and stability of motion for margin design [Herk 2004]. In gating/tracking based approaches, model of tumour motion should be able to quantify and monitor continually the tumour position, during treatment [Mageras and Yorke 2004, Neicu et al. 2003, Keall et al. 2001], and establish the most appropriate prior treatment gating strategy [Land 2006].

Tumour motion model can also be exploited to design motion prediction algorithms in order to compensate for time lags. Time lags can occur between the acquisition of tumor position and the radiation delivery. These time delays are introduced by the image acquisition, the image processing, the communication delays, the induction within the motor, mechanical damping and the radiotherapy machine control loop sampling. If such delays are not taken into account and compensated for, then, by the time the equip-

ment reacts, the organ may have moved to another location. There is, therefore, a need for tumour motion prediction in order to anticipate such motion. Delays ranging from 50 to 500ms have been reported in the literature [Keall et al. 2006b, Isaksson et al. 2005a, Jin and Yin 2005, Shirato et al. 2000b].

This Chapter presents a critical review of published papers on organ motion modelling and prediction for IGRT and ART. Section 3.2 reviews the models developed to date. Section 3.3 reviews tumour/organ motion prediction algorithms. A review of criteria used to assess the developed models is given in Section 3.4. The outcomes of the chapter are discussed in the last section.

3.2 Organ/tumour motion modelling

3.2.1 A need for organ/tumour motion model

Respiratory motion is one of the major sources of target uncertainty, especially, those located in thorax, abdominal and pelvic. This can appear during CT image acquisition and linac-based EBRT. Research has been conducted to study and analyse the respiratory motion in order to find the appropriate model that can replicate as much as possible breathing and hence, tumour motion. This new field of research in RT was enabled by the emergence of advanced imaging techniques, providing clinicians with knowledge of dynamic tumour motion. Such information is provided directly in real-time by means of fiducial markers surgically implemented within the PTV, or indirectly, using a signal correlated to tumour motion.

Based on such data and knowledge gained from different breathing motion studies, several modelling approaches have been developed to reproduce respiratory motion. In addition to motion characteristics estimation, a model of tumour motion may also be used to track tumour motion in real time, to simulate the motion in order to assess treatment machine, imaging system and delivery technique. This latter is considered under the QA procedure. In the following, a review of up to date tumour/organ motion models is considered.

3.2.2 Periodic models

Lujan et *al.* [Lujan et al. 1999] were among the first to propose an approach to adapt the beam delivery to moving liver tumor. It involved a mathematical model of intrafraction motion-induced breathing into the static dose distribution by including the probability distribution function (PDF) of tumor motion. A modified cosine function was employed to generate the tumor motion PDF, assuming fixed respiratory motion amplitude and period. A comparison between the convolved dose distribution and the static dose distribution in regions outside of the CTV was carried out. A difference of up to 26% was found,

highlighting the potential importance of liver tumour motion on the overall beam delivery. The modified cosine function model was given by:

$$z(t) = A_0 - A\cos^{2n}(\frac{\pi t}{\tau} - \phi), \tag{3.2.1}$$

where t is the time in second, A_0 is the position at exhalation, A is the average amplitude of breathing; hence, ($A_0 - A$) is the position at inhalation, τ is the average period of breathing cycle in seconds, ϕ is the starting phase and n is a parameter that controls the general shape (steepness and flatness) of the breathing patterns. Figure 3.1 illustrates this model for given sets of parameters. In Figure 3.1(a), the used parameters are: $\phi = 0$, $A = 4$, $A_0 = 2$, $n = 6$, $\tau = 10\ s$. In the second Figure 3.1(b), the parameters are : $\phi = 1$, $A = 10$, $A_0 = 1$, $n = 3$,$\tau = 5\ s$.

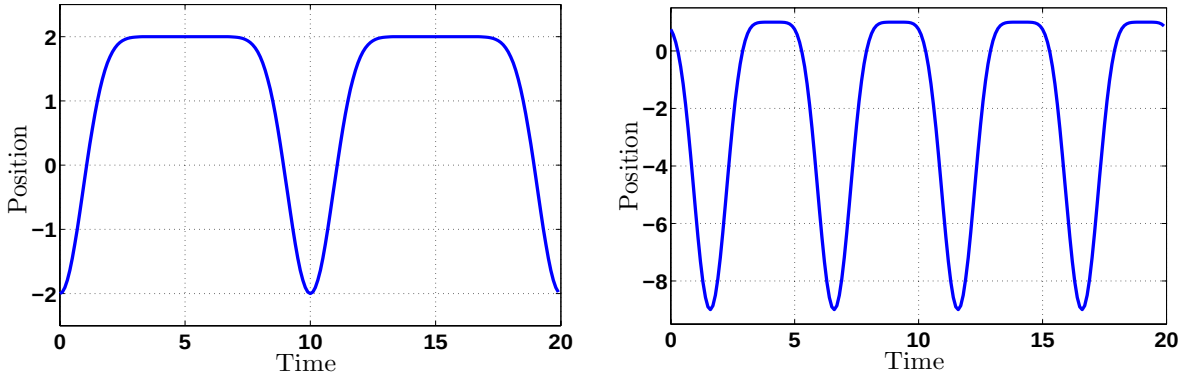

(a) (b)

Fig. 3.1: Lujan model with two sets of different parameters.

This model gives excellent fits for breathing patterns when parameters do not vary between and within breathing cycles. However, several studies have shown that the period and amplitude of the motion due to breathing can vary with time and from patient to patient [Shea and Guz 1992, Benchetrit 2000a, Ritchie et al. 1994, Sontag et al. 1996]. Moreover, the respiratory motion can be subject to random drift which is not taken into account in this model. Due to its simplicity, the Lujan model is still the most widely used model and will therefore be adopted as a benchmark in this work.

Jalden et *al.* [Jaldén and Isaksson 2001], have considered the breathing motion as a simple mass/spring system so that it can be employed to build a state-space system. In this system the state consisted of a base position, an offset from this base (equilibrium) position y , the first derivative of the offset (speed) v and a force constant d. The force act to bring the offset to zero by being negatively proportional to the

offset. In other words, the system is governed by the following system of first order equations:

$$\begin{cases} \frac{d}{dt}y(t) = v(t) \\ \frac{d}{dt}v(t) = -dy(t) \end{cases} \tag{3.2.2}$$

The above model was not assessed as typical model of breathing motion, but it was used to predict the breathing motion.

Seppenwoolde et *al.* [Seppenwoolde et al. 2002b], investigated 3D lung tumour motion of 20 patient treated using RTRT system [Shirato et al. 2000b]. The mathematical model proposed by [Lujan et al. 1999] was applied, whereby different parameters for every individual breathing cycles, such as the amplitude, the position of the tumor in the inhale and exhale phases, the average tumor position, and the length of the breathing cycle were identified. One of results in this work, is that the tumour position is more stable in the exhalation rather than in the inhalation.

George et *al.* [George et al. 2005], used data collated over a 12 month period using 24 lung cancer patients to assess the accuracy of the Lujan model [Lujan et al. 1999]. They showed that the correlation coefficient between respiratory motion and a simple harmonic oscillator $(n = 1)$ model is equivalent to that achieved with higher order sinusoidal models. The $\cos^2$ term is transformed to a term in $\cos(2\theta)$ using the relationship $\cos(2\theta) = 2\cos^2(\theta) - 1$. Although clearly the relationship can be extended recursively for all powers of $\cos$, this approach was not taken. A probability density analysis is carried out, showing data to be best modelled using a bimodal distribution, which is to be expected, given the nature of breathing movement.

In later studies [Le rest et al. 2000, Keall et al. 2002, Chetty et al. 2004], a periodic sinusoidal function was used to simulate the respiratory motion pattern.

$$z(t) = A_0 + A\cos(\omega t + \phi), \tag{3.2.3}$$

where t is the time in second, A is the amplitude, ω the angular frequency, ϕ is the phase and A_0 is an offset. In [Le rest et al. 2000] this model was used to model the motion of pixels in the moving organs. The problem with such models is that they are limited to specific regular and symmetrical breathing patterns. However, it has been found that the breathing cycle is not entirely symmetrical, with the patient usually spending a larger amount of time in the exhale phase than at inhale [Land 2006].

Neicu et *al.* [Neicu et al. 2003], developed a waveform model based on the ATT. The waveform model is normalized and averaged to better replicate the characteristics of the tumour motion. This model was

used in a beam tracking technique called SMART, under development in MGH. The concept of this technique is to derive the ATT from tumour motion data acquired at the treatment simulation stage, and then modify the original sequence of IMRT MLC leafs by taking into account tumour motion given by the ATT model. During treatment delivery, the tumour motion is monitored and the beam is on only when the leaf motion and tumour motion are synchronized at a specific breathing phase and turned off when the tumour position differs from the average trajectory. The simulation of the SMART treatment was performed using the derived ATT. Due to the small size of the data pool, the same dataset was used for both ATT derivation and SMART simulation. Ideally, the validation should involve dataset which was not been used for modelling.

Brewer et *al.* , [Brewer et al. 2004], described correlation based tracking of 2D motion of internal fiducial markers, employing two orthogonal fluoroscopy imaging. The accuracy of the tracker was determined using 10 data sets of 5 patients, and a root mean squared error (RMSE) in estimating 2D marker position was 0.47 mm on average. Moreover, a 3 sine wave description, $A_0 + A\sin(2\pi ft)$, of CC, AP and ML trajectory were developed to approximate the average and maximum 3D motion of the markers. The amplitude A and frequency f, were calculated from the global minima and maxima that correspond to full inspiration and expiration, for each breathing cycle. The offset A_0 was computed by averaging the values on the trajectory. The model was assessed on four pairs of trajectories, and an average RMSE of 3 mm was found.

Ruan et *al.* [Ruan et al. 2006] used subspace projection methods to derive models of periodic respiratory signals. These projection models used Fourier spectra and least-squared-error analysis to find the best fit periodicity of the respiratory signal. For each period within a physiologically reasonable range, a measured breathing signal is projected onto the subspace of all signals having that period to obtain the 'best fit' periodic signal in the least squared error (LSE) sense. A Fourier spectrum was used to initialize the optimization technique. To validate this method, trajectories of external fiducial markers placed on twelve patient's chest walls have been investigated. This approach has been compared to the modified cosine function developed by Lujan et *al.* [Lujan et al. 1999]. It was found that the subspace projection method was more representative, flexible, and computationally efficient. The main aim of this technique was to obtain the main principal period of breathing motion.

3.2.3 Phase-based modelling

Breathing motion has been modelled as function of breathing phase. Vedam et *al.* [Vedam et al. 2003a], characterized breathing as a cyclic process and subdivided breathing into eight phases: peak exhalation, early, mid, and late inhalation, peak inhalation, and early mid and late exhalation. The authors applied

this phase model to binning CT scans as a function of the breathing phase. Although the strategy was robust for a mechanical phantom and regular breathing cycles, the phase definitions broke down with irregular breathing patterns.

To address the issue of irregular breathing, Wu et *al.* [Wu et al. 2004] have designed and implemented a finite state model that characterizes a breathing cycles, as a combination of three normal breathing states: exhalation (EX), end-of-exhale (EOE) and inhalation (IN). Abnormal breathing that does not fall into any of the previous states was also taken into account by including a fourth irregular state (IRR). The first three states represent respectively, lung deflation, rest after lung deflation and lung expansion. In this model, each state was approximated by a line segment using a free and partial spline fitting. The transition from one state to another was guided by an adjustable thresholds of the velocity and amplitude changes.

This model was performed using real internal respiratory data for 23 patients with peak-to-peak motion greater than 7 mm. The average RMSE over all the patients was less than 1 mm and no patient had an error worse than 1.5 mm. Although, the finite state model produces good fitting results even for very complex breathing patterns, such as breathing with frequency changes, amplitude changes, base line shifting, or the combination of all the variations, the following limitations were identified: The model cannot handle the breathing motion with important cardiac signal as well as nonlinear breathing. By assuming rigid states for every breathing cycle, the model enforces an extra state even if the tumour moves between exhalation and inhalation.

3.2.4 Geometrical model

Low et *al.* [Low et al. 2005] proposed a mathematical model of tumour motion based on lung motion measurement and physiologic lungs function. This model describes the displacement of an object in the lungs as a linear function of tidal volume and airflow. The position of an object was described relative to its position P_0 at the reference tidal volume and zero airflow. An evaluation of the model using five-dimensional CT scans (acquired with simultaneous real-time monitoring of the tidal volume) of 4 patients have been carried out. For the 76 evaluated points, the average discrepancy (the distance between the measured and prediction positions) of the 15 locations for each tracked point was 0.75 ± 0.25 mm with an average maximal discrepancy of 1.55 ± 0.54 mm. The use of this model depends on its stability. It can be employed to assess the function of the lung as well as treatment planning and gating.

3.2.5 Summary

Various models of organ/tumour motion have been developed/investigated. A summary of up to date models is given in Table 3.1. These developed models have been utilized in different radiotherapy related applications, such as tumour tracking for gating, respiratory motion analysis, treatment planing, accurate dose calculation, and lung function assessment. The evaluation of each model has involved different kinds of clinical data. While the accuracy of the model was given in term of tracking error for tumour tracking application, an average modelling error has been applied in case of respiratory motion replication. In this latter, it was noticed the use of the average RMSE criterion in most of the models.

According to the RMSE criterion, the best model which gives small average RMSE was the model developed by [Wu et al. 2004]. Although, it gives a good replication of the respiratory motion, however, it does not exhibit any dynamics and it does not have a fixed number of parameters. Note that in some models, the same data were used for modelling and validation. In addition, it was noticed that none of the developed models was used to generate realistic respiratory data, in order to be used for QA procedure or motion compensation strategies assessment. The new challenge in this topic will be to develop a model with a RMSE less than 1.5 mm and which exhibits dynamical motion with small number of fixed parameters. Moreover, the model will be used to generate different types of realistic respiratory motion. These challenges will be addressed in Chapter 5.

Tab. 3.1: Summary table describing the various approaches to tumour/organ motion modelling.

Authors, year. Data set.	Anatomical site. Technique.	Model.	Results.	Comments.
[Lujan et al. 1999]	- Liver. - 1D SI motion.	- $z(t) = A_0 - A\cos^{2n}(\frac{\pi t}{\tau} - \phi)$. - Convolute static dose by tumour motion model.	- Improvement of 26% comparing to static dose.	- The model assumed fixed amplitude and period. - The model is widely used.
[Seppenwoolde et al. 2002b]	- Lung. - 3D Shirato data.	- $z(t) = A_0 - A\cos^{2n}(\frac{\pi t}{\tau} - \phi)$. - The model was fitted to 3D data.	- Average parameters of 3D motion were estimated. - Tumour more stable in exhalation.	- Least-squares method was used in estimation. - The amplitude and period were derived.
[Neicu et al. 2003]	- Lung. - 1D Shirato data.	- Model based ATT. - The average amplitude, period and mean position were used.	- Tracking error of 2 mm.	- The model was used for SMART gating technique.
[Vedam et al. 2003a]	- Lung and Phantom.	- Phase based model - Breathing were subdivided into 8 phases.	- Motion artefacts were significantly reduced.	- The phase definitions broke down with irregular breathing patterns. - Applied to binning 4D CT scans.
[Wu et al. 2004]	- Liver and lung. - 1D Shirato data.	- Finite state model. - Regular breathing cycle is represented by three line segments, exhale, end-of exhale and inhale, while abnormal breathing is represented by an irregular breathing state.	- The average RMSE among the 23 patients was less than 1 mm and no patient has an error worse than 1.5 mm. - The average processing time for each new measurement is less than 1 ms.	- It works even for complex breathing patterns. - Can be used for both on-line and offline data. - Can be applied to internal and external motions. - It does not deal with nonlinear states. - Cannot distinguish the respiratory motion from the cardiac motion when this more than half of motion amplitude. - Not used for prediction.
[Brewer et al. 2004]	- Not specified. - 3D motion data.	- $A_0 + A\sin(2\pi f t)$. - A and f calculated from the global minima and maxima. - A_0 is computed by averaging the values on the trajectory.	- Average RMSE was 3 mm. - Tracking error 0.47 mm in term of RMSE	- 10 data sets of 5 patients for tracking. - 4 pairs of trajectories for modelling. .
[George et al. 2005]	- Lung. - External chest markers.	- $z(t) = A_0 - A\cos^{2n}(\frac{\pi t}{\tau} - \phi)$. - Find the best parameters for each cycle.	- The mean position can be represented by a normal distribution. - Amplitude and period of the motion can be approximated with log-normal distributions.	-The $\cos^2$ term is transformed to a term in $\cos(2\theta)$.
[Low et al. 2005]	- Lung. - 5D CT scans of 4 patients.	- Geometrical model. - Linear function of tidal volume and airflow.	- Average maximal discrepancy of 1.55 ± 0.54 mm	- The model aims to obtain an accurate dose distribution. - The use of this model depends on its stability. - It may be used for treatment planning, gating and lung function assessment.
[Ruan et al. 2006]	- Lung - External fiducial markers	- Periodic funstion - Subspace projection methods.	- More representative, flexible, and computationally efficient compared to Lujan model.	- It can be used to obtain the main principal period of breathing motion.

3.3 Organ/tumour motion prediction

3.3.1 A need for organ/tumour position prediction

Recalling that real-time IGRT aims to adapt the radiation delivery to tumour motion during a treatment session based on the information provided by an imaging system. However, any adaptive response in beam delivery will be delayed with respect to the signal of the tumour's position. This time delay is mainly attributed to tumour location by image system, time response of treatment machine and communication delay in the control loop. In bibliography, Shirato et *al.* [Shirato et al. 2000b], reported a time delay of 0.09s between the time of the marker recognition and the start of irradiation in a gating system. This delay was measured with a film and phantom, and is the total delay which includes computational time in post-processing the image to locate the marker as well as delays in triggering the beam onset. The same time delay was reported in [Seppenwoolde et al. 2002b]. Jin and Yan [Jin and Yin 2005] proposed a reliable method of measuring/verifying the time delay in a gating system. Various port films and video tracking were taken for a motion phantom at different gating window levels. The gating system delay was measured by comparing the motion signal given by port films and video camera. It was concluded that the time delay including the response time of the LINAC and the delivery time was about (170 $\pm$ 0.03)ms.

In addition to the delay of imaging system to locate tumour position, gating or tracking based system can also have a delay [Isaksson et al. 2005a]. This delay represents the system time response to a corrective action, and which can range from 0.05s for the beam to be gated to several hundred milliseconds for the beam to be physically realigned. In a robotic-based radiation delivery system, the time delay including the response time of the robot was found to be in the order of 0.3s and for very slow motion could be up to 0.33s [Schweikard et al. 2000]. The CyberKnife, for example, has a 0.2s delay between acquisition of tumor coordinates and repositioning of the linear accelerator. This delay is in addition to image acquisition, read-out, and processing times [Keall et al. 2006b]. Repositioning an MLC aperture will likewise involve a time delay on the order of 0.1 to 0.2s or more [Keall et al. 2006b]. Ohara et *al.* [Ohara et al. 1989], reported a delay of 0.5s for a signal to interrupt the beam cycle.

Sometimes, it is difficult to track internal target directly, hence, surrogate signals are used instead. This can be for example a signal from a video camera monitoring the patient abdominal/chest wall movement, a Spirometer measuring flow and volume of the lung. However, a phase mismatch between the external markers and the internal target have been reported in [Tsunashima et al. 2004, Mageras et al. 2004]. Tsunashima et *al.* observed a phase ranged from 0 to 0.3s. Murphy and Dieterich [Murphy and Dieterich 2006] reported a latency of up to several hundred milliseconds. In [Minohara et al. 2000], a phase differ-

ence of about 0.2s between the position of the diaphragm and the respiratory signal was found. Sharp et *al.* , [Sharp et al. 2007], have noticed a phase delay of more than 0.1s in two of the four patient treated with gated proton therapy. Such time lag causes a mismatch between the location of the radiation beam and the tumour due to the motion of the tumour during the time lag interval. Consequently, it results in under-dosing to some parts of the target volume [Vedam et al. 2005]. It is important to note that measurement and verification of the time delay should be considered prior to the clinical use of any adaptive compensation technique. Unfortunately, only few contributions have investigated this issue [Jin and Yin 2005].

This problem with delay in RT has prompted researchers to investigate various types of commonly used predicative techniques. The next subsections will be devoted to review the existing models and techniques for motion prediction.

3.3.2 Discrete linear filters

The use of RTRT system by Shirato et *al.* [Shirato et al. 2000b], causes a 0.09s lag between actual markers position and gating of the treatment system, which is caused by image and gating process. A correction algorithm has been implemented that is based on the speed of tumour marker. Assuming a constant linear marker speed, the correct position correction is the speed of the tumor (or slope) multiplied by the delay time prediction time (Tp) (which is about 0.09s). At time t, the predicted marker position, $y(t|t)$, is thus given by:

$$y(t+Tp|t) = y(t|t) + Tp \times \frac{y(t|t) - y((t-\Delta t)|t)}{\Delta t}, \tag{3.3.1}$$

where Δt the imaging sampling time, $(t-\Delta t)$ is time of previous image frame, t is the time of the present image frame, $t+Tp$ is the anticipated time of gating (t plus the measured delay Tp), $y((t-\Delta t)|t)$ is the recognized marker coordinate in the previous frame (pair), and $y(t|t)$ is the recognized marker coordinate in the present frame (pair). The gating of the accelerator is based on the predicted position. The geometric accuracy of prediction is better than 1.5 mm for moving targets up to a speed of 40 mm$\cdot s^{-1}$. It was also found that for organ motion below 9 mm$\cdot s^{-1}$ the motion prediction was not necessary.

The feasibility of a linear autoregressive (AR) predictive filter model was investigated by Liu [Liu et al. 2003]. This was used to predict in real time one step ahead free breathing motion acquired using electromagnetic sensors attached to the subject's chest at frequency of 3Hz. The following model structure has been used:

$$x_t = \sum_{k=1}^{p} a_k x_{t-k} + e_t \tag{3.3.2}$$

where a_k are the auto-regression parameters which must to be estimated, x_t is the time series under investigation, p is the order (length) of the filter which is generally less than the length of the series and the white noise term e_t which represents the residual. Assuming that x_t is linear and stationary, the parameters of the model were estimated using three different algorithms and the effect of training length and model order were also investigated. It was found that the minimum mean absolute prediction error was 0.25 mm compared to the mean absolute shifted error which was 0.8 mm (error due to no prediction action was taken). The minimum mean absolute predicted error was realized when the data input length was 60 points (corresponding to 20 seconds or 3 full respiratory cycles of free-breathing of the subject), and the order was 1/4 of the input data length.

Sharp et *al.* [Sharp et al. 2004] used a linear prediction model to define the position of the organ by a combination of the known previous positions x_{t-1} through x_{t-n}, such that:

$$x_t = a_0 + a_1 x_{t-1} + ... + a_n x_{t-n}, \tag{3.3.3}$$

where x_t is the 3D position of the tumour at time t. The model was performed for different imaging rates (1,3,10, and 30Hz) and times horizons (33ms,200ms, and 1s). The lowest performance in term of RMSE was less than 2 mm for the highest imaging rate and short time prediction (33 and 200ms), and less than 6 mm for long time predication (1s). It was also concluded that use of prediction improves gated treatment accuracy for systems that have latencies of 200ms or greater, and for systems that have imaging rates of 10Hz or slower.

Extrapolation can be seen as a special case of linear prediction. It uses recent samples to find the signal velocity, and assumes that the signal will maintain constant velocity. In the following case the model used the previous two samples.

$$x_t = 2x_{t-1} - x_{t-2} \tag{3.3.4}$$

This model was found to have a higher error at all imaging rates. The reason behind the weakness of linear extrapolation is that the random noise makes it difficult to estimate the motion velocity from two points.

Murphy et *al.* [Murphy et al. 2002a] propose an adaptive linear filter to predict tumour motion using a combination of internal and external markers measurements and show the effectiveness of the filter for prediction times up to 0.8s. It was found that the accuracy deteriorated rapidly when predicting more than 0.2s in advance of the current position. The frequency of updating the filter coefficients was thought to have the most influence on prediction accuracy.

Vedam et *al.* [Vedam et al. 2004] have presented an application where two models are compared for

their ability to predict regular as well as irregular breathing patterns. The approach is based on fitting a model to past data and using it to predict a future position and then updating the prediction by taking into account the discrepancy between the predicted and the current position. One of the two models used was an adaptive filter, of similar structure to that of Liu et *al.* [Liu et al. 2003], which is expressed as follows:

$$x_{pred}(t_{n+\delta}) = \sum_{i=1}^{SHL} c_i x_{t_{n-i}} \tag{3.3.5}$$

where the filter parameters c_i are updated at each iteration using least-mean-square (LMS).

3.3.3 Sinusoidal model

A second model that was investigated by Vedam et *al.* [Vedam et al. 2004], was the sinusoidal model, which is given by:

$$x_f(t) = A\sin(Bt + C) + D, \quad t \in [t_n - SHL, t_n] \tag{3.3.6}$$

where A, B, C and D are parameters that are required to be identified and signal history lengths (SHL) define the amount of past data used to fit the model. The predictive position is calculated from the sinewave estimate as follows:

$$x_{pred}(t_n + \delta) = x_{act(t_n)} + [x_f(t_{n+\delta}) - x_f(t_n)] \tag{3.3.7}$$

The linear model was found to perform better than the sine wave model, however such linear models were found to have limitations for long term prediction due to the complex nature of organ motion. The accuracy of adaptive models shows a dependence on the learning period, the number of data points used to build and update the model coefficients. Outliers in the data may exaggerate prediction errors, and the user has to be careful to avoid adapting the model to accommodate these outliers, as this can degrade the fit to the overall pattern. The adaptive linear filter performed better and achieved prediction errors less than 2 mm in terms of standard deviation for prediction time less than 0.4s with 10Hz sampling rate.

3.3.4 The Kalman filter (KF)

The Kalman filter (KF) is a set of mathematical equations that implement a predictor-corrector type stochastic and recursive estimator, which gives the optimal system state in the sense that it minimizes the estimated error covariance (when some presumed conditions are met) [Kalman 1960]. It is dedicated to a linear systems based on the input-output measurement of this latter, and a model of the relation between

input and output. The Kalman Filter was one of the predictive models evaluated by Sharp et *al.* [Sharp et al. 2004], in their comparative paper. It was used to predict 3D marker position, assuming that the marker position is generated by a linear dynamic system model with no dependence on a control input. The maximum-likelihood values of the model parameters were estimated using an iterative algorithm called expectation-maximization on a set of training samples [Digalakis 1992]. The performance of KF was unsatisfactory, comparing with neural network (NN) (details are given later) due to the tuning of the filter from a small amount of data.

Murphy et *al.* [Murphy et al. 2002a] compared three methods, a tapped delay line filter, a KF and a NN, for predicting the future position of a tumour using fluoroscopic simulation data and external markers. More details about the algorithms used can be found in [Jaldén and Isaksson 2001]. A nonlinear (extended) Kalman filter was applied for the estimation and prediction of the breathing motion. The applied extended KF assumed that the breathing motion is sinusoidal. Since the breathing motion is not sinusoidal for most of the patients, it was discovered that the extended KF is of limited use for breathing prediction. However, it has less high frequency noise in the predicted motion compared to linear adaptive filter and the NN. The prediction performances of the this filter were evaluated using three trajectories. The largest normalized root mean squared error (nRMSE) values were 55.1%, 63.3%, and 65.1% for a prediction horizon of 0.2s, 0.5s, and 0.8s respectively.

Putra et *al.* [Putra et al. 2008], presents a multiple model approach to respiratory-induced tumour motion prediction using the interacting multiple model (IMM) filter. A combination of two models, constant velocity (CV) and constant acceleration (CA), are used to capture respiratory-induced tumour motion. A Kalman filter is designed for each of the local models and the IMM filter is applied to combine the predictions of those Kalman filters for obtaining predicted tumour position. The prediction performance of the IMM filter has been evaluated using 110 traces of 4-minute free-breathing motion collected from 24 lung-cancer patients. The simulation study was carried out for prediction time 0.1-0.6 s with sampling rates 3, 5 and 10Hz. It was found that the prediction of the IMM filter was consistently better than the prediction of the Kalman filter with CV or CA model. There was no significant difference of prediction errors for the sampling rates 5 and 10 Hz. For these sampling rates the errors of the IMM filter for 0.4 s prediction time were less than 2.1 mm in terms of the 95% CI criterion. For the prediction time 0.6s the errors were less than 3.6 mm in terms of the 95% CI criterion.

3.3.5 Non-parametric model

Ruan et *al.* [Ruan et al. 2007] proposed a non-parametric local weighted regression to predict lung's tumour motion. The first step in this approach consists of designing an augmented state space model

using the most current observation and one or more previous samples. The aim of this is to capture the local system dynamics in the time point of interest. In the next step a local weighted regression is applied to the pairs state-observation, which form a scatter-plot in a high-dimensional space. The regression weights are designed to reflect the distance between the state of interest and the training samples. Finally, the prediction is calculated by inferring the predictor response map from the behaviour of its neighbours in this high-dimensional space. For the purpose of real-time tracking and prediction, the inference weights are adaptively adjusted to incorporate the decaying temporal correlation among response patterns with longer time lags. A comparison with linear prediction, NN and KF to the same data is also performed. The accuracy of the predictor for various combinations of look-ahead length and sampling frequency, has been evaluated using RMSE and mean absolute error (MAE), between predicted tumour motion and its observed location for 10 patients. The proposed method reduced the prediction error for all imaging rates and latency lengths, particularly for long prediction lengths.

3.3.6 Dual-component signal based prediction

McCall et *al.* [McCall and Jeraj 2007] proposed a new approach to model-based prediction of respiration motion for RT. This approach is based on considering the respiratory motion as a dual-component signal. The periodic component is estimated using the best fit of the mean cycle, given by the equation:

$$[\mu]_{\varpi} = \frac{1}{N}\sum_{n=1}^{N}[X]_{\omega_n}, \tag{3.3.8}$$

where N the number of cycles, ϖ is the main wavelength, and $[X]_{\omega_n}$ is an individual cycle with length ω_n. The non-periodic component was deduced by subtracting the periodic component from respiratory signal and modelled as autoregressive moving average (ARMA) process. The predicted trajectory is given by adding the amplitude of the periodic component to one-step ahead prediction of ARMA model. The prediction accuracy of the model was assessed using a phantom based $MATLAB^{®}$ script that generates waveforms with variable and randomized amplitude and wavelength, to simulate the AP motion of the thorax. The prediction error was compared to the system without prediction. For a respiration pattern with ± 14% consistency in cycle length and ± 14% amplitude of motion, the prediction errors were 4.8 % of the total motion extent for a 0.5s ahead prediction, and increased to 9.4% at 1s lag. These prediction errors are expressed as a per cent of the motion extent observed or simulated in the respiration signal, where motion extent refers to the average distance traversed between end inspiration and end expiration.

3.3.7 Neural network (NN)

The NN technique is a method by which a computer can be trained to 'learn' a relationship between input and output data using mathematical functions designed to simulate the interactions between neurons and synapses in the human brain. This makes the NN a very powerful tool in situations where an explicit functional relationship between inputs and outputs cannot be determined analytically. If sufficient input/output data is readily available, the training of a NN may provide the best combination of speed and accuracy to replicate a desired function without a requirement for sophisticated technical knowledge from the operator. These facets have made NN the subject of research in the field of RT, where many complex non-linear relationships exist, and much onus is at present placed on human experts to analyze data using knowledge and experience in combination with purely numerical calculations. In many cases NN can accelerate these processes by either replicating human knowledge or carrying out computations which would otherwise be more time consuming using alternative methods.

Krell et *al.* [Krell et al. 1999] use a NN to track patient movement. A time-series prediction (TSP) NN with associative memory is trained off-line using data from an EPID which is subsequently incorporated into on-line data collected by a stereoscopic system which has been developed by the authors to track landmarks on the body surface of patients during treatment. The method is presented as a new in-treatment verification and no metrical comparison with existing methods is given. No details of the NN architecture are provided, although a Kohonen network [Hagan et al. 1997] seems to be most likely.

Sharp et *al.* [Sharp et al. 2004] investigated the performance of different predictive models to characterize the predictability of 3D tumour motion for different imaging rates and system latencies. The algorithms include two kinds of linear filters, two kinds of neural networks and a Kalman filter. Best results are achieved using a linear model for 33ms and 200ms latency, and a multi-layer perceptron (MLP) with one hidden layer for $1\ s$ latency. Best RMSE ranges from 1 mm for an imaging rate of 30Hz and 33ms latency to 6 mm for 1Hz and 1s latency. The TSP MLP is trained for exactly 2s for each record using 15s of data and the conjugate gradient (CG) algorithm. Note that only static forms of the predictors are used i.e. no on-line adaptive parameter adjustment is attempted.

Kakar et *al.* [Kakar et al. 2005] use an adaptive neuro fuzzy inference system (ANFIS) for prediction of organ movement for 11 breast cancer patients. Mean RMSE is reduced to sub-millimetre accuracy over a period of 20s for a 0.24s latency. Average RMSE if found to be 35% of respiratory amplitude for patients adopting free breathing and 6% for those previously coached to produce consistent breathing characteristics. The hybrid training algorithm implemented is a combination of least-squares optimization and gradient descent BP, taking 120s to converge for 20s of training data. The practicality of implementing

this in a real-time clinical situation is not discussed.

Isaksson et *al.* [Isaksson et al. 2005a] use an adaptive TSP MLP to predict lung tumour movement through correlating external and internal markers. Updating is carried out at 1 s and 5 s intervals using 2 s of data sampled at 10Hz. The LM training algorithm is used. All of the data points are used as inputs to a TSP MLP with 2 hidden neurons and 1 output neuron. All three neurons are sigmoidal. No indication is given as to whether they are logsig or tansig, and no justification is given for this architecture. From the explanation given, the training is therefore carried out using only one input data vector. Validation is carried out using a second 2s sequence, although whether this is the previous or following sequence is not explained. The tumour motion of 3 patients is analyzed, with the conclusion that an adaptive filter is superior to a stationary filter when the tumour motion is non-stationary.

Yan et *al.* [Yan et al. 2006] present a method to correlate internal and external marker motion using a linear NN. SD is used for training the NN. Unfortunately, details are not given of the sampling frequency used, which makes comparison with other methods difficult. A prediction error of 23% between external and internal marker position is reported.

Murphy et *al.* [Murphy et al. 2002a] The predictive performance of the adaptive linear filter was compared to the NN adaptive filter, using different frequencies of updating. A subsequent study in [Isaksson et al. 2005a] evaluated the relative performance of stationary linear filters, adaptive linear filters, and adaptive NN in correlating and predicting tumour motion for three representative examples of patient data. The results showed (unsurprisingly) that adaptive linear and nonlinear filters performed better on non-stationary data than the stationary filter. The study also found that as the irregularity of the tumour motion and breathing cycle increased, the nonlinear filter performed better than the adaptive linear filter. Furthermore, [Murphy and Dieterich 2006] show that nonlinear ANN outperforms linear ANN in predicting irregular breathing motion.

3.3.8 Summary

A summary of the main models/techniques to predict the target motion in advance is given in Table 3.2. This includes mainly the prediction performance, which is assessed with different error metrics for various combinations of lookahead length, sampling frequency and data sets. Note that the most investigated methods are linear predictor, NN and KF. It is important to state that the most relevant comparative study was carried out by Sharp et *al.* [Sharp et al. 2004]. In the latter, the most commonly used predictive algorithms were applied to the same data set. The best performance was given by the NN with a RMSE of about 5 mm for 1s ahead. For the same time horizon, Ruan et *al.* [Ruan et al. 2007],

achieved a RMSE of 2.5 mm using external data set with less noise. Although the use of KF can deal with noisy data, however it performs less the long time prediction compared to NN and linear prediction.

Tab. 3.2: Summary table describing the various approaches to organ/tumour motion prediction.

Authors, year.	Anatomical site. Data set.	Model. Technique.	Results.	Comments.
[Krell et al. 1999]	- Non-specific thoracic. - Stereoscopic system tracks landmarks on patients body surface during treatment.	- TSP NN with associative memory.	- In-treatment verification and no metrical comparison with existing methods is given.	- Kohonen network.
[Shirato et al. 2000b]	- Lung and static pelvic phantom. - 3D Shirato data.	- Linear extrapolation. - Assuming constant speed.	- Tp=90 ms- RMSE < 1.5 mm.	- Limited to very short prediction time. - Sensitive to measurement noise.
[Murphy et al. 2002a]	- Lung and pancreatic. - Combination of external and internal markers : 2 pairs of traces from four patients.	- Adaptive linear filter. - NN adaptive filter	- Tp=0.8 s; nRMSE=68.7%. - Tp=0.8 s; nRMSE=61.3%.	- The prediction performance depends on the updating of the algorthims.
[Vedam et al. 2004]	- Lung. - External chest markers. - Sixty traces of the Virginia data.	- Adaptive sinusoidal filter and adaptive linear filter.	- The linear filter is better than the sinusoidal filter.	- Satisfactory prediction performance, i.e. standard deviation of errors <2 mm, is achieved for Tp=0.2 s. - Prediction depends on SHL. Using a big SHL assure a small prediction error.
[Sharp et al. 2004]	- Liver and lung. - 3D Shirato data.	- NN. - KF - Linear Extrapolation. - Linear filter.	- Tp=33 ms-10/30 Hz- RMSE≈ 1.8 mm. - Tp=0.2 s-10/30 Hz- RMSE≈ 2.5 mm. - Tp=1 s-10/30 Hz- RMSE≈ 5 mm. - Tp=33 ms; 10-30 Hz; 1 mm<RMSE<1.2 mm. - Tp=0.2 s; 10-30 Hz; 2 mm<RMSE<2.2 mm. - Tp=1 s; 10-30 Hz; RMSE≈ 7 mm. - Tp=33 ms; 10-30 Hz; 2 mm<RMSE<2.7 mm. - Tp=33 ms; 30Hz; RMSE≈ 1.2 mm. - Tp=200 ms; 30Hz; RMSE≈ 2 mm. - Tp=1 s; 10 Hz; RMSE≈ 5.5 mm.	- Conjugate gradient back propagation. - The prediction depend on imaging rate. - Parameter of the model are estimated with EM algorithm. - Tuned KF is better than a normal KF. - No need for pre-filtering. - Based on extrapolation of velocity. - Limited to very short prediction time. - Sensitive to measurements noise.

Authors, year.	Anatomical site. Data set.	Model. Technique.	Results.	Comments.
[Isaksson et al. 2005a]	- Lung, correlating external and internal markers - The tumour motion of 3 patients	- Adaptive TSP MLP: 2 hidden neurons and 1 output neuron. - Updating is carried out at 1 s and 5 s intervals using 2 s of data sampled at 10 Hz.	- Tp=0.2s- nRMSE $\approx 25\%$. - Tp=0.5 s- nRMSE $\approx$ 50%. - Tp=0.8 s- nRMSE $\approx$ 60%. - Adaptive filter is superior to a stationary filter when the tumour motion is non-stationary.	- LM algorithm for training. - The results of NN were compared to linear filter.
[Kakar et al. 2005]	- Breast - Organ movement for 11 breast cancer patients.	- Adaptive Fuzzy inference System (ANFIS)	- The latency was 0.24 s - Mean RMSE is reduced to sub-millimetre accuracy over a period of 20 s: 35% of respiratory amplitude for patients adopting free breathing and 6% for those previously coached to produce consistent breathing characteristics.	- Hybrid - back propagation +least-mean squares.
[Yan et al. 2006]	- The same as in [Murphy et al. 2002a]	- Linear NN.	- The latency was 0.25-1 s. - A prediction error of 23% between external and internal marker position is reported.	- SD is used for training - Details are not given of the sampling frequency used.
[Ruan et al. 2007]	- Lung or its vicinity - Chest markers of 10 patients	- Non-parametric local weighted regression	- Tp=0.2 s; 10-15-30 Hz; RMSE=2.5 mm. - Tp=0.6 s; 10-15-30 Hz; RMSE=2.5 mm. - Tp=1 s; 10-15-30 Hz; RMSE=2.5 mm.	- This methods was compared to the linear prediction, neural networks and Kalman filtering. - The accuracy of the predictor was evaluated using RMSE and MAE. - The prediction error is reduced for all imaging rates and latency lengths, particularly for long prediction lengths
[Putra et al. 2008]	- Lung. - 110 traces of 4-minute free-breathing motion.	- Linear models (CV & CA) and their hybrid combination i.e. IMM filter.	- Average RMSE of 0.98 mm is achieved for Tp=0.2 s with IMM filter.	- The IMM filter is better than individual Kalman filters.
[Goodband and Haas 2008]	- Lung. - The EM-Virginia data.	- The TSP MLP. - The GRNN	- The CGBP: Tp= 0.2 s/0.4 s-$\overline{\mathbf{RMSE}} = 0.63/1.20mm$. - LM: Tp= 0.2/0.4 s-$\overline{\mathbf{RMSE}} = 0.76/1.61mm$. - BP+CG: Tp= 0.2/0.4 s-$\overline{\mathbf{RMSE}} = 0.48/0.97mm$. - Tp= 0.2/0.4 s-$\overline{\mathbf{RMSE}} = 0.77/1.69mm$.	- Regularization improve prediction performance.

3.4 Assessment criteria

The efficiency of a RT treatment strategy is usually evaluated by considering the radiobiological impact of the treatment uncertainties in the dose delivered to the tumour site and surrounding tissues [Booth 2002]. This is currently achieved by various radiobiological models including tumour control probability (TCP), normal tissue complication probability (NTCP), and uncomplicated tumour control probability (UTCP). The first quantity is defined as the probability of killing all tumour cells in a given tumour volume by irradiation to a certain total dose. The second one is the probability that a certain percentage of the patient population will incur unfavorable reactions in the surrounding tissue at a particular dose. The probability for controlling a given tumour without complications is termed the UTCP and is given as $UTCP = TCP.(1 - NTCP)$. In general, the aim is to maximize the TCP while the NTCP remains below some 'acceptable' (usually very low) level.

Various approaches for modelling and predicting the motion of moving organs/tumours have been reviewed in the previous section. However, in order to compare and assess the performance of each model, a criterion is required. Concerning modelling performance, a standard metric criterion named the RMSE between the observed position and the simulated one, was previously used in [Wu et al. 2004]. As consequence, it is used here for comparison with previous results. Additionally, two other criteria are investigated in this work, namely MAE and the new (in the context of ART) criterion maximum absolute error (MaxAE). The introduction of the last criterion was prompted by the fact that in radiotherapy treatment and for safety reasons, it is very important to have a small maximum error, to avoid the radiation of healthy tissues. First of all, let's define the modelling error at time-step k by:

$$SE(k) = y_{act}(k) - y_{sim}(k), \tag{3.4.1}$$

where $y_{sim}(k)$ denotes the simulated estimate of the observed marker position $y_{act}(k)$ at time k. Then the cited criteria can be defined for N observed marker position, as follow:

$$\mathbf{RMSSE} = \sqrt{\frac{1}{N}\sum_{k=1}^{N}\Big(e_{sim}(k)\Big)^2}, \tag{3.4.2}$$

$$\mathbf{MASE} = \frac{1}{N}\sum_{k=1}^{N}\Big|e_{sim}(k)\Big|, \tag{3.4.3}$$

$$\mathbf{MaxASE} = \max_{0\leq k\leq N}\Big|e_{sim}(k)\Big|. \tag{3.4.4}$$

Usually, a model is evaluated using different trajectories from different patients. Therefore, an overall mean of each criterion is required. For example, the overall mean $\mathbf{RMSSE}$, denoted by $\overline{\mathbf{RMSSE}}$, for

the M breathing traces given by: $\overline{\mathbf{RMSSE}} = \frac{1}{M}\sum_{j=1}^{M}(\mathbf{RMSSE})_j$.

The previous criteria provide an overall figure of accuracy for a given model. However, it is important to examine where/when the large errors take place. Hence, one can plot the time-domain variation of the modelling error (given by the equation 3.4.1). This can be applied to the respiratory motion which characterized by different phases.

The second type of models deal with prediction of tumour/organ motion. The prediction error at time-step k is defined by

$$PE(k) = y_{act}(k) - y_{pred}(k|k-T_p), \tag{3.4.5}$$

where $y_{act}(k)$ denotes the actual tumour position at time-step k and $y_p(k|k-T_p)$ denotes the predicted tumour position at time-step k for given measurement up to time-step $k-T_p$, with T_p is the prediction time horizon. Several criteria, which are summarized in Table 3.3, have been used to evaluate the performance of prediction algorithms for IGRT based on the error definition (3.4.5), [Vedam et al. 2004, Sharp et al. 2004, Putra et al. 2006, Isaksson et al. 2005b, Murphy and Dieterich 2006, Yan et al. 2006]. Criteria to assess the prediction performance would be useful in terms of clinical applications if they could provide information for treatment-plan evaluation. In general, the criteria listed in Table 3.3 do not provide such information. Therefore, it is of interest to develop new criteria that satisfy this requirement.

Tab. 3.3: Some criteria have been introduced to evaluate prediction algorithms in radiotherapy.

Criteria	**Formula**
Standard deviation (**SD** or σ)	$\sqrt{\frac{1}{N}\sum_{k=1}^{N}(PE(k)-\mu)^2}$, $\mu = \frac{1}{N}\sum_{k=1}^{N}PE(k)$
RMSPE	$\sqrt{\frac{1}{N}\sum_{k=1}^{N}PE(k)^2}$
nRMSPE	$\sqrt{\sum_{k=1}^{N}PE(k)^2 / \sum_{k=1}^{N}\left(y_{act}(k)-\sum_{k=1}^{N}y_{act}(k)\right)^2}$
MAPE	$\frac{1}{N}\sum_{k=1}^{N}\lvert PE(k)\rvert$

The dose volume histogram (DVH) has been accepted as a tool for treatment-plan evaluation and can be used to compute TCP and NTCP [Webb and Nahum 1993]. For a given dose profile, DVH is defined by target coverage (TC). Prediction errors is related to TC through the confidence interval (CI) of the errors. The CI of prediction errors provides information in terms of probability that the actual target position lies within a particular distance from the predicted position. A 95% CI of Y mm tells that for a given prediction y_p mm it is expected with 0.95 probability (confidence level) that the actual target position y_{act} lies within the interval $[y_p - Y, y_p + Y]$, i.e. P$(y_p - Y \leq y_{act} \leq y_p + Y) = 0.95$.

The CI criterion is derived from the distribution of the prediction error PE. To illustrate the principle, let suppose the distribution of the error PE can be approximated by a Gaussian distribution with mean μ and standard deviation σ. The probability that the error PE lies within the interval $[\mu - m\sigma, \mu + m\sigma]$ for

a positive number m is given by

$$\mathrm{P}(\mu - m\sigma \leq PE \leq \mu + m\sigma) = \frac{1}{\sigma\sqrt{2\pi}} \int_{\mu-m\sigma}^{\mu+m\sigma} \exp(-\frac{(PE-\mu)^2}{2\sigma^2})\mathrm{d}PE \quad (3.4.6)$$

$$= \frac{2}{\sqrt{\pi}} \int_{0}^{m/\sqrt{2}} \exp(-u^2)\mathrm{d}u = \mathrm{erf}(m/\sqrt{2}), \quad (3.4.7)$$

where erf$(\cdot)$ is called the erf function [Kenney and Keeping 1962]. For a given confidence level L, equation (3.4.7) allows calculation of the interval $[\mu - m\sigma, \mu + m\sigma]$ defined by $m = \sqrt{2}\mathrm{erf}^{-1}(L)$, where erf^{-1} denotes the inverse erf function. For example, the values of the parameter m for 68.3% and 95% confidence levels are equal to 1.00 and 1.96, respectively. The CI criterion, for a given confidence level, is defined by

$$\mathrm{CI} = |\mu| + m\sigma. \quad (3.4.8)$$

Note that for $\mu \neq 0$ the margin interval $[\mu - m\sigma, \mu + m\sigma]$ is asymmetric, i.e. left margin is not equal to right margin, and the CI criterion takes the largest one. The CI criterion (3.4.8) takes into account systematic errors due to μ as well as random errors due to σ.

From the definition of CI, the CI criterion (3.4.8) can be used to specify the margin needed to accommodate the prediction errors. Furthermore, the confidence level of CI criterion can be adjusted to match a specific dose distribution objective. If the objective is, for example for a homogeneous dose profile, to achieve 100% of the target volume receive at least 95% of the prescribed dose then the confidence level should be set to 95% [Putra et al. 2007]. These advantages and the relation of CI to TC and DVH make the CI criterion suitable for assessing the performance of prediction algorithms for IGRT. Note that SD criterion listed in Table 3.3 can provide the certainty region, which is related to CI, only in the case $\mu = 0$, i.e. unbias predictors. In this case, SD criterion is the same as RMSE and the 68.4% CI criteria, see Table 3.3 and equation (3.4.8).

3.5 Discussion

A variety of surrogate motion modelling and prediction techniques have been reviewed in this Chapter. The surrogate motion models developed can be divided into three main different modelling approaches. The first category is based on periodic models, where a sinusoidal model with constant amplitude and period, is used [Lujan et al. 1999, Neicu et al. 2003, Ruan et al. 2006]. The second technique considers the modelling of the breathing phases [Vedam et al. 2003a, Wu et al. 2004]. The third method considers that breathing motion can be parametrised as a function of tidal volume and breathing flow [Low et al.

2005].

The goal of the above models was either to reproduce the respiratory motion or capture their characteristics, so that they can be applied in different aspect of RT treatment. The natural understanding of breathing process has been employed and the most common approach is based on a single function which depends on time [Lujan et al. 1999]. It was also observed that only modelling techniques based on time series data were used, and some of the models did not contain any dynamics (see for example [Wu et al. 2004]) and did not exhibit a variability of breathing period and amplitude (see for example [Lujan et al. 1999]). Moreover, breathing perturbations such as drift, measurement noise and heart beat were not included. In term of modelling, there is still a need for an accurate model to describe surrogate(s) motion. The widely used Lujan model [Lujan et al. 1999] will be used here as a benchmark against which to assess the new models developed in this work.

Another category of models addresses the prediction of surrogate motion to compensate for the delay induced by the tracking and delivery systems. The most dominant predictive models are based linear filters, NNs and KF. At the time the work started, all the existing prediction methods, except the sinusoidal filter of [Vedam et al. 2004], were non model-based approaches. Note that the KF of [Sharp et al. 2004] is considered as non model-based because the matrices in the KF were obtained from the time series data. The prediction based NNs was found to perform better for the long prediction horizon.

There is a lack of a common motion data base for QA purpose and to compare modelling and prediction strategies. This results in each research group selecting their own data, which makes a fair comparison of the algorithms developed to date difficult. Such finding prompted the development of realistic respiratory data that could be used as a benchmarks. Prediction models developed to date are able to predict between 0.09s and 1s in advance with an accuracy in the range of 1.2-2.5mm in term of RMSE. The evolution of the developed modelling and prediction techniques has involved different clinical data and assessment criteria have been also reviewed.

Chapter 4

Respiratory surrogate motion analysis

4.1 Introduction

Currently, several real-time imaging systems can effectively track either the location of tumour motion inferred from the position of fiducial markers implemented near the tumour and/or the position of external markers positioned on the patient's thorax. The information gained from the monitoring of these surrogates was exploited to calculate treatment margin and design methods to compensate for organ motion (see Chapter 2). The surrogate motion has also been used to model the respiratory motion and predict the future evolution of the tumour position (see Chapter 3). Among the widely published surrogate motion data there is the internal SI motion data obtained using the RTRT system at Hokkaido University (Japan) and the external AP motion data collected at VCU (USA). These two types of data are involved in this research to develop a new motion modelling and predicting techniques.

Several delivery systems and strategies are commonly in use to compensate for respiratory motion (see Chapter 2). To ensure that these delivery systems and compensation methods are effective, their design should take into account patient/surrogate motion. To evaluate the clinical performances of the delivery systems, specific QA procedure and equipment are being developed. In particular, the MAESTRO Coventry team has developed a thorax phantom able to move both an artificial 'tumour' along three independent axes of motion together with chest and rib cage motion along two axes of motion [Land 2009]. To provide the phantom with a realistic yet demanding set of motion trajectories encompassing as wide a range/type of motion as possible within an acceptable signal duration, a realistic model replicating observed behaviour is required.

In this Chapter, a pre-processing, statistical analysis such as minimum, maximum, average and relative variation in percentage, histograms and distributions will be performed to identify such range of typical

motion for both internal and external surrogate motion. In the following section, the internal and external clinical data are presented. A frequency analysis of the aforementioned data is performed in Section 4.3. The respiratory motion characteristics such as motion amplitude and duration, velocity and acceleration are presented in Section 4.4 and 4.5. Discussion and conclusions are given in the last section.

4.2 Clinical respiratory motion data description

The amount of internal/external surrogate lung motion data available in this work varies depending on the location of the tumour, and also type and direction of motion. The database utilised in this work include breathing-induced tumour motion measured by tracking the location of surrogate fiducial markers surgically implanted within the tumour and an external surrogate marker located onto the patient/volunteer chest and abdomen tracked by a video camera. In addition, a new experiment was designed using signals from which the organ motion can be inferred, namely the air flow measured by a spirometer and the chest and abdomen motion measured by a tracking system called Polaris (see Chapter 2 and 6).

A system for intra-fraction tumour motion tracking has been implemented by Shirato et *al.* [Shirato et al. 1999]. During each fraction, dual fluoroscopes track fiducial markers implanted in or near the tumour, providing their 3D spatial coordinates at 30 frames per second. Sometimes the realisation of internal motion tracking is difficult and expensive to realise, hence, an external respiratory signal may be used. Following this principle and in order to improve the gating technique, George et *al.* assessed the impact of audio and video gating on breathing motion [George et al. 2006]. An external marker box attached to the chest was used to measure the breathing motion at sampling frequency of 30 Hz.

The use of such clinical data will enable some comparison with previous research involving the same data. It is important to note that most researchers, that investigated the internal markers data, do not use all the them. However, they specify how many traces they have used but not which ones.

4.2.1 Internal motion data

One of the most significant clinical data sets investigated in this work provides the motion of fiducial markers attached to the lung tumours. This data was obtained during the treatment of 40 lung tumour patients treated between 2001 and 2002 using the RTRT system at Hokkaido University [Shirato et al. 1999; 2000b]. More than 300 data sets in SI direction were obtained, courtesy of Wu [Wu et al. 2004] and Shirato [Shirato et al. 2000b]. Some of these data were utilised for modelling and prediction (see Chapter 3). Concerning the analysis of these data, Seppenwoolde et *al.* [Seppenwoolde et al. 2002b], examined

a 3D data in terms of the amplitude and curvature of the tumour motion, the differences in breathing level during treatment, hysteresis (the difference between the inhalation and exhalation trajectory of the tumour), and the amplitude of tumour motion induced by cardiac motion. It was found that the average greatest motion was in CC direction ($12 \pm 2\ mm$), for tumours situated in the lower lobes and not attached to rigid structures such as the chest wall or vertebrae. For lateral and AP directions, it was ($2 \pm 1\ mm$), for both upper- and lower-lobe tumours. It was also observed a measurable motion in range of $1 - 4\ mm$ caused by heart beat.

Neicu et *al.* [Neicu et al. 2003], have carried out an analysis of breathing pattern regularity of 11 datasets. The average amplitude (for every dataset) was $7.6 - 22.5\ mm$, with relative standard deviations of amplitude ($\sigma / A_{avg}\ in\%$) $6\% - 49\%$. Wu et *al.* [Wu et al. 2004], developed a model based breathing states, which was used for breathing motion analysis [Wu et al. 2007]. It was found that EOE state has the longest average duration ($1.46\ s$), while the average IN duration ($1.33\ s$) is longer than the average EX duration ($0.99\ s$). For the velocity, The EOE velocity is small and has very limited variation, while both IN and EX velocities are widely spread. It was noticed that EX velocity is correlated with the IN velocity in a more complex manner. Shirato et *al.* , [Shirato et al. 2006] examined the amplitude and speed of tumour motion detected using RTRT system. It was found that the average absolute amplitude was $8.2 \pm 6.5\ mm$, $10.7 \pm 8.64\ mm$ and $8.8 \pm 7.0\ mm$ for ML, CC, and AP respectively. For the average speed, it was $21.1 \pm 8.9\ mm \cdot s^{-1}$, $9.9 \pm 5.4\ mm \cdot s^{-1}$ and $6.6 \pm 3.6\ mm \cdot s^{-1}$ for ML, CC, and AP respectively.

The number of trajectories used to analyse the data differs in each publication. While, Sharp et *al.* [Sharp et al. 2004] have used only 14 patients with peak-to-peak breathing amplitude greater than $8\ mm$, Wu et *al.* [Wu et al. 2004], selected 23 patients with peak-to-peak breathing amplitude greater than $7\ mm$, and Neicu et *al.* [Neicu et al. 2003], used 11 data-sets with maximum peak-to-peak tumour motion greater than $10\ mm$ among 41. Note that these data selection choices were not justified by the investigators. As this research concerns only the respiratory motion and in order to be able to validate the new proposed modelling approach, only 9 traces with more than $90\ s$ duration have been investigated amongst 358 trajectories.

An example of three samples of the excluded data is shown in Figure 4.1. Figure 4.1 shows irregularities between the respiratory cycles and in the end of exhalation (sub-figure (a) and (b)), sudden large spikes (sub-figure (a) and (b)), and an important measurement noise (sub-figure (c)). These abnormalities in the respiratory data can be either caused by the movement of the fiducial markers during the acquisition, the imaging system itself or the movement of the patient.

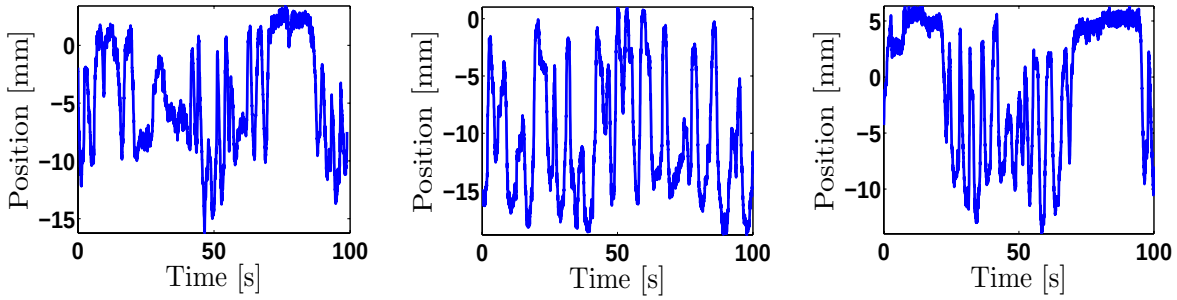

Fig. 4.1: Some examples of the excluded internal respiratory data.

Having examined the selected trajectories, it was noticed that breathing patterns are different from a patient to another and even within the same patient. Such findings are in agreement with [Shea and Guz 1992, Benchetrit 2000a, Ritchie et al. 1994, Sontag et al. 1996], who found that motion exhibits intra and inter patient variability. A summary of different breathing cases is shown in Figure 4.2. An example of regular breathing motion is given by the sub-figure (a). The main irregularities in breathing motion are time varying of frequency and amplitude which are illustrated by the sub-figures (b) and (c) respectively. The baseline drift of breathing pattern is presented in sub-figure (d).

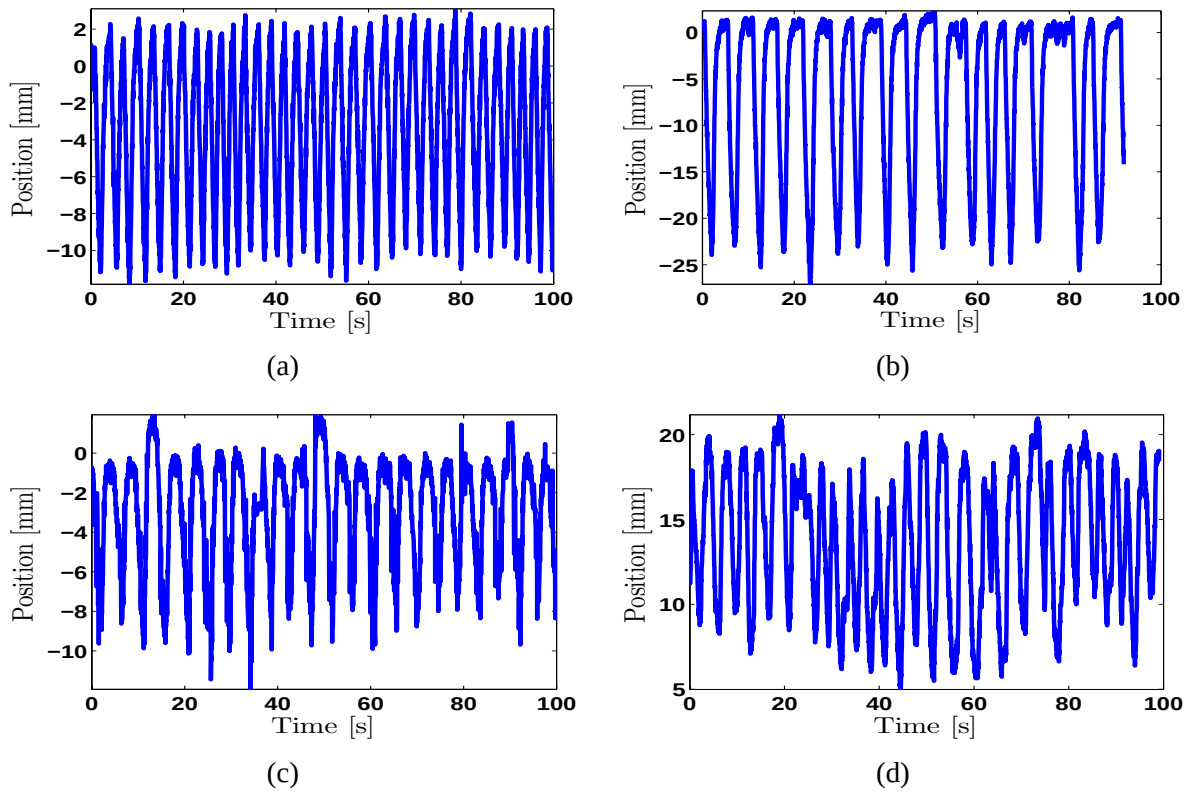

Fig. 4.2: Time domain characteristics of IFM: (a) regular breathing, (b) frequency changes, (c) amplitude changes, (d) baseline drift.

There are several benefits from using this clinical data. Firstly, it represents realistic and clinically relevant surrogate motion. Secondly, it provides the means to evaluate the proposed modelling and prediction techniques described in Chapter 5 and 7.

4.2.2 External motion data

The second clinical data considered in this research was acquired from a breathing training database collected at VCU (USA) [George et al. 2006, George 2005]. These measurements represent a total of 331-4 minutes respiratory traces, collected 30 times per second from 24 lung cancer patients. A reflective marker box resting on the patient's abdomen between umbilicus and xyphoid allowed tracking of respiratory motion in the AP direction using the RPM system (Varian Medical Systems, Palo Alto, CA). The software installed on a PC interfaced with the tracking system detects the marker motion digitally and records it. The aim of the study was to determine whether audio-visual biofeedback can improve respiratory reproducibility by decreasing residual motion for displacement and phase-based gating.

The experiment considered three different cases namely, FB, AI and AVB. The FB session was used to obtain the average frequency of the patient's breathing and displacement of the marker. Thus, this average frequency was served as an input for the AI. The average peak-to-peak range of motion provided the formulation of the input for the visual biofeedback for the AVB. The AI method used instructions to 'breath in' or 'breath out' at a periodic intervals deduced from the patients' own FB patterns. In the AVB, the patients were shown a real-time trace of their abdominal wall motion due to breathing and asked to maintain a constant amplitude of motion.

Examples of breathing traces 80 s in length and for all three breathing feedback types are shown in Figure 4.3. The trajectories, shown in Figure 4.3, appear to be more regular compared to the internal motion data. In contrast to the latter, the shown external motion trajectories do not exhibit a large amount of measurement noise. Finally, one can notice the existence of a baseline drift in the three trajectories.

Each respiratory motion data file that was obtained contained information about the position of the external marker, the phase of the breathing cycle ($0\ to\ 2\pi$) at that particular position, and the time ($0 - 240\ s$) at which the samples were collected for the particular breathing-type technique sampled at 30 Hz. The position values for the patient respiratory motion moved negatively for anterior motion of the abdomen and positively for posterior motion of the abdomen. For an abdominal breathe, posterior motion of the abdomen corresponds with inhalation and anterior motion of the abdomen corresponds with exhalation. Patients positioned with their arms extended above their head (typical for lung treatments) predominantly use their abdomens for breathing.

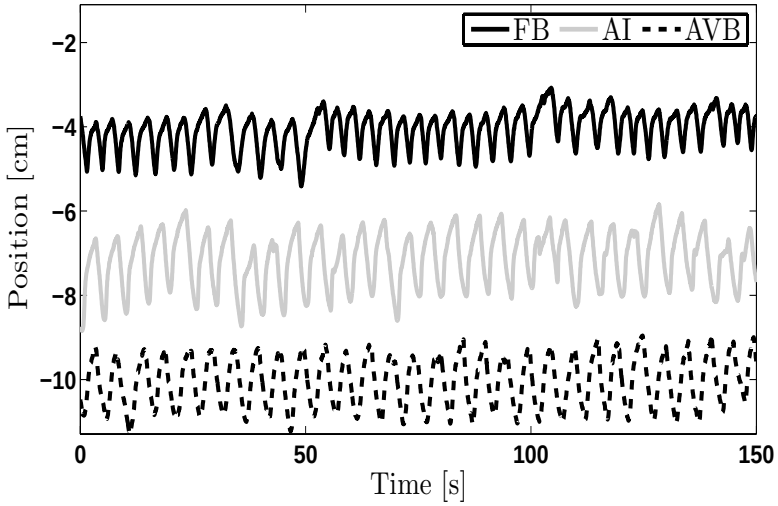

Fig. 4.3: Example of a respiratory trace for FB, AI, and AVB. A constant y-offset value has been added to the displacement values of each these traces to improve the clarity of the figure.

Similarly to the previous data, some of the EM data were removed due to their large irregularity. Therefore, the number of data has been reduced from 110, 111 and 109 to 64, 84 and 81 for FB, AI and AVB respectively. Figure 4.4, illustrates three examples of highly irregular data leading to their exclusion from the data set considered for analysis purpose. Sub-figure (a) shows a sudden change in the movement of the external marker which can be due for example to a movement of the patient or a change in the breathing of the patient. In sub-figure (b) an abnormality in one of the breathing cycles can be noticed. Sub-figure (c) presents an example of spikes that can occur between the breathing cycles.

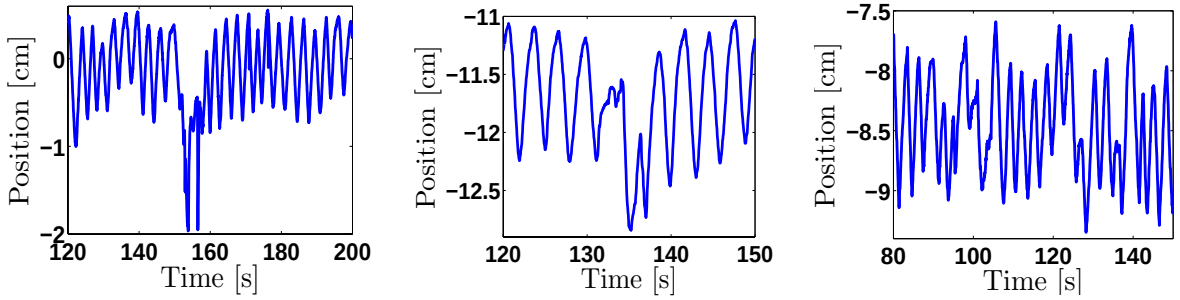

(a) (b) (c)

Fig. 4.4: An example of three excluded external surrogate respiratory data.

This data was utilised by the experiment investigator George et *al.* [George et al. 2005] to inspect various issues, including the cosine power of the Lujan model [Lujan et al. 1999], the cycle-to-cycle variation of

breathing parameters, including mean position, amplitude of motion, and period as well as their pdfs, and finally, quantification of the pdf of the entire respiratory motion. It was realized that the mean position can be represented by a normal distribution, and amplitude and period of the motion can be approximated with log normal distributions. This finding confirms the fact that the breathing parameters should not be assumed to be constant, as it was stated by previous studies [Herk et al. 2003, Chetty et al. 2003]. Moreover, A bimodal model was found to have the highest correlation with the pdf of the overall patient respiratory motion, although the normal model exhibited a strong correlation. The overall standard deviations of respiratory motion were 0.48, 0.57, and 0.55 cm for FB, AI, and AVB, respectively. In other words the proposed gating methods present more motion dispersion than the FB.

4.3 Frequency analysis

In addition to the variation of the respiratory amplitude over time, the time domain description of the respiratory data has revealed the existence of a baseline shift (especially for the EM data), the changes of respiratory period, and some respiratory abnormalities that might occur during the breathing process. Moreover, it was essentially useful to pick out the acceptable respiratory signals to be analysed. Examples of the time domain characteristics of IFM and EM data are shown in Figure 4.2 and Figure 4.3 respectively. Notice that such representation does not provide the spectral content of the respiratory signal.

The experimental data is usually corrupted by undesirable signals known as noise, disturbances or even loss of signal [Vaseghi 2006]. These disturbances can be caused by external sources or by the system itself. The relevant question is to identify the disturbances that should be removed from the data, and that which should be considered in the modelling process. In the frequency domain, these disturbances can be divided into high, low frequencies, and occasional bursts. High and low frequency disturbances are defined according to the frequencies of interest of the system (lung in this work). The frequency representation is powerful tool to visualize the frequency characteristics of a temporal signal, which can be performed by the Fourier Transform. The latter is computationally very attractive since it can be calculated by using an extremely efficient algorithm called the Fast Fourier Transform (FFT). This algorithm is available in the $MATLAB^{®}$ software under the function FFT which requires the signal to be transformed and the number of points where the FFT is performed.

By applying the FFT function to the preselected clinical data, it was observed that some of the IFM data contained heart beat signals, which act particularly on the end of exhalation (see sub-figure 4.5(a)). In Figure 4.5, the time domain representation of a sample internal motion trajectory is given in sub-figure (a) and its frequency representation is shown in sub-figure (b) and (c). Sub-figure (b) illustrates that the most

dominant frequency components which represent the respiratory signal are in the range of 0.3-0.4Hz, which is in agreement with those given in literature review (see chapter 2). Sub-figure (c) shows a peak around 1.2 Hz which represents the heart signal and with less significant power spectrum a pick around 0.6 Hz which represents some breathing signals with small amplitudes at the end of exhalation. The components with a power spectrum less than 0.005 are considered as noise (see sub-figure (c)).

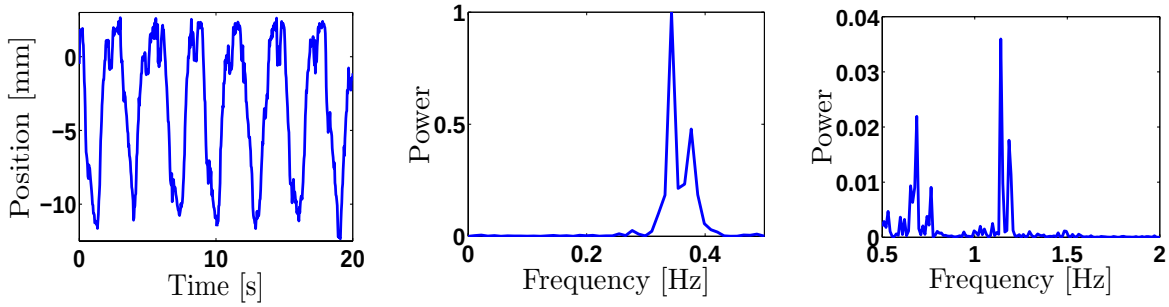

(a) (b) (c)

Fig. 4.5: An example of a frequency analysis performed on a trajectory from the IFM: (a) Time domain representation, (b) The respiratory components, (c) Heart beat, disturbances and measurement noise components.

More advanced frequency analysis of the breathing motion has been performed using a time-frequency representation, which has been adopted [Cohen 1995]. The fundamental idea behind this representation is to describe and understand how the frequency is changing in time. Figures 4.6 to 4.9 show an example of spectrogram from each preselected data sets as well as their time and frequency domain representations. Analysing the spectrogram of the different respiratory data, it can be noticed that the variation of the different frequency components do not exhibit a regular pattern. Moreover, the range of the respiratory frequencies is more important for the external trajectories rather than the internal one. The time-frequency representation has also shown some irregularities that can occur during breathing. These latter take places in different points in times. Such analysis can be employed to design a time-frequency filter to remove the undesirable signals, as it can be useful for modelling the frequency changing in time or predict the irregularities.

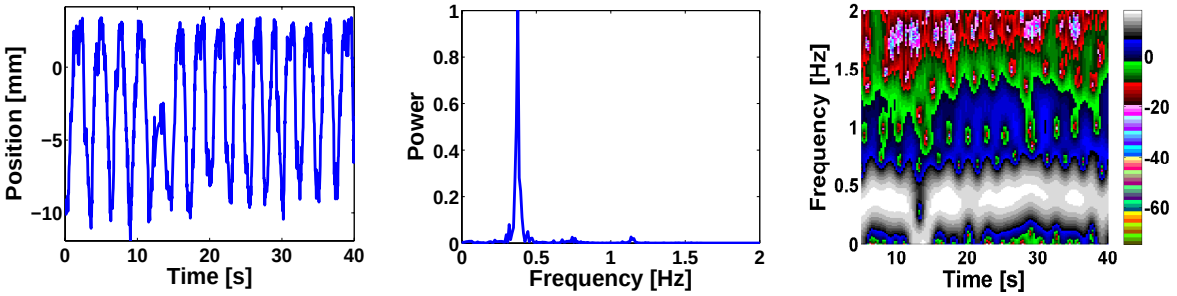

(a) (b) (c)

Fig. 4.6: An example of (a) time series representation , (b) frequency representation, and (c) spectrogram for a IFM trajectory.

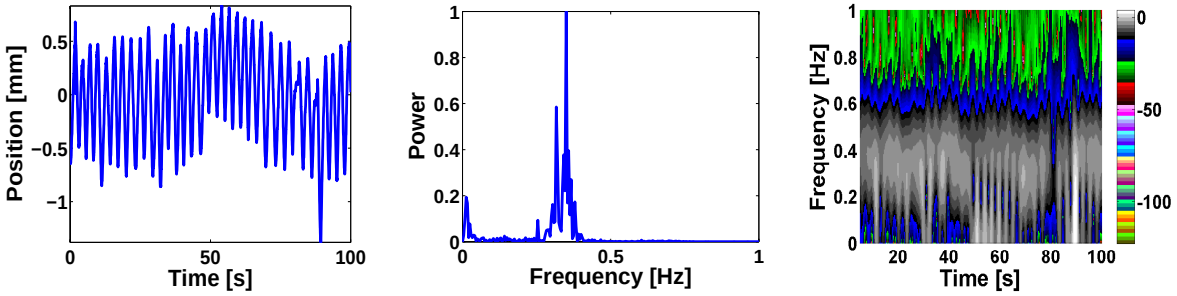

(a) (b) (c)

Fig. 4.7: An example of (a) time series representation , (b) frequency representation, and (c) spectrogram for a FB trajectory.

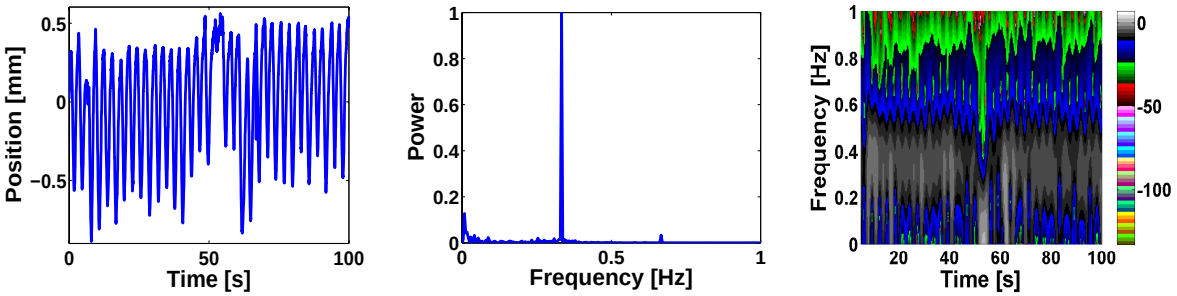

(a) (b) (c)

Fig. 4.8: An example of (a) time series representation , (b) frequency representation, and (c) spectrogram for a AI trajectory.

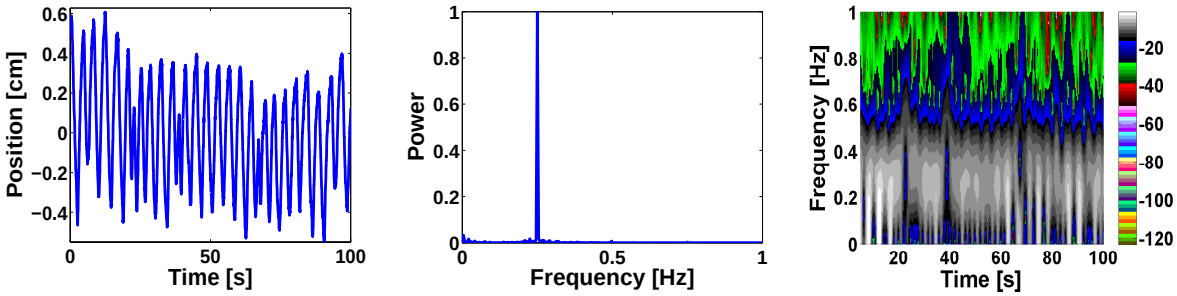

(a) (b) (c)

Fig. 4.9: An example of (a) time series representation , (b) frequency representation, and (c) spectrogram for a AVB trajectory.

Due to the large amount of clinical respiratory data used in this chapter and in order to have a global idea about every selected data-set, it was more convenient to consider the overall spectrum. The normalised spectrum of each subset of selected breathing data was carried out, and an overall normalised power spectrum plots have been performed in Figure 4.10. From the latter one can deduce that the frequency band can be divided into three main ranges of frequency components. The dominant breathing frequency (between 0.1 and 0.4 Hz) are caused by breathing motion, which differ from patient to patient and even within the same patient [Benchetrit 2000b]. This is in accordance with literature findings [Seppenwoolde et al. 2002b]. The low-frequencies components (below 0.1 Hz) are characteristic of drift or baseline shift. These low frequency changes have been found to be more important for external data. Concerning the high-frequency components, one can notice the heart beat in the internal data, noise patterns and localised distortions signals caused mainly by the measurement process. The heart beat signal is located between 1-1.2 Hz, and was detected only in 4 trajectories. According to [Seppenwoolde et al. 2002b], this is especially for tumours close to the heart. Note that the range of the frequency axis was chosen to give a better view of the respiratory components and heart beat for the IFM. The informations gained in this part will be used to design adequate filters to extract the respiratory signals as well as the other signals contained in the clinical data. There is a wide range of different respiratory frequency components in the FB data (sub-figure (b)) and IFM data (sub-figure (a)), which highlight the presence of breathing irregularities. Conversely, in the AI data (sub-figure (c)) and AVB data (sub-figure (d)), one can see the effect of frequency gating, as the range of breathing frequencies as well as the number of distinct breathing frequencies is reduced.

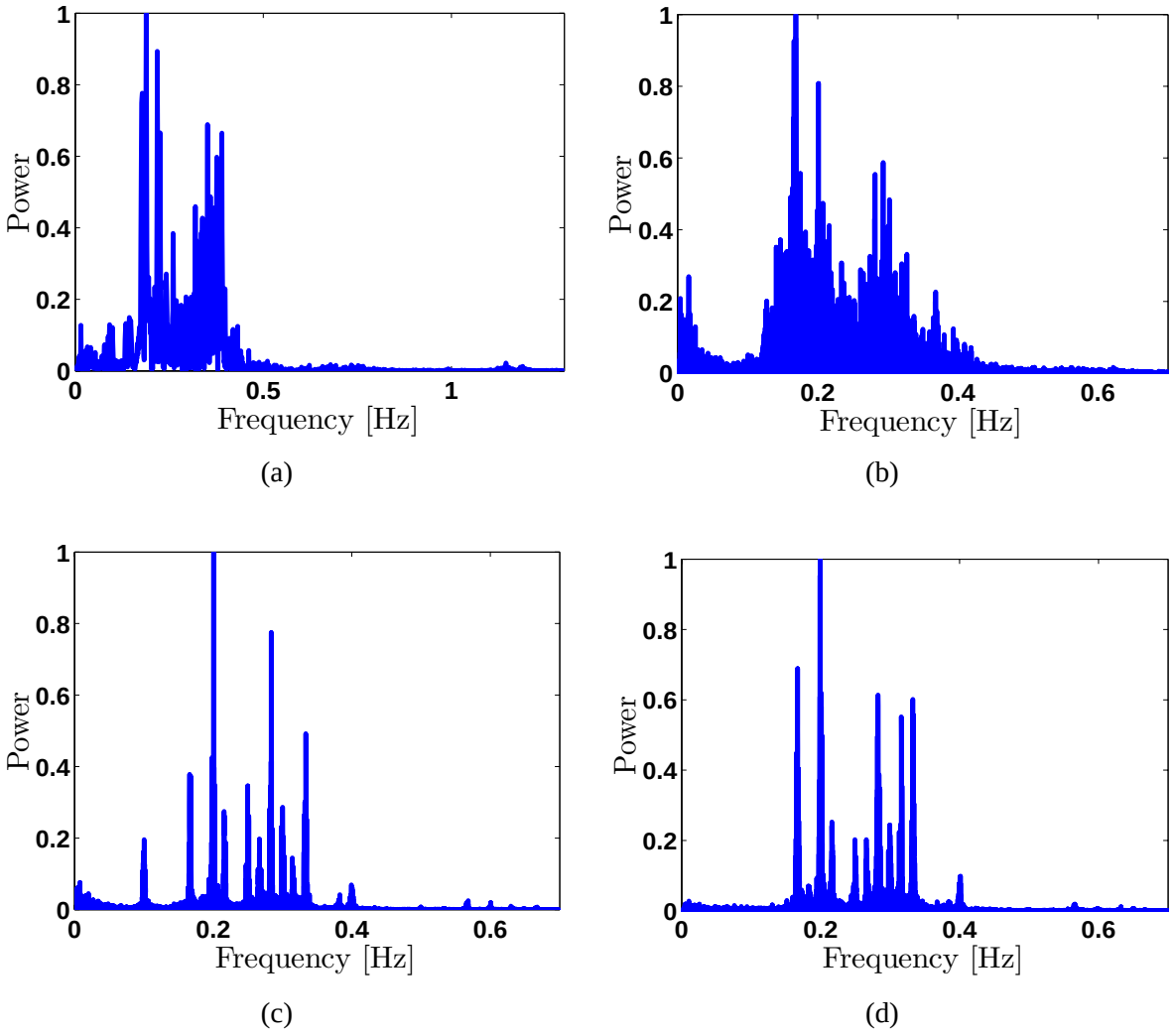

Fig. 4.10: The overall normalised power spectrum for (a) IFM, (b) FB, (c) AI and (d) AVB.

4.3.1 Respiratory disturbances and measurement noise

The respiratory function is susceptible to different kinds of disturbances that is driven by complex unknown physiological processes [Bruce 1996], or might be induced by the patient's anatomy, health and movement. Moreover, tumour motion acquisition can also be influenced by the measurement noise. These disturbances are defined as high frequency random fluctuations which is mainly due to external sources such as measurement devices. In literature, Sharp et *al.* [Sharp et al. 2004] have described the small distortions in the IFM data, as intra-cycle Gaussian noise, which found to be around $1-2\ mm$. Such Gaussian noise cannot be directly correlated to the expansion of the lungs, and could therefore be eliminated from the respiration signal during pre-processing by applying a band-limited or smoothing filter. Additionally to the Gaussian noise, a noise spike of up $10\ mm$ has also been noticed in the IFM data

[Sharp et al. 2004]. On the other hand, the main investigators of RTRT experiment, Shirato et *al.* [Shirato et al. 2000b] have mentioned an average noise on the detected IFM position of $0.5\ mm$.

By contrast to [Neicu et al. 2003, Seppenwoolde et al. 2002b] in which a 30-point median filter was used to remove measurement noise, a non-causal filter (filtfilt) is implemented in the $MATLAB^{®}$ software package [MathWorks 2006] using a 3rd-order Chebyshev low pass filter [Shenoi and Wiley 2006]. The Chebysev filter is designed to have $0.3\ dB$ peak-to-peak ripple gain and 0.5 Hz cut-off frequency. Such choice of cut of frequency removes both noise and heart beat motion. Note that in the data sets considered the heart beat motion was not significant. In order to examine the difference between the two filters, a comparison has been performed, and results are shown in Figure 4.11. One can observe that the 30-point median filter smooths the end of exhalation and inhalation more than the Chebyshev filter. This generates a filtering error larger than 2 mm and therefore, loss of respiratory information.

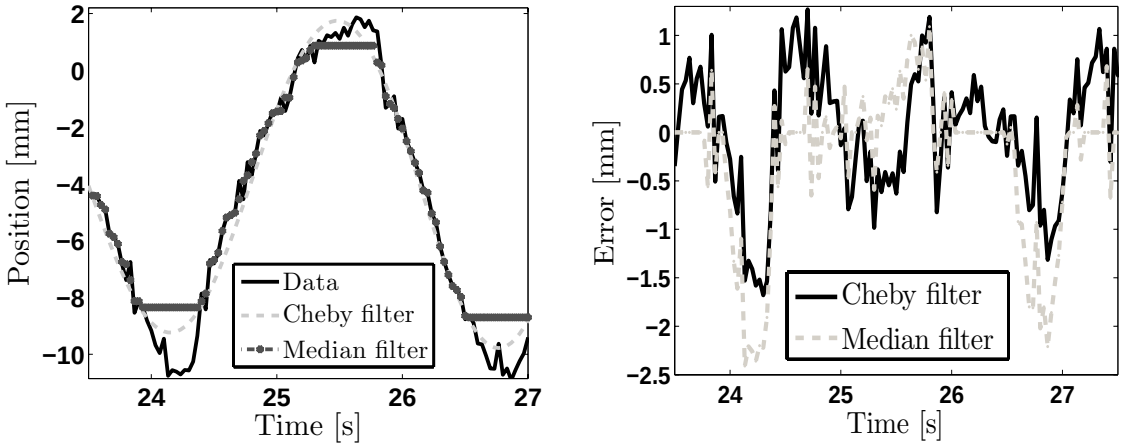

(a) (b)

Fig. 4.11: A filtering performance comparison between Chebyshev low pass filter and 30-point median filter on a sample of IFM. (a) Filtered signals against real signal, (b) filtering errors

To assess the effectiveness and applicability of the proposed Chebychev low pass filter, the normalised power spectrum of the filtered data was compared to that of the original data, for one patient (see Figure 4.12) and for the overall data (see Figure 4.13). In the Figure 4.12, the filter was able to smooth enough noise, without losing the breathing frequency information in the four cases. This result was confirmed while comparing the filtering performance of the overall data (Figure 4.13).

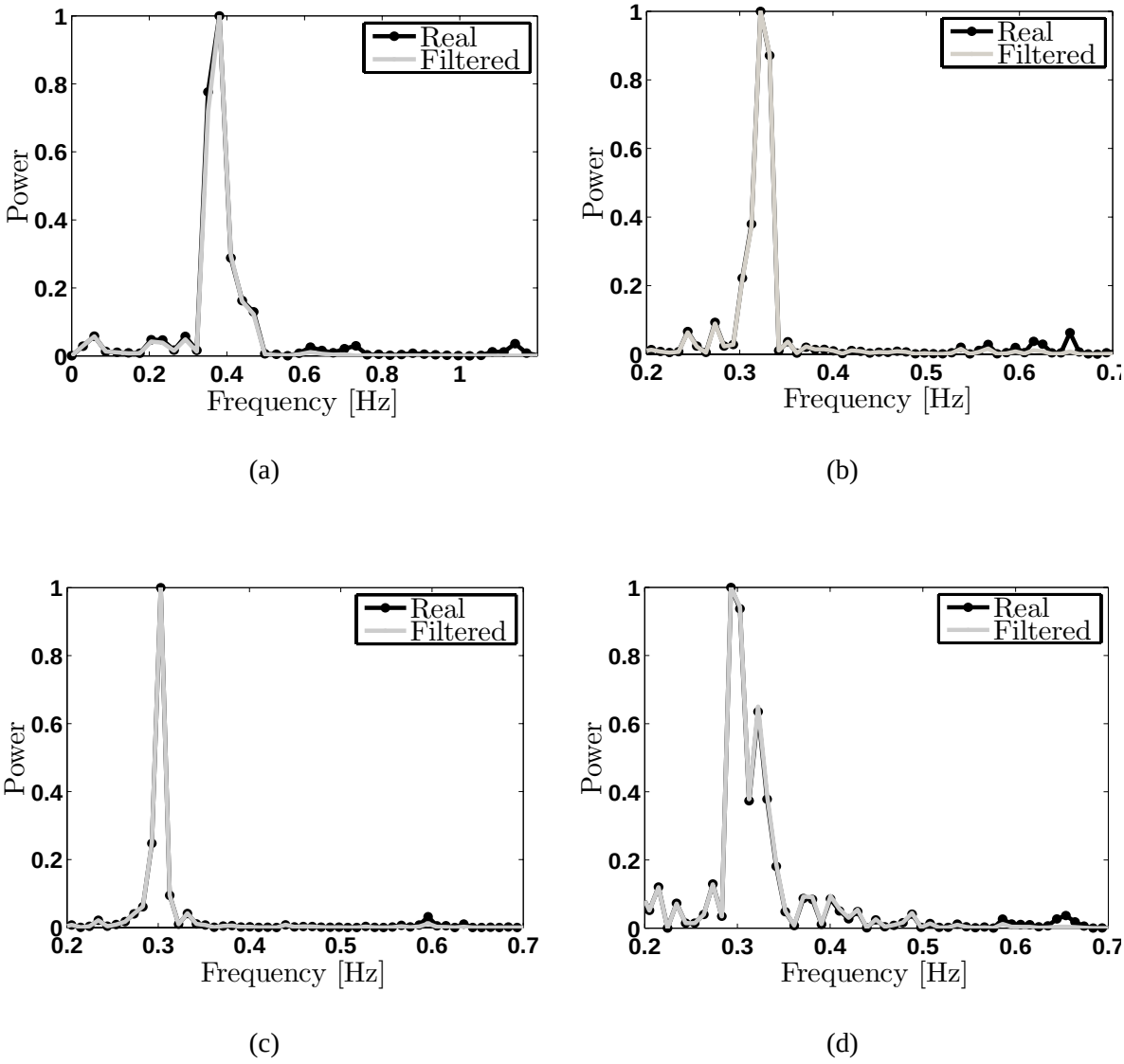

Fig. 4.12: An example of normalised power spectrum comparison between real and filtered data for (a) IFM, (b) FB, (c) AI and (d) AVB.

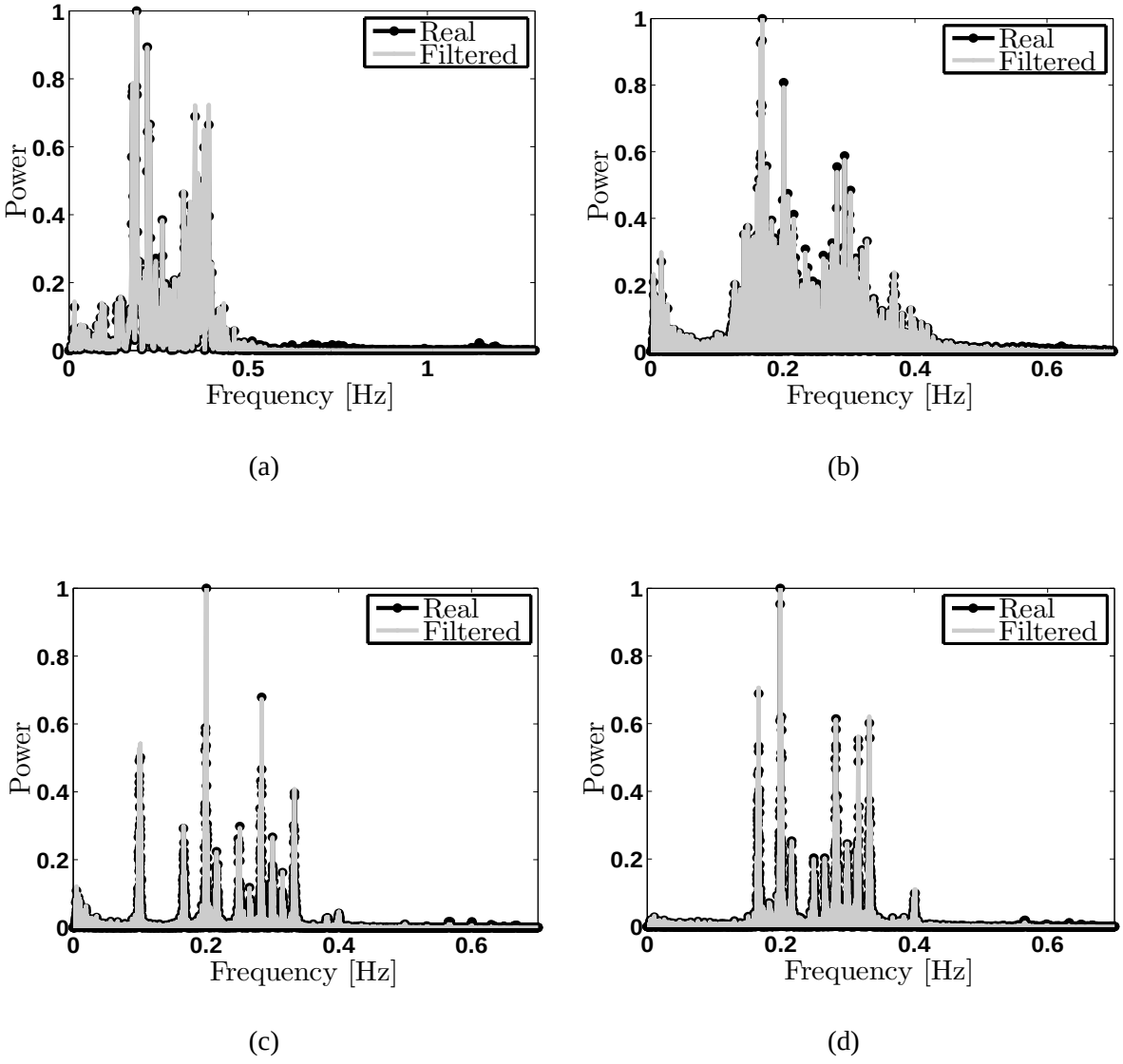

Fig. 4.13: The overall normalised power spectrum comparison between filtered and real data for (a) IFM, (b) FB, (c) AI and (d) AVB.

The characteristics of the filtered trajectories in temporal domain was also carried out, see Figure 4.14. The aim of this last comparison, is to show that there is no significant discrepancy between the real and filtered signals, and to make sure that the filtered signal contain the tumour location information.

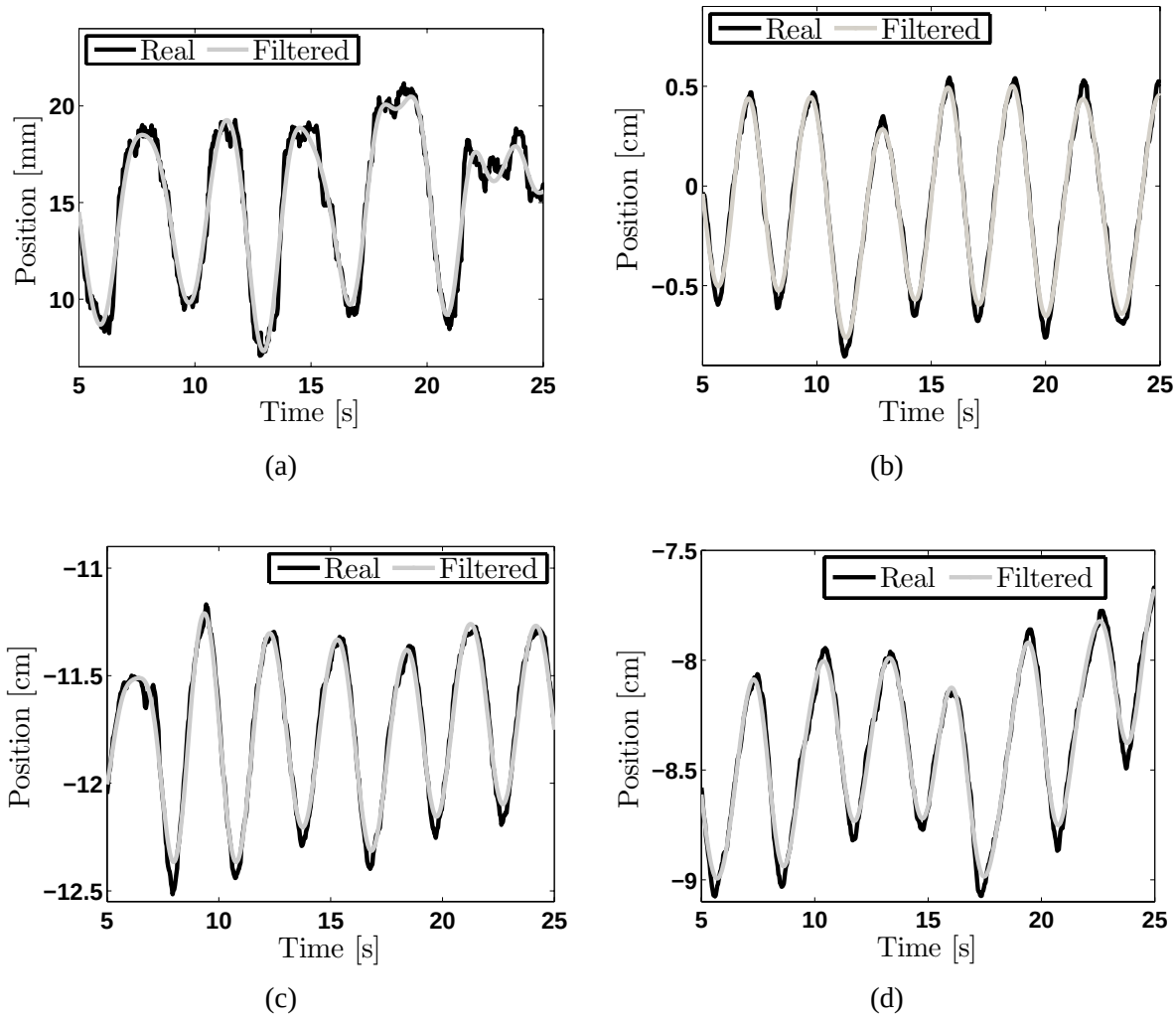

Fig. 4.14: An example of filtered and real respiratory data in time domain for (a) IFM, (b) FB, (c) AI and (d) AVB.

Once the data is filtered, the measurement noise ω, can be extracted from real data y, using the relation $\omega = y - y_f$, where y_f is the filtered signal. The histograms depicted in Figure 4.15, show the distribution of measurement noise for (a) IFM, (b) FB, AI, and AVB. It can be seen that the distribution of the measurement noise can be approximated by a Gaussian distribution, with mean $\mu = 0.00\ mm$ and standard deviation $\sigma = 0.86\ mm$, $\sigma = 0.06\ cm$, $\sigma = 0.06\ cm$ and $\sigma = 0.06\ cm$ for IFM, FB, AI and AVB respectively. Moreover, one can observe that the amount of noise in internal data is larger than external data. This is because of the use of fluoroscopy acquisition.

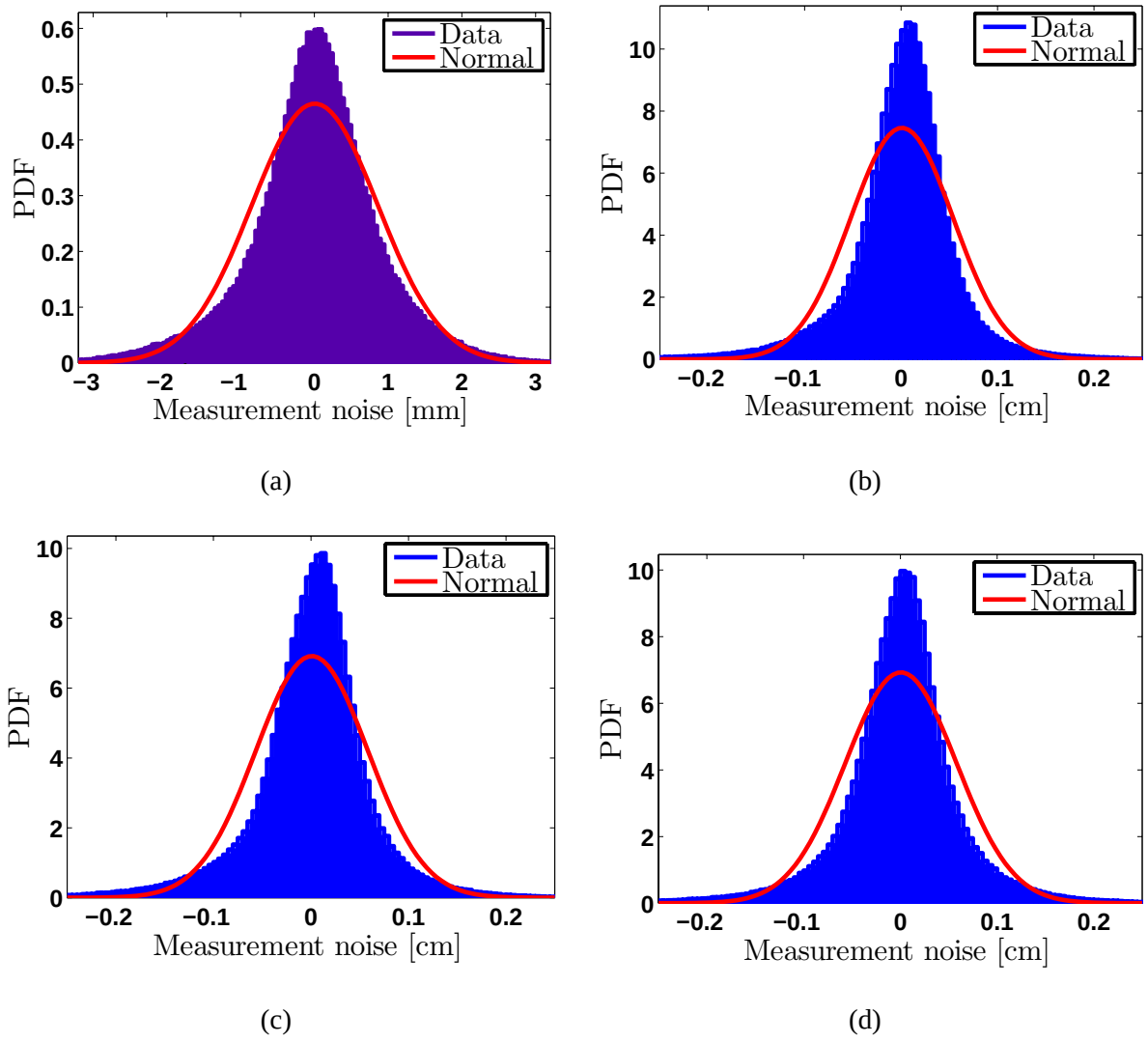

Fig. 4.15: Distribution of measurement noise of (a) IFM, (b) FB, (c) AI and (d) AVB.

4.3.2 Heart beat

In the literature, the effect of heartbeat on tumour motion has been discussed in several contributions. For example in [Seppenwoolde et al. 2002b], tumour motion due to heartbeat was detected in 7 out of the 20 patients. The amplitude of this motion was $1-4\ mm$, mostly in the ML direction. Tumour movement with heartbeat was most significant for tumours near the heart or attached to the aorta. In the fluoroscopy study by Ekberg et *al.* [Ekberg et al. 1998], it was observed that for tumours located close to the heart, cardiac movement was a major contributor to tumour motion. In a twenty patient study by Ross et *al.* [Ross et al. 1990], measurements using an ultra-fast CT scanner, have demonstrated tumour motion of $9-6\ mm$ in the ML and AP directions which was attributed to aortic pulsation, cardiac contraction, and respiration. Neither author distinguished between tumour motion caused by breathing or cardiac

motion.

The frequency analysis has shown the existence of the heartbeat signal, which was only noticed in the internal data. From the nine selected internal motion trajectories, four have showed heartbeat signals. Figure 4.16, illustrates the normalized spectrum of these trajectories. The frequencies of the heartbeat are between 1 and 1.3 Hz. These signals are considered as disturbances which have been removed by the applied filter.

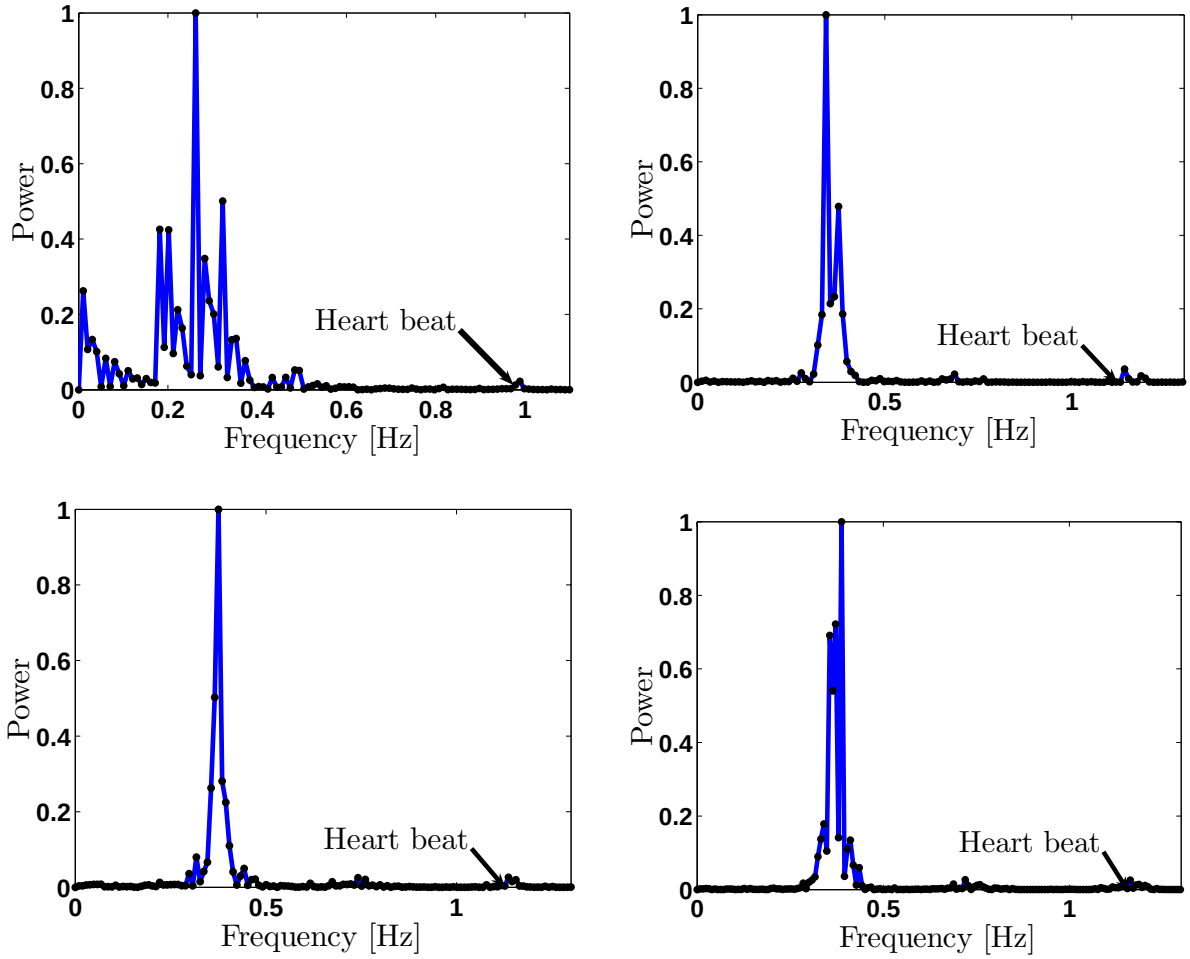

Fig. 4.16: Frequency spectrum of the 4 IFM trajectories where the heartbeat influence was noticed.

4.3.3 Baseline drift

Baseline trend or drift refers to a gradual change in the mean value over a long period of time. It is a common issue in the respiratory motion, which can stem from the respiratory process itself, patient's movement, or measurement devices. In the breathing process this drift is mainly due to the respiratory muscles tones. The patient relaxation throughout the treatment or the gravity acting on compliant lung tissue shortly after the patient assumes a supine position can also induce a drift [Seppenwoolde et al.

2002b]. The use of physiological monitor such as a Spirometer showed a long-term drift of the baseline during breathing [Zhang et al. 2003]. Moreover, the variation of the interaction between movement sensors and the body can generate a drift for the tracking systems based video camera. A systematic inter-fraction shift can also occur [Seppenwoolde et al. 2002b, Shirato et al. 2004b]. This could result from a slight shift in patient position, or simply a change in the level at which the patient started breathing. The variation of the latter is larger than intrafraction shift as reported in [Seppenwoolde et al. 2002b, Shirato et al. 2004b].

The range of drift amplitude has been assessed in the previous works. For example, Chen et *al.* [Chen et al. 2001], found an upward drift of the skin marker position by 2.5 mm in superior direction, while the range of the marker motion with breath is only 2.0 mm. This drift was found to be breathing phase independent. A baseline drifting of 5 mm or more has been observed in two of the four patients investigated during gated proton therapy [Sharp et al. 2007]. The effect of this phenomena on diverse tumour motion compensation techniques has also been discussed in the literature. For example, Murphy et *al.* [Murphy et al. 2002b] showed that a slow, steady drift of tumor position occurs in the breath-holding technique during an extended sequence of held breaths. It has also been noted that this baseline drift may cause the beam to turn on during an unintended interval [Mageras and Yorke 2004]. Concerning margin design technique, it can lead to underestimating the margin as mentioned in [Engelsman et al. 2005]. Some models that have been used to model the respiratory motion such as the one in [Lujan et al. 1999] may break down when a drift is considered.

The identification of the trend signal has always posed a problem, since the drift and the remaining components of a time series are latent variables. Hence, assumptions about the drift signal have to be made. Generally, the trend is thought of as a smooth and slow movement over a long term. The practice of removing the trends and periodic components from the signal prior to analysis is an established method of signal processing [Pollock et al. 1999], and is referred to as partitioning or the decomposition of the time series. The periodicities are removed by fitting trigonometric or other periodic functions to the data; otherwise, the mean cycle is subtracted. This decomposition method can be applied to respiration dynamics because the periodic nature of breathing has been extensively studied and several methods exist for estimating and extracting the periodic patterns from the data. Such methods include the modified sinusoidal model developed by Lujan et *al.* [Lujan et al. 1999] and the Ruan projection models [Ruan et al. 2006].

In the frequency domain representation performed previously, it was found that the drift components are below 0.1 Hz. Based on this information, a low pass filter was designed to remove the drift signals from the noise free clinical data. An illustration of the filtering technique used is shown in Figure 4.17.

Sub-figure (a) shows the time and frequency domain characteristics of the noise-free signal. In the latter the respiratory and drift frequencies are shown. In sub-figure (b) the extracted drift signal as well as its frequency representation are shown. Sub-figure (b) illustrates the time and frequency representation of drift-free signal. In this last sub-figure, it can be noticed that drift component is completely removed from the noise free signal.

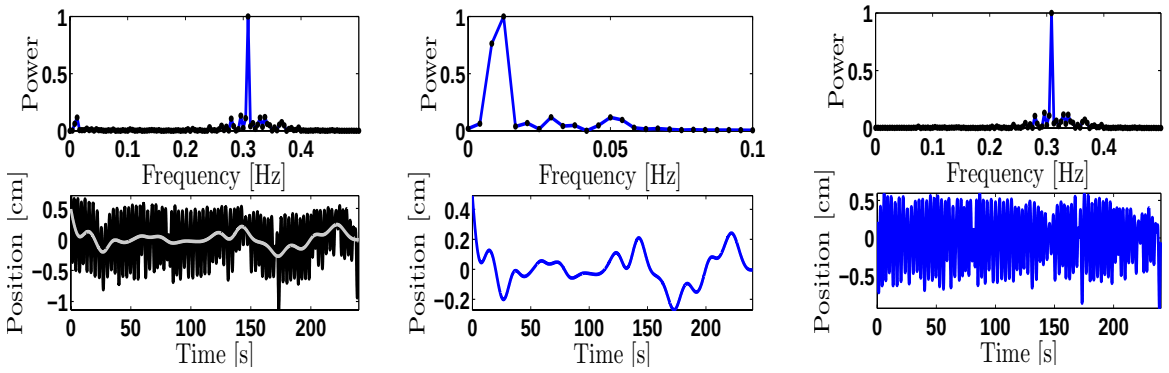

(a) (b) (c)

Fig. 4.17: Spectrum and time series plots for (a) noise-free signal, (b) drift signal and (c) drift-free signal.

After removing the drift from the respiratory data, the overall distributions of the different preselected data sets have been established (see Figure 4.18). It can be noticed that the drift is normally distributed with: (i) mean $\mu = -0.04\ mm$ and standard deviation $\sigma = 0.81\ mm$ for IFM; (ii) mean $\mu = 0\ mm$ and standard deviation $\sigma = 0.14\ cm$ for FB; (iii) mean $\mu = 0\ mm$ and standard deviation $\sigma = 0.15\ cm$ for AI; (iv) mean $\mu = 0\ mm$ and standard deviation $\sigma = 0.09\ cm$ for AVB. The EM data exhibit an important drift comparing the IFM data. This is due to the measurement devices used and treatment techniques adopted. Compared to the overall dispersion of the drift signals and measurement noise, one can observe that the dispersion of the measurement noise is larger for the drift in EM data and comparable for the IFM. A comparison to the overall respiratory motion will be performed thereafter.

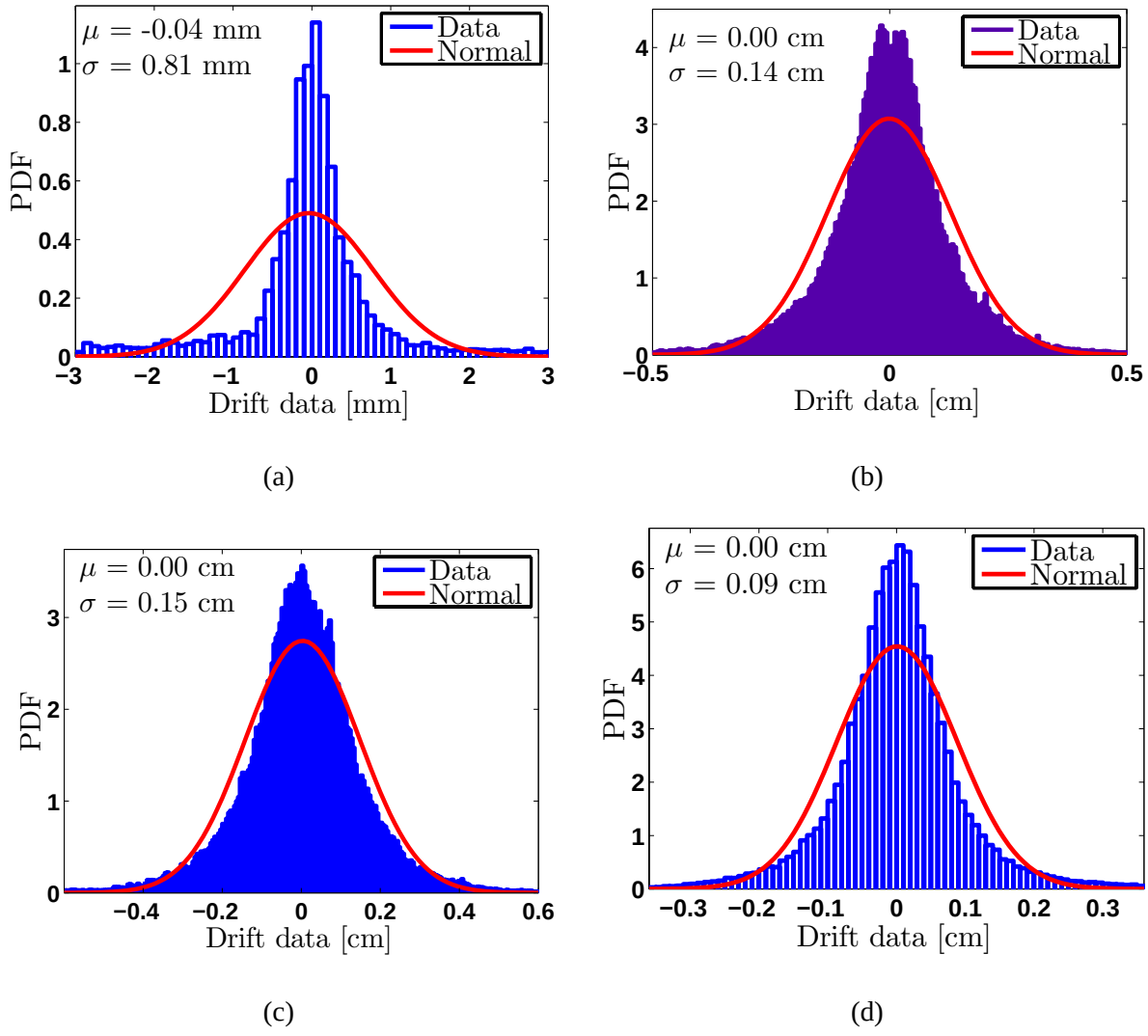

Fig. 4.18: Distributions of drift signal for (a) IFM, (b) FB, (c) AI and (d) AVB.

4.4 Respiratory motion amplitude and durations

The main respiratory motion parameters which consist of the amplitude and period are essential for various tumour motion compensation techniques. While the motion amplitude is involved to design safety margins [Herk 2004, Engelsman et al. 2005], both amplitude and period are used to quantify the reproducibility of position for gated treatment [Mageras and Yorke 2004, George et al. 2006], and for planning treatments that use beam tracking [Neicu et al. 2003, Murphy 2004]. However, it is difficult to detect the variabilities of these parameters as well as motion direction. An understanding of the nature of breathing parameters is necessary to assess the regularity and reproducibility of the breathing patterns for both free and coached breathing. Moreover, this analysis will help to validate a simulation model of respiratory motion, which is one of the aims in this work. Whilst previous analysis have been performed on different

sets of breathing data using a Lujan model [Lujan et al. 1999], see Chapter 2, this section will be devoted to the pre-selected data, adopting a new respiratory parametrization and algorithm to estimate these parameters.

As it is stated in [Wu et al. 2004, Neicu et al. 2006, Berbeco et al. 2005, Keall et al. 2004a], the breathing process is composed of three successive states called EX (lung deflation), EOE (rest after lung deflation) and IN (lung expansion). Sometimes, this rule is not validated and additional states can take place between or within regular breathing cycles. Other breathing irregularities such as changes in frequency and amplitude can also happen. This irregularity can be attributed to various sources related to the patients, for example young persons have been shown to exhibit more regular breathing patterns [Tobin 1983]. Other factors include, mental state, patient's anatomy, presence of breathing difficulties, patient's motion and measurement devices used to measure the breathing motion.

By contrast to the breathing representation used in [Wu et al. 2004], in this work, the breathing process has been divided into two states as shown in Figure 4.19. This was raised from the fact that the combination of the EX and EOE states can be approached by a typical response of second order system. According to this description, a breathing cycle starts from the beginning of exhalation and ends by the end of inhalation. The period and peak-to-peak (PTP) amplitude are defined for every cycle. It has been observed that the start of exhalation and end of inhalation may not have the same position, in this case the average PTP amplitude between the PTP EX and PTP IN amplitudes is believed to be the most appropriate in this case. It is important to add that this difference in breathing levels can generate a drift. In this work the drift was mostly removed from the data prior to the detection of the PTP amplitude.

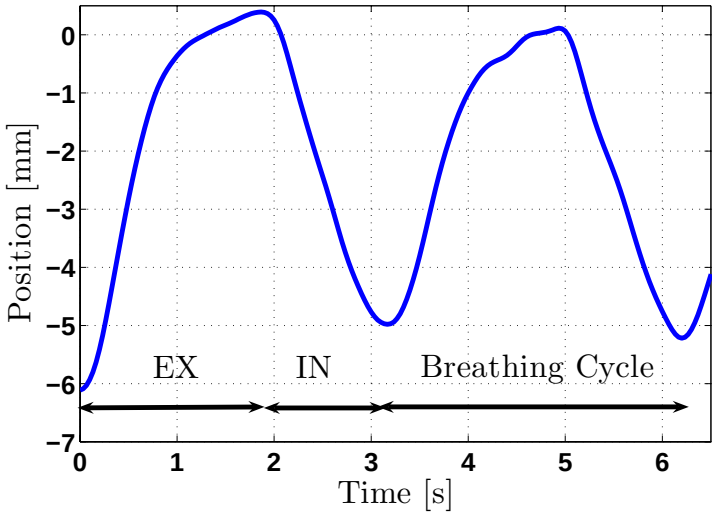

Fig. 4.19: Respiration states description.

After a pre-processing of the measured data by extracting the main respiratory components, an off-line

algorithm based on gradient changing has been developed to identify the peaks and valleys of each breathing cycle. A previous algorithm has been utilised in [Sahih et al. 2005] for the same objective, which was based on zero crossing. Both two algorithms needs the mean value of the motion to be known in advance. This is possible in the case when the baseline drift is removed. An advantage of the developed algorithm is that it is able to avoid local maxima and minima due to the measurement process or patient breathing difficulties (see Figure 4.20).

For each type of respiratory data and each preselected data set, various information were estimated for each breathing cycle. In the end an overall vector for each parameter was built representing each type of data. This includes duration and amplitude for both IN and EX phases, which will be denoted by T^{in}, T^{ex}, A^{in} and A^{ex}, as well as breathing cycle period (T) and amplitude (A), the relative standard deviations of the period (σ_T/T) and amplitude (σ_A/A). In addition to duty cycle (D), average and absolute amplitudes (A^{ave}, A^{abs}), and minimum and maximum values for the said parameters. Duty cycle parameters describes the ratio of exhalation duration for a given breathing period ($D = T^{ex}/T$). This last quantity is necessary to quantify the predominant state during a breathing cycle.

Once the parameters are calculated, the mean and relative standard deviation can be deduced for each data set. It is important to differentiate between the average and absolute PTP breathing amplitudes. Whilst the first is more appropriate from a modelling point of view, the second definition is considered for moving target, since the maximum and minimum displacement are required. The average and absolute amplitudes are respectively, the mean breathing cycle amplitude and the distance between the maximum and minimum positions. For every breathing trajectory the following steps can be applied to estimate the adopted parameters:

Algorithm 1 Breathing Parameters Extraction Algorithm

1: **for** $traj = 1{:}M$ **do**
2: Frequency analysis to identify breathing, drift and noise frequencies.
3: Keep the respiratory components by filtering the drift and noise components using two low-pass filters.
4: Identify the peaks and valleys of each breathing cycle.
5: Calculate A^{in}, A^{ex} and the PTP amplitude A for every cycle.
6: Deduce the average amplitude A^{ave} for each cycle.
7: For every trajectory deduce the absolute amplitude A^{abs}.
8: For every pre-selected data-set the overall average θ_{ave}, overall relative standard deviations $\sigma_\theta/\theta_{ave}$, overall minimum and maximum values of each parameter are calculated.
9: **end for**

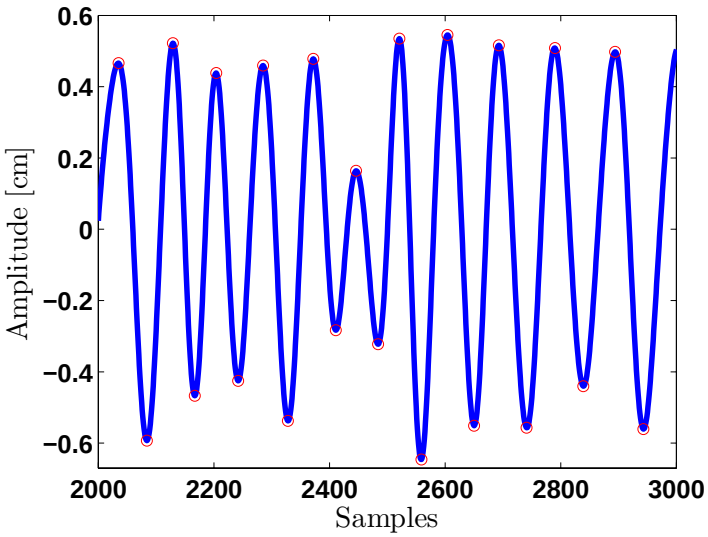

Fig. 4.20: Peaks and valleys detections.

The results of the statistical analysis of the adopted variables for free and coached breathing defined above are shown in Table 4.1. It was recognized for both external/internal data that the tumor spends longer duration in the EX phase than it is in the IN phase. This is confirmed by the D parameter whereas the average of this latter is 56%, 56%, 54% and 52% for FB, AI, AVB and IFM respectively. The duration T^{ex} exhibits more fluctuation than T^{in} for all datasets. This can be observed from the comparison of relative standard deviation of the two said parameters. The relative standard deviation of T^{ex} is 39% comparing to 24% for T^{in}, in FB data, 31% against 21% for AI, 31% versus 23% for AVB, and 50% comparing to 22% for IFM. One can also deduce from this comparison that the variability of the duration parameters is more important for a free breathing than coached cases and motion is more stable in IN phase.

Concerning the average T, one can state that it is larger for external datasets than it is for the internal datasets. This can be probably due to the motion direction and markers positions. For the external breathing data the effect of gating can be noticed. In other words, the relative average standard deviation of T was reduced from 31% in free breathing session to 24% for AI and AVB sessions. The range of average T is different for each data set. In FB data, it varies from $1.83\ s$ to $9.07\ s$, for AI it is between $1.90; s$ and $8.93\ s$, AVB ranging from $1.83\ s$ to $7.80\ s$, and IFM $2.20 - 10.13\ s$.

Concerning the analysis of PTP breathing amplitude, it showed that it is almost similar for both EX and IN for all datasets. This is the result of removing the baseline shift from the data before the analysis. As consequence of this last finding, the correlation between A^{in} and A^{ex} was carried out and results

are illustrated in Figure 4.21. There is a strong linear correlation between the two parameters. In terms of average PTP amplitude it was noticed that gating increases the amplitude of motion and reduces the variation of the average relative standard deviation, since this value is larger for free breathing than the AVB and AI. In percentage this is equivalent to 47% for free breathing and 38% for AI, while it is 39% for AVB. This can be the effect of the compromise between frequency and amplitude gating. In terms of stability, the external data is more stable than the internal one. Regarding the gated data, it was found that A^{ave} is increasing from 1.03 cm in FB to 1.25 cm and 1.30 cm for AI and AVB respectively.

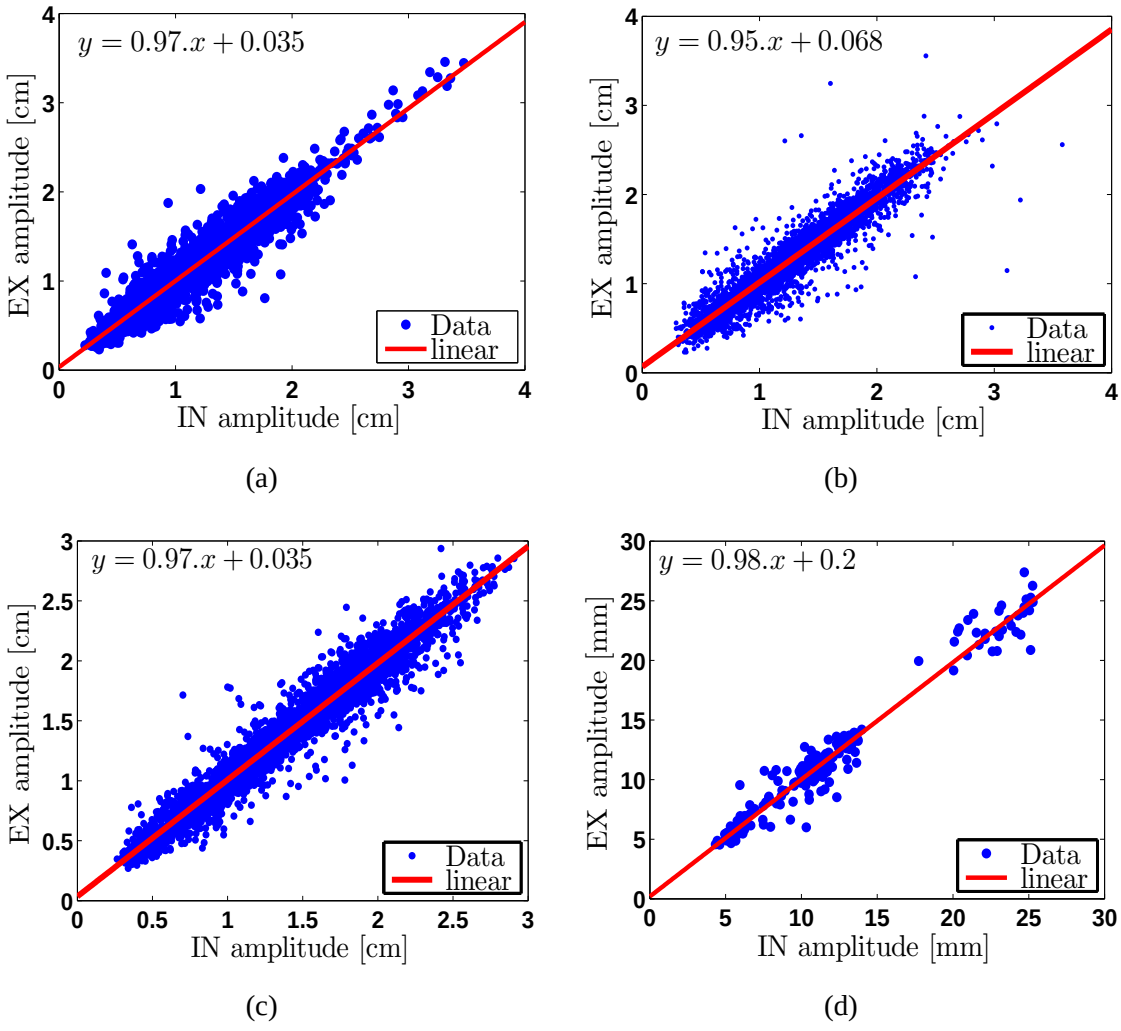

Fig. 4.21: Correlation between EX and IN amplitudes for (a) FB, (b)AI, (c) AVB and (d) IFM.

Tab. 4.1: The range of durations and amplitudes for free and coached respiratory data.

Data (Nb. of traces)	Proprieties	θ	θ_{ave}	$\sigma_\theta/\theta_{ave}$ [%]	θ_{max}	θ_{min}
FB (64)	Duration (s)	T^{in}	1.59	24	3.77	0.90
		T^{ex}	2.08	39	5.83	0.93
		T	3.67	31	9.07	1.83
	Duty cycle (%)	D	56	10	75	27
	Amplitude (cm)	A^{in}	1.03	47	3.48	0.22
		A^{ex}	1.03	47	3.46	0.23
		A^{ave}	1.03	47	3.46	0.25
		A^{abs}	1.53	40	3.58	0.52
AI (84)	Duration (s)	T^{in}	1.69	21	3.50	0.87
		T^{ex}	2.18	31	5.80	0.87
		T	3.87	24	8.93	1.90
	Duty cycle (%)	D	56	10	80	31
	Amplitude (cm)	A^{in}	1.25	38	3.58	0.29
		A^{ex}	1.25	38	3.56	0.23
		A^{ave}	1.25	38	3.07	0.29
		A^{abs}	1.80	31	3.59	0.71
AVB (81)	Duration (s)	T^{in}	1.75	23	3.83	0.90
		T^{ex}	2.12	31	5.73	0.87
		T	3.87	24	7.80	1.83
	Duty cycle (%)	D	54	11	80	28
	Amplitude (cm)	A^{in}	1.30	39	2.91	0.26
		A^{ex}	1.30	39	2.94	0.27
		A^{ave}	1.30	39	2.88	0.30
		A^{abs}	1.69	38	3.95	0.61
IFM (9)	Duration (s)	T^{in}	1.53	22	3.23	1.10
		T^{ex}	1.75	50	8.57	1.10
		T	3.28	31	10.13	2.20
	Duty cycle (%)	D	52	13	85	33
	Amplitude (mm)	A^{in}	10.73	47	25.28	4.33
		A^{ex}	10.73	47	27.38	4.55
		A^{ave}	10.73	46	26.04	4.45
		A^{abs}	16.46	60	37.61	6.54

The previous analysis has given an idea about the variability of breathing characteristics by means of statistical tools. Another type of statistical analysis will be devoted to visualize the distribution shape of different characteristics of breathing motion. This is very important for several reasons. First, it can be used to summarize a data set to better understand general characteristics such as shape, spread, or location. In turn, this information can be used to suggest transformations or probabilistic models for the data. Second, these methods might be helpful to check model assumptions, such as symmetry, normality, etc.

An adequate design of margin around the CTV is usually used to reduce the effect of breathing-induced tumour motion during the treatment delivery. The width of the margin is commonly based upon the quadrature sum of the standard deviations of the contributory errors over patient population and for a particular treatment site. This approach is applicable when the PDF of the component errors are Gaussian. Respiratory motion uncertainty was considered as Gaussian by Van Herk [Herk 2004], however McKenzie did not agreed with this assumption [McKenzie 2000]. As part of the analysis, the distribution of respiratory motion will be assessed, in order to check the normality hypothesis on current data.

Figure 4.22 illustrates the distributions of the different respiratory data investigated in this work. Indeed, both internal and external respiratory data used in this work can be approximated by Gaussian distributions with different parameters. Concerning external data, one can see that there is more fluctuation in AI data compared to FB and AVB. The standard deviation of FB, AI and AVB are $0.14\ cm$, $0.19\ cm$ and $0.10\ cm$ respectively.

Since the number of trajectories of internal movement is small compared to external movement, it seems obvious that the distributions for these latter are more representative than the former. However it can be considered as Gaussian distribution. The standard deviation of this latter is $1.29\ mm$. By comparing the distribution of the drift and the breathing signals, one can observe that the standard deviation is roughly similar for external data and larger for the respiratory signal in the internal movement. This confirmed that the external measurement are more indisposed to the baseline shift. This finding will be useful to validate a simulation model of breathing.

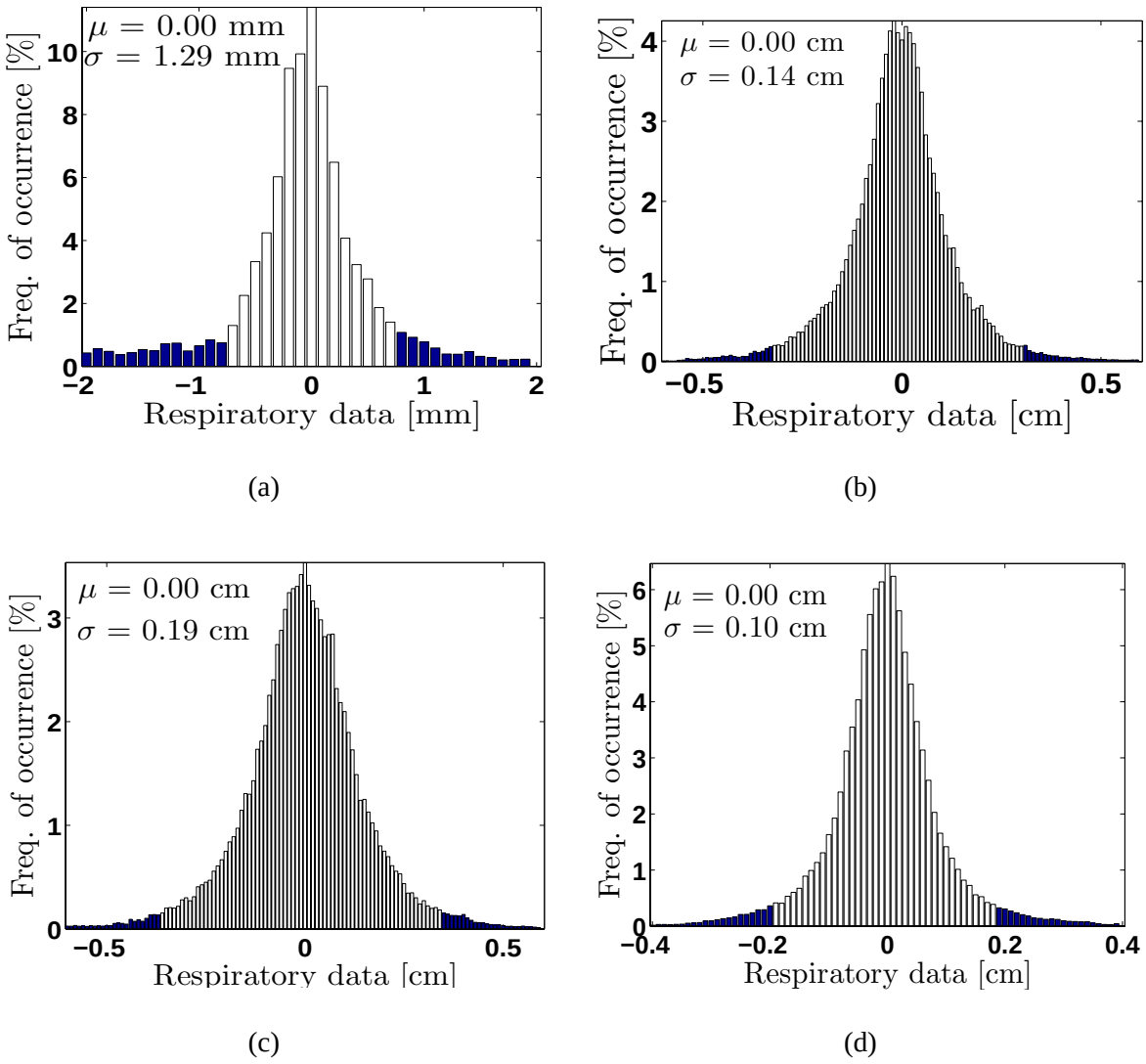

Fig. 4.22: Distributions of the respiratory data for (a) IFM, (b) FB , (c) AI and (d) AVB .

The overall population's distributions for breathing durations and amplitudes have also been investigated. At the first instance, only the durations are considered, especially, the period T and the ratio D. The parameter $T1$ and $T2$ are not involved since they are correlated to T. The main aim of evaluating the distributions of the quantities T and D, is to create a model of breathing frequencies as well as state changes in order to be used in the simulation of respiratory movement later on. For the four type of trajectories a PDF of each parameter for an overall population was fitted.

Figure 4.23 and 4.24 show the distributions of T and D for FB, AI, AVB and IFM respectively. In the external markers data, the most dominant periods are between 2.5-3.5s for FB, 3-4s for both AI and AVB. The gating has increased the period of breathing, by increasing the importance of the periods between 4.5-5.5s. For the internal markers data, the main periods are located between 2.5-3s. Regarding the

distribution of D one can see that the dominant range is 50%-55% for the fours datasets. In order to model the data distributions, several distributions have been carried out. It was found that generalized extreme value (GEV) distribution is the more appropriate distribution for T and D. The GEV distribution is a flexible three-parameter model that combines the Gumbel, frechet and Weibull maximum extreme value distributions. It has the following PDF:

$$f(x|k,\mu,\sigma) = \begin{cases} \frac{1}{\sigma}\exp\left(-(1+k\frac{(x-\mu)}{\sigma})^{-\frac{1}{k}}\right)\left((1+k\frac{(x-\mu)}{\sigma})^{-1-\frac{1}{k}}\right) & \text{if } k \neq 0 \\ \frac{1}{\sigma}\exp(-\frac{(x-\mu)}{\sigma} - \exp(-\frac{(x-\mu)}{\sigma})) & \text{k= } 0 \end{cases}$$

where k, σ,μ are the shape, scale, and location parameters respectively. The scale must be positive ($\sigma > 0$), the shape and location can take on any real value.

The idea of modelling the respiratory motion period and duty cycle distributions was motivated by the need of a realistic respiratory motion data generator that can be used by researches for example to assess their motion compensation strategies or developed algorithms.

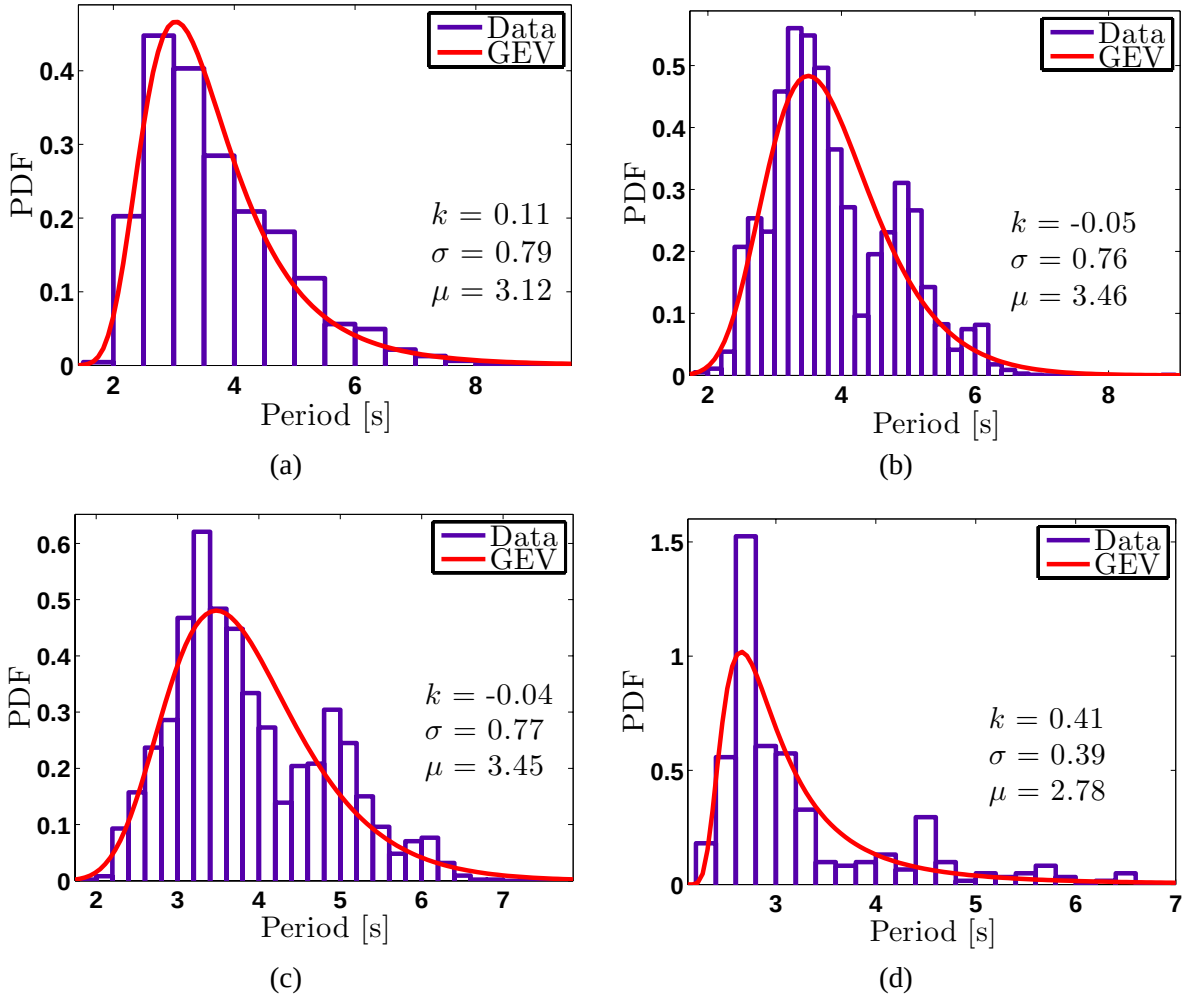

Fig. 4.23: Distributions of the period for (a)FB, (b) AI, (c) AVB and (d) IFM.

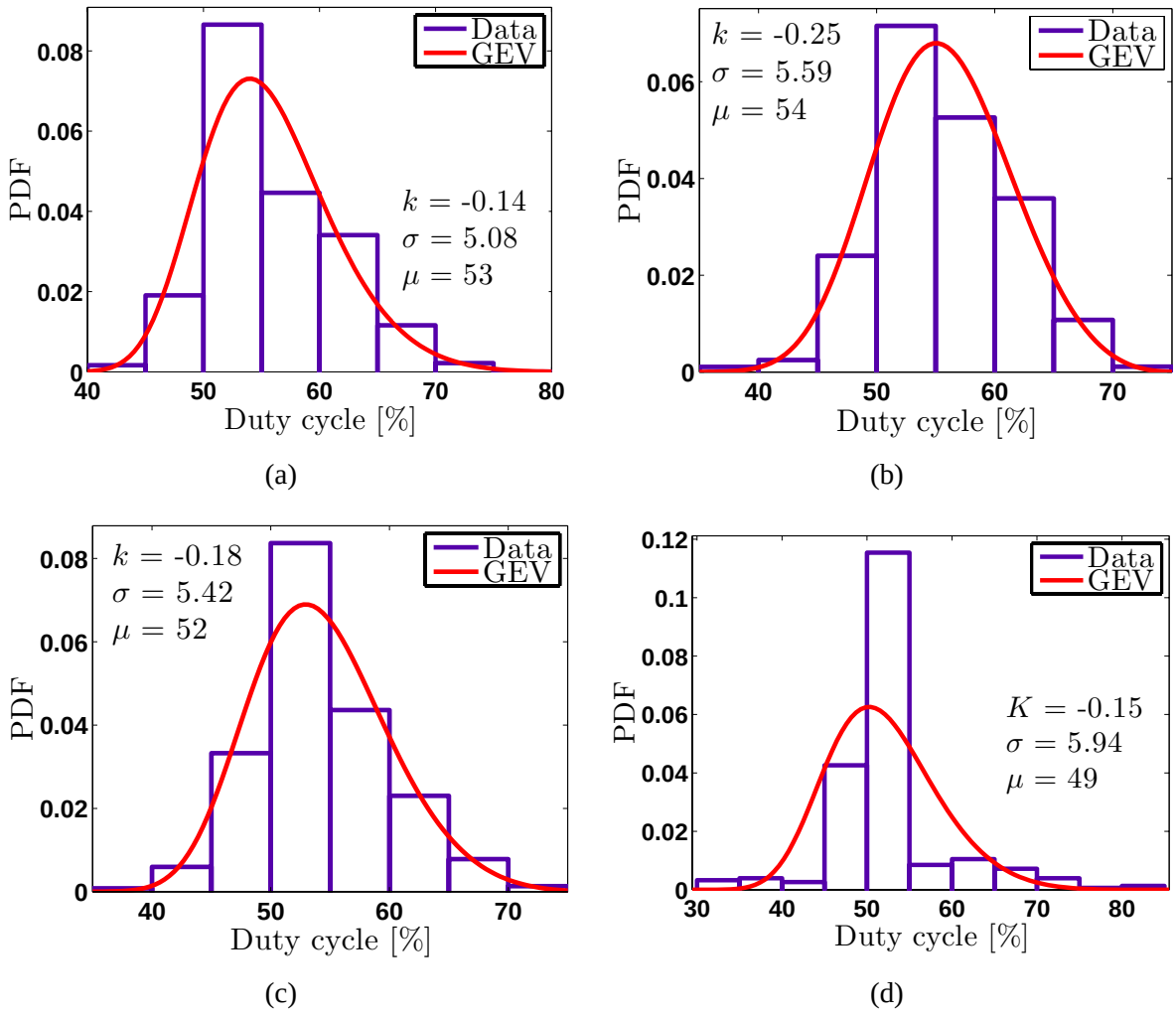

Fig. 4.24: Distributions of duty cycle for (a)FB, (b) AI, (c) AVB and (d) IFM.

The distributions of the overall absolute amplitude for FB, AI, AVB and IFM data sets are shown in Figures 4.25. The range of the overall absolute amplitudes of the three internal motion data are not comparable. In the FB data the most important absolute amplitudes are between 0.5-2cm. The AI test has generated an increase in the absolute amplitudes where the dominant values are between 1-2.5 cm. In the AVB test the absolute amplitude of the trajectories was reduced to a range of 1-1.5 cm. Concerning the IFM data set, the regular absolute amplitude values are between 1 cm and 1.5 cm.

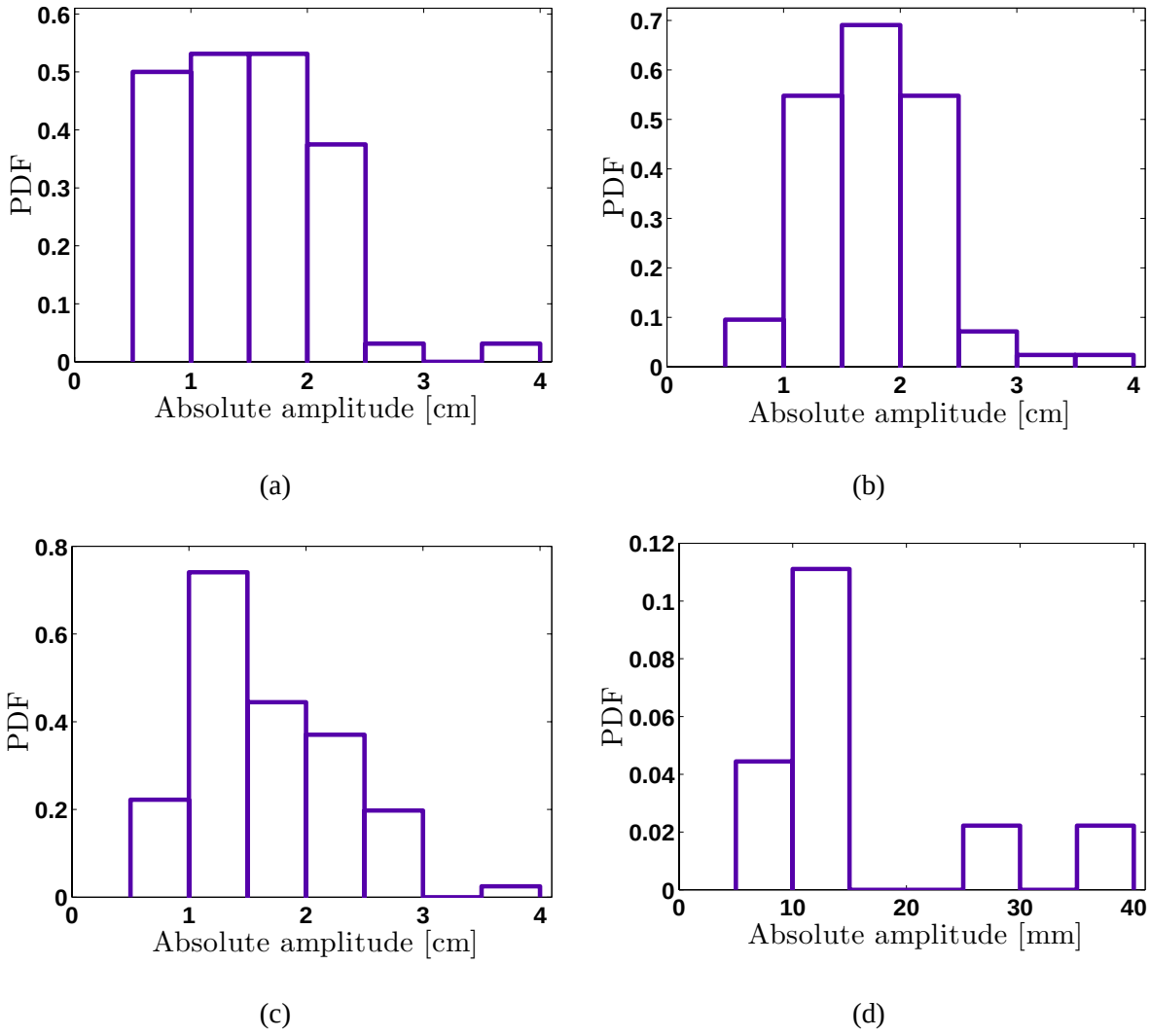

Fig. 4.25: Distributions of the overall absolute amplitude for (a) FB, (b) AI, (c) AVB and (d) IFM.

4.5 Respiratory velocity and acceleration

The velocity and acceleration of respiratory motion are crucial variables for different RTTT techniques such as a DMLC [Wijesooriya et al. 2005], PSS [D'Souza et al. 2005] or robotic arm [Schweikard et al. 2004] (see Chapter 2). Note that the PSS based method is a closed-loop system unlike the DMLC and robotic arm or LINAC which are open-loop systems. In the three approaches the limits of the respiratory velocity and acceleration are required for suitable system design and greater accuracy. This latter can be achieved by measuring or estimating the velocity and acceleration in real-time. Furthermore, the design of dynamic lung phantom for QA evaluation, has to consider the speed of motion [Shirato et al. 2000b]. Finally, the said parameters can be used to predict the tumour motion position in order to compensate for different treatment delays, as it is the case in [Shirato et al. 2000b, Putra et al. 2008].

It is important to remember that only few contributions have given the range of velocity and acceleration information. The velocity can be defined as the rate of change of position. It is a vector physical quantity; both speed and direction are required to define it. The speed of tumour can be calculated from the following formula:

$$v = \frac{dx}{dt} \tag{4.5.1}$$

The acceleration is defined as the rate of change of velocity, or as the second derivative of position (with respect to time). It can be calculated from the following formula:

$$a = \frac{d^2x}{dt^2} \tag{4.5.2}$$

The velocity and acceleration of respiratory motion were calculated for the different breathing motion using the filtered data. An illustration of the breathing position, velocity and acceleration profiles for the FB case, are given in Figure 4.26. It was noticed from the latter that the velocity and acceleration depend on the amplitude and period of breathing. To demonstrate this result, the velocity and acceleration of breathing exhibited by the tumour due to respiration was performed utilising the standard tumour motion model [Lujan et al. 1999] given by (3.2.1). The corresponding velocity and acceleration are as follows:

$$v = (2nA\frac{\pi}{\tau})\cos^{2n-1}(\frac{\pi t}{\tau} - \phi)\sin(\frac{\pi t}{\tau} - \phi) \tag{4.5.3}$$

$$\begin{aligned} a = {} & 2An(\frac{\pi}{\tau})^2\big[-4\cos^{2n-2}(\frac{\pi t}{\tau} - \phi)\sin^2(\frac{\pi t}{\tau} - \phi) \\ & + \cos^{2n}(\frac{\pi t}{\tau} - \phi) + \cos^{2n-2}(\frac{\pi t}{\tau} - \phi)\sin^2(\frac{\pi t}{\tau} - \phi)\big]\Bigg(\end{aligned} \tag{4.5.4}$$

It was found that for a typical tumour motion pattern (A=10 mm, τ=4 s, n=2) the maximum acceleration and the maximum velocity are 49 $mm \cdot s^{-2}$ and 31 $mm \cdot s^{-1}$, respectively. For extreme (hardly realistic) case of tumour motion (A=30 mm, τ=3 s, n=4) these quantities are 263 $mm \cdot s^{-2}$ and 251 $mm \cdot s^{-1}$,

respectively.

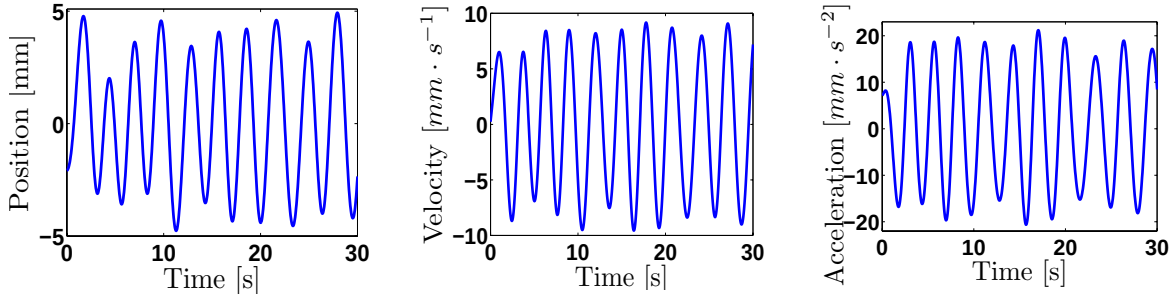

(a) (b) (c)

Fig. 4.26: An example of signals representing (a) position, (b) velocity and (c) acceleration.

In order to evaluate the overall range, average and relative standard deviation (in percentage) of breathing motion speed and acceleration for both free and gated data, a statistical analysis has been performed. The numerical results of this analysis are shown in Table 4.2. In addition to the speed and acceleration of the overall breathing cycles, the mentioned variables have also been estimated for the overall IN and EX phases. This will help to compare the speed and acceleration between IN and EX.

Concerning the speed of breathing in IN phase compared to the EX, it was noticed that in the first one the motion of lung is much faster than in EX, except for the IFM data that exhibits almost the same speed for both states. This is the opposite case for the acceleration. These last two results seem to be logical, since the respiratory system function is based on the help of muscles. These latter need more energy during the inhalation compared to the exhalation. Concerning the average speed comparison, it was found that it is 6 $mm \cdot s^{-1}$ for FB and 7 $mm \cdot s^{-1}$ for AI, AVB and IFM. The increase of average speed for the external data is caused by the increase of the amplitude by the gating method. The average acceleration is 11 $mm \cdot s^{-2}$, 12 $mm \cdot s^{-2}$, 13 $mm \cdot s^{-2}$ and 15 $mm \cdot s^{-2}$ for FB, AI, AVB and IFM respectively.

In term of speed and acceleration fluctuations, it can be seen that, there is more variation in the EX phase compared to IN. The audio and audio video gating have reduced this fluctuation, but they increase their ranges. The maximum speed and acceleration were larger for AVB and AI with (51 $mm \cdot s^{-1}$,117 $mm \cdot s^{-2}$) and (46 $mm \cdot s^{-1}$,108 $mm \cdot s^{-2}$) comparing to FB and IFM with (31 $mm \cdot s^{-1}$,71 $mm \cdot s^{-2}$) and (26 $mm \cdot s^{-1}$,58 $mm \cdot s^{-2}$).

Tab. 4.2: The range of speed and acceleration for internal and external respiratory data.

Data (Nb. of traces)	Proprieties	States	Avg.	Std./Avg. [%]	Max.
FB (64)	Speed ($mm \cdot s^{-1}$)	IN	6	73	31
		EX	5	76	26
		Cycles	6	76	31
	Acceleration ($mm \cdot s^{-2}$)	IN	10	83	66
		EX	13	88	71
		Cycles	11	88	71
AI (84)	Speed ($mm \cdot s^{-1}$)	IN	8	67	46
		EX	6	76	35
		Cycles	7	73	46
	Acceleration ($mm \cdot s^{-2}$)	IN	10	80	93
		EX	15	82	108
		Cycles	12	85	108
AVB (81)	Speed ($mm \cdot s^{-1}$)	IN	8	73	51
		EX	6	75	33
		Cycles	7	75	51
	Acceleration ($mm \cdot s^{-2}$)	IN	11	86	105
		EX	14	89	117
		Cycles	13	89	117
IFM (9)	Speed ($mm \cdot s^{-1}$)	IN	7	79	26
		EX	7	77	25
		Cycles	7	78	26
	Acceleration ($mm \cdot s^{-2}$)	IN	13	68	44
		EX	16	76	58
		Cycles	15	73	58

The overall distribution of velocity and acceleration were carried out and results are shown in Figure 4.27 and 4.28. The profile of the velocity and acceleration distributions for the external data has two modes. One representing the exhale phase and the other one represents the inhale phase. It was notice that the most dominant range of velocities are between $\pm 10\ mm \cdot s^{-1}$, while for the acceleration was between $\pm 20\ mm \cdot s^{-1}$. Concerning the internal data, the profile of the velocity distribution has 7 modes. This results from the variability of the respiratory motion in this type of data. However, the main values of the velocity are between $\pm 10\ mm \cdot s^{-1}$.

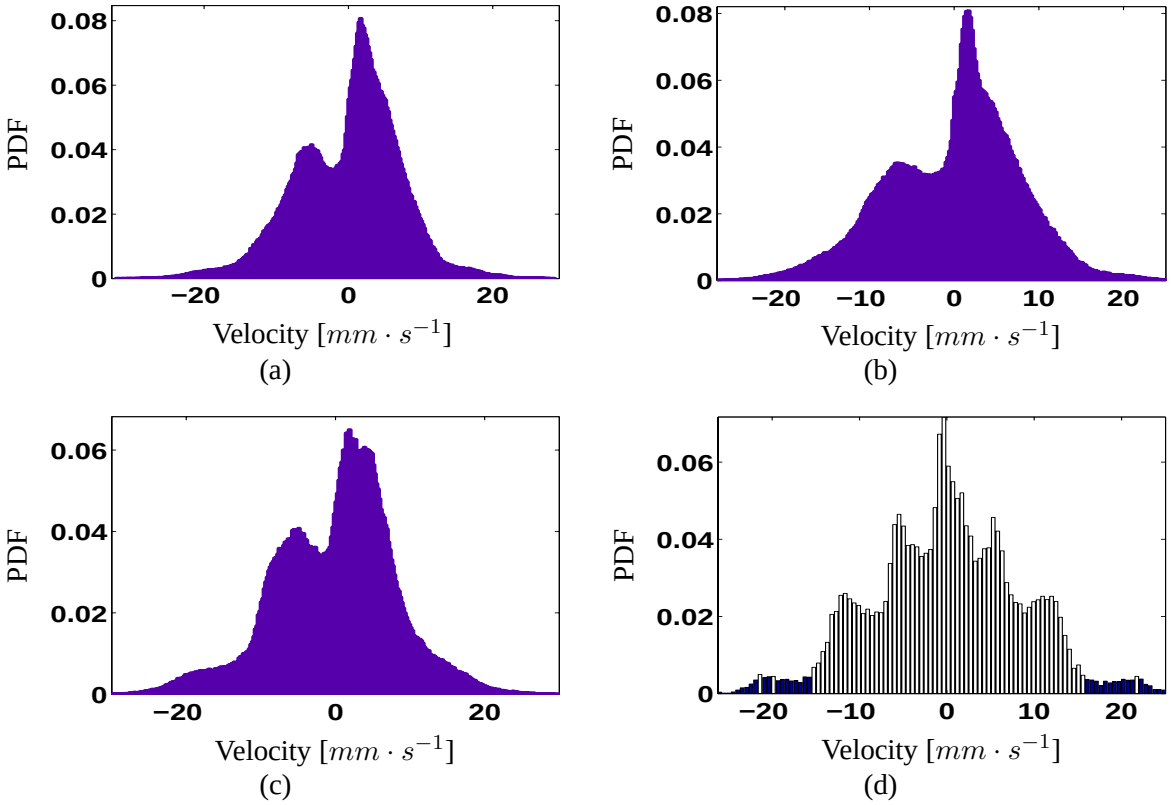

Fig. 4.27: Motion velocity distributions for (a) FB, (b) AI, (c) AVB and (d) IFM.

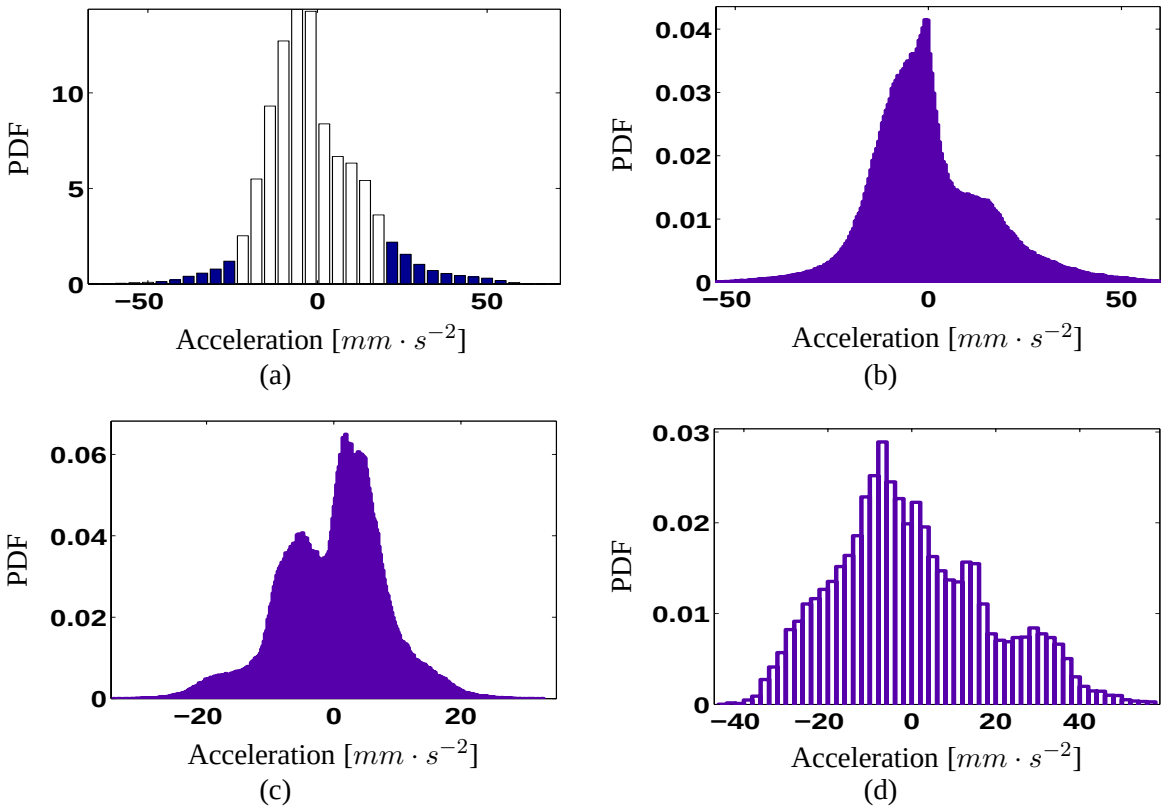

Fig. 4.28: Motion acceleration distributions for (a) FB, (b) AI, (c) AVB and (d) IFM.

4.6 Discussion and conclusions

This chapter has presented an analysis of internal/external surrogate respiratory motion data. The latter involves both the internal SI displacement of fiducial markers implemented around the tumour and the AP motion of external markers attached to the chest. For an accurate analysis of the respiratory motion, trajectories that exhibited abnormalities/irregularities (e.g. sudden large position change), were excluded from the both data sets. An analysis in the time and frequency domains of the selected signals was carried out. This has highlighted the presence of signals such as measurement noise (>0.5 Hz), baseline drift (<0.1 Hz), and heart beat (between 1-1.2 Hz) in addition to the breathing-pattern (between 0.1-0.4 Hz).

The respiratory, drift and measurement noise signals were approximated by Gaussian distributions with different parameters. By comparing the standard deviation of the three distributions, it was found that the breathing distribution is roughly similar to the drift one for the external data and larger in the internal data. Both respiratory and drift distributions have a larger standard deviation than the measurement noise in the external data, and similar between the drift and the measurement noise in the internal motion.

By contrast to current approaches that divided respiratory motion in three phases, two phases were considered in this work, as the external motion data seldomly require three phases to be described appropriately. In addition the modelling approach adopted enable one to include the third phase within the first. The breathing was therefore modelled as a succession of exhalation and inhalation with varying amplitude and duration. The average period T and duty cycle D were (3.67s, 56%) ,(3.87s, 56%), (3.87s, 54%) and (3.28s, 52%) FB, AI, AVB, and IFM respectively. There was more fluctuation of the average period in the free breathing rather than the gated ones. The average amplitude of respiratory was found to be 1.03 cm, 1.25 cm, 1.30 cm, and 1.07 cm for FB, AI, AVB, and IFM respectively.

The statistical distributions of the period and duty cycle were calculated and found to be non-Gaussians. Such information is used in subsequent chapters, to generate realistic motion data from the new model developed in Chapters 5. Finally, the velocity and acceleration of the both motions were calculated. The average surrogate speed was of the order of 7 $mm \cdot s^{-1}$, the maximum velocity were between 26 $mm \cdot s^{-1}$ and 51 $mm \cdot s^{-1}$. The average acceleration was below 15 $mm \cdot s^{-2}$ and the maximum acceleration, which occurred rarely, was between 58 $mm \cdot s^{-2}$ and 117 $mm \cdot s^{-2}$. The maximum average speed and acceleration were larger for AVB and AI data comparing to the FB and IFM. Such findings informed other members of the MAESTRO team as to the requirement that was imposed on the PSS control system in term of ability to compensate for relatively small motion together with the requirement for the overall system velocity and acceleration. Moreover, the findings were used to define the design requirements of the developed lung phantom [Land 2009].

In conclusion, the analysis of the respiratory motion has helped to identify motion pattern, evaluate breathing irregularities and select the minimal number of variables needed to describe the motion. Moreover, it has provided a valuable information that can be used for clinical practice, including motion modelling, treatment planning and motion prediction for real-time treatment delivery.

Chapter 5

A new bilinear model for markers-based respiratory motion simulation

5.1 Introduction

Having reviewed current modelling and prediction algorithms in chapter 3 and analysed the clinical surrogate motion trajectories, the current chapter describes two new respiratory models which aim to: (i) replicate the movement of respiration during the radiation delivery, (ii) evaluate treatment strategies on simulations, (iii) provide realistic motion trajectories that could be followed by an artificial phantom, (iv) be used together with the statistical information collected in Chapter 4 to generate a set of benchmark trajectories to be used by other researchers.

The first model is based on a second order bilinear system (BLS) defined by an input/output difference equation. The model structure is derived from the knowledge gained from the clinical respiratory motion analysis performed in Chapter 4. The model parameters are then estimated off-line and on-line. While the former is considered to simulate the respiratory motion, the latter is desirable to accommodate for breathing changes. The proposed model and the parameter estimation are validated using the clinical data presented in Chapter 4.

A polynomial and filtering approaches was used to remove the drift signals from the respiratory motion prior to modelling and simulation. In both instances, the parameters of the models were analysed and the generalizability of the mean average bilinear model for each respiratory data set was assessed. The bilinear model with fixed parameters was used to generate a set of respiratory data that can be used to realistically simulate breathing motion. Moreover, a set of different types of drift signals were added to the simulated respiratory motion in order to take into account the baseline drift in the respiratory motion.

The second method to model the respiratory motion has considered the modelling of the breathing cycles based on an on-line polynomial structure with the same number of parameters as the widely adopted modified cosine function. The latter has been implemented on-line and used as a benchmark to compare the performance of the polynomial model.

This chapter is organised as follows: Section 5.2 gives some background about the modelling framework of the bilinear systems. Section 5.3 presents an overview about the system identification technique. The new bilinear approach for respiratory motion modelling is discussed in Section 5.4. Section 5.5 presents an adaptive bilinear approach for respiratory motion modelling. Modelling based on the cosine and polynomial functions are shown in Section 5.6 and 5.7 respectively. The process of generating the set of respiratory motion data is described in Section 5.8. Finally, conclusions are drawn in the last Section.

5.2 Background on modelling framework of bilinear systems

The concept of BLSs was introduced in the 1960's (see the surveys of references [Bruni et al. 1974, Mohler and Kolodziej 1980]). The BLSs form a subclass of nonlinear systems which are distinguished by their linearity in both state and input (or control), when considered separately. The bilinearity arises as a product between a system states and input [Mohler 1973a]. Being linear separately with respect to the state and the input, but not jointly, has enabled the extension to bilinear systems of the theory developed for linear systems both time-variant and time-invariant. Such systems were firstly applied to the control field, when Mohler et *al.* considered a control system with multiplicative mode for modelling and controlling a nuclear reactor [Mohler 1973a]. The non-linear structure of BLSs offers some important advantages comparing to the linear case. With regard to modelling framework, the multiplicative term allows the modelling of those systems whose dynamic exhibit variability.

BLSs have been found to be natural approximation of many types of systems commonly encountered in fields such as biology, socio-economics and engineering applications, see for example [Bruni et al. 1974, Mohler and Kolodziej 1980, Dunoyer 1996, Mohler 1970; 1971; 1972, Biondi et al. 1972, Leontief 1970, Disdell 1995, Mohler 1973b, Figalli et al. 1984, Mohler et al. 1996, Schwarz et al. 1996, Weeb et al. 1996], The widespread use of BLSs has motivated the development of various algorithms for estimating the parameters of BLSs, such as subspace-based parameter estimation methods for BLSs [Favoreel et al. 1999, Verdult and Verhaegen 1999]. Maximum Likelihood and associated methods for parameter estimation have also been applied to BLSs [Gibson et al. 2005].

In order to understand the characteristics of the BLSs, the following single-input single-output (SISO)

discrete-time bilinear state-space representation of a BLS is considered:

$$\mathbf{x_{k+1}} = \mathbf{A}\mathbf{x_k} + \mathbf{u_k}\mathbf{N}\mathbf{x_k} + \mathbf{B}\mathbf{u_k} + \mathbf{w_k}, \tag{5.2.1}$$

$$\mathbf{y_k} = \mathbf{C}\mathbf{x_k} + \mathbf{D}\mathbf{x_k} + \mathbf{v_k}. \tag{5.2.2}$$

Where, at each sample k, $\mathbf{x_k} \in \mathbb{R}^n$ is the system state vector, $\mathbf{u_k} \in \mathbb{R}^m$ and $\mathbf{y_k} \in \mathbb{R}^p$ are the model input and output respectively. The matrices $\mathbf{A} \in \mathbb{R}^{n\times n}$, $\mathbf{N} \in \mathbb{R}^{n\times m\times n}$, $\mathbf{B} \in \mathbb{R}^{n\times m}$, $\mathbf{C} \in \mathbb{R}^{p\times n}$, $\mathbf{D} \in \mathbb{R}^{p\times m}$ parameterise the system. The sequences $\mathbf{w_k}$ and $\mathbf{v_k}$ are the unobserved state and measurement noise signals, respectively. This system may be rewritten in a time-varying linear (LTV) form as:

$$\mathbf{x_{k+1}} = \widetilde{\mathbf{A}}(\mathbf{u_k})\mathbf{x_k} + \mathbf{B}\mathbf{u_k} + \mathbf{w_k}, \tag{5.2.3}$$

$$\mathbf{y_k} = \mathbf{C}\mathbf{x_k} + \mathbf{D}\mathbf{x_k} + \mathbf{v_k}, \tag{5.2.4}$$

where, for each sample k, $\widetilde{\mathbf{A}}(\mathbf{u_k}) = [\mathbf{A} + \mathbf{u_k}\mathbf{N}]$ represents an input dependent 'system' matrix. A similar combination can be achieved by considering the input vector $\mathbf{B}$, yielding to a state dependent input vector.

The stability of linear systems has been clearly defined compared to nonlinear systems. However, if the control input is bounded from the above and below, i.e. $u_{min} < u < u_{max}$, then it is possible to determine stability in term of the equivalent of the eigenvalues of the linearized system at some input dependent operating point [Dunoyer 1996]. This condition was taken into account in this work by using input signals that are bounded. Considering the linearised system given by (5.2.3) and (5.2.4), the stability may be deduced from the zeros of $det[\lambda\mathbf{I} - \widetilde{\mathbf{A}}(\mathbf{u_k})] = 0$.

An equivalent quasi-linear transfer function representation may be defined as the ratio [Mohler 1973b]:

$$\frac{N(s)}{D(s)} \approx \frac{b_m s^m + b_{m-1}s^{m-1} \cdots + b_1 s + b_0}{s^n + (a_{n-1} - \eta_{n-1}u)s^{n-1} \cdots + (a_0 - \eta_0 u)}, \tag{5.2.5}$$

where s is interpreted as $s = d/dt$ without the rigour of the Laplace variable associated with linear models. The bilinear parameters are denoted by η_i and the linear part of the system is described by a_i and b_i. Since $\widetilde{\mathbf{A}}(\mathbf{u_k})$ is an input dependent quantity, the input $\mathbf{u_k}$ will affect both the dynamic and steady state characteristics of the system. To illustrate this effect a steady state output and gain were performed as in [Dunoyer 1996]. These can be written as follow:

$$Y_{ss} = \frac{b_0 U_{ss}}{a_0 - \eta_0 U_{ss}}, \tag{5.2.6}$$

$$G_{ss} = \frac{U_{ss}}{Y_{ss}} = \frac{b_0}{a_0 - \eta_0 U_{ss}}, \tag{5.2.7}$$

where, Y_{ss} and U_{ss} are defined as the steady state input and output, respectively. Such a static characteristics is shown in Figure 5.1. While the linear system corresponds to the case $\eta_0 = 0$, the BLS characteristics corresponds to $\eta_0 > 0$ and $\eta_0 < 0$. It is important to note that the steady-state gain is increasing for $\eta_0 > 0$ and reducing for $\eta_0 < 0$, with increased steady-state input. A considerable modelling error might occur if a linear model is used to replicate a nonlinear phenomena. For the case of the respiratory process which exhibits IN and EX states, it is expected to have a positive η for the former and a negative η for the latter.

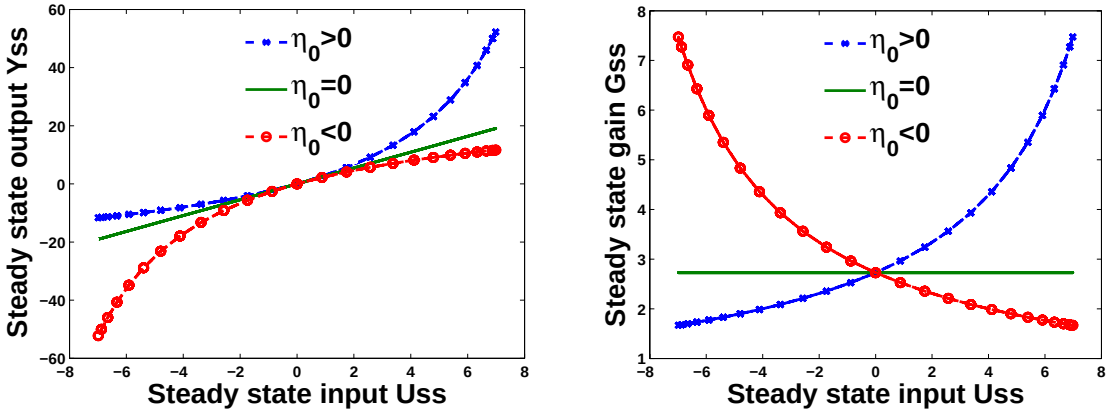

(a) (b)

Fig. 5.1: BLS steady-state characteristics for: (a) system output, and (b) system gain.

In this research the modelling process deals with observation in discrete-time obtained using various data-acquisition devices. The discrete-time representation of a discrete time-invariant SISO class of BLS is described by a bilinear model in the form of a Nonlinear Autoregressive with eXogenous Variables (NARX) process (so called input/output difference equation), of the form:

$$A(q^{-1})y_k = B(q^{-1})u_k + \sum_{i=1}^{p}\sum_{j=1}^{r}\eta_{ij}u_{k-i}y_{k-j} + \epsilon_k, \tag{5.2.8}$$

where k is the integer time index, $r \leq n_a$, $p \leq n_b \leq n_a$, n_a and n_b are the orders of the A and B polynomials, q^{-1} is the backward shift operator, defined by $q^{-1}x_k = x_{k-1}$, u_k, y_k are the input-output sequences and ϵ_k represents additive output noise. The polynomials $A(q^{-1})$ and $B(q^{-1})$ are given by

$$A(q^{-1}) = 1 + a_1q^{-1} + ... + a_{n_a}q^{-n_a}, \tag{5.2.9}$$

$$B(q^{-1}) = b_1q^{-1} + ... + b_{n_b}q^{-n_b}, \tag{5.2.10}$$

where, a_i, b_i are constant coefficients. Moreover, the bilinear parameter η_{ij} is also constant.

Having introduced the notion of bilinear approach for system representations with the abilities to model nonlinear characteristics, hence replicate the behaviour of a plant more appropriately and over a wider operating range than linear models, the next section focuses on a brief introduction to the field of system identification.

5.3 System identification : An overview

In most practical applications the system under investigation is not known and has to be estimated by making use of all available information. This technique is called system identification, and is about constructing a mathematical model from measurement data. This is often referred to black-box model estimation, when the parameters of the model have no physical interpretation, and grey box, when the parameters reflect physical proprieties. There exist several different methods to solve the system identification problem, for example PEM [Ljung 1999], subspace methods [Overschee and De Moor 1996] and non-parametric [1] correlation and spectral analysis methods [Ljung 1999]. System identification involves the following steps: Data set recording, structure identification, parameter identification and model validation, all of which include choices that are subject to personal judgement supported by a range of decisions criteria to evaluate the appropriate use of the solution.

The data recording

The system input-output data are collected through an experiment. Usually, a so called identification experiment is designed to maximise the information carried by the recorded data. The experiment may involve the choice of signals to be measured, and when can be measured, as well as the input (or test) signal choice, the sampling interval, etc. In some situations the possibilities to obtain data are much more limited and it is not possible to control for external factors that influence the outcomes. In this work, the data were recorded from human volunteers and patients under different conditions. Some patients were subjected to various stimuli whilst others were left to breath freely. Whilst the 'output' was measured, the stimuli received by the patient were not. The initial step of the work was to define an appropriate 'input' to the model which would results in the observed organ/patient motion.

[1] In the system identification literature a distinction has been made between parametric and non-parametric methods. The parametric methods deals with estimating a specified number of parameters, whereas the non-parametric methods deals with estimating e.g. entire spectra or step responses

Structure identification

Structure identification is considered as the most important, and at the same time the most difficult issue in system identification. Roughly speaking the problem can be divided into three sub-problems. The first one is to specify the type of model set to use. This involves the selection between linear and nonlinear structure, between black box, grey box and physically parametrised approach, and so on. The next issue is to decide the size of model set. This includes the choice of possible variables and combination of variables to use in the model. It also involves fixing orders and degree of the chosen model types, usually to some intervals. The last item to consider how to parametrise the model set so that the estimation algorithm will be successful in finding reasonable parameter values.

The aim of the model developed in this work is to be generalisable to replicate a range of realistic motion. From a practical perspective the simplest possible model should be used with the minimum number of parameters. The structure of the models developed in this Thesis comprises linear and bilinear structures ranging from second-order to third-order models. The second-order model structure was used for the clinical data (see 5.4), since the analysis of the latter showed that the respiratory data is similar to the response of a second order system. Whilst in the data collected from the carried out experiment a set of model structures including second and third orders were assessed (see 6.4). The third order models were also investigated to see whether they can perform better.

Parameter identification

The next step is to find the parameters of the selected models that explain better the experimental data. It is called the parameter identification (or estimation) problem, in which a high model accuracy is desirable and the numerical solution should be tractable and reliable. Usually, the first criterion is defined by the cost function to be minimised [Ljung 1999]. It is very common in engineering problems to choose a quadratic cost function for its convex property. A commonly used cost function is the mean squared prediction error (MSPE) between the measured and the h_p-step-ahead prediction of the system output. This quantity depends on the parameters of the model to be estimated and is defined as follow:

$$MSPE(\theta) = \frac{1}{N}\sum_{k}\left[y(k) - \hat{y}(k|k-h_p,\theta)\right]^2, \tag{5.3.1}$$

where h_p is typically chosen as unity, or is represented as an integer multiple of the sampling interval, N the number of data, and θ vector of parameters to be estimated. Minimising such a cost criterion leads to a parameter identification framework, which is known as PEM. One particular subset of PEM, which

is known as output error (OE) minimisation, is extensively used in this research work to build simulation models of the respiratory motion. In general, it can be interpreted as having an horizon h_p tending towards infinity, or at least to a number N of samples or observations. The corresponding minimised cost function defines the mean squared simulation error (MSSE), and is given by

$$MSSE(\theta) = \frac{1}{N}\sum_{k=1}^{N}\left[y(k) - \hat{y}(k|k,\theta)\right]^2, \tag{5.3.2}$$

which is the MSSE between the measured output y of the system and the simulated output $\hat{y}$ of the model. The model parameters are obtained by minimising the introduced cost criteria (depends on the model purpose). For example the minimising parameter vector for a simulation model is defined by:

$$\widehat{\theta} = \arg\min_{\theta\in\mathcal{D}} MSSE(\theta) \tag{5.3.3}$$

This operation is known as the optimisation process which attempt to find an optimal numerical solution. In this work constrained and unconstrained Nelder−Mead Simplex Method [Lagarias et al. 1998], were used for this purpose. It is important to state that the two presented cost criteria can also be used as a means to assess the performance of the different modelling techniques. Additionally, in the case where recursive estimation techniques are applied to obtain a time-varying model, use is made of the standard deviation of the estimated parameters, denoted $std(\hat{\theta}(k))$.

Model validation

When a model is identified, the next step is model validation. This step involves the assessment of whether the estimated model is generalisable and adequate for its purpose. This is usually carried out by dividing the measured data obtained from the real system into two distinct sets. The first set is called the identification set which is utilised as, its name implies, to identify the model parameters and the second one, called validation sets, allowing the model to be tested on unseen data, i.e. data not used for the identification. The conceptual idea behind such a process is that the model should aim to replicate the system behaviour (the identification set(s)) as best as possible, but not at the detriment of the generalisation to other data sets (the validation set(s)) issued from the same system.

The developed models in this work were validated using different respiratory data including clinical data from VCU (USA) and Hokkaido University School of Medicine (Japan) as well as data acquired from an investigated experiment. The steps of system identification technique are used next to determine model-based simulation of the respiratory motion.

5.4 Bilinear time-invariant (BTI) model for respiratory motion

The main motivation behind this modelling work is to investigate the applicability of system identification technique and, more particularly, the bilinear modelling framework to model and simulate respiratory motion. The new approach considers the lung as a dynamic system replicating the motion in response to a generated input signal. The latter is analogous to having a signal generated by the nervous system, which is the main responsible for the breathing process (see Section 2.4). In this work, the breathing process is considered as a succession of two states, i.e. IN and EX. Subsequently, a virtual input signal is modelled as a square wave with fixed amplitude and varying frequency/duty cycle corresponding to the irregular time switching between IN and EX. Fixed amplitude as well as amplitude depending on the inhale and exhale amplitudes were trialled, however the latter require more parameters to be identified. This Section, therefore, considers that the virtual input signal is of fixed amplitude.

Figure 5.2 illustrates an example of input signal generated from respiratory data described in Section 4.2 using the algorithm 1 described in Section 4.4. The input signal switch between a high level corresponding to the exhalation phase and the low level representing the inhalation phase. The main information exhibited by the generated input signals is the frequency characteristics of the respiratory motion. It is however important to notice that there is a time switching uncertainty due the accuracy of the input generation algorithm. In some simulations the switching level was between the maximum and minimum values of the respiratory motion instead of 1 and -1.

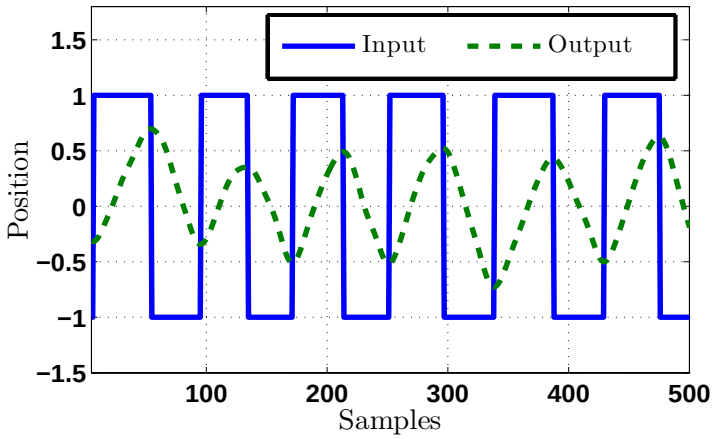

Fig. 5.2: An example of generated input signal.

Disturbances that can affect the respiratory motion include measurement noise, heart beat and amplitude drift over time (see Chapter 4). The main aim being to model only the respiratory motion, the remaining signals are considered as external signals, separated from the main respiratory signal. An illustration of the proposed overall modelling approach is shown in Figure 5.3. The measurement noise is assumed to

be above 3 Hz and is removed using a third order low pass Chebysev filter, which is applied twice, first in forward direction and then in reverse direction to obtained zero-phase shift, i.e. non-causal filter. The filter utilised here, is the function 'filtfilt', $Matlab^{®}$ software package. The same principle can be used to remove the heart beat component in the IFM.

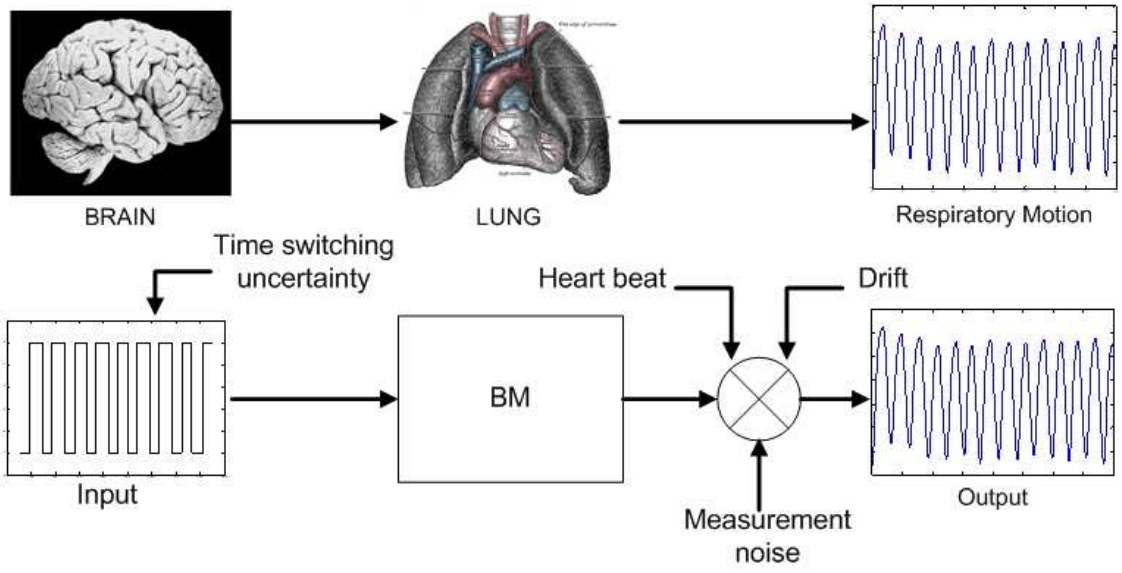

Fig. 5.3: Schematic of the overall modelling approach adopted in this work.

It was also shown in the respiratory data analysis performed in Chapter 4 the existence of a drift signal, which is more important in the external data. These low frequency components in general have a negative influence on the estimation results. They cause a considerable bias of the model and do not average out because of their low frequency behaviour. Hence, it is natural to remove them from the data. Two different approaches have been used for drift correction. The first one is to estimate the trends and to remove them from the signals. A polynomial function with different orders was initially fitted to the respiratory data. It was found that the drift is satisfactory modelled by 10^{th} and 20^{th} order polynomial function for internal and external data, respectively.

Figure 5.4 shows an example of drift modelling and elimination using a polynomial model. The latter is divided into sub-figure (a) and (b) which illustrate respectively an example of respiratory signal including the drift and the corresponding drift-free signal. The polynomial method to remove the drift was able to extract the drift from the respiratory data. The modelled drift signal will be removed from the filtered data before modelling and validation process. The surrogate motion can subsequently be reconstructed by adding the drift to the simulated breathing signal (see Figure 5.3).

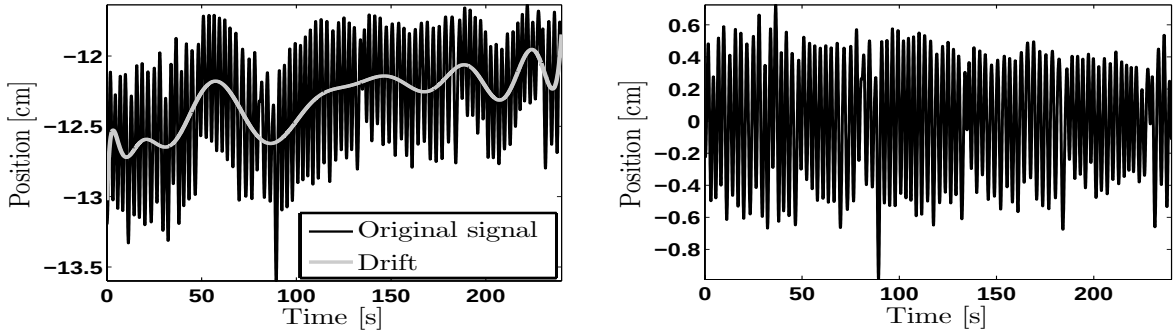

Fig. 5.4: Drift elimination using the polynomial model: (a) noise-free signal including the drift, (b) the drift-free signal.

Whilst the polynomial model is a known practice to deal with quadratic drifts, it might include some respiratory components because the choice of the polynomial order is approximate. Moreover, it is sensitive to the initial conditions. To overcome such issue padding strategies can be used.

The second 'model based'approach involves prior information about the frequency of the drift signal to filter it using a low pass-filter designed to remove the frequency components below 0.05 Hz. This cut-off frequency was chosen to make sure that only the drift signal is removed. An illustration of the proposed aforementioned approach is shown in Figure 5.5. The temporal and frequency representation of the noise-free respiratory signal with the drift is presented in sub-figure (a), and drift-free signal is shown in sub-figure (b). As it can be seen from the frequency representation of both noise-free and drift-free, the used filter was able to remove the low-frequency component and keep only the respiratory information. Note that a high-pass filtering can also be performed to remove the drift signal.

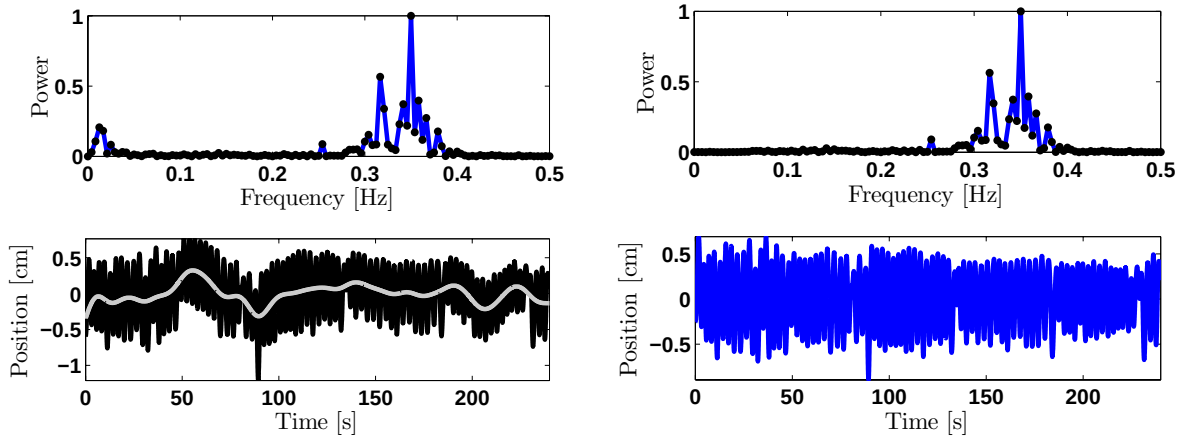

Fig. 5.5: Drift elimination via pre-filtering: (a) noise-free signal including the drift, (b) the drift-free signal.

After removing the external signals the next step is to find a model structure for the respiratory motion. It

has been demonstrated by several authors, see for example [Crooke et al. 2002, Kanae et al. 2004, Ben-Tal 2006], that the respiratory system is a nonlinear process. A bilinear model is an example of a suitable candidate for a nonlinear model which has been found in [Sahih et al. 2005; 2007] to be appropriate for simulating the respiratory cycles. The choice of the bilinear model (BM) stems from the analysis of the respiratory motion performed in Chapter 4, which showed that the exhale phase can be approximated with a second order system response and the inhale phase with first order response (see Figure 4.19). This results in an asymmetric response. Thus, the following second order BM structure is chosen to model the respiratory motion:

$$y_k = -a_1\, y_{k-1} - a_2\, y_{k-2} + b\, u_{k-1} + \eta\, y_{k-1}u_{k-1} + d + e_k. \tag{5.4.1}$$

The offset d is added in the model to compensate for the constant drift between the model output and real output due to the fact that the amplitude of the input u_k is constant. The modelling error (or residual) is represented by e_k.

5.4.1 Parameter estimation

Once the model structure is chosen, next stage will be parameters estimations. Given (5.4.1), the regression model can be written as follow:

$$y_k = {\boldsymbol{\varphi}_{bls}}^T(k)\boldsymbol{\theta} + e_k, \tag{5.4.2}$$

where the parameter vector $\boldsymbol{\theta}$ and regressor (or data vector) $\boldsymbol{\varphi}_{bls}$ are defined as follow:

$$\boldsymbol{\theta} = [-a_1\ , -a_2\ , b\ , \eta\ , d\ ]^T, \tag{5.4.3}$$

$$\boldsymbol{\varphi}_{bls}(k) = [y_{t-1}, y_{t-2}, u_{t-1}, y_{t-1}u_{t-1}, 1]^T. \tag{5.4.4}$$

From the measurement data the vector $\boldsymbol{\varphi}_{bls}(k)$ can easily be calculated at each instant $k = l, \ldots, N$, then $N - l + 1$ regression equations can be derived as:

$$\boldsymbol{y} = \boldsymbol{\Phi\theta} + \boldsymbol{e} \tag{5.4.5}$$

where

$$\boldsymbol{y} = [y(l), y(l+1), \ldots, y(N)]^T, \tag{5.4.6}$$

$$\boldsymbol{\Phi} = [\boldsymbol{\varphi}(l), \boldsymbol{\varphi}(l+1), \ldots, \boldsymbol{\varphi}(N)]^T, \tag{5.4.7}$$

$$\boldsymbol{e} = [e(l), e(l+1), \ldots, e(N)]^T. \tag{5.4.8}$$

Given that the goal of the model is to simulate the respiratory motion, it is proposed to estimate the parameters by minimising the $MSSE$, defined by (5.3.2). As such, the $MSSE$ relates to the Euclidean distance between the measured and simulated output, by opposition to the more communally used one step-ahead prediction, which utilised past output measurement. The resulting problem is non-linear and does not have explicit solution. An approximation can be made by use of an optimisation technique. In this particular case, use was made on the unconstrained Nelder−Mead Simplex Method [Lagarias et al. 1998]. In practice a non-linear minimising procedure is exposed to the risk of getting trapped in a local minimum. In order to avoid this problem, an initial estimate in the neighborhood of the minimum must be provided. Usually, an estimator in the category of prediction error method (PEM) is used for this purpose. A least squares (LS) method is one of those that minimises the criterion function J defined as a sum of squared errors

$$J^{LS} = \left\| \boldsymbol{y} - \boldsymbol{\Phi}\boldsymbol{\theta} \right\|_2^2 \tag{5.4.9}$$

The initial estimate is then given by

$$\hat{\theta}_i = (\boldsymbol{\Phi}^T \boldsymbol{\Phi}^{-1}) \boldsymbol{\Phi}^T \boldsymbol{y} \tag{5.4.10}$$

Finally, the introduced models were estimated and validated using the internal and external breathing motion in the SI and AP direction respectively . The steps of the applied algorithm can be summarised as follows:

Algorithm 2 Modelling and Validation Procedures of the Respiratory Motion

1: For a given respiratory signal $\{\mathbf{Y}^N\}$, where N is the number of samples considered.
2: Remove measurement noise and drift.
3: Generate a squares wave signal $\{\mathbf{U}^N\}$ with fixed amplitude by detecting the peaks corresponding to the end of the inhalation and the exhalation phases from $\{\mathbf{Y}^N\}$.
4: Separate data in two sets, the first set for modelling $\{\mathbf{U}_1, \mathbf{Y}_1\}$, and the other set of unseen data $\{\mathbf{U}_2, \mathbf{Y}_2\}$ to validate the model.
5: Estimate an initial vector parameter $\widehat{\boldsymbol{\theta}}_i$, for input-output observations $\{\mathbf{U}_1, \mathbf{Y}_1\}$, using linear least squares (LLS), which is based on minimising one step ahead prediction. This latter is then used to initialise the iterative optimisation technique in the next step.
6: Estimate using a nonlinear optimisation technique, the parameters of the model $\boldsymbol{\theta}$ iteratively by minimising the MSSE, for input-output $\{\mathbf{U}_1, \mathbf{Y}_1\}$.
7: Use the input observations $\{\mathbf{U}_2\}$ and the model to simulate the estimated unseen data $\{\widehat{\mathbf{Y}}_2\}$.

5.4.2 Simulation results for polynomial drift

The preliminary procedure utilised in this work to eliminate the drift signal was based on polynomial fitting. For every respiratory motion signal, the measurement noise was subtracted and a polynomial function with different orders were fitted using a least squares method (see an illustration in Figure 5.4). The input signals were then generated with the minimum and maximum values corresponding to the minimum and maximum of the respiratory trajectories. Having the input-output signals for every respiratory signal, a BTI model is built and validated using algorithm 2. The number of samples considered for both modelling and validation was N=1000, which is equivalent to 33s time for a sampling frequency of 30 Hz.

The modelling and validation procedures presented in the algorithm 2 were applied to the four different respiratory motion data-sets and a sample result from each data-set is given in Figure 5.6. Sub-figure (a) shows the modelling and validation results from a sample IFM data. In the first 1000 samples, an average BTI model of respiratory motion with different time constant for exhalation and inhalation is estimated. In the second 1000 samples, the estimated average BTI model was able to replicate the unseen data with an accuracy of 0.80 mm in term of MASE. The lower performances of the average BTI model were mainly noticed in the end of the inhalation and sometimes when an unusual motion within the end of exhalation occurs.

The performance of the BTI model applied to a sample trajectory from the FB dataset is shown in sub-figure (b). In the latter, a MASE of 0.94 mm was achieved by the BTI model in the validation step. Similar to the previous case the lower performances were noticed in the end of the inhalation. In sub-figure (c) and (d) a sample result from the AI and AVB data-sets respectively are shown. The BTI model performs the validations sets with a MASE of 1.17 mm for the former and 0.49 mm for the latter. One might notice that the MASE in validation stage for the AI sample has the largest value compared to the other samples from the remaining data-sets. This was mainly due to an irregular breathing cycle located after 500 samples (see sub-figure (c)).

The same remark as in the previous trajectories, the BTI model has a problem to catch the end of the inhalation in some breathing cycles. In conclusion, despite some respiratory motion irregularities, the BTI model can replicate adequately the respiratory motion with a MASE less or around 1 mm. The BTI model was able to replicate the slow respiratory motion such as the one given by the IFM as well as the fast motion which characterise the external markers data. In the case of a constant respiratory motion the BTI model can be used to track the respiratory measurement in the validation set.

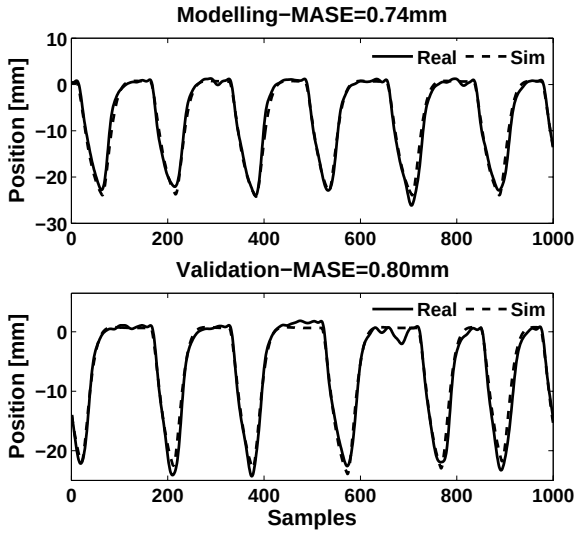

(a) Internal fiducial markers

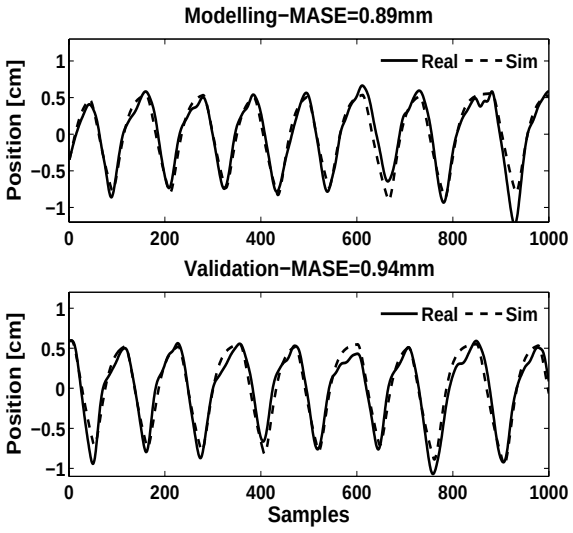

(b) Free breathing

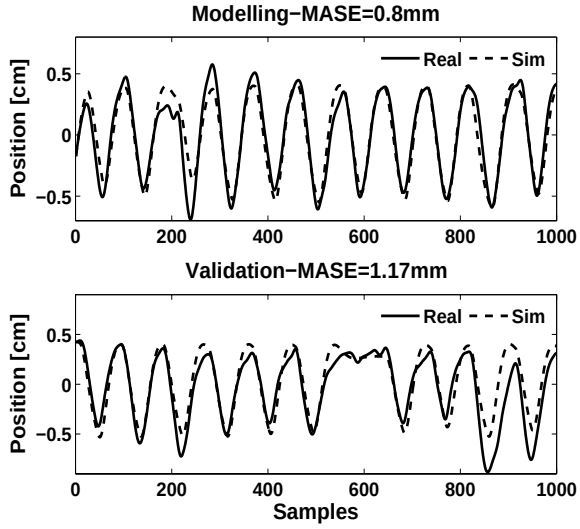

(c) Audio instruction

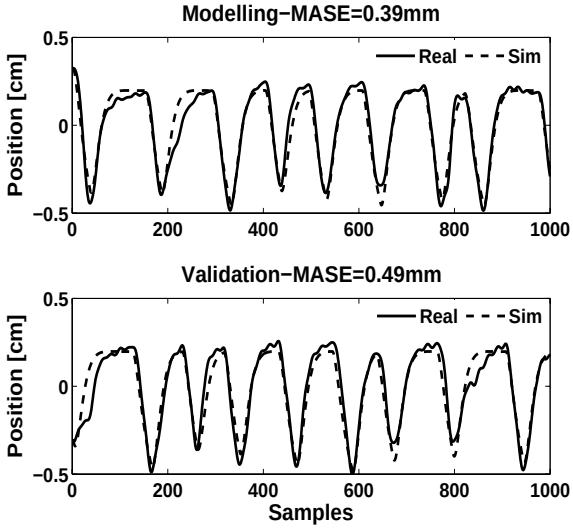

(d) Audio-visual biofeedback

Fig. 5.6: Bilinear time-invariant model applied to an example of each clinical data set after the polynomial drift removal.

The performance of the developed models were assessed by means of the criteria (3.4.2)-(3.4.4), and an overall average of these criteria was assessed over the number of the trajectories M (see Table 5.1). In term of modelling, the BTI gives an overall mean absolute simulation error ($\overline{MASE}$) less than 1mm for all patients and an overall $\overline{RMSSE}$ less than 1.27mm. However, the overall $\overline{Max.ASE}$ is larger than 3mm for all the data sets. This is mainly due to the irregularities of some of the respiratory data which were included in this simulations. A comparison between the modelling performance of the BTI

model against the performance of the model presented in [Wu et al. 2004], both involving the IFM data, was carried out. It was found that the $\overline{RMSSE}$ criteria for the BTI model is a slightly bigger than the phase based modelling approach. However, the BTI model exhibits dynamic and has fixed number of parameters.

Comparing the performance of the investigated data, it may be noticed that the model conforms rather well to real patient data in case of AVB with respect to AI, FB, and IFM. This is mainly due to the fact that patients are provided with guiding instructions which are characterised by a same regular breathing amplitude and frequency, to help them to keep their normal breathing. This is in agreement with the results given in validation phase, as the three adopted criteria are small for the AVB data set. This confirm clinical observation linked with the usefulness of methods allowing patients to monitor their breathing. It is important to highlight the interest of the maximum error criterion which is not in agreement with the MASE and RMSSE for the modelling phase (see the performance of the IFM data).

Tab. 5.1: Simulation error evaluation for polynomial drift (the best results are indicated in bold).

Respiratory data	M	$\overline{MASE}$ [mm]		$\overline{RMSSE}$ [mm]		$\overline{Max.ASE}$ [mm]	
		Mod.	Val.	Mod.	Val.	Mod.	Val.
IFM	9	**0.84**	1.05	**1.12**	1.39	3.81	4.54
FB	110	0.93	1.17	1.18	1.51	**3.64**	4.67
AI	111	0.99	1.29	1.26	1.71	3.82	5.65
AVB	109	0.94	**1.04**	1.20	**1.35**	3.69	**4.10**

An assessment of models' parameters was also carried out to analyse the developed models and check whether a generalisable model is realisable. For each data set, the mean and standard deviation of the overall estimated parameters were calculated, see Table 5.2. The mean value of the estimated parameters are slightly different for the four data sets. This dissimilarity in the overall mean values can be attributed to the variability in the characteristics of breathing motion including the amplitude and frequency motion. A large deviation of the parameters from their mean values was also noticed, which suggests difficulties to achieve a single model.

It was also noticed that the overall standard deviation of the models parameters is larger for FB and AI data sets compared to the IFM and AVB. The overall mean bilinear term η was found to be negative for the FB and IFM data sets and positive for the AI case. The overall mean of the constant offset parameter is very small for the external data and larger for the internal data. This is mainly due to the polynomial order, which is higher for the internal motion data and lower for internal motion data.

Tab. 5.2: An overall parameters analysis for polynomial drift.

Resp. data	M	a_1	a_2	b	η	d
		$\overline{a}_1 \pm \sigma_{a_1}$	$\overline{a}_2 \pm \sigma_{a_2}$	$\overline{b} \pm \sigma_b$	$\overline{\eta} \pm \sigma_\eta$	$\overline{d} \pm \sigma_d$
IFM	9	-1.8194 ± 0.0872	0.8284 ± 0.0835	0.0067 ± 0.0038	-0.0003 ± 0.0004	-0.0205 ± 0.0396
FB	110	-1.7418 ± 0.3410	0.7489 ± 0.3352	0.0076 ± 0.0103	-0.0053 ± 0.0173	0.0004 ± 0.0014
AI	111	-1.8090 ± 0.2343	0.8152 ± 0.2272	0.0048 ± 0.0041	0.0004 ± 0.0174	0.0001 ± 0.0011
AVB	109	-1.8650 ± 0.0855	0.8699 ± 0.0838	0.0040 ± 0.0032	0.0000 ± 0.0025	0.0001 ± 0.0006

Simulation studies were carried out to evaluate the modelling performance of the overall mean BTI model against the validation sets of each data set. This was achieved by estimating the unseen data $\{\widehat{\mathbf{Y}}_2\}$ using the input observations $\{\mathbf{U}_2\}$ and the average model parameters ($\overline{\theta}$), which their values are given in in Table 5.2. The MASE is then calculated using (3.4.3). Figure 5.7 shows the results of simulation studies. Sub-figure (a) shows that the most dominant MASE errors are around 3 mm which were obtained in 40 % of the IFM trajectories. Concerning the external motion data, the most dominant errors were found around 1 mm with a percentage of 34%, 25% and 35% for the FB, AI and AVB, respectively. The main idea behind this simulations is to quantify the number of trajectories that can be simulated by the average BTI model.

Knowing that a MASE of 1 mm can be considered as a good result for respiratory motion modelling, the percentage of the trajectories that have a MASE near 1 mm is around 20%, 60%, 40% and 55% for IFM, FB, AI and AVB data sets, respectively. Even though the FB, AI and AVB data still include some irregular breathing data, the results given by average BTI model are considerably good. There is an important number of data that cannot be modelled by the average model in the IFM data set. This is mainly due to the variation of the breathing motion, which can be from patient to patient, and even within the same patient. Moreover, in addition to the heart beat component, which is still in the internal data, and the data which contains some abnormalities, were also included in the simulation.

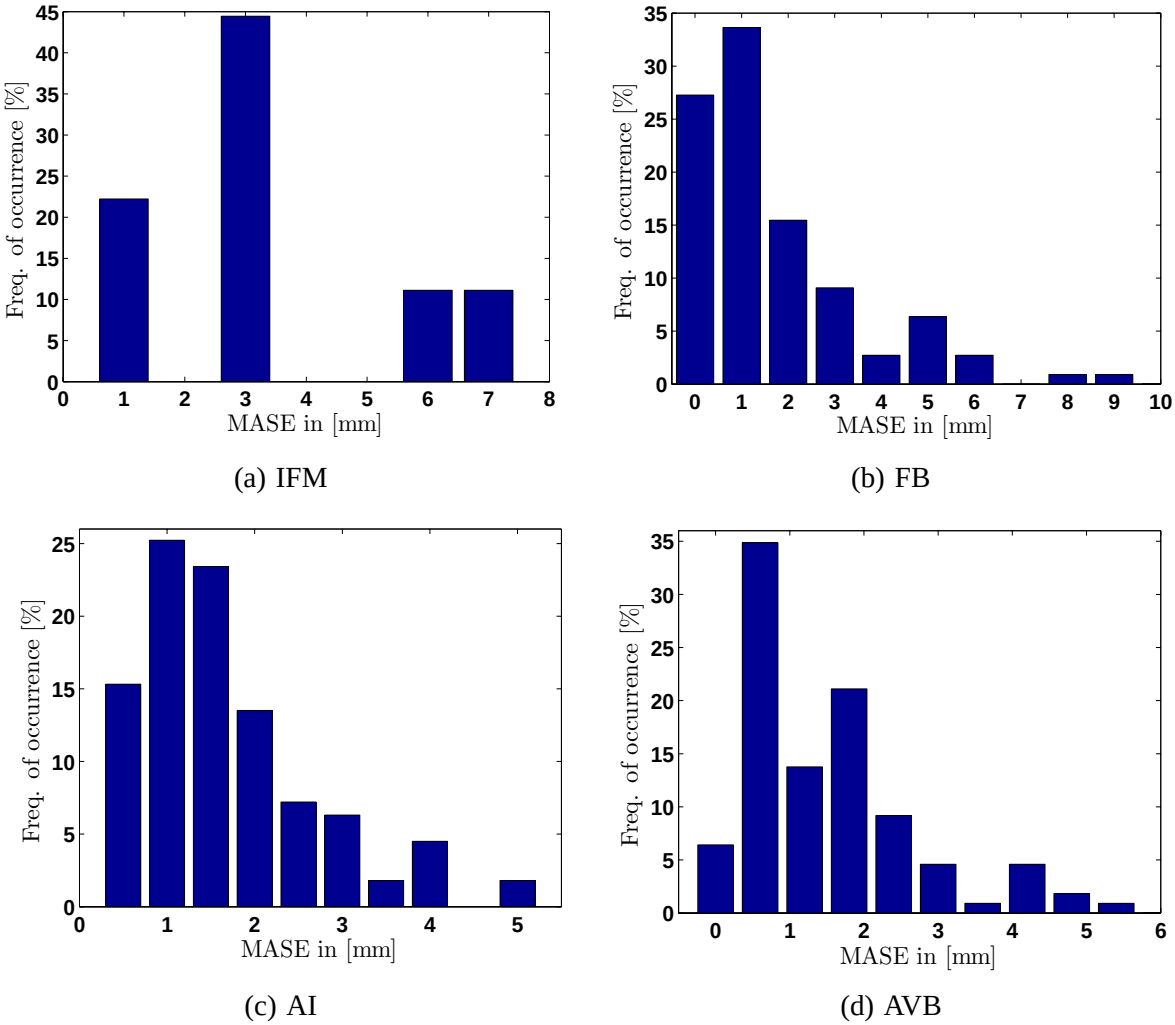

(a) IFM (b) FB

(c) AI (d) AVB

Fig. 5.7: An average BTI model applied to different types of surrogate motion for polynomial drift removal.

5.4.3 Simulation results for pre-filtered drift

The second approach investigated in this work, in order to remove the drift signals is based on low frequency signal filtering. The design of an appropriate filter requires a good knowledge about the frequency characteristics of the respiratory signals. Note that the frequency spectrum of the clinical data was already performed in Chapter 4 as well as the low-pass filter design. Compared to the polynomial method, pre-filtering exploits a priori knowledge about the respiratory signals characteristics and should not lead to an over parameterised model such as that which can occur with the polynomial method. Similarly it is possible to extract the 'true' signal without the drift by applying a high pass filter.

Contrary to the previous simulations, the number of samples used in this case for the modelling and validation of EM is N=2000 samples, which is equivalent to 1 min for a sampling frequency of 30 Hz.

Due to the short time duration of the internal data, the same number of samples as the previous simulations for modelling and validation was used. The level of the generated input signals were fixed between -1 and 1. To ensure that the model are generalisable and stable the values of their poles are constrained. The concept of the poles is introduced here as the amplitude and frequency of the respiratory motion depend of poles of the model used to generate the breathing motion. Therefore, in order to avoid a large respiratory amplitudes and frequency which can lead to a large modelling error, the range of models poles has to be chosen properly.

Considering the approximate second order BLS expressed in discrete-time:

$$\frac{N(z)}{D(z)} = \frac{bz}{z^2 + (a_1 - \eta u_\alpha)z + a_2}, \tag{5.4.11}$$

where z is a complex number. Alternatively, Equation 5.4.11 can be expressed as follow:

$$\frac{N(z)}{D(z)} = \frac{bz}{(z - p_1)(z - p_2)}, \tag{5.4.12}$$

where $p_{1,2} = f(\theta, u_\alpha)$. The equivalent poles of the system can (loosely) be expressed in term of model parameters:

$$(a_1 - \eta u_\alpha) = -(p_1 + p_2), \tag{5.4.13}$$

$$a_2 = p_1 p_2, \tag{5.4.14}$$

where u_α is the known value of the input signal and p_1, p_2 are the poles of the system. The parameters of the model can be estimated by minimising $MSSE$. This can lead to several solutions, including those which correspond to an unstable system. To ensure that the model remains stable, an optimisation technique with constraints has been used. This is equivalent to applying regularisation technique, by constraining the parameters to be bounded on an interval. Assuming that $\alpha \leq p_{1,2} \leq \beta$, such as $\alpha = 1/2$ and $\beta = 0.9$. By using (5.4.13) and (5.4.14), it can be deduced that $-\beta \leq a_1 \leq -\alpha$ and $\alpha^2 \leq a_2 \leq \beta^2$.

Simulation studies were carried out by applying algorithm 2 in which the nonlinear optimisation part has considered constrains on the estimated parameters to make sure that the resulting estimated systems are stables. Results of simulation studies, for a sample from the internal and external data sets, are depicted in Figure 5.8 and 5.9, respectively. The performance of the BTI model on the internal sample data in term of MASE was found to be 0.88 mm for modeling and 0.93 mm for simulation. Although these results are slightly larger than those found for the polynomial removal drift, they are still better than the ones given by the previous models reviewed in Chapter 3. The increase of the MASE in pre-filtering drift case can

be due to the constrained optimisation technique considered.

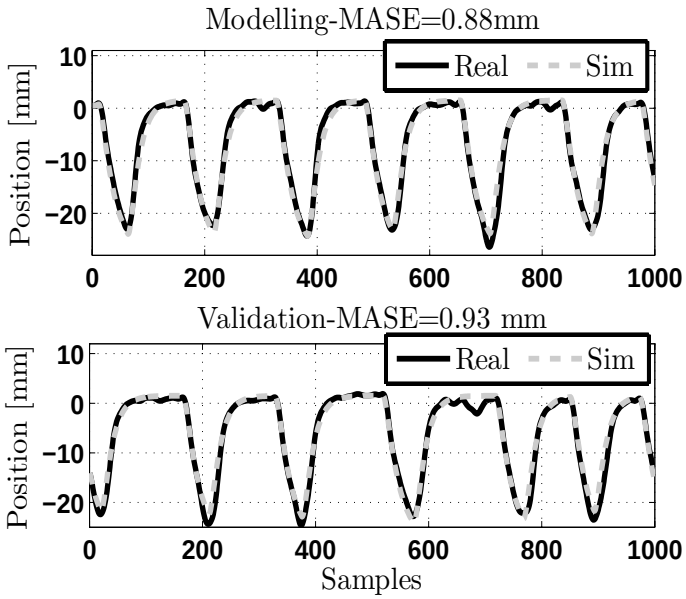

Fig. 5.8: BTI applied to a sample IFM data after pre-filtering drift removal.

Concerning the external motion data, although the length of the latter is larger than the previous case (see subsection 5.4.2), the BTI model performs well these data. In term of modelling, the MASE for FB,AI and AVB was 1.05 mm, 0.99 mm and 0.44 mm respectively. For the validation sets, the MASE was found to be 1.02 mm, 0.84 mm and 0.48 mm for FB,AI and AVB data respectively. The modelling performance on the data with audio and video gating was better than the case of FB data.

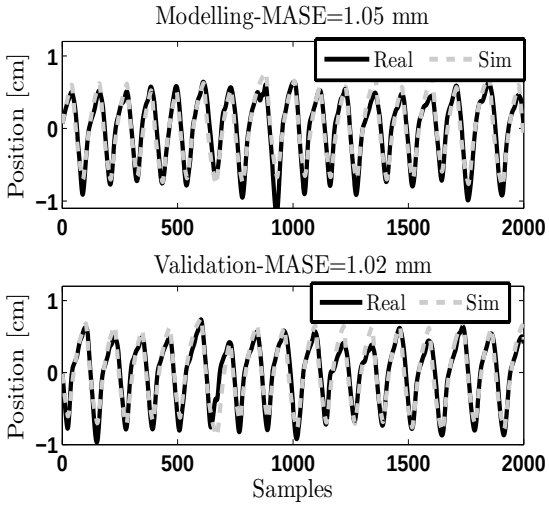

(a) FB

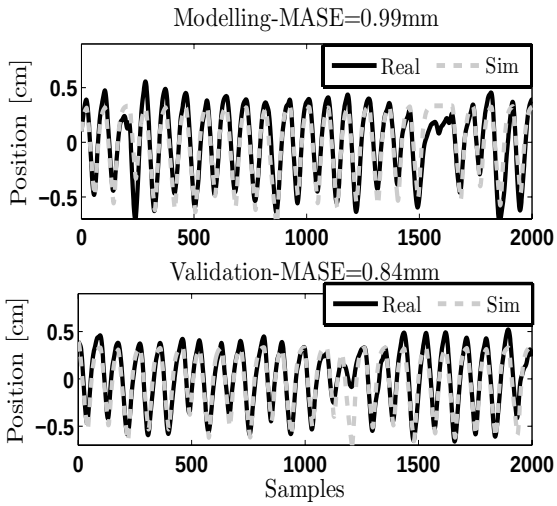

(b) AI

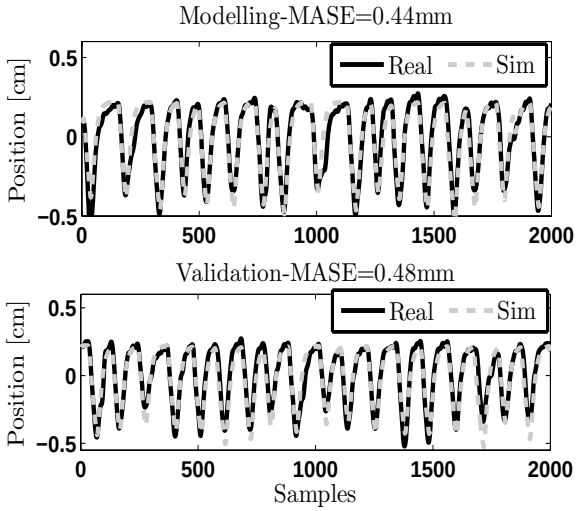

(c) AVB

Fig. 5.9: BTI applied to different types of external surrogate motion after a pre-filtering drift removal.

The performance of the developed models was also assessed using the criteria (3.4.2)-(3.4.4), and results are shown in Table 5.3. Concerning the internal data which involve the same number of samples, the constrained optimisation technique has slightly decreased the $\overline{MASE}$ and $\overline{RMSSE}$ criteria but increased the $\overline{Max.ASE}$ for modelling compared to the case of polynomial drift removal. However, the $\overline{RMSSE}$ criteria is still slightly larger compared to the $\overline{RMSSE}$ of the model developed in [Wu et al. 2004]. The maximum value of the $\overline{MASE}$ and $\overline{RMSSE}$ were noticed in AI data for modelling by 1.14 mm and 1.50 mm respectively. Concerning the validation stage, the maximum value of the $\overline{MASE}$ was 1.32 mm, found in the AI data, while the maximum value of the $\overline{RMSSE}$ was 1.94 mm, noticed in AVB data. The

best performance between the three external data sets was noticed in FB case. Compared to the previous simulation results, one might notice that the assessment criteria are a slightly larger in the second case. As in the polynomial drift case, a large overall $\overline{Max.ASE}$ was observed.

Tab. 5.3: Simulation error evaluation for pre-filtered drift (the best results for the external data are indicated in bold).

Respiratory data	Nb. of traj.	$\overline{MASE}$ [mm]		$\overline{RMSSE}$ [mm]		$\overline{Max.ASE}$ [mm]	
		Mod.	Val.	Mod.	Val.	Mod.	Val.
IFM	9	0.82	1.04	1.11	1.42	3.84	4.70
FB	110	**1.02**	**1.17**	**1.33**	**1.67**	**4.64**	7.78
AI	111	1.14	1.32	1.50	1.73	5.42	**6.22**
AVB	109	1.06	1.29	1.38	1.94	4.75	9.57

Table 5.4 shows the overall mean and standard deviation of the estimated parameters. The overall mean value of the parameters a_1, a_2 and b is approximately similar for the external respiratory data. The overall standard deviation of the parameters a_1 and a_2 is larger for the FB data set compared to the other data sets. The overall mean value of the bilinear term is negative. Comparing the results from the previous approach and the current one, it can be observed that there is a trade-off between the simulation error and the persistency of parameters.

Tab. 5.4: An overall parameters analysis for pre-filtered drift.

Resp. data	Nb. of traj.	a_1	a_2	b	η	d
		$\overline{a}_1 \pm \sigma_{a_1}$	$\overline{a}_2 \pm \sigma_{a_2}$	$\overline{b} \pm \sigma_b$	$\overline{\eta} \pm \sigma_\eta$	$\overline{d} \pm \sigma_d$
IFM	9	-1.7750 ± 0.0402	0.7845 ± 0.0390	0.0630 ± 0.0336	-0.0018 ± 0.0024	-0.0327 ± 0.0588
FB	110	-1.7331 ± 0.341	0.7405 ± 0.335	0.0069 ± 0.010	-0.0039 ± 0.017	-0.0009 ± 0.001
AI	111	-1.7479 ± 0.1316	0.7540 ± 0.1310	0.0067 ± 0.0044	-0.0024 ± 0.0085	-0.0009 ± 0.0012
AVB	109	-1.7507 ± 0.1091	0.7572 ± 0.1075	0.0064 ± 0.0038	-0.0032 ± 0.0123	-0.0008 ± 0.0011

The assessment of the average BTI model is shown in Figure 5.10. In sub-figure (a) the performance of the average BTI on IFM data is presented. More than 40% of the IFM validation sets can be simulated by theBTI model with a MASE around 1 mm. Sub-figures (a), (b) and (c) represents the results for the FB, AI and AVB validation sets respectively. The best result for these three validation sets was noticed in the FB case in which around 32 % of the data can achieve a MASE of around 1 mm, while in AI and AVB data the percentage was found to be 29% and 23% respectively. In overall, the percentage of the trajectories that have a MASE near 1 mm is around 55%, 47%, 37% and 27% for IFM, FB, AI and AVB data sets, respectively. Compared to the previous results in the case of polynomial drift removal the performance of the average model was improved for the IFM data set and decreased for the three external data sets.

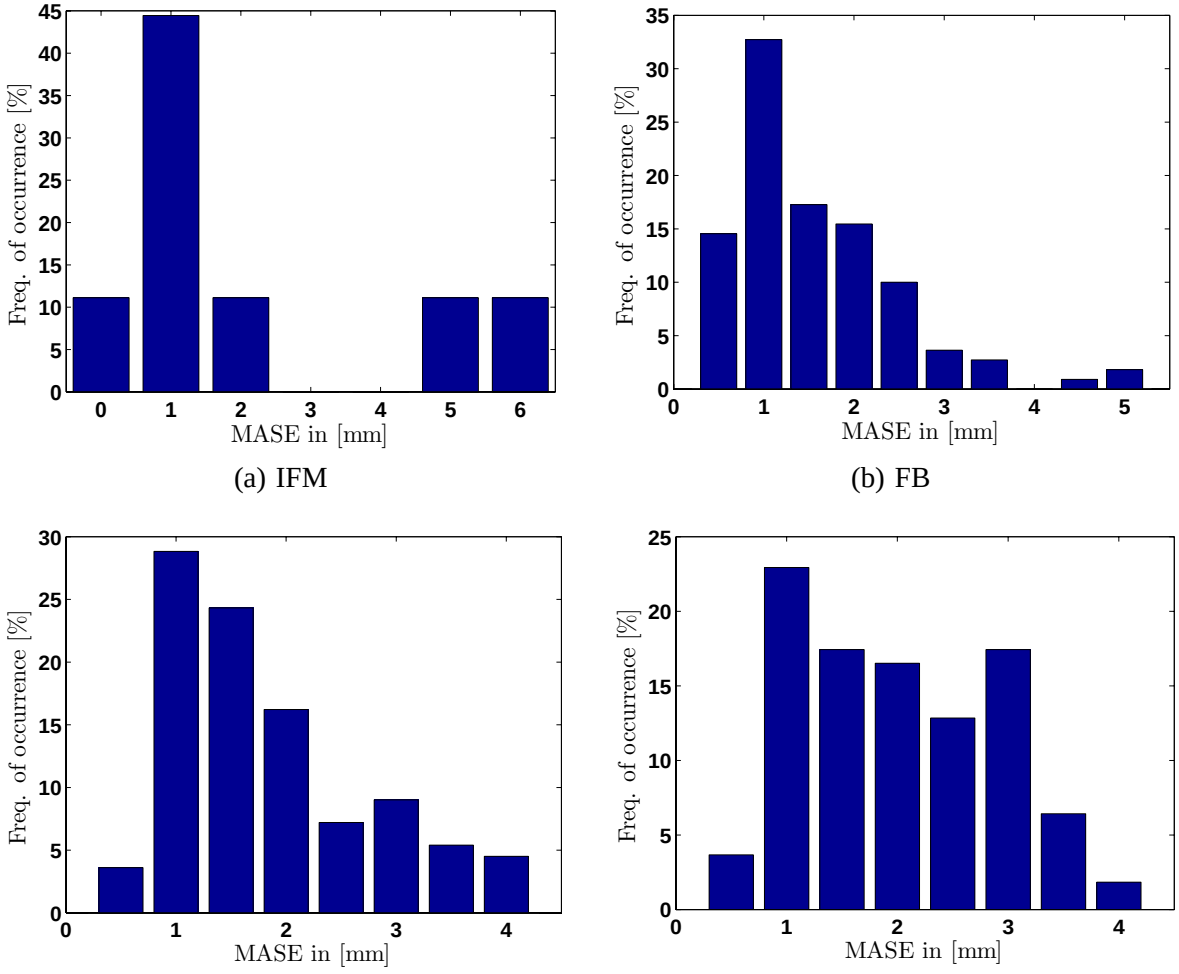

(a) IFM (b) FB

(c) AI (d) AVB

Fig. 5.10: An average BTI model applied to different types of surrogate motion for pre-filtered drift.

5.4.4 Simulations with original data

The performance of the BTI model was also applied to the original IFM data and some example results are shown in Figure 5.11. In sub-figure (a) the model was unable to capture some irregularities such as the patient/markers movement during the position acquisition. Therefore, the modelling and simulation errors in term of MASE were 1.57 mm and 1.92 mm respectively. In sub-figure (b) a quite regular and noisy respiratory motion trajectory that could be modelled and replicated by the BTI model. The MASE in this case was 0.30 mm for modelling set and 0.38 mm for the validation set. The trajectory considered in sub-figure (c) exhibits an important measurement noise and a slow respiratory motion. In the latter case, the BTI model was able to model the trajectory with a MASE equal to 1 mm. However, in the validation step the model replicates the data with a MASE equal to 1.48 mm. This difference in the MASE is mainly due to the change of the respiratory motion patterns during the validation set and some

sudden spikes. In sub-figures (d), (e) and (f), the trajectories taken into consideration have a slow motion and an important amount of noise in the end of exhalation and inhalation. In sub-figure (d), the model achieved almost a similar MASE for both modelling and validation sets, as the patient was breathing with the same rhythm. In the case presented in sub-figure (e), the simulation error is smaller in the validation set compared to the modelling set, while it is the opposite in the example shown in sub-figure (f).

As conclusion, it can be deduce that irregularities in the respiratory data can slightly degrade the modelling and validation errors. The ability of the BTI model to replicate the respiratory motion even in the presence of irregularities can achieve MASE less than 2 mm. These irregularities include measurement noise, occasional or sudden motion and amplitude/frequency changes. The BTI model can be used here to define the main breathing characteristics, such as the amplitude and period. Note that the optimisation process takes more time to find the optimal parameters than in the noise-free data case. In practice, the problem of the measurement noise can be resolved by using an online filter that cut-off the noise frequencies. However, this latter can generate a delay that has to added to the data after acquisition process. Concerning the other irregularities, one might consider a respiratory motion gating.

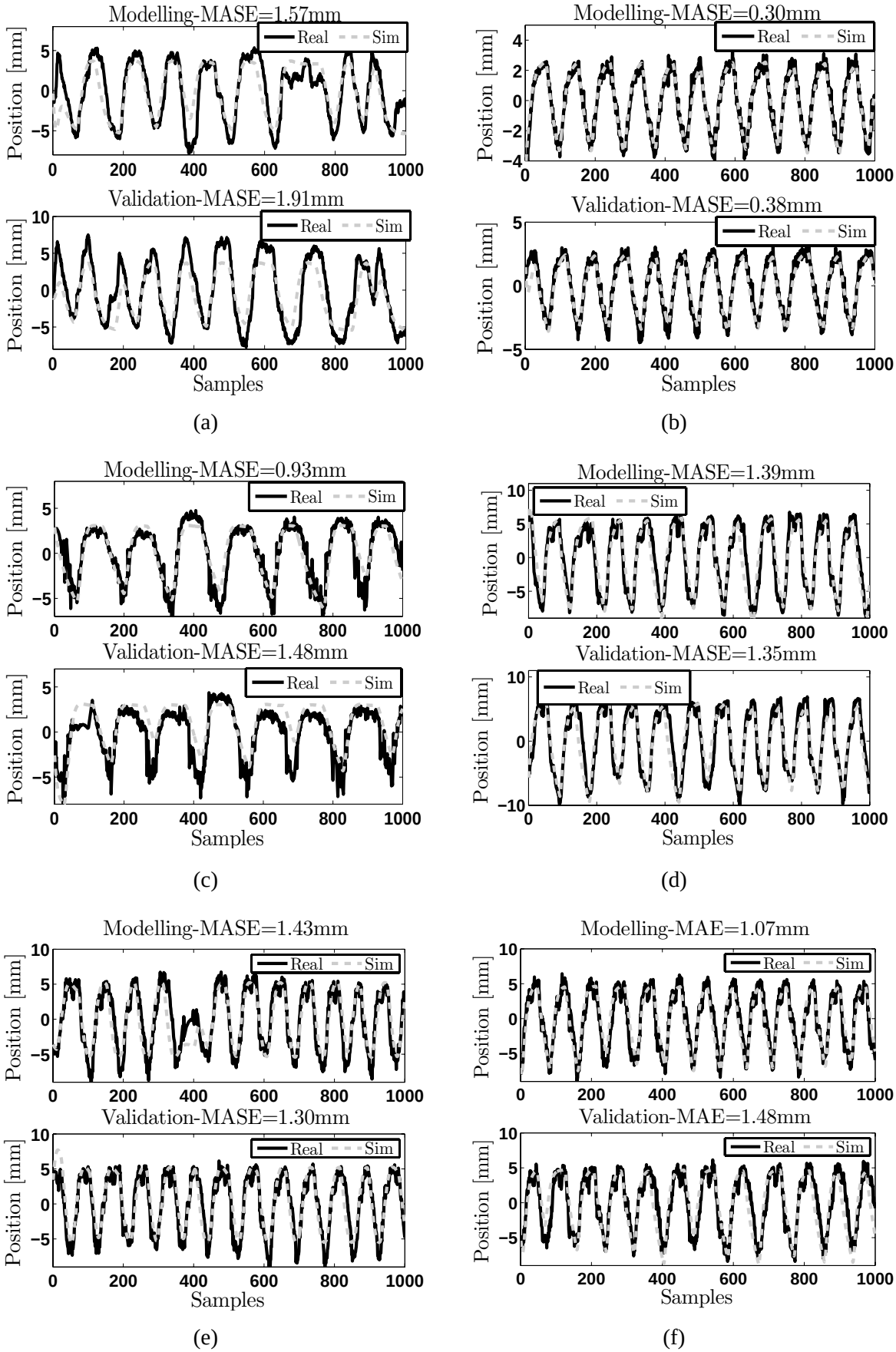

Fig. 5.11: BTI model applied to data with measurement noise.

5.5 Bilinear time-varying (BTV) model for respiratory motion

Usually during radiotherapy treatment the position of the tumour is acquired online via an imaging system (see Chapter 2 for more details). Therefore, an adaptive model is required that can adapt their parameters by taking into account new measurements. The most widely used adaptation algorithms are the LMS and the recursive least-squares (RLS) methods. They have established themselves as the principal tools for linear adaptive filtering. Assuming that the parameters can be changing with time (5.4.1) can be written as follows:

$$y_k = -a_{1k}\, y_{k-1} - a_{2k}\, y_{k-2} + b_k\, u_{k-1} + \eta_k\, y_{k-1} u_{k-1} + d_k \tag{5.5.1}$$

The RLS algorithm is considered in this section to identify the varying parameters of the above BTV model structure.

5.5.1 Parameter estimation

The RLS algorithm minimises the cost function specified in (5.4.9), in a recursive manner, i.e. the current estimation $\hat{\boldsymbol{\theta}}_k$ only bases on the previous estimation $\hat{\boldsymbol{\theta}}_{k-1}$ and the current observations. One extension of the said algorithm is the RLS with forgetting factor, which is also called adaptive LS. In this case the cost function to be minimised is:

$$J_{\Lambda}^{RLS} = (y-\hat{y})^T \Lambda (y-\hat{y}) = \left\| y-\hat{y} \right\|_{\Lambda}^2 \tag{5.5.2}$$

where Λ is a diagonal matrix defined by:

$$\Lambda = \begin{pmatrix} \lambda^{N-1} & & & \\ & \ddots & & \\ & & \lambda & \\ & & & 1 \end{pmatrix} \tag{5.5.3}$$

The forgetting factor or weighting factor λ is a positive scalar ≤ 1, which controls the adaptivity of the RLS algorithm and its choice is of crucial importance. In this work the weighting used in the simulation was $\lambda = 0.97$. The RLS algorithm with fixed forgetting factor is given by the following three steps:

$$L_k = \boldsymbol{P}_{k-1}\, \boldsymbol{\varphi}_{bls}(k) \left[1 + \boldsymbol{\varphi}_{bls}^T(k)\, \boldsymbol{P}_{k-1}\, \boldsymbol{\varphi}_{bls}(k)\right]^{-1} \tag{5.5.4}$$

$$\boldsymbol{P}_k = \left[I - L_k\, \boldsymbol{\varphi}_{bls}^T(k)\right] \boldsymbol{P}_{k-1}/\lambda \tag{5.5.5}$$

$$\hat{\boldsymbol{\theta}}_k = \hat{\boldsymbol{\theta}}_{k-1} + L_k \left[y_k - \boldsymbol{\varphi}_{bls}^T(k)\, \hat{\boldsymbol{\theta}}_{k-1}\right] \tag{5.5.6}$$

5.5.2 Simulation results

Using the RLS algorithm, the parameter of the BTV model were estimated. A simulation study was performed using internal and external respiratory data, and two examples are depicted in Figure 5.12. Note that the data was filtered prior to the adaptive estimation of the markers position by means of an online algorithm and the generated input square wave signal was between the minimum and maximum values of the respiratory signals. As it can be seen in these Figures, the BTV model gives a good fitting for both internal markers (RMSE=0.004 mm) and external markers (RMSE=0.002 mm). The largest errors between the real and estimated markers positions were noticed during the respiratory transition between exhalation and inhalation.

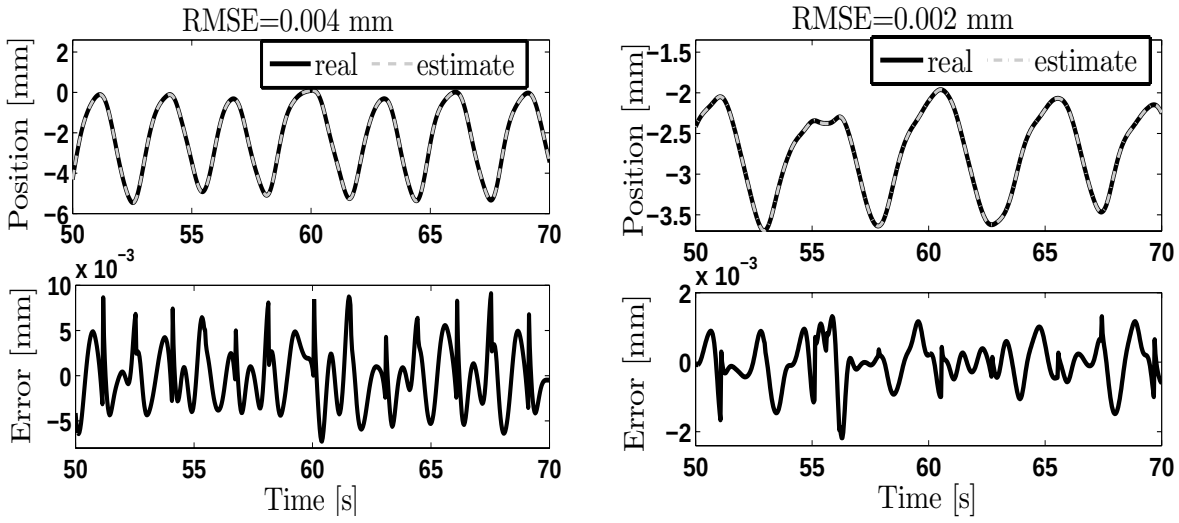

(a) (b)

Fig. 5.12: Simulation results of BTV model for an example of: (a) internal data, and (b) external data.

The time variation of the bilinear model parameters are also shown in Figure 5.13-5.15. A large variation was noticed in the parameter b_k, which represents the gain of the bilinear filter. Although the bilinear term has a small change compared to the other parameters, it does compensate for the large gain. The parameters a_{1k} and a_{2k} are varying around the values 1 and -2 respectively. Accordingly, the linear part of the model can be considered as a linear extrapolation (see Chapter 3). The varying offset between the input and output signals was also illustrated in Figures 5.15. These latter are changing randomly and the rate of change is roughly similar for internal and external markers.

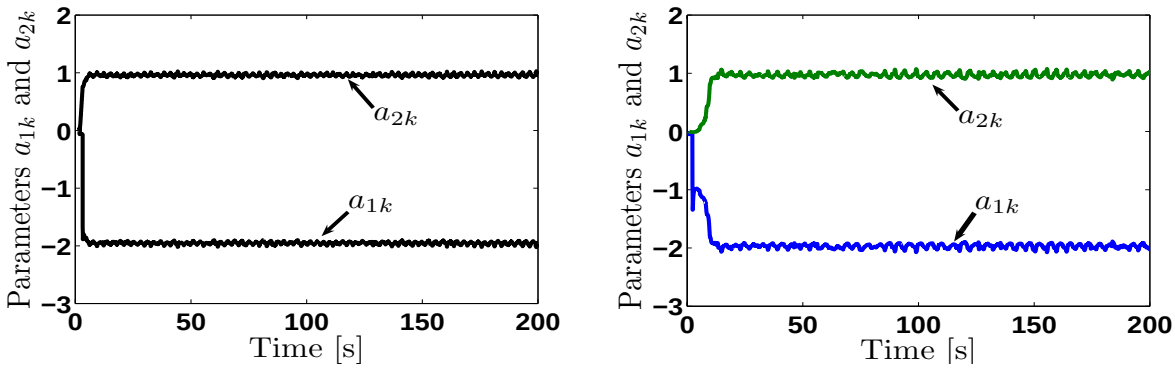

Fig. 5.13: Temporary changing of the parameters a_{1k} and a_{2k} for an example of: (a)internal data, and (b) external data.

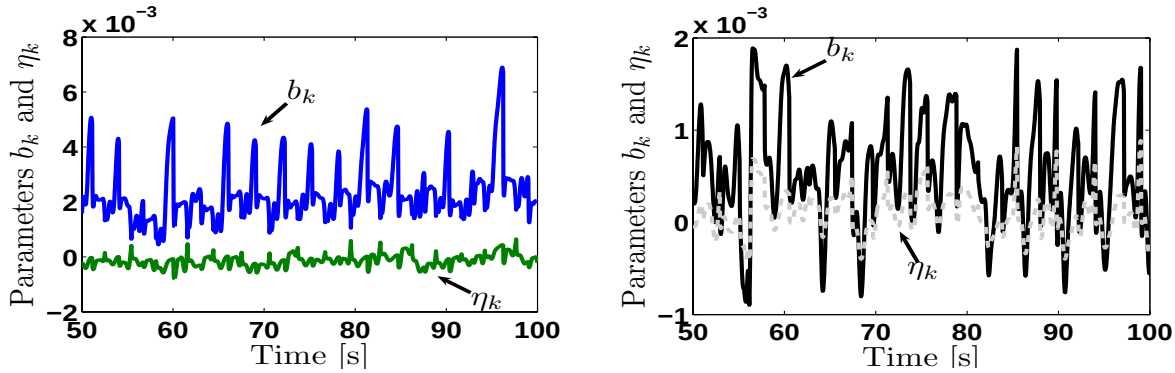

Fig. 5.14: Temporary changing of the parameters b_k and η_k for an example of: (a)internal data, and (b) external data.

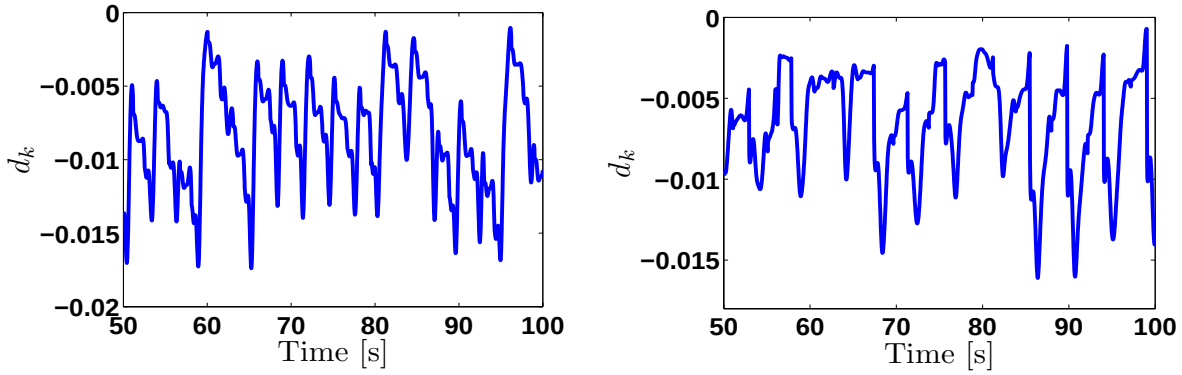

Fig. 5.15: Temporary changing of the parameter d_k for an example: (a)internal data, and (b) external data.

5.6 Model-based modified cosine function

One of the outcomes of Chapter 3 was that the modified cosine function model introduced in [Lujan et al. 1999] is the widely acceptable model for the respiratory motion. Therefore, the results of an online class of this model are included here to provide a benchmark. The online modelling approach consisted in modelling each breathing cycle with a modified cosine function. For each cycle, the time is set to zero and the model parameters are estimated online using an iterative non linear optimisation scheme [Lagarias et al. 1998]. The latter was initialised with an approximate estimate of each parameter. For a given value of n={1,2,3,4}, a model of each cycle is obtained. The 'best' value is that which minimises the mean squared error (MSE) criterion.

Figure 5.16 shows an example of two typical sets of regular and irregular breathing motion chosen from the internal motion dataset. These two data will be referred to D1 and D2 respectively, and will be used in the simulation study. The data set D1 exhibits a shorter period at the end of the EX compared to D2. A changes in terms of frequency and amplitude are also observed. A further difficulty associated with the modelling of these data is pattern changes and the presence of Gaussian and 'spiked' noise [Sharp et al. 2004], due to the acquisition process. To reduce the effect of noise, the data was smoothed with a three point median filter.

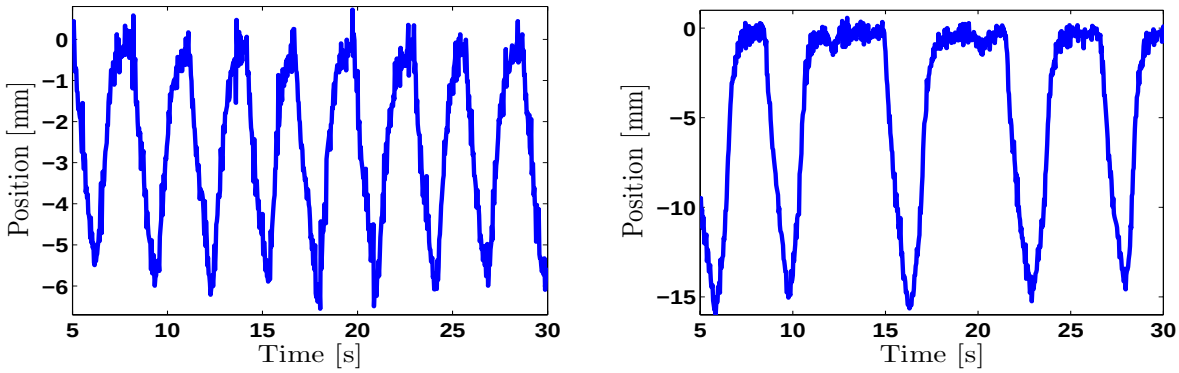

(a) D1 (b) D2

Fig. 5.16: The two different types of breathing motion used for simulations

Evolutions of the parameters T_1 (duration of the first half period), T_2 (duration of the second half period), period and peak to peak amplitude over the breathing cycles of data D1 are shown in Figure 5.17. It is interesting to note that whilst the duration of EOE, and hence T_1, may change significantly between two successive cycles, T_2 remains fairly constant at 1.33s with a standard deviation of 0.08 s, see Table 5.5. The amplitude is usually similar for adjacent cycles with a few exceptions where it varies by about 20%.

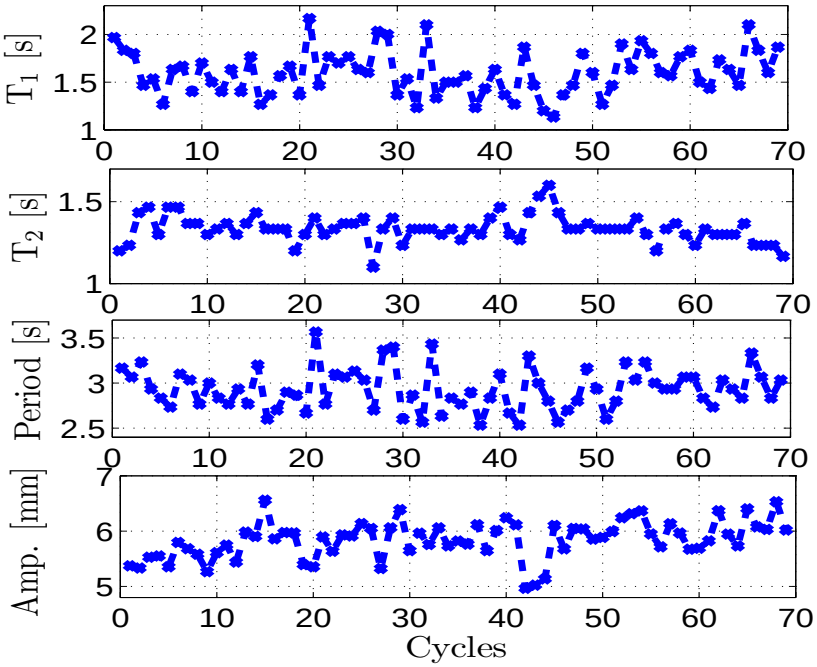

Fig. 5.17: Cycle-to-cycle variation T_1, T_2, period and amplitude of data D1.

Tab. 5.5: The range of the breathing parameters for data D1.

Parameters	Mean	SD
T_1	1.6s	0.24s
T_2	1.33s	0.08s
Period	2.93s	0.23s
Amplitude	5.84 mm	0.34 mm

The simulations results of the applied cosine model are depicted in Figure 5.18. The estimated signal is noted with a plain line and the real data with starts. In each of the graphs showing the fitting errors, the overall value of the MSE is given (top left right side). The advantage of this model is that it requires only five parameters, which relate to the characteristics of the signal, i.e. may be interpreted. Comparing the MSE criteria, it is interesting to note that fitting regular respiratory motion data gives better results than irregular respiratory data. The mean and standard deviation of the estimated parameter are presented in Table 5.6. The latter shows that the first three model parameters replicated to regular data changing less than irregular ones. A Comparison between the results of the respiratory analysis and the estimated parameters of cosine model for data D1 shows that amplitude and period of the motion can be quantified. Consequently, this model can be used in margin calculation. In addition to the amplitude and period, a motion static drift can be also identified.

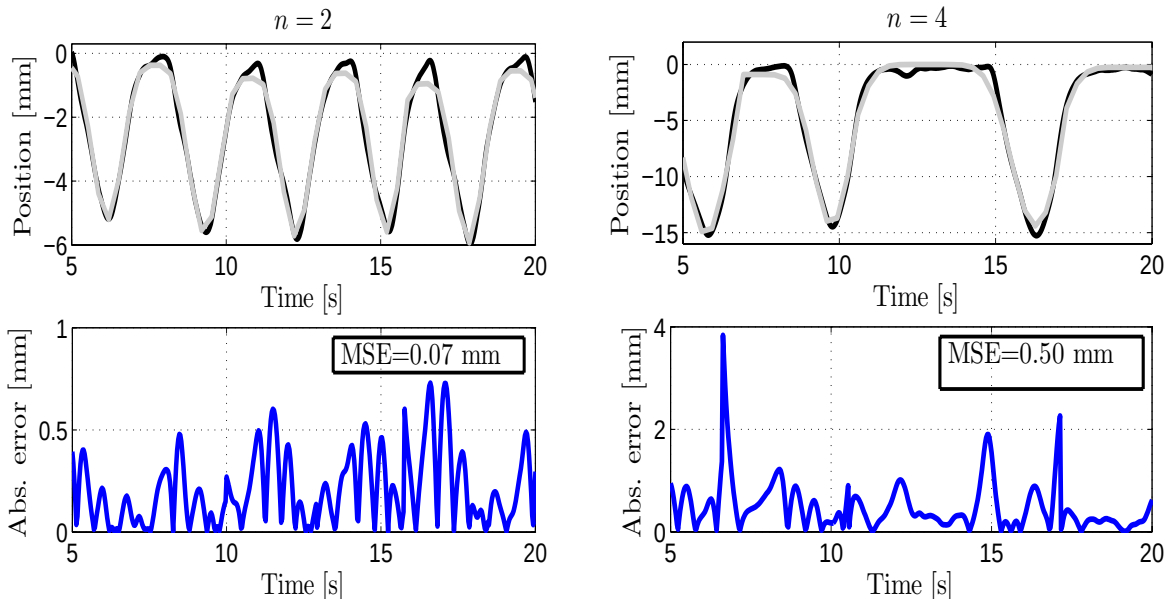

Fig. 5.18: Online curve fitting using cosine function model for (a) regular and (b) irregular respiratory data. The black line corresponds to the measured data, the grey line corresponds to the fitted data.

Tab. 5.6: The range of cosine model parameters for data D1 and D2.

Parameters	Mean		SD	
	D1	D2	D1	D2
A_0	0.46 mm	-0.57 mm	0.32 mm	0.40 mm
A	5.41 mm	14.06 mm	0.36 mm	0.43 mm
Period	2.95s	5.92s	0.22s	0.75s
Phase	9.19s	9.00s	1.06s	0.96s

5.7 Model-based polynomial function

The polynomial function is often used for curve fitting in order to approximate a time series data. A model based polynomial function is proposed here as a new approach (at the time of publication [Sahih et al. 2005]) to model the respiratory motion. Unlike the sinusoidal model, the polynomial model is linear in the parameters. Consequently LLS can be applied to estimate the parameters. The polynomial function can be considered as weights which increases the importance of the related powers. The following polynomial

function has been used in this work:

$$y(t) = a_0 + \sum_{k=1}^{n} a_k (t - t_0)^k \quad t_0\text{: initial time for each cycle.} \tag{5.7.1}$$

An online algorithm was designed, which consists in fitting each respiratory cycle by different order polynomial function. The time was re-initialise to zero for each cycle according to (5.7.1). Figure 5.19 illustrates the modelling performance of the a 5th order polynomial model applied to a regular and irregular breathing motion. The polynomial model performs the regular and irregular breathing with a MSE of 0.03 mm and 0.39 mm, respectively. Compared to the modified cosine model and for the same number of parameters the polynomial model gives a better fit according to the MSE. Moreover, the online curve fitting using the polynomial model is faster in terms of being less computationally intensive. As shown in 5.7, It is possible to improve the model fit significantly by increasing the order of the polynomial, noting that the lowest order is desirable. In this work the best order is obtained by determining a polynomial which achieves a mean error of less than 1 mm.

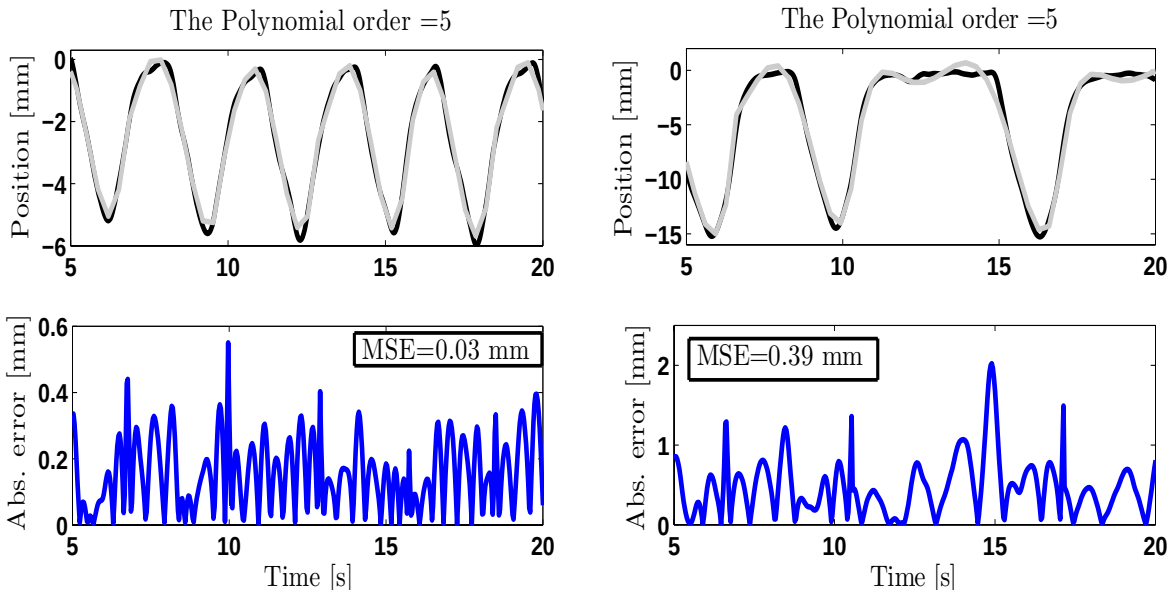

(a) (b)

Fig. 5.19: Online curve fitting using polynomial function model for (a) regular and (b) irregular respiratory data, using the same order polynomial. The black line corresponds to the measured data, the grey line corresponds to the fitted data.

Tab. 5.7: Error analysis for different polynomial order for Data D1 and D2

Orders	Mean [mm]		SD [mm]		Max. [mm]	
	D1	D2	D1	D2	D1	D1
5	0.15	0.50	0.10	0.39	0.93	2.11
6	0.11	0.42	0.08	0.37	0.47	2.14
8	0.09	0.26	0.07	0.23	0.34	1.29

Figure 5.20 shows a comparison between the polynomial and the sinusoidal models. It can be noticed the flexibility of the polynomial model to reproduce fairly accurate breathing cycles, with small end-of-exhale time and the changing gradient. Such result was obtained by concatenating the model cycles to give the overall response. The polynomial models developed offers more flexibility than the periodic cosine model to reproduce non symmetrical breathing cycles. The BM approach, whilst less accurate when compared to the polynomial and sinusoidal models, is found to produce a better average model.

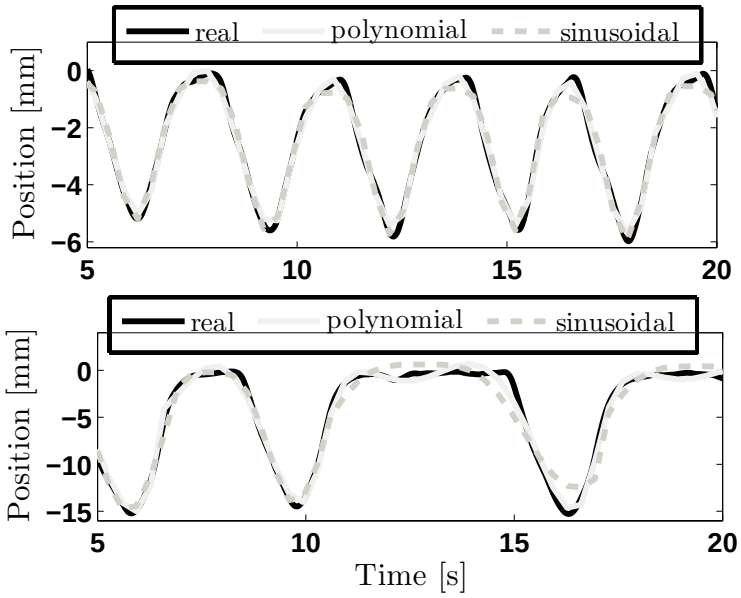

Fig. 5.20: Comparing curve fitting for regular breathing (upper) and irregular breathing (lower) using the polynomial and sinusoidal models.

5.8 Simulated respiratory data generation

The clinical respiratory data that have been used in this research played a significant role in the development of the new respiratory motion model. Alternatively, such data can also be employed in other radiotherapy related applications such as tumour tracking, radiotherapy strategies assessment, treatment

planning, and radiotherapy equipments calibration. There are to date only a few data set available to researchers in the field. As a consequence most researcher design motion modelling and prediction algorithm based solely on their data, which makes comparison between algorithms difficult. Further when common data bases are used it is current practice for published research to base the results on a subset of the whole data set. The aim of this section is to overcome the current deficit in respiratory data to compare alternative algorithms by creating a set of signals against which to evaluate current motion prediction algorithms. This respiratory motion database exploits the bilinear model formulation presented in this Chapter.

5.8.1 Respiratory motion simulation

The simulation of the respiratory motion data has involved the previously developed BTI models. To drive the latter, a set of virtual input square wave signals, which contain the frequency and duty cycle information of breathing motion has been randomly generated. The period and duty cycle characteristics of the square wave were generated based on the statistical distributions previously modelled, see Section 4.4. One square wave signal was generated for each type of data set corresponding to internal and external motion for different experimental conditions. In order to generate the respiratory motion a distribution of the period and the duty cycle have been used to produce a square wave signal. A square wave which period are generated base on the period frequency distribution is initially generated. Subsequently the square wave is modified by changing its duty cycle based on the duty cycle distribution. The number of cycles was fixed to 80 cycles, which is equivalent to signal of 5 minutes duration at a sampling time of 30 Hz. Note that the number of cycles can be changed by the user. The bilinear models estimated previously in Section 5.4, were used to generate different trajectory dynamics and amplitude.

Figure 5.21 shows an example of generated data with their frequency characteristics and the used input signals for every data set. It can be seen from the power spectral components of the generated respiratory signals that they contain various respiratory frequencies as well as some typical breathing irregularities. Some of the respiratory models give unstable responses, because their frequency bandwidths are smaller than the ones of the input signals. A further advantage of this approach is that it can generate internal respiratory data with long duration, which is not the case in the original data. The amplitude and period of the generated signals can also be changed by modifying the amplitude and period of the simulated input signals. This is another way of adapting to amplitude change of the respiratory signals as opposed to changing the gain of the bilinear model.

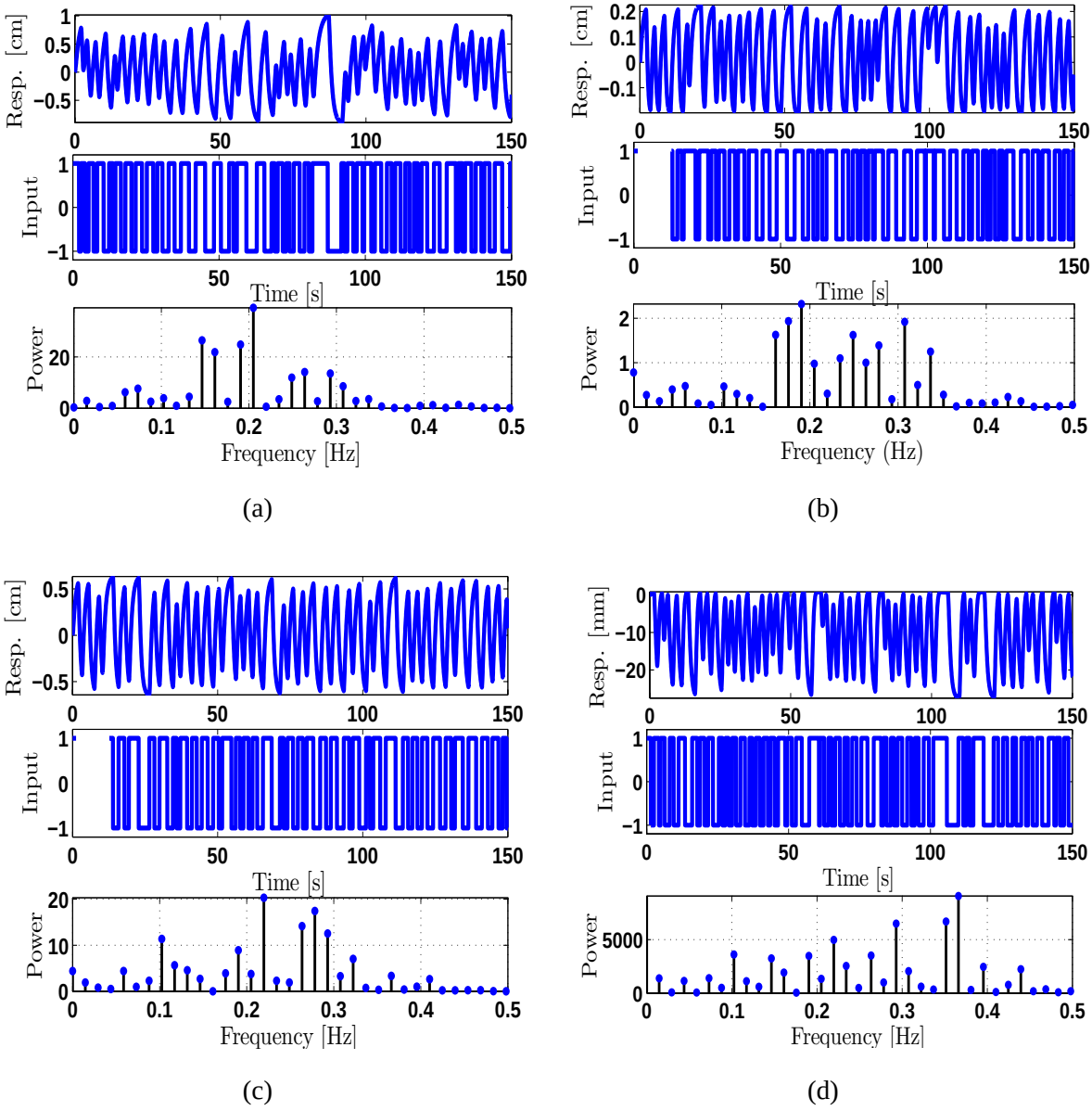

Fig. 5.21: An example of the generated respiratory data for the cases : (a) FB, (b) AI, (c) AVB and (d) IFM.

5.8.2 Baseline drift adding

Different drift signals were generated to be added to the test signals, as baseline shift is an inherent part of any respiratory motion. The aim of such an approach was to realise realistic respiratory signals with a wide range of typical characteristics. A set of different randomly generated drift signals was generated to account for four different types of baseline shift observed in clinical data: low frequency sinusoidal, triangular as well as spikes and steps, see Figure 5.22. The maximum and minimum values of the extracted drift signals from the investigated clinical data were initially calculated and are used to

define the amplitude limits of the simulated drifts signals.

Sub-figure (a) illustrates the generated random drift signal that was produced by joining the amplitude and frequency knowledge of the original drift signals. A random signal with varying frequencies between 0.0042 Hz and 0.025 Hz was concatenated to another random signal generated by a uniform distribution with its amplitude extracted from clinical drift signals. The resultant signal exhibits varying amplitudes and frequencies. In sub-figure (b), a sinusoidal drift signal that its frequency varies between 0 and 0.025 Hz is shown. The latter is characterised by constant amplitude and a frequency that increase with time. The third drift that is depicted in sub-figure (c) is a triangular signal with the same amplitude than that of the sinusoidal drift. This drift simulates a succession of linear drifts that may be cause by the motion acquisition device. The last drift signal is a step signal, which simulates the spikes or sudden motion-see sub-figure (d). Finally, in addition to the previous drifts, a mixture of sinusoidal, triangular and spikes signals has also been generated to create a signal combining all the different types of drift observed (see sub-figure (e)).

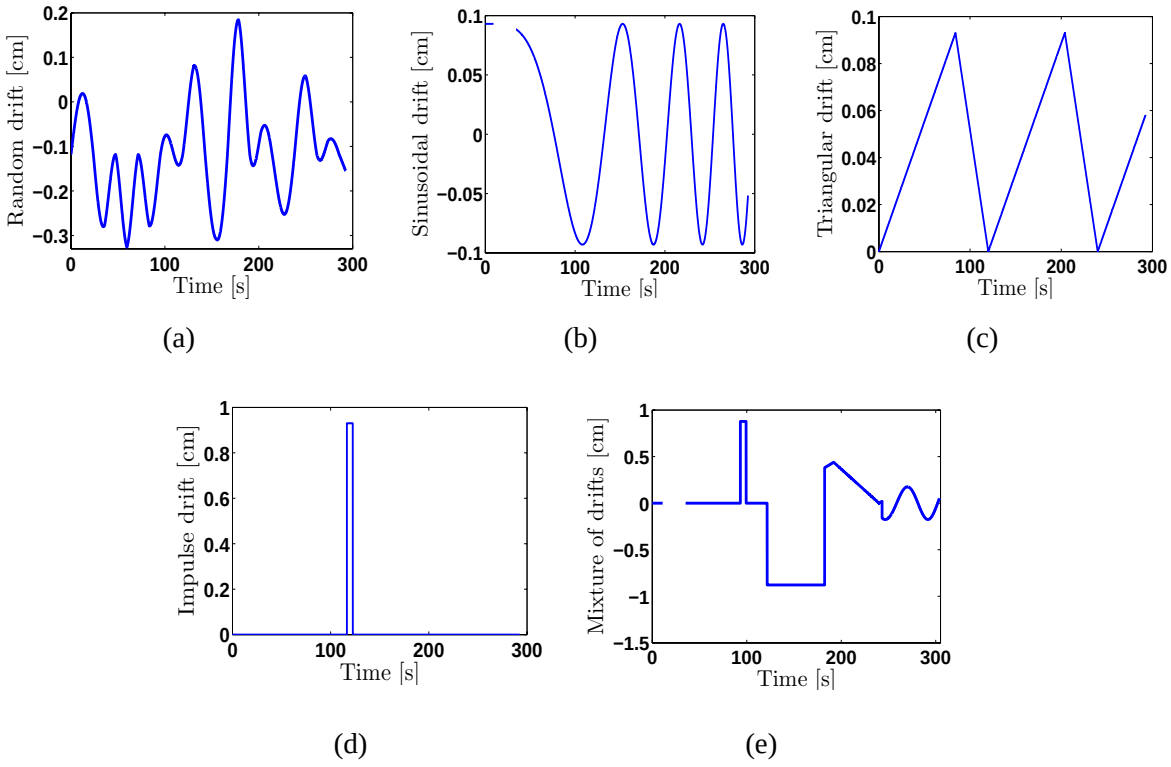

Fig. 5.22: Different types of generated drift signals: (a) random, (b) sinusoidal, (c) triangular, (d) impulse and (e) mixture of drifts.

The above drift signals were added to the test trajectories generated for each data set and some examples are represented in Figures 5.23-5.27. The common point between the illustrated trajectories is that they exhibit a variation of the amplitude and frequency as in real clinical respiratory motion. Figure 5.23 illustrates the generated respiratory trajectories to which a random drift signal was added. The effect of the random drift on the respiratory data is different as this type of drift was generated with random frequencies and amplitudes between realistic values gained from the drift analysis. Figure 5.24 illustrates the effect of the sinusoidal drift on the generated respiratory data. The sinusoidal drift has introduced a slight drift into the mean respiratory motion position. Figure 5.25 shows example of trajectories that contains a triangular drift. This sort of drift introduces an increasing/decreasing linear drift to the respiratory motion. A sudden movement was modelled by an impulse signal-see Figure 5.26. Sometimes different types of drifts can occur in the same time. This situation was also simulated by considering a mixture of drift (Figure 5.27).

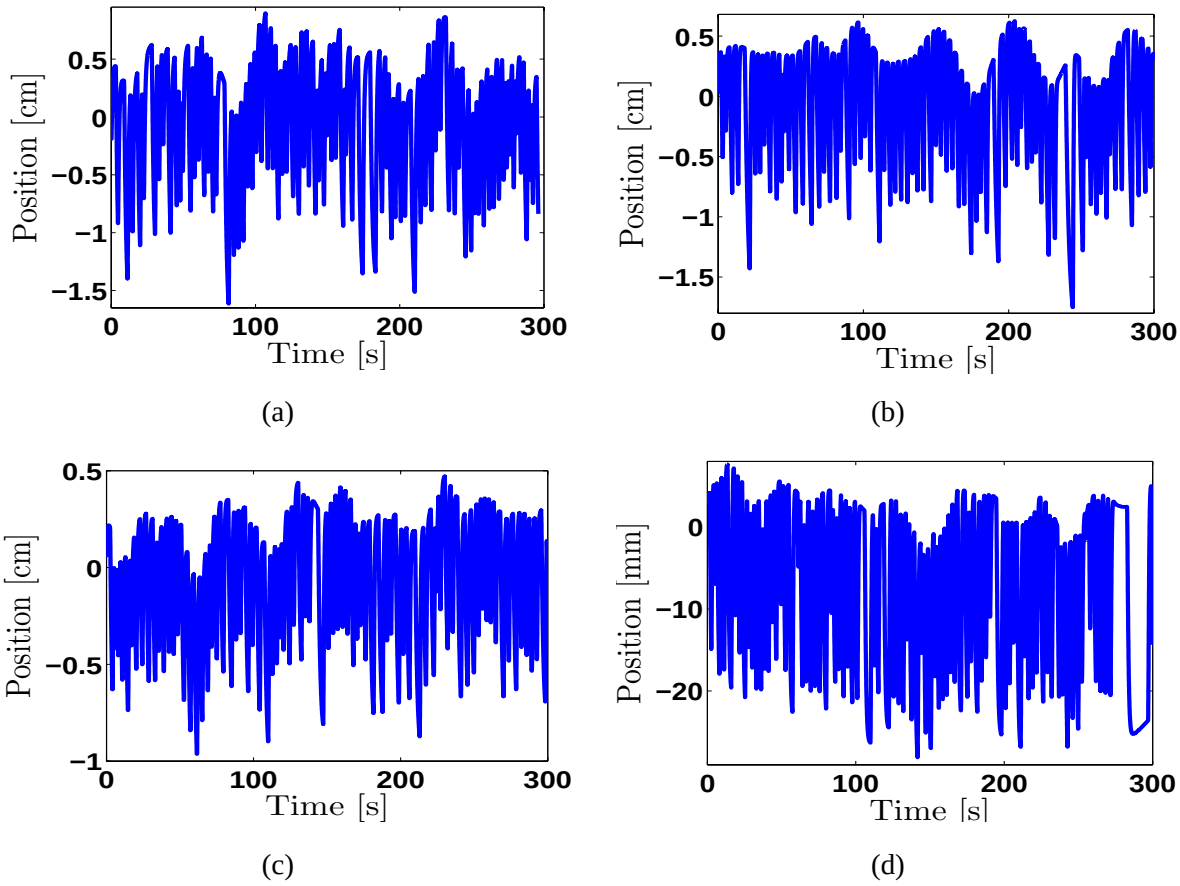

Fig. 5.23: Random drift added to the generated respiratory data for (a) FB, (b) AI, (c) AVB, and (d) IFM

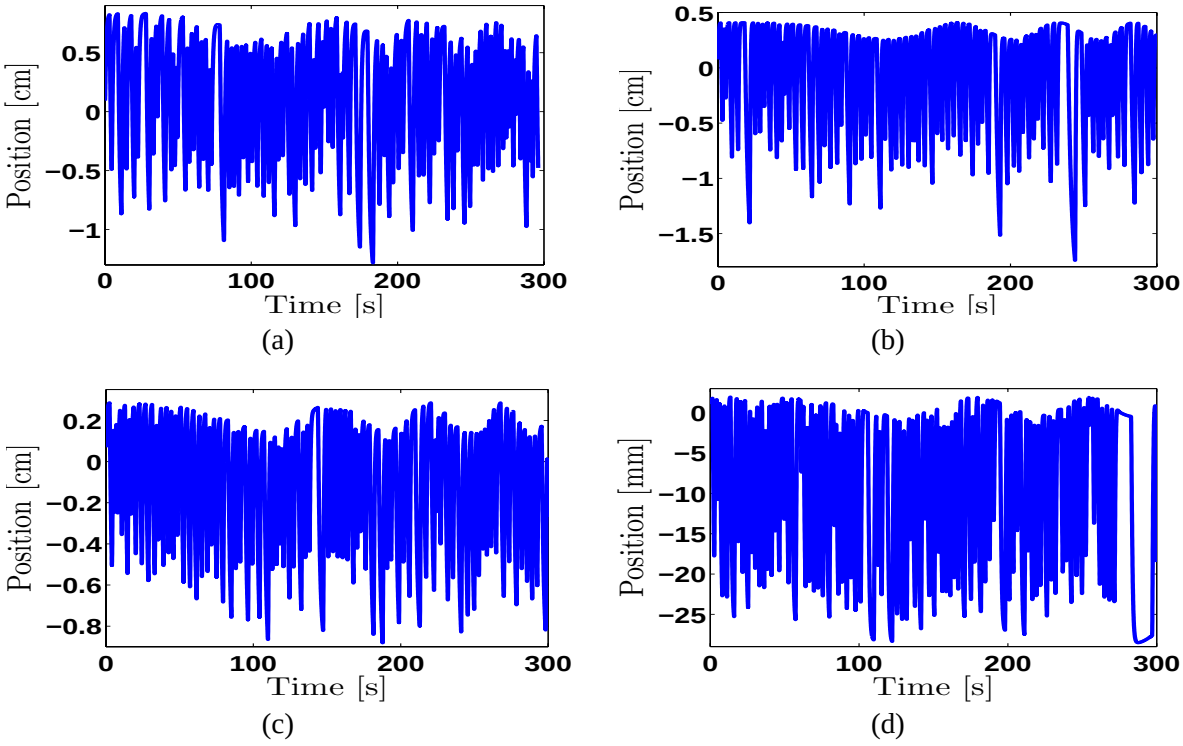

Fig. 5.24: Sinusoidal drift added to the generated respiratory data for (a) FB, (b) AI, (c) AVB, and (d) IFM

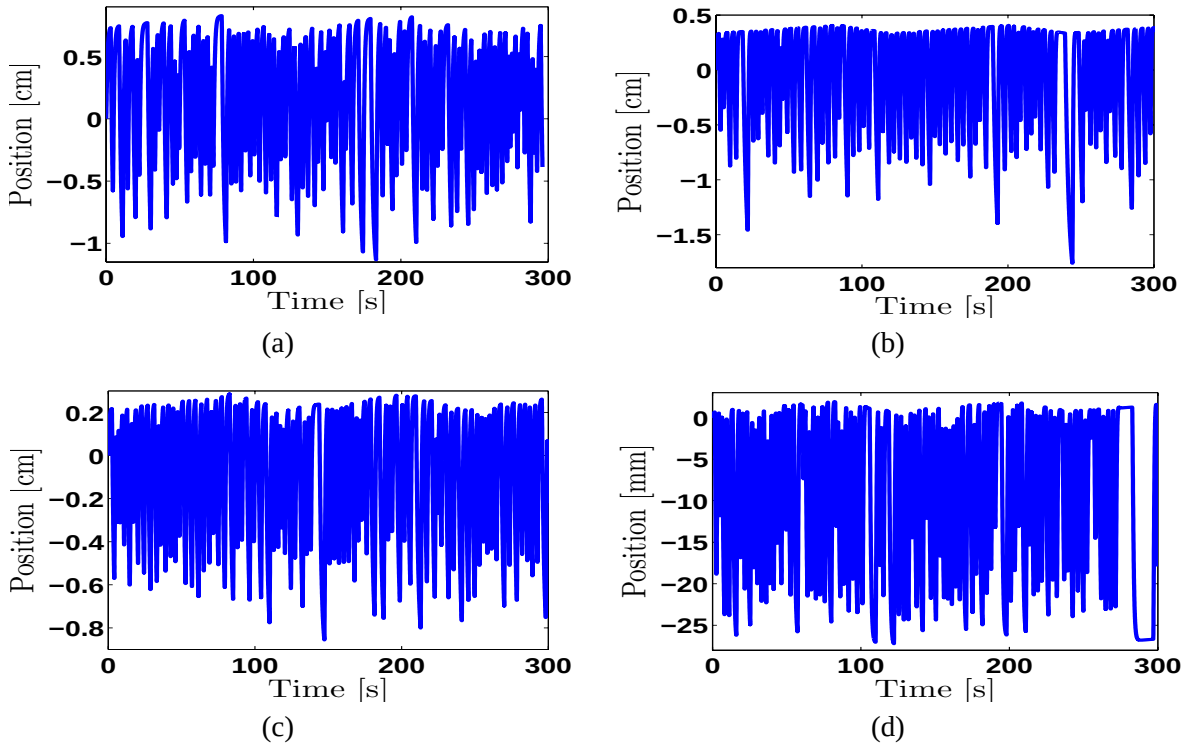

Fig. 5.25: Triangular drift added to the generated respiratory data for (a) FB, (b) AI, (c) AVB, and (d) IFM

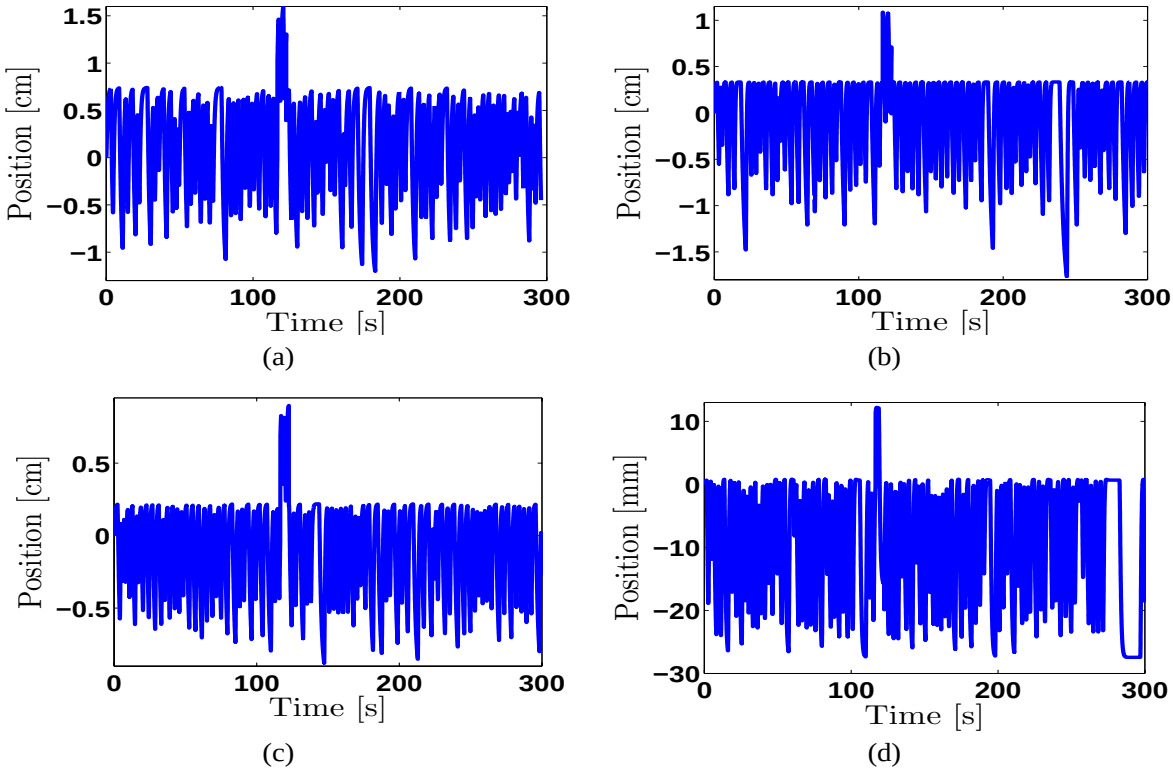

Fig. 5.26: Impulse drift added to the generated respiratory data for (a) FB, (b) AI, (c) AVB, and (d) IFM

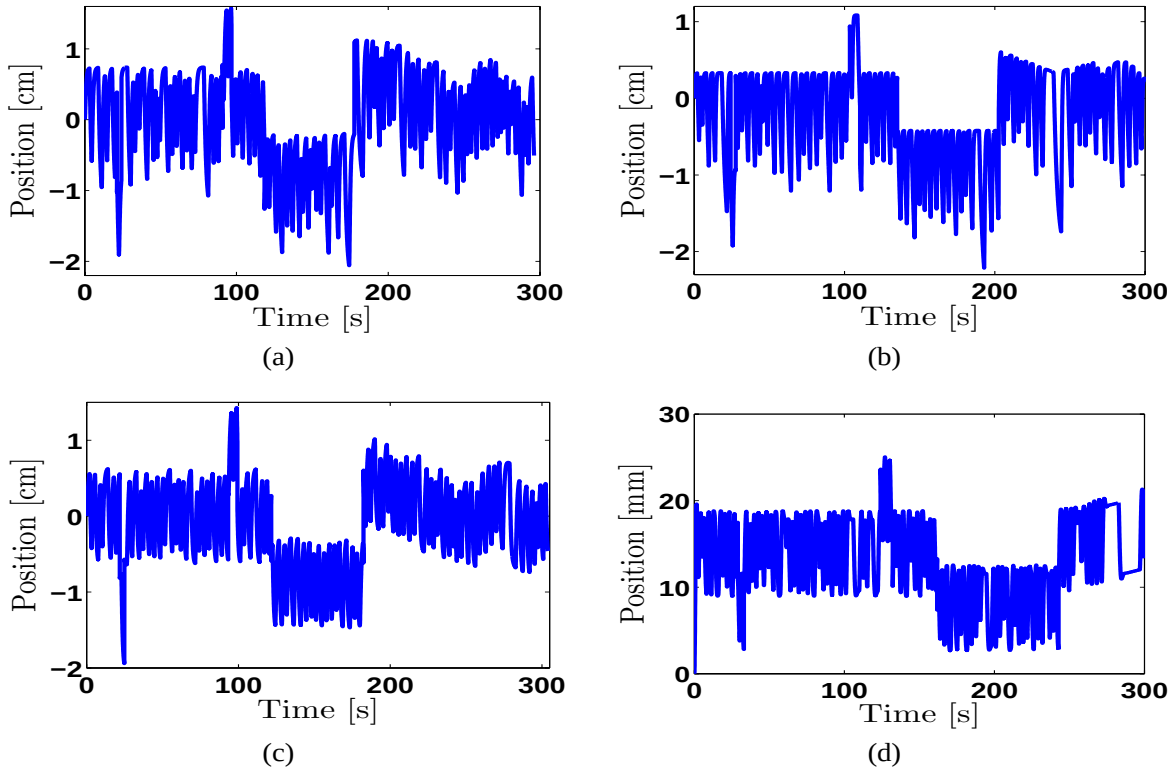

Fig. 5.27: Mixture of different drift signals (sinusoidal, triangular, and spikes) added to the generated respiratory data for the cases : (a) FB, (b) AI, (c) AVB, and (d) IFM

5.9 Conclusions

This Chapter has addressed the development of surrogate motion models for the purpose of simulation. Two new approaches, namely a BM and polynomial function were introduced. The BM approach was inspired from a simplified representation of the respiratory system. It considers the lung as a bilinear model driven by a square wave with varying frequency and duty cycle. This input signal can be interpreted as a stimuli signal generated by the nervous system, which its period and duty cycle correspond to the ones of the respiratory motion data. As reported in Chapter 4, the respiratory motion data contain additional components including measurement noise, heart rate and baseline drift. The bilinear modelling approach has considered the aforementioned signals as external components, which were removed before modelling and simulation.

Two methods to deal with the drift signals were adopted. The first models the drift as a polynomial function with different orders. The second removes the frequencies corresponding to the drift using a low-pass filter. The parameters of the bilinear model were estimated using a non-constrained nonlinear optimisation technique for the polynomial drift removal and a constrained non-linear optimisation technique for the pre-filtered drift. For both methods, it was shown that the estimated models have validated the clinical data with a MASE around 1mm. The mean average bilinear model, was found to be generalisable when the motion irregularities are excluded. The bilinear modelling approach has also shown a good performance when it was assess on unfiltered respiratory surrogate data. Finally the new bilinear modelling framework was used to generate a set of realistic respiratory surrogate motion data including different types of drift scenarios.

A new polynomial model was adopted to model respiratory motion cycles. The performance of the polynomial model has been assessed against the widely used Lujan model [Lujan et al. 1999], using two clinical data sets from VCU and Hokkaido University School of Medicine. It was shown that the polynomial model offers more flexibility than the periodic cosine model to reproduce non-symmetrical breathing cycles.

Chapter 6

Respiratory simulation and predictive tracking based on spirometry/external markers

6.1 Introduction

Usually, the ART process involves IGRT techniques to monitor the tumour position in real-time by means of an imaging system (see Chapter 2). It is, however, possible to monitor other biological signals such as breathing flow, lung volume and pressure as well as the heartbeat. The current chapter aims to investigate if there is any benefit in combining respiratory motion information with biological signals to improve modelling, simulation and predictive tracking of respiratory motion. In order to do so, an experiment has been carried out with medical equipment used for research. A 3D motion of three external markers attached to a special tool placed onto two different positions on the thorax of healthy persons have been recorded. At the same time, breathing flow, respiration rate, heartbeat and pressure signals were also measured.

The concept, based on an input-output signals to simulate and predict the respiratory motion presented in Chapter 5, is extended here by replacing the artificially generated input by a measured air flow signal. A pre-processing and statistical analysis of the measured data were performed prior to their use to select the input and output signals of the system to be identified. The predictive tracking approach was assessed in practice using a video tracking system developed within MAESTRO project. The latter involves a simple video camera and $LabVIEW^{\text{TM}}$ software.

This chapter is organised as follows. Section 6.2 gives a simulation framework of the predictive tracking. Section 6.3 describes the design of new respiratory motion experiment as well as the acquisition process, pre-processing and analysis of the collected data. In Section 6.4, modelling and simulation of the respiratory motion is carried out. The effect of using a physical input signal was investigated in Section 6.5. In the latter, a comparison to the modelling approach used in Chapter 5 was also carried out. Section 6.6 describes the online approach for predictive tracking of the respiratory motion. Conclusions are drawn in Section 6.7.

6.2 An overview of the predictive tracking simulation

The most effective prediction process must be able to deal with the full range of respiratory behaviour. The likelihood of highly irregular breathing increases with patients whose pulmonary function has been compromised by disease. Regular breathing can be interrupted by irregular transient periods (e.g., coughing, hyperventilation, etc). Some breathing behaviours are highly irregular by nature. Irregularities in breathing makes modelling and prediction difficult. Therefore, a simulation of respiratory motion tracking needs to be carried out before any clinical evaluation.

The motion prediction system can be simplified by the scheme given by the Figure 6.1. In the latter, the breathing model aims to provide a realistic respiratory motion based on different breathing information, which can be used as an input-output of the system to be modelled. As shown in the analysis of the respiratory motion, different disturbances can occur. These disturbances can be simulated and added to the simulated respiratory motion.

An on-line prediction model uses the measured input-output to predict a number of samples in advance. A so-called prediction horizon that corresponds to the treatment system delay has to be predicted. The time delay is due to the communication between the imaging systems and the treatment delivery control system, the dynamic of the control system and sampling time of the imaging system as well as control system (see Chapter 3). These latencies can be modelled by an adjustable delay block.

This scheme is useful to carry out a simulation study to evaluate tracking of the respiratory motion prior to any clinical implementation. Note that this scheme can be extended by involving a model of the PSS and/or MLC, in order to simulate the process of the EBRT treatment.

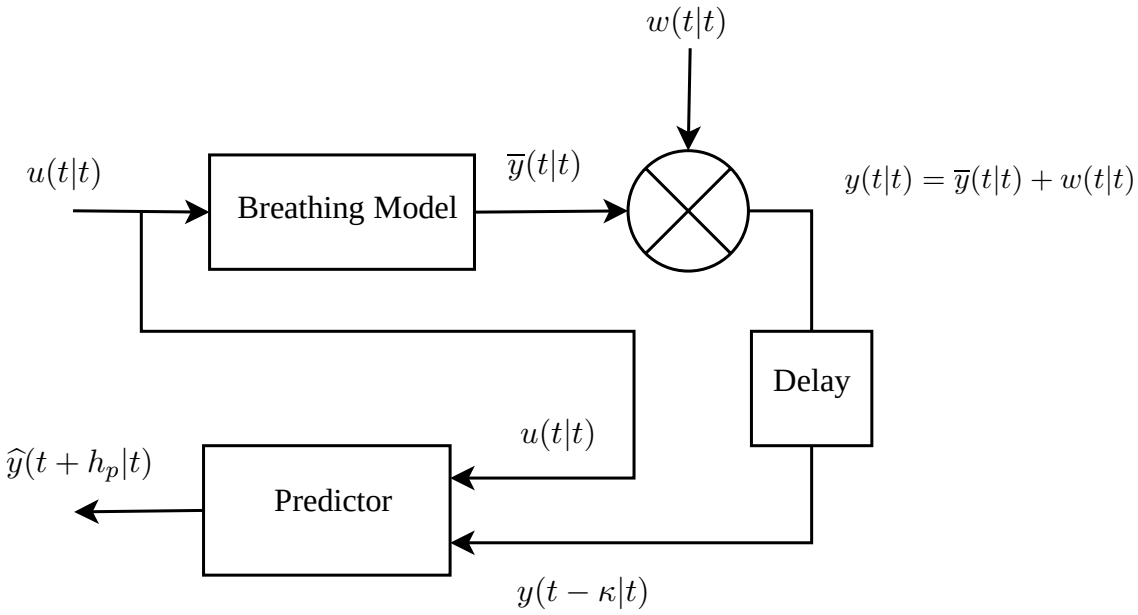

Fig. 6.1: Block diagram of respiratory motion simulator and predictive tracking scheme.

6.3 A novel respiratory motion acquisition experiment

6.3.1 Experiment description

The modelling work carried out so far in this thesis was based on clinical data, corresponding to the position of internal/external markers (see Chapter 5). For each of those trajectories an 'artificial' input signal was generated and established upon the frequency changes, in order to apply the system identification approach (see Chapter 5). This Chapter investigates the feasibility of replacing such an 'artificial' signal with a measurable input signal. One of the critical conditions to the success of the approach is the choice of signals to be measured.

Variables that are related to the respiration process can involve airflow, volume, pressure and heart rate. The air flow represents the rate of change of the lung volume, and is driven from a region of relatively high pressure to one where the pressure is lower. It was reported in the literature that tumour motion (or external motion related internal motion) can be linked to the volume of lung variation [Low et al. 2005]. Thus, the key signals that have to be measured are lung volume and external chest motion.

An experiment was designed and conducted with support of some MAESTRO co-workers. Note that a university research committee approval was required to perfrom this experiment (see Appendix B). The latter took place in the Control Theory and Application Centre (CTAC) Laboratory and involved 13 healthy human volunteers (12 males and 1 female) of different ages and weights. The participants were

positioned comfortably on a table and asked to breath normally for two sets of 4 minutes each. The same acquisition period was adopted in [Hoisak et al. 2006, George et al. 2006]. The experimental procedure is described in Appendix B.1. In this experiment a set of biological and geometrical information related to the breathing process were acquired in real-time by two different means.

A Spirometer DATEX AS3 (see Figure 6.2(b)) on loan from UHCW, measured breathing flow, lung volume and pressure, and an electrical recording of the heart or Electrocardiogram (ECG). The Spirometer set-up was connected to a separate PC via the $dSPACE^{©}$ DS1104 Controller Board installed in this latter and data was collected via $MATLAB/SIMULINK^{©}$.

A 3D tracking system $Polaris^{®}$ (see Figure 6.2(a)) on loan from $Elekta^{®}$, was connected to a separate workstation. This accurate tracking system was utilized to measure real-time 3D position and orientation of optical markers affixed to two "tools" (see Figure 6.2(c)) specifically designed for the experiment. The tool was positioned onto the thorax (on abdomen) with an elastic band. Each subject had the tool initially located on the upper chest (upper test), and then the tool was positioned in the vicinity of diaphragm (lower test), in order to evaluate the influence of diaphragm motion on chest abdominal breathing patterns. An illustration of the experiment set-up for one of the subject taking part is given in Figure 6.2(d).

(a) (b) (c)

(d)

Fig. 6.2: Illustration of (a) Polaris system with its coordinates, (b) Spirometer equipment, (c) Tracked tool, and (d) The set-up for a subject taking part in the experiment.

The Polaris system can be described as a portable 3D infrared vision system able to track, with sub-millimetre accuracy the motion of active or passive tool [Wiles et al. 2004]. In this work passive tools were used (Figure 6.2(c)). Each tool comprises a set of infrared reflective spheres. The infrared tracking system emits infrared light that is reflected by these spheres. The reflections are detected by the infrared tracking system and used to determine the position of the sensors. Note that the RMSE is $0.35\ mm$ when using only one marker [Wiles et al. 2004]. The number and positioning of the spheres was designed to minimise the tracking error.

A new data collection software was developed by a MAESTRO co-worker (for more detail see [Haas et al. 2005]). An example of the data collected by the Polaris system via the new software is demonstrated in Table 6.1.

Tab. 6.1: Illustrating the format of the data collected by Polaris.

Frame number	X	Y	Z	q_0	q_x	q_y	q_z	Error	Mark
27798	160.56	199.2	-1408.74	0.9865	-0.1564	-0.0247	0.0412	0.2768	1

The data collected includes:

- A frame number that is an internal counter that starts at power up and relates to the time at which the coordinates were returned by Polaris. It can be used to indicate the time in terms of samples at which the data was collected.
- The position of the tool tracked in Cartesian coordinate system (X, Y, Z) where reference is given with respect to Polaris'own coordinate system (see Figure 6.2(a)).
- The quaternion (q_0, q_x, q_y, q_z) that indicates the orientation of the tool.
- An error indicating the discrepancy (in term of RMSE value) between the marker position measured on the rigid body and the marker position defined in the tool description.
- An indicator denoted 'Mark' that is employed by the user to indicate specific events during the tracking process. The latter has been implemented to facilitate data processing.

A sample signals for two different subjects with the measurement tool in the upper position, obtained from the Spirometer and Polaris are shown in Figure 6.3 and 6.4 respectively. While the flow rate, pressure and volume signals exhibit oscillatory patterns, the heart rate signal is characterised by periodic patterns. The pressure and volume measurements are affected by a negative offset which was due to the initial configuration of the Spirometer. Moreover, the pressure signal is distinguished from the rest of the

signals by having a higher level saturation and a large amount of measurement noise. It was noticed from the ECG data that there is an offset which causes negative values in the heart beat measurement. The signals obtained from the Spirometer were in Volts, so a conversion to the real units was performed. Note that the 3D position data were transformed to have the initial position as a reference. Concerning the the Polaris signals, one might notice that the motion data in Y and Z direction exhibit more measurement noise compared to the X motion. In addition, a baseline drift was also noticed in the the three motion data. It is important to mention that it was not possible to electronically synchronise the Polaris and Spirometer as both equipments have different data acquisition process.

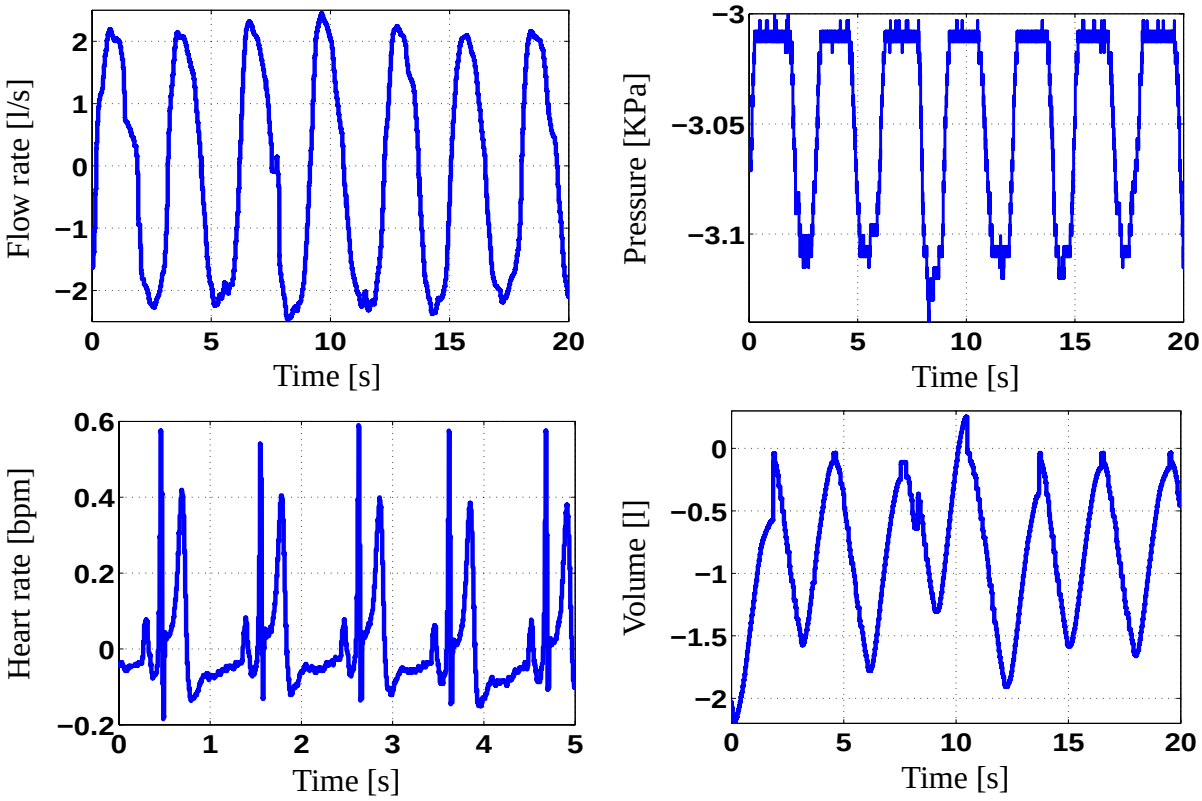

Fig. 6.3: Spirometer measurement for subject number 1 obtained during the upper test.

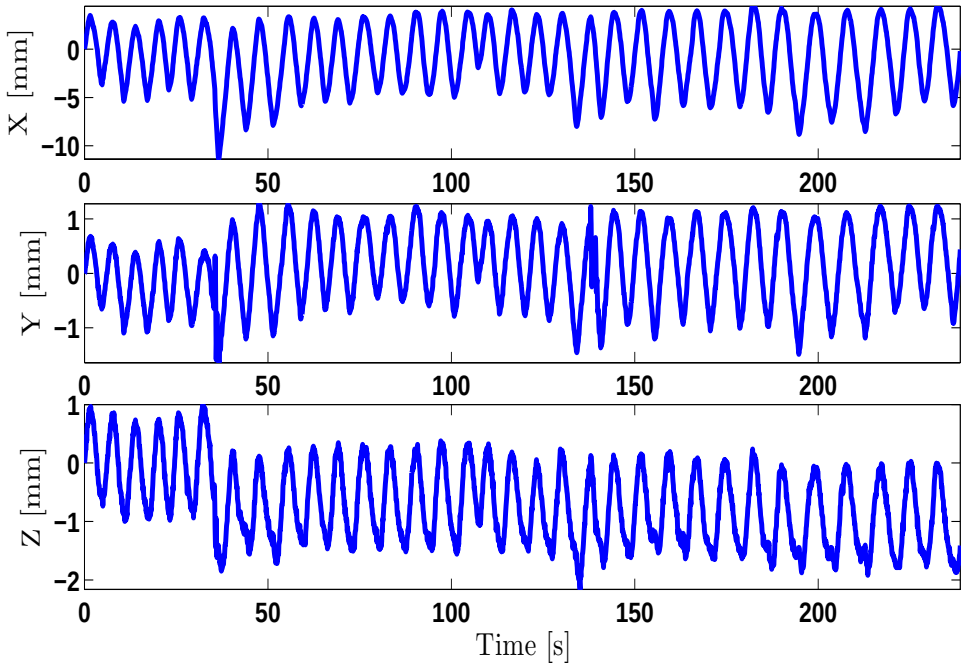

Fig. 6.4: The 3D markers motion for subject number 10 obtained during the upper test.

6.3.2 Respiratory data pre-treatment

Once the data were collected, it was noticed that they are not suitable for an immediate use. Therefore, a data pre-processing was performed. The first difficulty that was noticed is the loss of the tool by the Polaris tracking system in the external chest measurement (see an example in Figure 6.5(a)). Among the data where the missing values were detected, there is subject 1, 8, 11 for the upper test and subject 7 for the lower test. The first step in data pre-processing is to handle these missing values. It was decided to consider only the data without any missing values, i.e. the part of the signal where the missing values occur, was completely removed.

The second issue with the data collected was some irregularities in the Polaris data which might be caused by subjects movement/coughing, movement of the measurement tool within the body and a large amount of measurement noise. These data were noticed especially in the lower sets and will be considered as bad data. An example of such data is shown in Figure 6.5(b). Such data will not be considered for modelling.

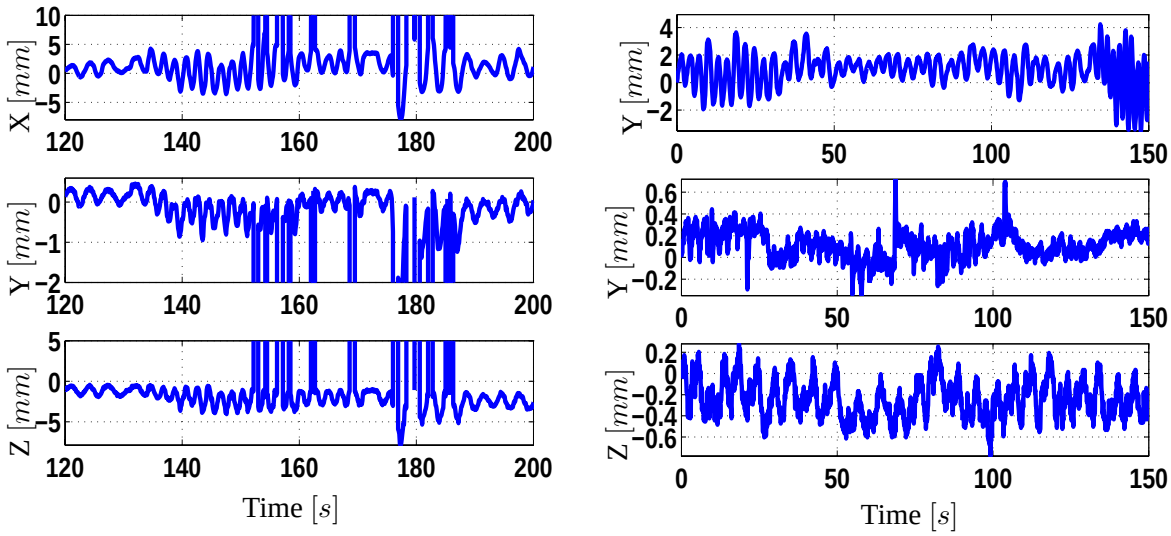

(a) (b)

Fig. 6.5: Illustration of (a) data where loss of the tool by the tracking system Polaris and (b) some bad data.

The last issue within this experimental data was the dissimilarity in the sampling time between Polaris and the Spirometer. While the data in Polaris was acquired at sampling rate of 10 Hz, the Spirometer has a sampling rate of 1000 Hz. Consequently, the sampling rate of Spirometer data was reduced to 10 Hz to have the same sampling frequency as Polaris data. Two re-sampling methods have been investigated. The first one consists in down-sampling the data by a factor of 100 and the second approach takes the average value of a moving 100 samples window. The first method will be called re-sampling method 1 and the second one will be referred to re-sampling method 2. The following Figure shows a comparison between the real signal and the re-sampled signal by the two above mentioned methods. It can be noticed from Figure 6.6 that the resultant re-sampled signals exhibit the same pattern as the real. Moreover, the both re-sampling methods have reduced the amount of noise present in the measured data.

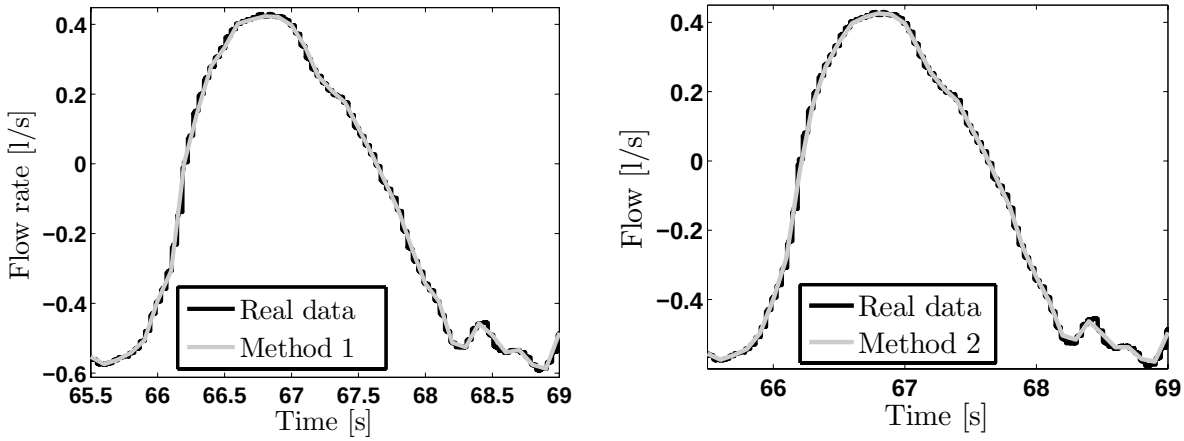

(a) (b)

Fig. 6.6: A comparison between the real signal and (a) re-sampling method 1 and (b) re-sampling method 2.

In order to compare the two methods, a common measure called the Signal-to-Noise Ratio (SNR) or ratio of variance can be used. It is defined by $SNR = 10\log\left(\frac{\sigma^2_{signal}}{\sigma^2_{noisel}}\right)$. A high SNR ($\gg 1$) indicates high precision data, while a low SNR indicates noise contaminated data. The variance of the noise component is not known. Consequently, data has to be filtered in order to remove approximately the measurement noise. Before doing that, a frequency spectrum is required to define the cut-off frequencies. The FFT algorithm was applied to the Spirometer data and a sample results from each variable are illustrated in Figure 6.7. The latter shows the presence of the respiratory components below 0.5 Hz in the flow, volume, and pressure. The signals with frequency higher than 1 Hz for flow, volume, and pressure, and above 2 Hz for the heart rate signals were considered as noise. The main heart beat frequency was found to be around 1 Hz.

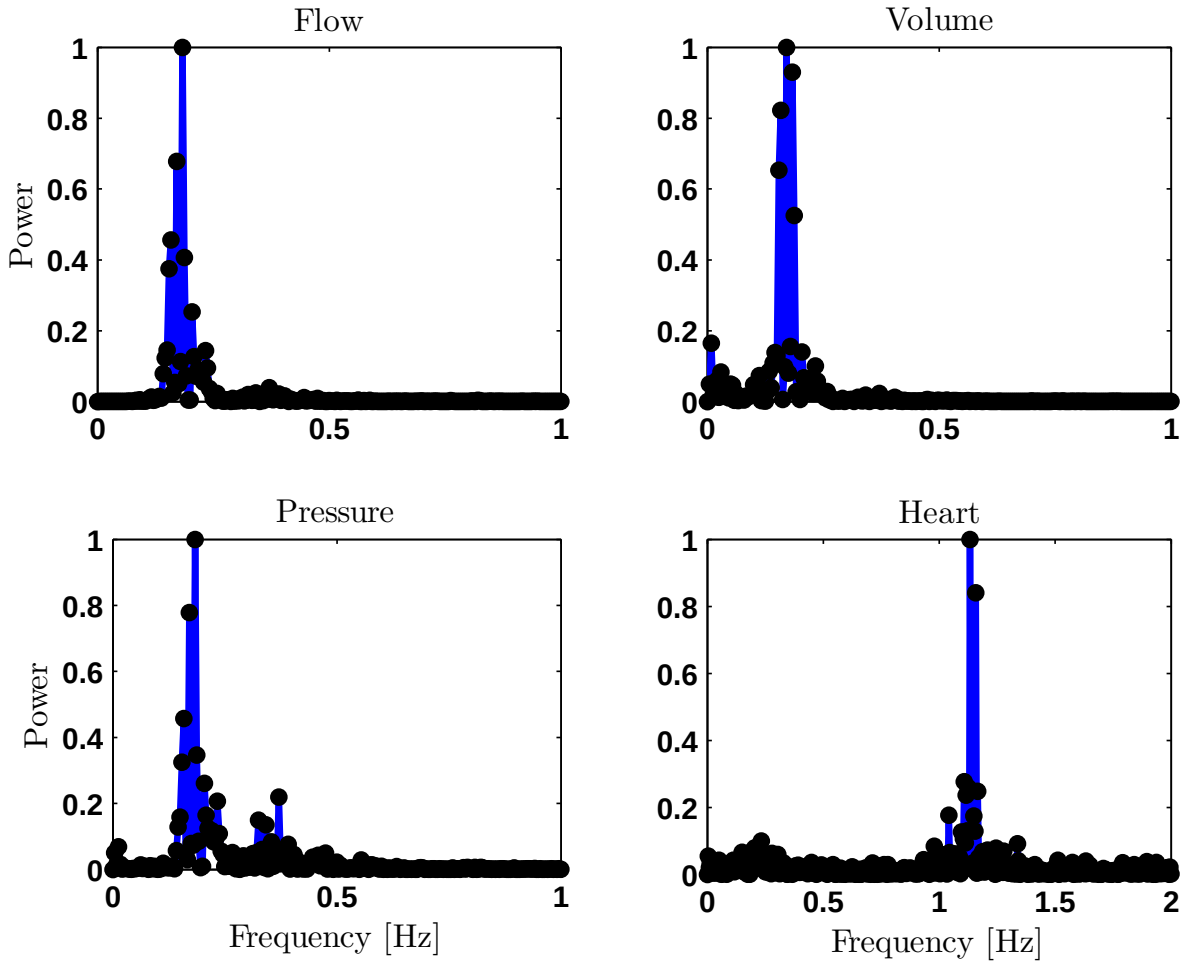

Fig. 6.7: An example of Spirometer data spectrum for subject 3 in upper test.

A third order Chebychev low-pass filter with 0.1 db peak-to-peak ripple was utilised to remove the noise. An example of the filtering performance of Spirometer 1 in the upper test is shown in Figure 6.8. The filter was able to remove noise component from the four signals and keep the main information.

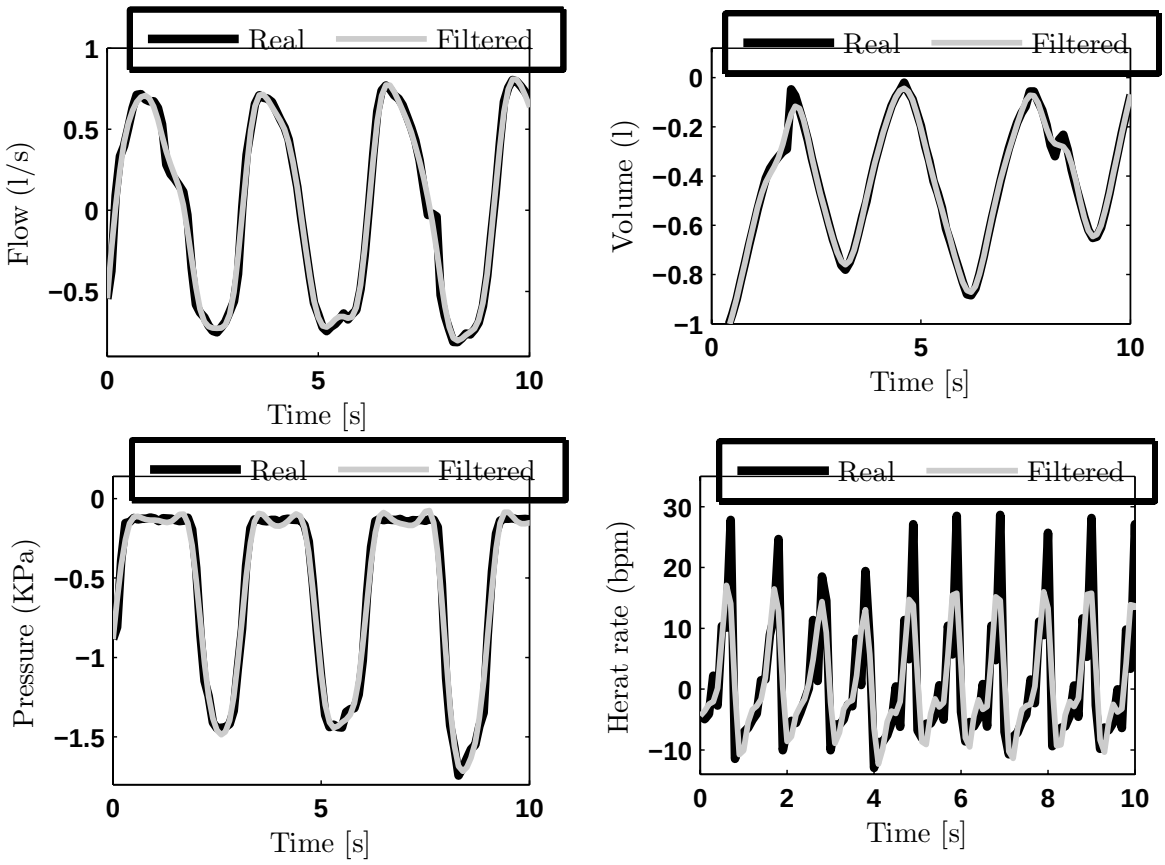

Fig. 6.8: Filtering performance of Spirometer data for subject 1 in the upper test.

The measurement noise signals were extracted from the flow, volume and pressure signals and their overall distribution were carried out (see Figures 6.9). The standard deviation of the overall noise distribution for the flow, volume and pressure which were denoted by σ_F, σ_V and σ_P respectively, were also quantified. Comparing the overall measurement noise distributions, one might notice that these latter have a peak distributions with different standard variations. The pressure signals have more noise compared to the flow and volume signals. This is probably due to the Spirometer configuration and calibration. It was also noticed that the lower and upper sets have approximately the same quantity of noise. This supports the selection of the cut-off frequencies and supports the assumption that the noise on the data is typically due to the measurement device.

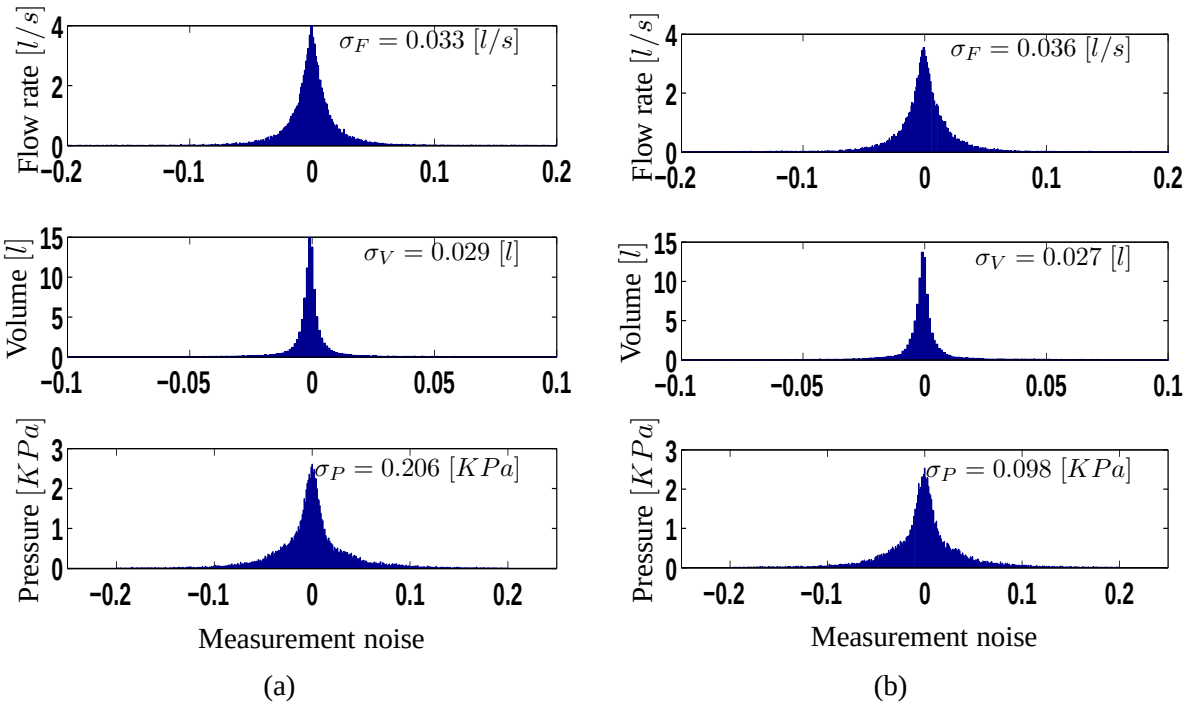

Fig. 6.9: Spirometer measurement noise distribution for (a) upper test and (b) lower test. The standard deviations of noise distributions are represented by σ_F, σ_V, and σ_P for the flow, volume and pressure respectively.

Once all data have been filtered, the SNR was calculated for every subject and the two different tests. Figure 6.10 shows a comparative example of the flow signal for lower and upper tests. From the latter, one can notice that the SNR of the data re-sampled using method 2 is higher than the re-sampled data via method 1. This means that the second method removes more noise than the first one. Therefore, only the re-sampled data by the method 2 will be used later on in modelling and prediction.

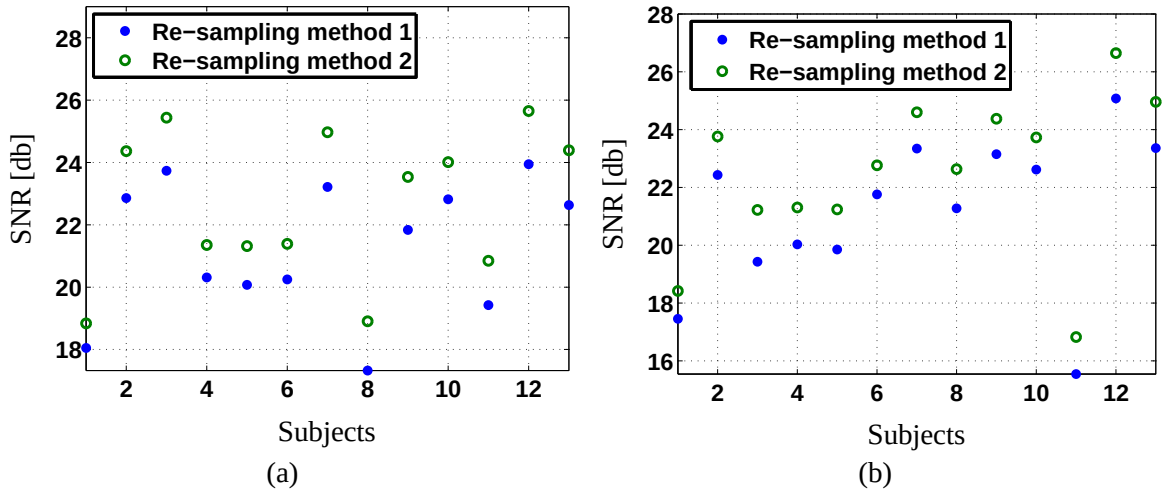

Fig. 6.10: A comparison of the two re-sampling methods via SNR factor for (a) upper test and (b) lower test.

This time the comparison involves the SNR measurement of different variables over all the subjects (see Figure 6.11). As result, the flow and volume are the variables that are less influenced by the measurement noise compared to pressure and heart rate. This is applicable for all the subjects and for different markers positions. This finding is very important since it is preferable to have less noise in the signals that will be utilized to track the breathing motion for more accuracy.

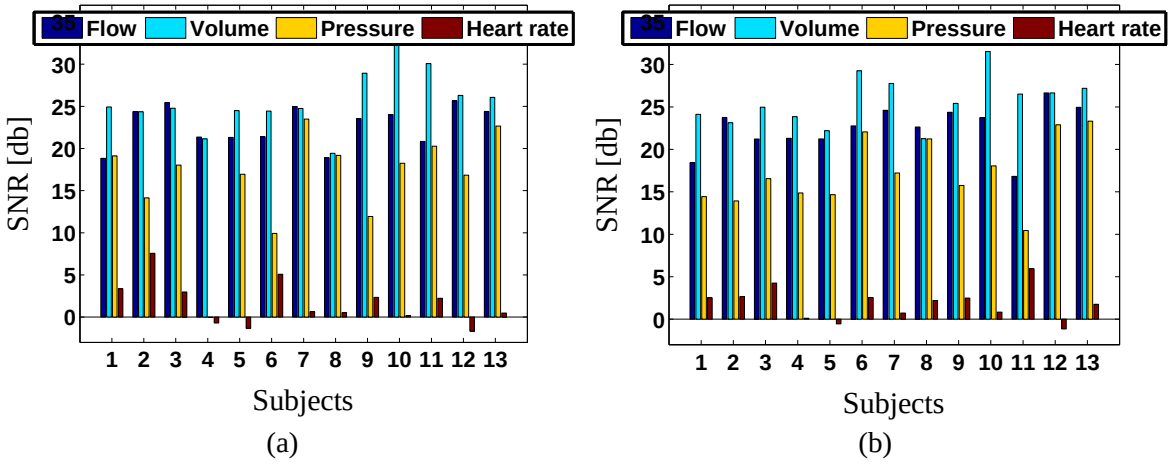

Fig. 6.11: A comparison of SNR for different variables and subjects: (a) upper test and (b) lower test.

The frequency spectrum of the external markers data in the three directions was also performed and an example of a Polaris data spectrum for subject 5 in the upper test is given in Figure 6.12. Sub-figure (a) shows the breathing information (between 0.1 and 0.3 Hz) and the drift component (below 0.05 Hz). In sub-figure (b) the noise components characterised by the frequencies above 0.6 Hz are illustrated.

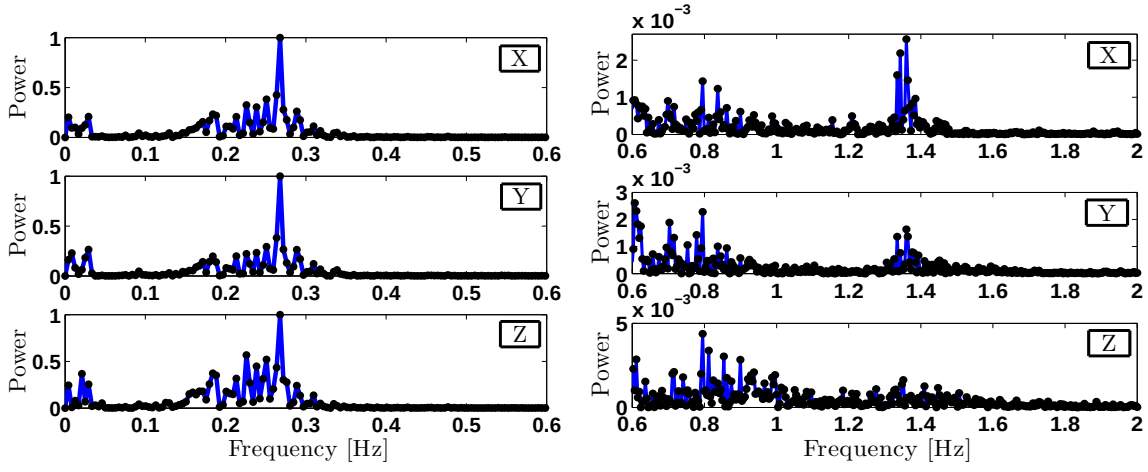

Fig. 6.12: An example of frequency spectrum of Polaris data for subject 5 in the upper test: (a) respiratory and drift components (b) noise component.

Similarly, to the Spirometer data, a third order low pass filter was applied to remove the signals that have a frequency above 0.6 Hz. Figure 6.13 shows a comparison between an original Polaris data sample and the its filtered signal. It is clear for the latter that the used filter has removed adequately the noise signals and maintains only the respiratory and drift components.

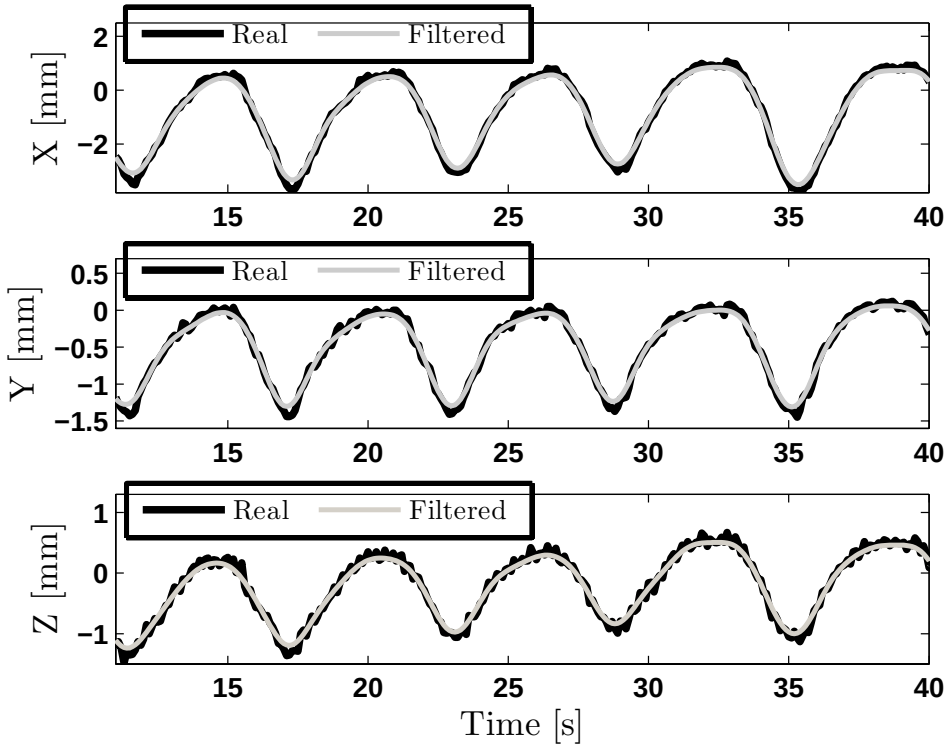

Fig. 6.13: Filtering performance of Polaris data for subject 2 in the upper test.

The removed noise signals were found to have a Gaussian distribution as shown in Figure 6.14. The standard deviation of the noise distributions for the X, Y and Z directions were respectively 0.22 mm, 0.11 mm and 0.11 mm for the upper test and 0.36 mm, 0.13 mm and 0.12 mm for the upper test. These values show that there is more noise in the X direction compared to Y and Z directions. This is due to the fact that the breathing motion is more important in the X direction. Note that more noise was noticed in the lower position. The amount of noise in the Y and Z directions are almost similar.

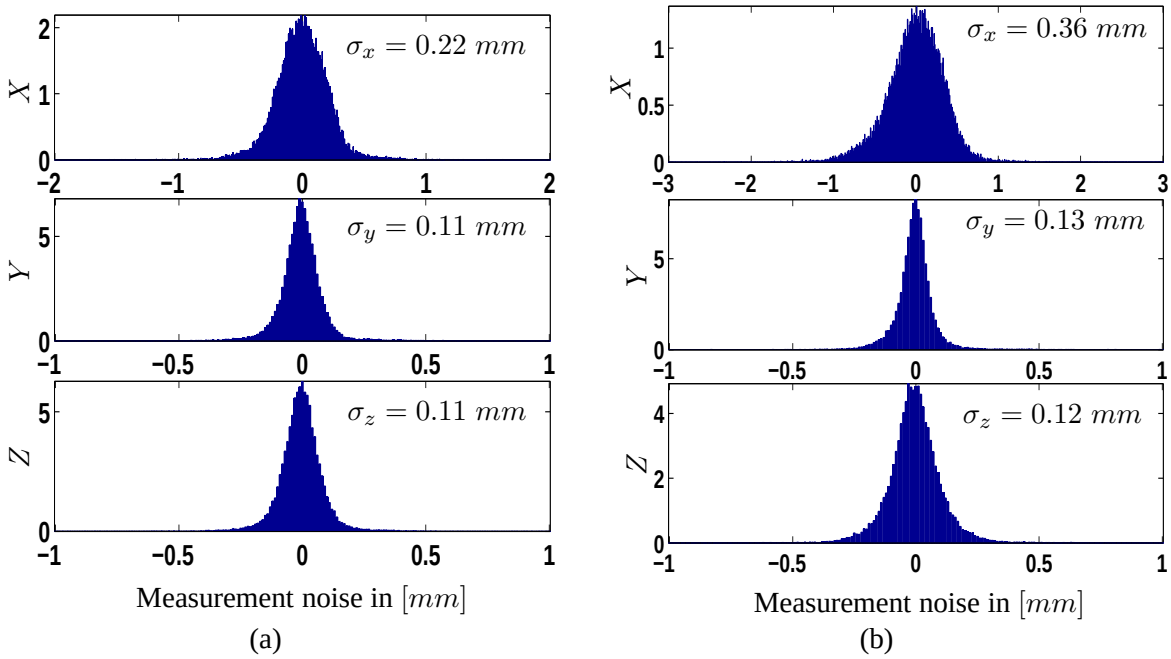

Fig. 6.14: Polaris measurement noise distribution for (a) upper test and (b) lower test.

A comparison between the level of the 3D position and the level of the noise was performed for all subjects and different markers positions (see Figure 6.15). By comparing the SNR values, it was noticed that the effect of noise level changes depending on the X, Y or Z axes as well as from subject to subject. The variable X has in most cases the highest SNR compared to Y and Z direction, especially for the lower sets. This type of analysis can be useful to investigate the origins of noise level differences and to improve the quality of the signals acquired.

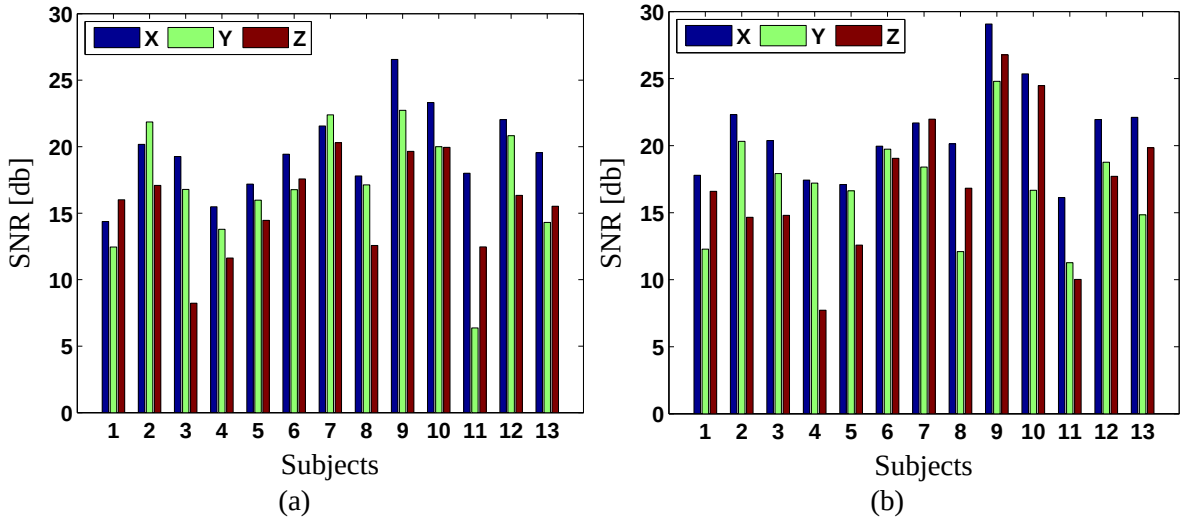

Fig. 6.15: A comparison between the level of the 3D information and noise level for different subjects in (a) upper test and (b) lower test.

6.3.3 Respiratory motion analysis

The overall distribution of the Polaris data for the two investigated tests was performed here to evaluate the range of breathing motion amplitude in the three axes X, Y, and Z. The frequency spectrum of the Polaris data carried out previously has shown the presence a baseline drift. Therefore, the latter has to be removed from the Polaris data before performing the overall distribution of the external markers motion amplitude. A high-pass filter was used to retain the frequencies above 0.05 Hz.

Figure 6.16 illustrates both the time and frequency characteristics of (a) noise-free signal representing the movement of the chest markers in the X direction for subject 2 acquired in the upper test and (b) the corresponding drift-free signal. The performed frequency spectrum were useful for the assessment of the drift removal. The frequency spectrum of the drift-free signal shows that the latter contains only the respiratory frequencies

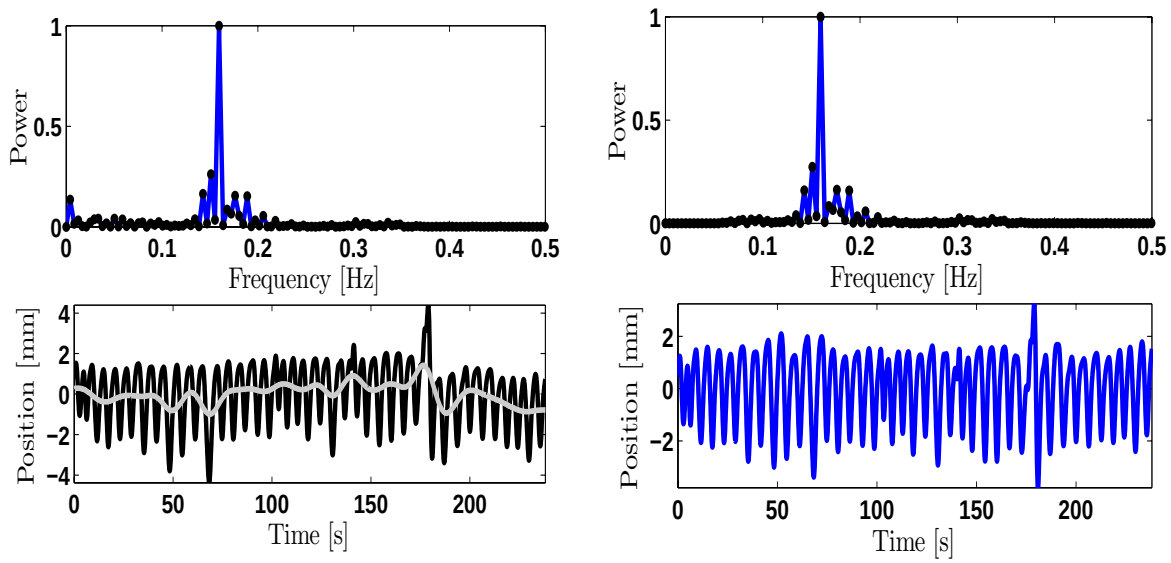

(a) (b)

Fig. 6.16: Time and frequency characteristics of X movement for subject 2 acquired in the upper test: (a) noise-free spectrum and (b) drift-free spectrum.

Subsequently, the overall distribution of the drift signals for upper and lower tests were carried out-see Figure 6.17. The latter shows that the overall distribution of the drift signals do not have a Gaussian shape as it was found for the previous clinical data. It was also noticed that the range of the overall drift amplitude is more important in the X direction compared to Y and Z directions. This was due to the fact that the breathing motion was more important in the X direction. Except for the Y direction, the lower test involves a significant drift compared to the upper test.

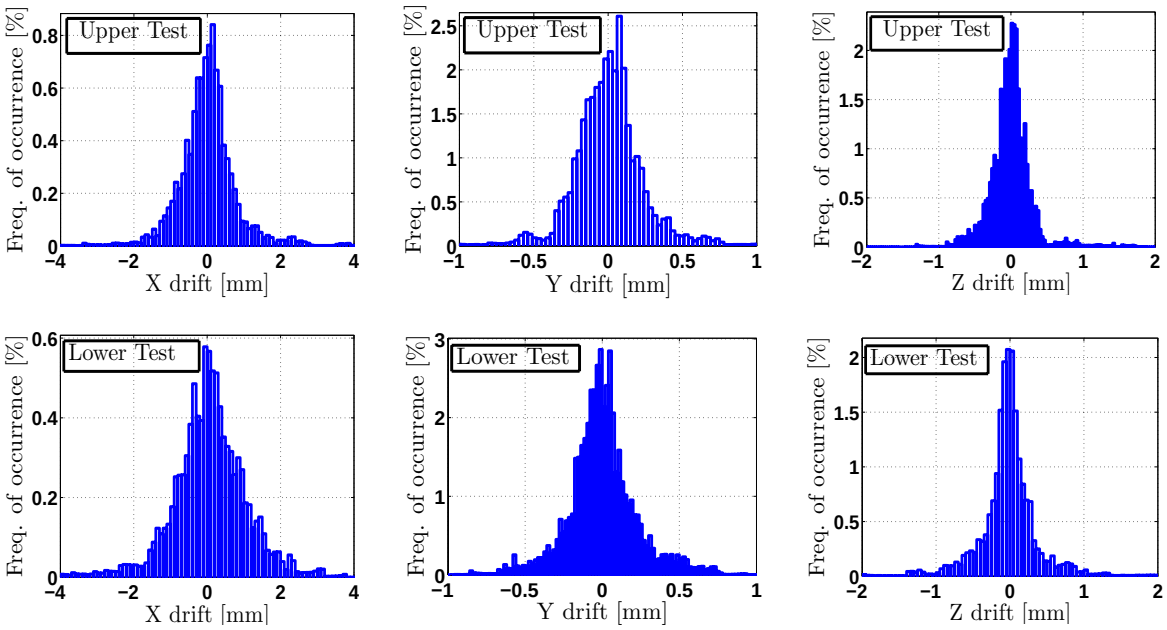

Fig. 6.17: The overall distributions of the 3D drift data for the upper (Top) and lower (Bottom) tests.

The overall distributions of the respiratory part are illustrated in Figure 6.18. While the distribution of the motion in X direction has the shape of a bimodal distribution, the motion in Y and Z directions have more sharply peaked distributions. One might also notice that the motion in X direction is larger compared to the other directions. Comparing these distributions to those for the clinical data, it can be seen that the respiratory fluctuation in the X direction for the upper test and in the Y direction for the lower test are comparable.

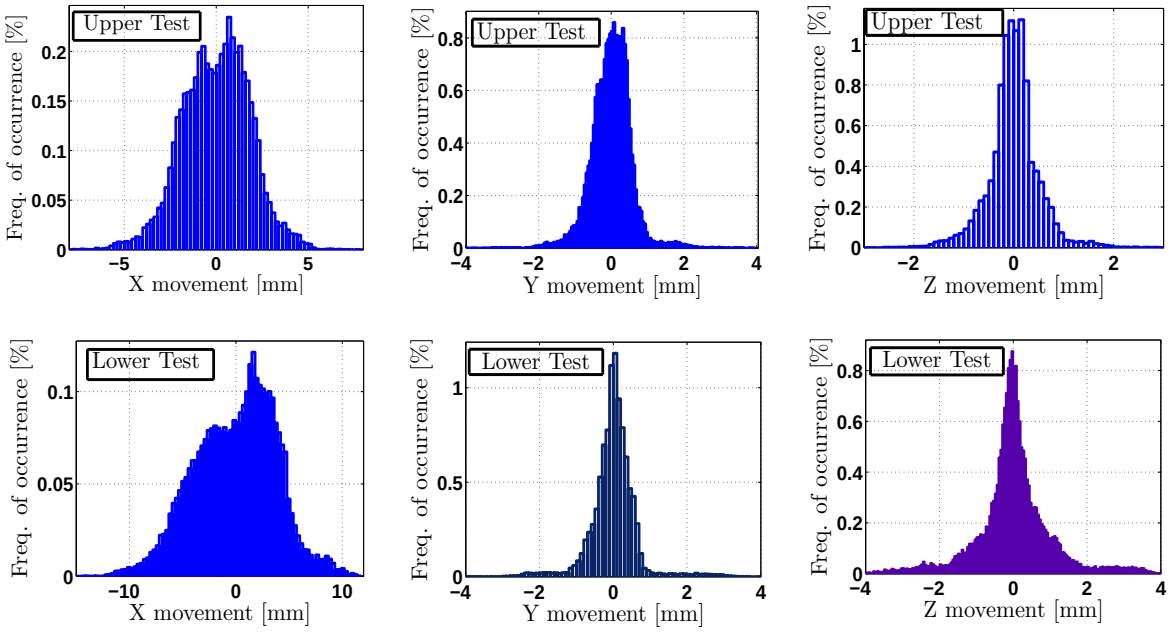

Fig. 6.18: The overall distributions of the 3D respiratory data for the upper and lower tests.

6.3.4 Variables correlation analysis

Recalling that one of the main objectives of the performed experiment was to develop a simulation model of the respiratory motion in the first place and a practical and easy way to track the latter, both tasks based on simple equipments such as Spirometer and video camera. The modelling technique adopted here assumes that the lung is a *black box* system with a number of inputs and outputs. While the input signals will be provided by the Spirometer, the output will be a position of the chest markers. It is very important to examine the correlation between the different variables in order to assess the relationship between the latter and reduce the number of variables in case there is any correlation. A scatter plot was performed here to measure the degree of relationship between the 3D markers positions and the Spirometer data (flow, pressure and volume).

Figure 6.19 and 6.20 illustrate an example of scatter plot of the considered variables for subject number 1 with markers in upper and lower positions, respectively. The correlation test between the 3D external markers motion has shown that these latter are linearly correlated for the markers in the upper position, whilst in the test with the markers in lower position, the linear correlation was noticed only between the X and Z motion. Concerning the Spirometer data, a nonlinear correlation between these latter was noticed for both upper and lower test. The nonlinear correlation between the flow and the volume is due to the fact that the latter represents the first derivative of the former. The assessment of the correlation between the Polaris and Spirometer data was also carried out. The latter has revealed that there is a nonlinear relation between the Polaris data and Spirometer data for both performed tests.

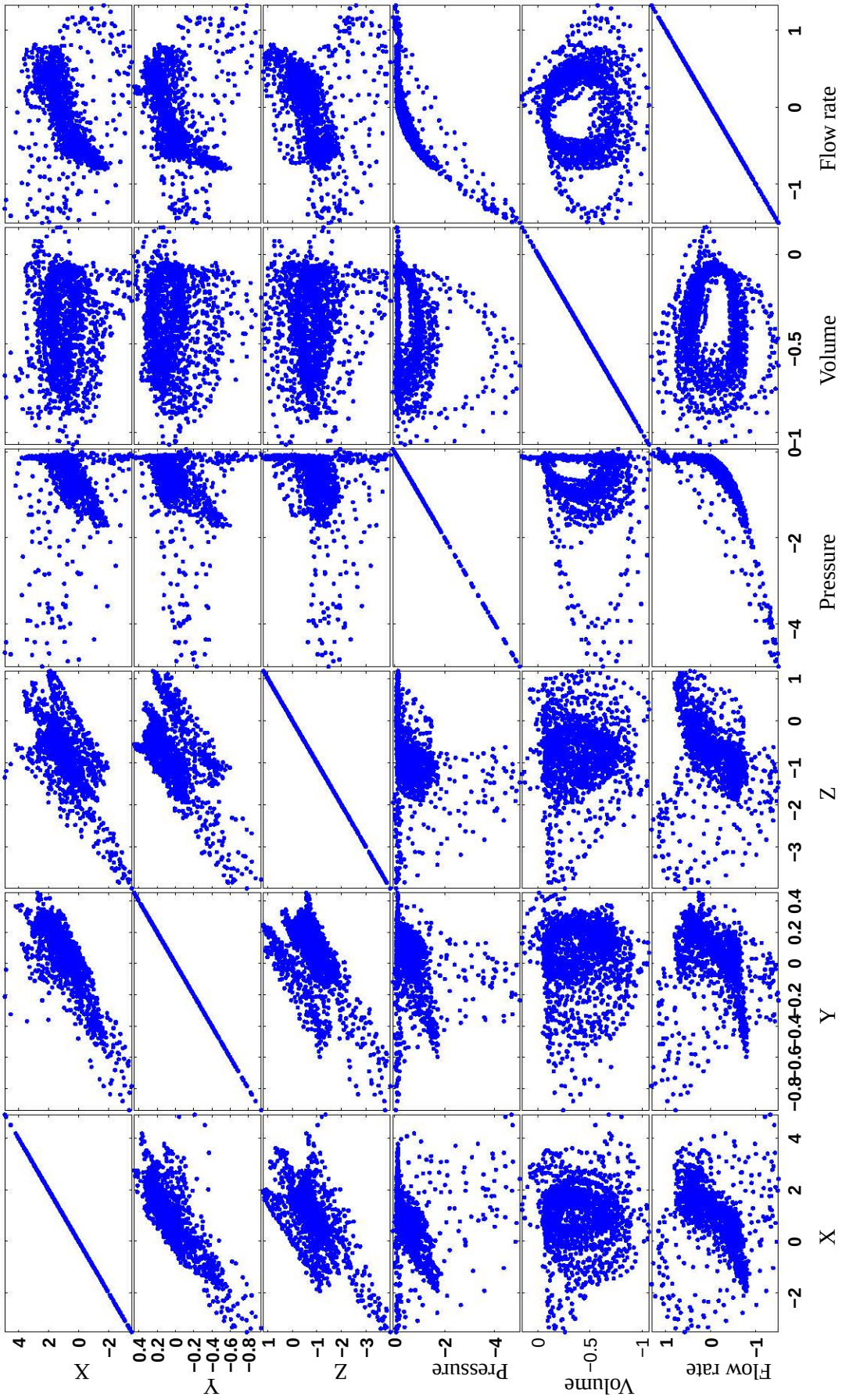

Fig. 6.19: An example of the scatter plot of the measured data for subject 1 in upper test.

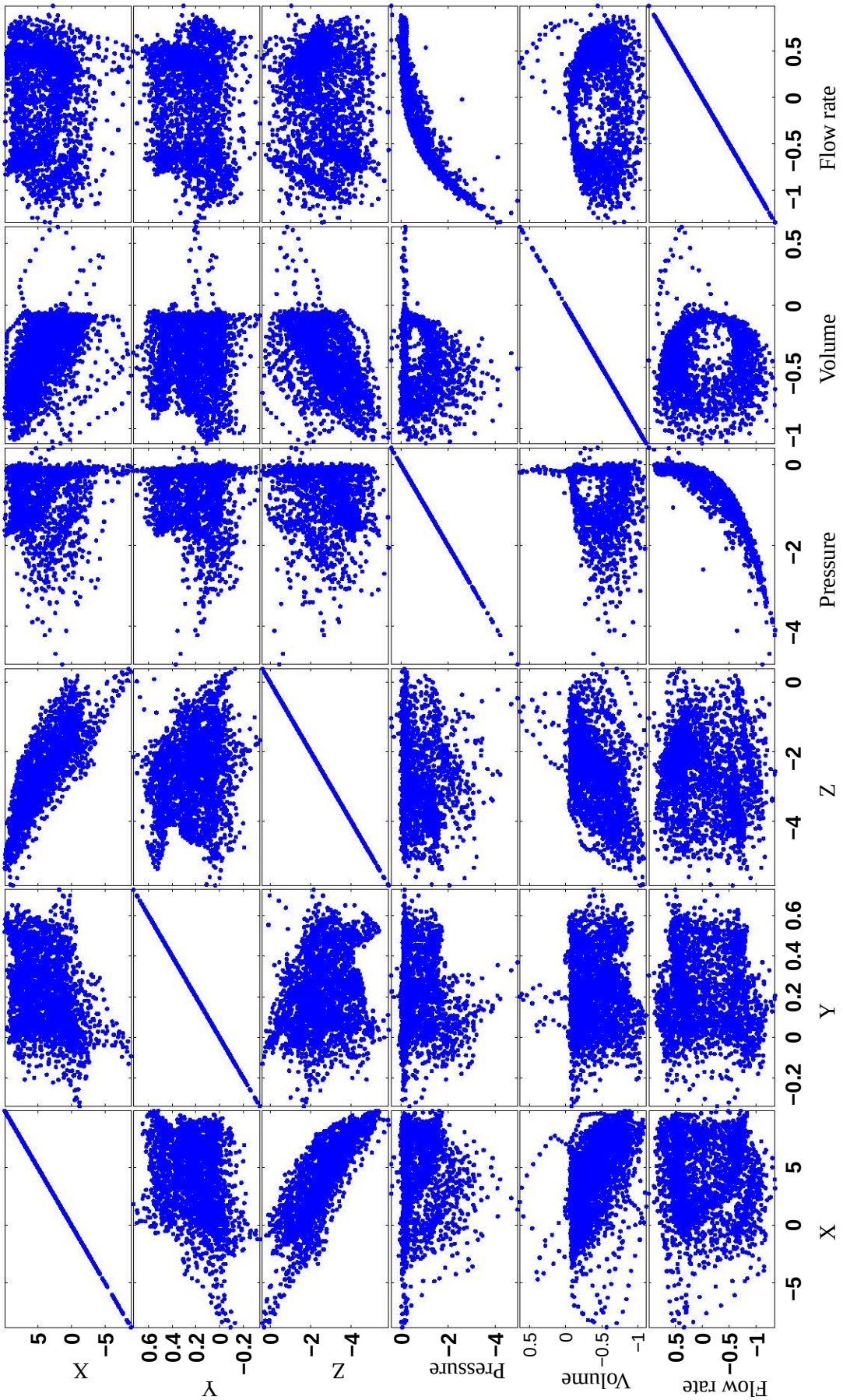
X
Y
Z
Pressure
Volume
Flow rate

In contrast to a scatter plot, which graphically depicts the relationship between two data series, correlation analysis expresses this same relationship using a single number. The correlation coefficient is a measure of how closely related two data series are. In particular, the correlation coefficient measures the direction and extent of linear association between two variables. A correlation coefficient can have a maximum value of 1 and a minimum value of -1. A correlation coefficient less than 0 indicates a negative linear association between the two variables i.e. when one increases the other decreases.

Figure 6.21 represents the correlation coefficients between the variables acquired for subject 1 performing (a) the upper test and (b) lower test. Comparing the coefficient of correlation of the Polaris variables, one might notice that highest linear correlation involved the X movement with the Y and Z movement. Concerning the Spirometer variables, the highest coefficient of correlation was between the pressure and flow.

As conclusions, the Spirometer signals that can be considered as input to the system are flow and pressure. From the analysis performed previously, it was found that the pressure signals have more noise than the flow signals. Moreover, this latter is more correlated to the Polaris data than the pressure signals, especially with X direction. Accordingly, only the flow and X motion signals will be used as an input and output in the identification process of the lung.

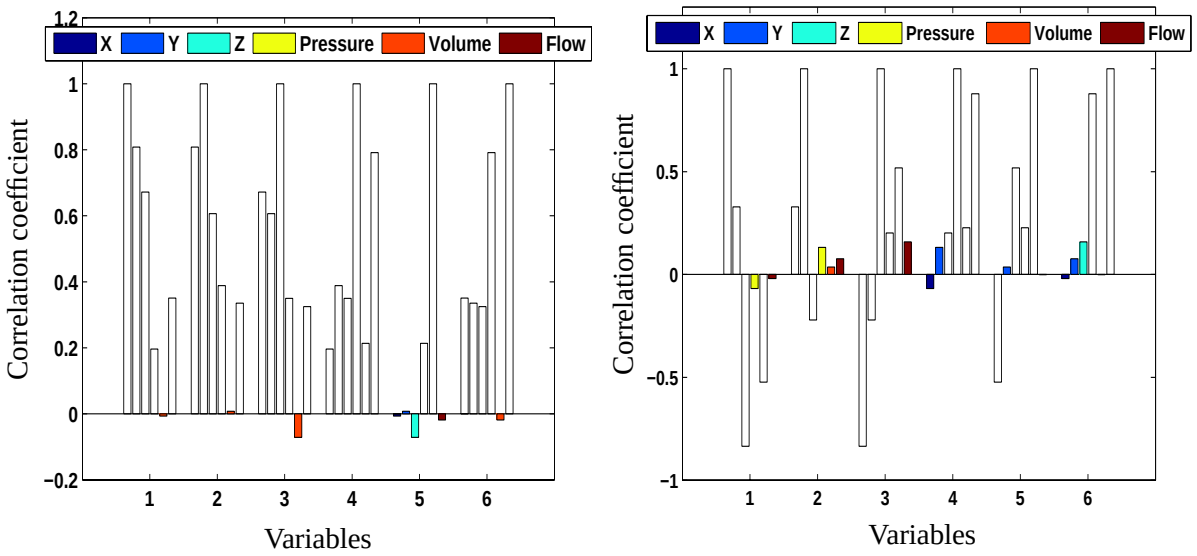

Fig. 6.21: Coefficient of correlation comparison for (a) upper test and (b) lower test.

6.4 Simulation model of respiratory motion

An identification experiment was established previously, and the measurement data from Spirometer and Polaris system were acquired, pre-processed and analysed. One of the outcomes of the latter is that the relevant signals that can be used for respiratory motion modelling and prediction are the breathing flow and the external markers motion in X direction. Consequentially, the type of models to be identified are known as SISO systems. In this work, the system in question is the lung, where the observable signal (i.e. system output), represent the markers position, and while the signal (referred to as input), which drives the system, is the breathing flow.

The disturbances, such as high frequency noise and low frequency drift, are not considered here, since the signals were filtered prior to the identification process. A set of candidate models including linear and bilinear models structures, autoregressive with exogenous variables (ARX) and bilinear autoregressive with exogenous variables (BARX) were compared. These two models structures are specified by the Equations 6.4.1 and 6.4.2 respectively. Note that an additional parameter d was added to both models to account for the static drift between the input and the output. The ARX model structure is given by the following equation:

$$y_k = \sum_{i=1}^{na} -a_i y_{k-i} + \sum_{i=1}^{nb} b_i u_{k-i} + d + e_k \tag{6.4.1}$$

While the BARX model structure is described as follows:

$$y_k = \sum_{i=1}^{na} -a_i y_{k-i} + \sum_{i=1}^{nb} b_i u_{k-i} + \sum_{i=1}^{nb}\sum_{j=1}^{na} \delta_{ij}\eta_{ij} u_{k-i} y_{k-j} + d + e_k \tag{6.4.2}$$

where δ_{ij} denotes the Kronecker δ-function for which

$$\delta_{ij} = \begin{cases} 1 & \text{if } i = j, \\ 0 & \text{otherwise.} \end{cases}$$

Several model orders have been considered, including second and third orders. The second order choice was the result of knowledge gained from the analysis of the breathing motion in Chapter 4. While the third order models are used here to see whether they can give a better results. Notice that for the bilinear term, only the data with same time shift was considered (see Equation 6.4.2). The identification process starts by removing the mean value from the input and output signals. Then, the same optimisation technique as in Chapter 5 was applied. The stability of the estimated system is satisfied by constraining the parameters of the denominators (a_i), such that in Chapter 5.

A simulation study was carried out to estimate a model for each subject's respiration, acquired during the

two tests. The models obtained were then validated and compared using the MASE criterion, and results for both tests are depicted in Table 6.2. Note that the best results in term of MASE criterion for each subject and for the modelling and the validation sets, are indicated in bold and underlined. Assessing the results of Table 6.2, It can be noticed that the performance of the applied models for the upper test are considerably better than the ones in the lower test. This is mainly due to the poor quality of the flow measurement acquired in the lower test compared to the ones obtained in the upper test.

Considering the modelling results of the upper test data, one might notice that the accuracy of the considered models is different from one subject to another and within the assessed models. In terms of modelling and validation performances, it was found that the subjects 6, 7, 8, 11, and 13, have the largest MASE compared to the rest of subjects. The MASE in modelling stage was near/higher than 1 mm for the five above subjects, while the mentioned quantity was less than 1 mm for the other subjects.

It is important to mention that the models that consider only a single numerator parameter such as ARX(2,1), ARX(3,1), BARX(2,1,1), and BARX(3,1,1) have the larger MASE for modelling and validation compared to the other models, and for the overall subjects. In order to find out, which is the best model structure, is suitable for the acquired data, a comparison between the model performances has been made. By examining the linear models, it was observed that the best model structure was ARX(2,2), which performs better in 6 subjects followed by ARX(3,2) in 4 subjects and ARX(3,3) in 2 subjects. On the other hand the bilinear models structure BARX(2,2,2) and BARX(3,3,2) has the lowest MASE error for 4 subjects, then comes BARX(3,2,1), BARX(3,2,2), and BARX(3,3,3) for 3 subjects. It can be deduced from this comparison that the second order linear model ARX(2,2) is the best model for such data. For the lower test data, the best modelling performance was given by the model ARX(2,2) with 3 subjects for linear model sets, and BARX(2,2,2), BARX(3,3,1), and BARX(3,3,2) with 3 subjects, for the bilinear sets.

An illustration of the modelling and validation performances of the ARX(2,2) and BARX(2,2,2) models applied to data of subject 1 carrying out the upper test is shown in Figure 6.22. Note that the input-output signals were normalised to fit on the same graph. While in the modelling stage, the both models achieved a MASE of 0.37 mm, in the validation stage the ARX(2,2) and BARX(2,2,2) models replicate the data with a MASE of 0.90 mm and 0.96 mm, respectively. In the last 150 samples of the validation set the amplitude of the input signal has increased and delay between the input and out signals was noticed. This latter has generated a large simulation error. In Overall, both models perform well the experimental data; however, any changes in the input or output signals can lead to a large simulation error. A way to deal with these changes is to use gating based audio and video instructions to limit the range of the motion amplitude and frequency or use an adaptive model that can take into account these changes.

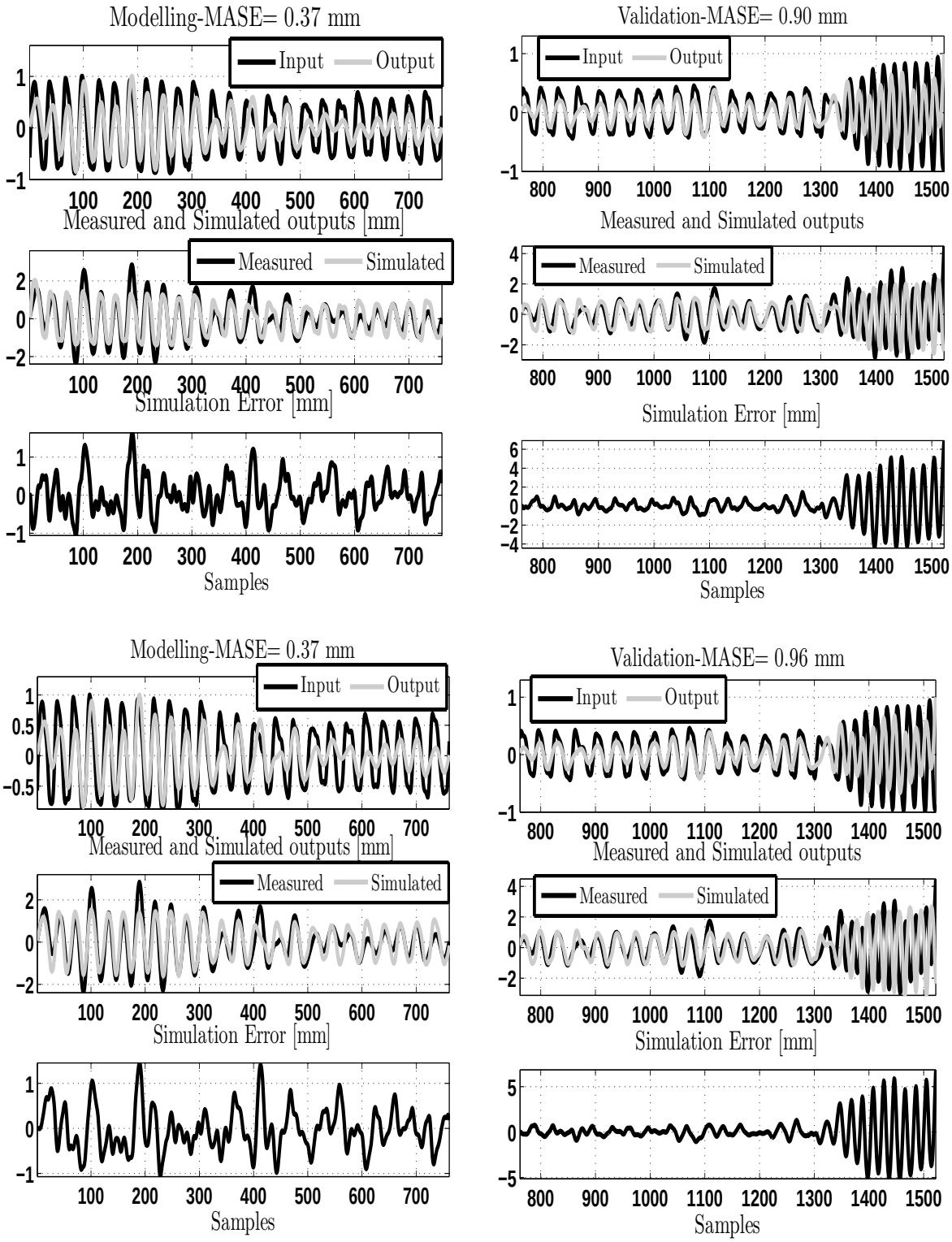

Fig. 6.22: The modelling and validation performances of the ARX(2,2) model (top) and BARX(2,2,2) model (bottom) applied to subject 1 for the upper test.

Tab. 6.2: Models comparison for both upper and lower tests (the best results are indicated in bold and underlined).

Model Structures And Orders	The Upper And Lower Tests	Subjects																									
		1		2		3		4		5		6		7		8		9		10		11		12		13	
		MASE [mm]		MASE [mm]		MASE [mm]		MASE [mm]		MASE [mm]		MASE [mm]		MASE [mm]		MASE [mm]		MASE [mm]		MASE [mm]		MASE [mm]		MASE [mm]		MASE [mm]	
		Mod.	Val.	Mod.	Val.	Mod.	Val.	Mod.	Val.	Mod.	Val.	Mod.	Val.	Mod.	Val.	Mod.	Val.	Mod.	Val.	Mod.	Val.	Mod.	Val.	Mod.	Val.	Mod.	Val.
ARX(2,1)	Up	0.38	0.94	0.51	**0.91**	0.55	1.05	0.21	0.73	0.48	0.85	1.03	1.56	0.99	1.27	1.08	1.78	0.55	0.90	0.61	1.24	1.06	1.29	0.44	1.01	1.05	1.55
	Down	1.58	1.68	1.93	2.48	0.94	1.69	0.85	1.25	1.03	1.62	1.63	2.76	2.65	3.12	2.32	2.78	1.32	2.49	1.71	4.03	2.29	2.47	**1.43**	2.31	1.16	2.20
ARX(2,2)	Up	**0.37**	0.90	**0.41**	0.94	**0.50**	1.04	**0.20**	0.74	0.48	0.87	1.00	1.53	**0.97**	1.25	**0.84**	1.39	0.52	0.84	0.59	1.28	0.99	1.29	0.43	1.00	1.03	1.48
	Down	1.57	1.71	1.67	**2.41**	0.86	1.68	**0.83**	1.24	1.03	1.57	1.46	2.23	**2.20**	2.63	2.30	3.46	1.17	2.39	1.66	3.74	2.16	2.09	**1.43**	**2.28**	1.16	2.11
ARX(3,1)	Up	0.54	**0.70**	0.66	1.01	1.05	**0.90**	0.43	**0.66**	0.72	0.94	1.03	1.48	1.68	3.00	1.16	1.89	0.98	1.53	0.61	**1.23**	1.63	1.26	1.03	1.14	0.97	1.77
	Down	1.57	**1.62**	2.53	3.87	1.53	–	0.90	**1.20**	1.43	2.04	3.16	4.67	3.13	3.29	2.47	3.47	2.24	2.84	2.32	5.95	2.48	2.98	2.57	4.65	1.91	2.57
ARX(3,2)	Up	**0.37**	0.98	0.50	0.99	0.58	1.10	0.25	1.59	0.56	0.90	0.99	1.51	**0.97**	1.25	0.85	1.36	0.64	0.97	**0.57**	1.28	1.16	1.23	0.48	1.09	**0.93**	1.59
	Down	1.57	1.67	2.60	3.51	1.17	2.13	0.86	**1.20**	1.94	3.57	2.07	3.33	3.00	3.46	2.19	4.18	1.59	2.76	1.75	4.24	2.39	2.77	2.45	6.98	1.63	2.15
ARX(3,3)	Up	**0.37**	0.82	**0.41**	0.98	0.60	1.11	0.21	0.74	0.48	0.86	1.02	1.48	1.08	1.36	0.85	1.33	0.47	**0.76**	0.60	1.32	1.14	1.27	0.45	1.02	0.97	1.47
	Down	1.56	1.64	1.69	2.51	1.07	1.93	**0.83**	1.25	1.04	1.56	1.43	2.44	3.09	3.86	1.78	**2.67**	1.12	2.30	1.69	4.23	2.08	2.08	1.59	2.70	1.18	2.38
BARX(2,1,1)	Up	0.39	0.94	0.81	0.98	0.62	1.13	0.23	0.76	0.48	0.84	1.04	1.60	1.01	1.30	1.08	1.78	0.65	0.97	1.52	2.19	1.03	1.31	0.42	1.02	1.05	1.56
	Down	1.61	1.71	**1.66**	2.44	1.07	1.85	0.93	1.25	1.93	1.99	1.53	2.77	2.40	2.72	2.43	3.47	2.34	3.58	2.59	**3.59**	2.30	2.44	1.88	2.53	1.17	2.63
BARX(2,2,1)	Up	**0.37**	0.90	0.42	0.94	0.56	1.06	0.21	0.74	0.48	0.84	**0.97**	1.48	0.98	**1.22**	1.19	1.49	0.54	0.84	0.62	1.26	1.04	1.30	0.44	**0.99**	1.06	1.50
	Down	1.57	1.71	1.71	2.50	0.93	1.67	0.84	1.25	**1.01**	1.67	1.61	2.64	2.21	2.64	2.16	3.07	1.21	2.32	1.67	3.75	2.11	**2.07**	1.52	2.47	**1.13**	2.23
BARX(2,2,2)	Up	**0.37**	0.96	**0.41**	0.94	0.53	1.05	0.21	0.75	**0.47**	**0.82**	0.98	1.55	0.98	1.30	1.11	1.60	0.48	0.88	0.62	1.24	**0.97**	1.31	0.43	1.04	1.07	1.57
	Down	**1.55**	1.72	1.67	**2.41**	**0.81**	**1.54**	0.84	1.25	**1.01**	1.68	1.43	2.02	2.88	3.08	2.08	3.10	1.10	2.34	1.67	3.72	2.15	2.08	1.44	2.34	1.15	2.13
BARX(3,1,1)	Up	0.53	–	0.77	0.96	1.21	3.26	0.34	0.80	0.58	0.98	1.14	1.77	1.68	3.02	1.24	1.88	1.03	1.50	0.96	1.54	1.59	1.32	1.02	1.17	0.97	1.71
	Down	2.41	2.10	2.54	3.86	1.76	6.27	0.93	1.34	1.96	3.56	2.95	4.52	3.09	3.33	2.31	-	3.50	3.80	2.31	8.75	2.48	2.80	2.60	5.04	1.48	2.49
BARX(3,2,1)	Up	**0.37**	0.80	0.43	0.93	0.55	1.06	0.26	0.73	0.51	0.91	**0.97**	1.49	1.24	1.78	0.86	1.32	0.54	0.88	0.66	1.26	1.18	1.22	0.44	1.02	**0.93**	1.58
	Down	1.59	1.65	2.55	3.74	1.07	2.11	**0.83**	1.22	1.39	6.49	1.59	2.69	2.96	3.71	2.26	-	1.42	2.63	1.76	4.35	2.46	2.79	1.77	3.00	1.53	2.26
BARX(3,2,2)	Up	0.38	0.84	0.49	1.00	0.58	1.06	0.24	0.85	0.48	0.91	1.01	**1.44**	1.27	1.61	0.86	**1.30**	0.45	0.85	0.63	1.25	1.15	**1.17**	0.43	1.01	**0.93**	1.57
	Down	2.24	-	2.56	3.59	1.13	2.26	0.85	1.22	1.47	2.75	2.08	3.38	2.59	2.00	2.20	-	1.43	2.60	1.77	4.26	2.43	2.89	1.63	2.54	1.54	2.57
BARX(3,3,1)	Up	**0.37**	0.81	0.42	0.96	1.08	1.78	**0.20**	0.74	0.48	0.87	1.03	1.58	1.18	1.58	0.85	1.35	0.49	0.79	0.60	1.24	1.12	1.27	0.44	1.00	0.98	1.48
	Down	**1.55**	1.64	1.71	2.63	1.14	2.06	0.85	1.22	1.04	1.56	1.44	2.51	3.05	-	1.80	2.89	**1.09**	**2.29**	**1.60**	3.91	2.08	2.10	1.67	2.50	1.17	2.37
BARX(3,3,2)	Up	**0.37**	0.80	0.46	0.97	1.01	1.52	0.21	0.75	0.51	0.90	0.98	1.50	1.19	1.44	**0.84**	1.34	**0.45**	0.78	0.60	1.27	1.16	1.34	**0.40**	1.00	0.98	**1.46**
	Down	1.56	1.65	1.91	2.63	0.97	1.74	**0.83**	1.28	1.02	1.59	**1.32**	1.83	3.09	3.51	**1.75**	2.85	1.35	2.51	1.83	4.26	2.08	2.13	1.67	2.57	1.18	2.30
BARX(3,3,3)	Up	0.39	**0.70**	0.53	0.99	0.75	1.13	0.21	0.74	**0.47**	0.85	1.00	1.49	1.08	1.34	**0.84**	1.33	0.59	1.00	0.60	1.24	**0.97**	1.34	0.43	1.01	0.97	**1.46**
	Down	**1.55**	1.64	1.83	2.63	1.01	1.91	0.85	1.26	1.04	**1.55**	1.57	**1.77**	2.60	**1.78**	1.79	3.18	1.11	2.37	1.82	4.18	**2.05**	2.95	1.50	2.66	1.37	2.58

6.5 The impact of using a 'virtual' input signal

The modelling technique introduced in Chapter 5 was used here in order to assess the effect of generating a virtual input signal from the respiratory data rather than using a physical input signal. The performance of the BARX(2,1,1) model for both virtual and physical inputs using the respiratory motion of the different subjects for the two tests has been compared, and results are shown in Table 6.3. It is clear from the latter that using a virtual input signal gives a better result form modelling and validation of the subjects trajectories.

An illustration of the modelling and validation procedures of the BARX(2,1,2) model applied to measurement data from subject 7 in the upper test is given in Figure 6.23. The MASE of BARX(2,1,2) model was found to be 0.87 mm and 0.59 mm for the modelling and validation sets respectively. Despite the large simulation error in the modelling step, which is due to the sudden change in the motion amplitude, the use of a virtual input signal has shown good overall modelling and simulation performances.

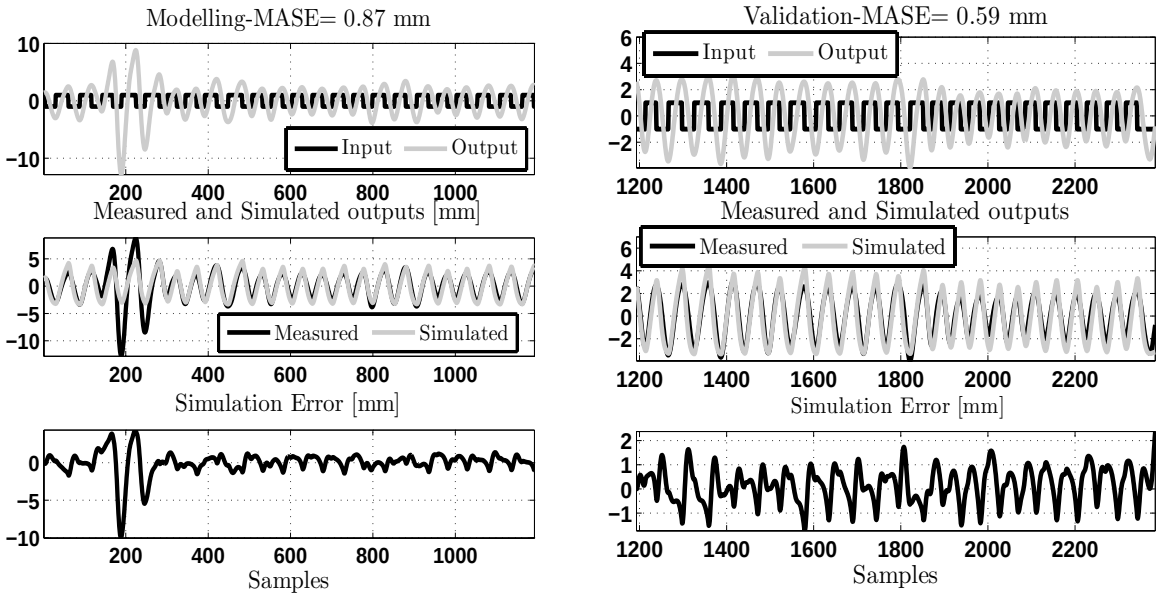

Fig. 6.23: An example of modelling and validation performance of the BARX(2,1,2) model, using a virtual input, applied to subject 7 for the upper test.

Tab. 6.3: The performance of the BARX(2,1,1) model based virtual input applied to the Polaris respiratory motion data.

The Used Input Signals	Model Structures And Orders	The Upper And Lower Tests	Subjects																									
			1		2		3		4		5		6		7		8		9		10		11		12		13	
			MASE [mm]		MASE [mm]		MASE [mm]		MASE [mm]		MASE [mm]		MASE [mm]		MASE [mm]		MASE [mm]		MASE [mm]		MASE [mm]		MASE [mm]		MASE [mm]		MASE [mm]	
			Mod.	Val.	Mod.	Val.	Mod.	Val.	Mod.	Val.	Mod.	Val.	Mod.	Val.	Mod.	Val.	Mod.	Val.	Mod.	Val.	Mod.	Val.	Mod.	Val.	Mod.	Val.	Mod.	Val.
Virtual	BARX(2,1,1)	Up	0.43	0.50	0.21	0.39	0.46	0.47	0.11	0.21	0.26	0.28	1.50	1.62	0.87	0.59	0.60	0.75	0.34	0.72	0.45	0.63	0.78	0.70	0.28	0.42	0.33	0.50
		Down	2.29	–	0.74	0.78	0.55	1.34	0.30	0.34	0.44	0.55	0.71	0.63	1.07	0.89	0.98	1.47	0.97	0.91	0.99	0.88	1.38	1.28	0.66	0.79	0.67	1.20
Physical	BARX(2,1,1)	Up	0.39	0.94	0.81	0.98	0.62	1.13	0.23	0.76	0.48	0.84	1.04	1.60	1.01	1.30	1.08	1.78	0.65	0.97	1.52	2.19	1.03	1.31	0.42	1.02	1.05	1.56
		Down	1.61	1.71	1.66	2.44	1.07	1.85	0.93	1.25	1.93	1.99	1.53	2.77	2.40	2.72	2.43	3.47	2.34	3.58	2.59	3.59	2.30	2.44	1.88	2.53	1.17	2.63

6.6 Online predictive tracking of respiratory motion

The online predictive tracking of breathing induced tumour motion has been achieved by different time-series based models using either internal or external markers motion data (see Table 3.2). Spirometry has been used as a respiratory surrogate to monitor patient's lung volume in different steps of the RT (see for example [Hoisak et al. 2006, Kubo and Hill 1996]). However, it has never been used for predictive tracking of the breathing motion. In this section, an online predictive tracking method of respiratory motion based on flow-rate and on external markers signals is proposed. This approach was motivated by the satisfactory modelling performance carried out in Section 6.4 and the simplicity of the tools that can be used such as Spirometer and video tracking system.

The proposed approach consists in modelling the external markers position online for a time period and then predict h_p-step-ahead. The modelling and prediction were both based on the RLS algorithm with forgetting factor described by the Equations 5.5.4-5.5.6. The forgetting factor used in this algorithm was $\lambda = 0.97$. In the modelling stage the parameters of the model were estimated by minimising the MSPE cost function defined by 5.3.1. This consisted in minimising the error between the measured and the hp-step-ahead prediction of the model output.

A test was carried out in the CTAC laboratory consisting of acquiring in real-time both the flow-rate and external markers position using a Spirometer and the developed video camera system, and predicting short time ahead in advance. The number of predicted samples considered was 2, which is equivalent to 0.2s for an acquisition frequency of 10Hz. The model structure used for modelling and prediction was the ARX(2,2) as the latter was found to be the appropriate model for such measurement data. The model parameters were estimated online during the first 100 seconds, and then these parameters were used for prediction.

Figure 6.24 shows the predictive tracking performance of the developed approach for 0.2 s ahead prediction. The latter shows both the comparison between the real motion trajectory and the predicted one as well as the prediction error. The latter was quantified by means of the RMSE criterion which was found to be 0.42 mm. Comparing the real and the predicted signals one might notice that the motion prediction was able to follow the respiratory motion including motion changes. This approach can be easily implemented in clinical environment as it requires only a simple tracking devices such as video camera and a Spirometer.

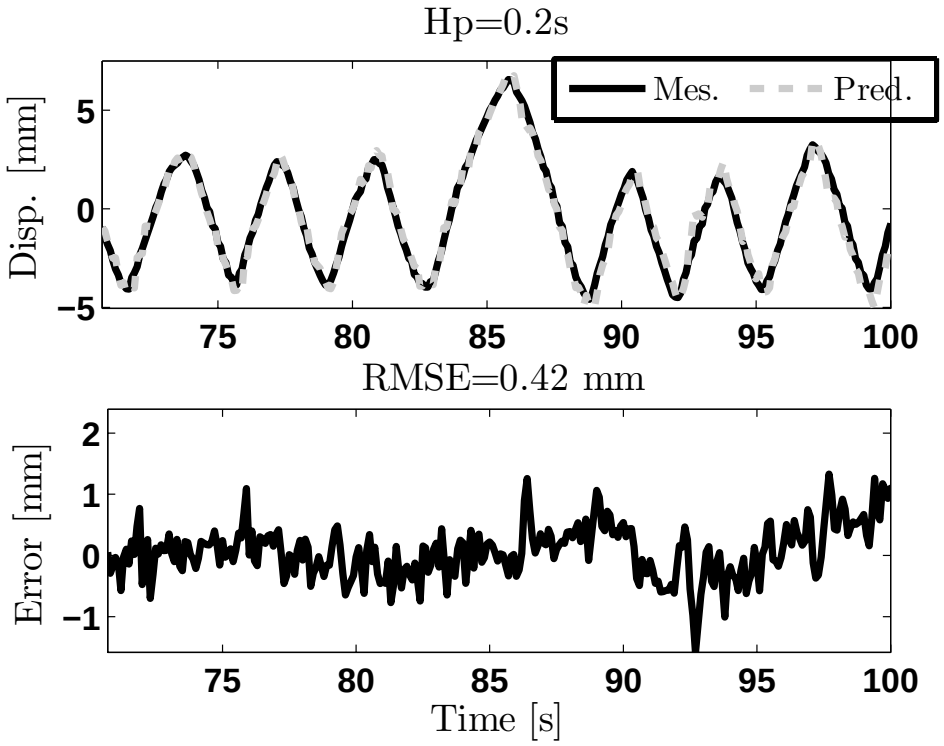

Fig. 6.24: Illustration the online prediction performance for 0.2s ahead.

6.7 Conclusions

This chapter has described the modelling, simulation and predictive tracking of the respiratory motion based on two surrogates breathing signals namely flow rate and external chest marker. An experiment was designed and carried out involving 13 healthy subjects. The aim of the latter was to obtain some biological and external markers data in order to investigate if there is any benefit of combining motion information with biological signals to improve motion simulation and prediction. The acquired data were pre-processed and statistically analysed prior to their use. A comparison between linear and bilinear models with up to third order models was performed. This comparison has shown that the second order linear model is more appropriate for the acquired data.

The impact of using a virtual input signal instead of physical one was also assessed. The outcome of the latter was that using the former gives better results in term of the used assessment criterion. A new technique for predictive tracking of respiratory motion was introduced. This was based on acquiring both the flow rate and external markers in real time and a second order linear model. The parameters of the model were estimated online by mean of RLS with a forgetting factor that minimising hp-steps-ahead prediction error. The performance of this technique was tested in practice by involving the acquisition of the flow rate and external chest markers in real time. The acquisition of the latter was performed by

means of a video tracking system developed within the MAESTRO project.

In contrast to the previous contributions that use only the respiratory surrogate motion, this work has proven that the modelling, simulation and prediction of the respiratory motion can be achieved by considering both flow rate and external chest markers data. By considering the flow measurement as input signal and external chest markers motion as output signal, it is possible to build a model of the respiratory motion that can be used to simulate this latter. In the case of regular breathing motion, the modelling approach was found to achieve a simulation error less than 1 mm for most of the subjects. Compared to the results of the previous prediction algorithms presented in Chapter 3, the introduced strategy has given a good prediction performance for h_p=0.2 s. However, the modelling and prediction results can be improved by ameliorating the data acquisition process and synchronising the input output signals.

Chapter 7

Predictive tracking for respiratory surrogate motion compensation

7.1 Introduction

Chapter 3 has discussed the problem of the delay in EBRT and reviewed different time-delays reported in the literature. This has prompted the current research to consider tumour motion prediction. Therefore, two new approaches to predict tumour motion described by external markers are presented. While the first approach is based on an adaptive bilinear model, the second method is based on a polynomial model. A new comparative study between different prediction approaches involving the same respiratory data has also been carried out. The latter has involved the maximum prediction error as a new assessment criterion in the context of ART. Some of the algorithms developed in MATLAB were modified by the author to enable their implementation in embedded $MATLAB^{®}$ functions within Simulink to be used in clinical application.

A variety of approaches to accommodate the uncertainties caused by respiration has been discussed in chapter 2. The MAESTRO Coventry team has introduced a strategy-based feedback control scheme developed by MAESTRO co-workers [Skworcow et al. 2007, Skworcow 2008, Paluszczyszyn 2008]. The approach was initially tested on simulation using a predictive bilinear feedforward filter. The whole approach involves a controlled PSS to automatically reposition the patient in order to keep the moving tumour in the path of the radiation beams. The PSS-based approach is potentially able to compensate for 3D motion of the tumour, whilst a MLC-based approach is only able to compensate for 2D motion [D'Souza et al. 2005]. Furthermore, the approach only requires basic modification of the currently available PSS technology and retains the existing gantry-based treatment machine, which is less expensive

and a more efficient option compared to the robotic-arm-based approach that needs a new machine configuration. In the above mentioned approach a model of the PSS was required. Work has been carried out in this chapter toward achieving a simulation model of the PSS. The developed motion compensation strategy was demonstrated in clinical environment at the UHCW.

The schematic of the proposed strategy is illustrated in the following Figure 7.1.

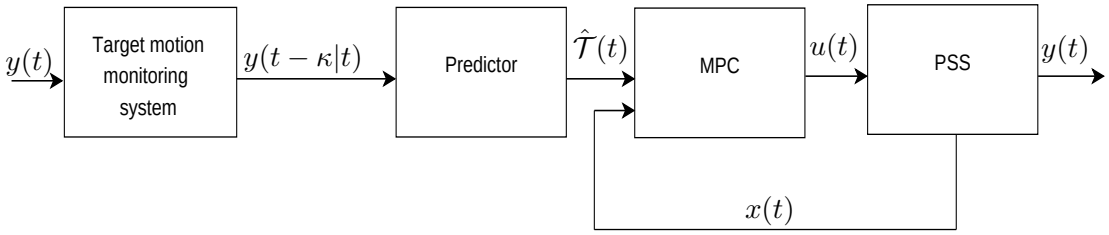

Fig. 7.1: Schematic of the proposed MPC control system with predicted reference and state-feedback.

Where $y(t)$ is the actual tumour position at time t while $y(t-\kappa|t)$ represents the most recent measurement of target position available at time t, $\hat{\mathcal{T}}(t)$ is a vector of predicted target positions, $y(t)$ and $u(t)$ are PSS output and input, respectively, and $x(t)$ denotes the state variable feedback.

The second section of this chapter presents the investigation of different prediction algorithms. This is followed by a Section of PSS modelling to develop an appropriate simulation model to represent the actual PSS behaviour. The evaluation of the prediction algorithm combined with the control system is carried out in Section 7.3. Section 7.5 shows some clinical assessments of the newly introduced compensation strategy which has been carried out at the UHCW. Conclusions are given in the last section.

7.2 Respiratory motion prediction

The sequential actions corresponding to position acquisition, data processing and time response of the PSS generate a delay between actual change in tumour position and the action taken to accommodate, hence compensate this change [Sharp et al. 2004]. In addition to such widely recognised issue, it should be noted that the dynamic response of the equipment used to either track or compensate for the tumour motion is also influencing the speed of response from the image acquisition to the machine reaction. For this reason, the estimated position of the tumour must be quantified and predicted in advance. The amount of the prediction horizon (h_p) must be at least equivalent to the total delay of the systems involved in the compensation strategy. Figure 7.2 illustrates different delays in the proposed control scheme. Delays i, j and k denotes data processing time of each subsystem, while delay l denotes time required for the PSS

to reach a desired position for a given load and reference signal conditions. In this case the value of h_p to be predicted should be at least equal to $i + j + k + l$.

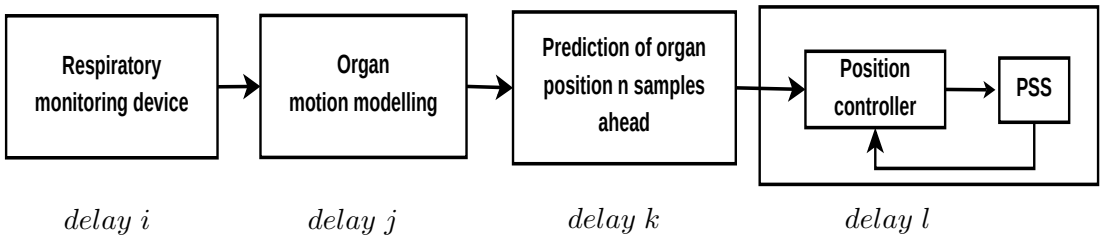

Fig. 7.2: Illustrating different delays in the proposed control scheme.

Various proposals have been put forward for predicting such motion, see chapter 3. In this work, two motion prediction approaches namely BTV and sliding polynomial models have been proposed. These methods were compared to the 'in-house' developed approaches, particularly IMM, KF assuming CV and CA [Putra et al. 2008] and two structures of NN; a TSP MLP and GRNN, with four different training algorithms [Goodband and Haas 2008]. A full description of IMM, KF and NNs based algorithms is given in Appendix C. As opposed to existing studies, all algorithms are compared using the same data and a new criterion is introduced to demonstrate potential issues with the various algorithms. Some of these approaches will be used to generate predicted reference trajectories that are suitable for a receding horizon MPC scheme. The predicted trajectories are then utilised to determine an optimal control that is calculated based on a minimisation of future predicted tracking errors. The following subsections will be devoted to the description of the BTV and sliding polynomial algorithms.

7.2.1 Bilinear model-based prediction

In Chapter 5, an adaptive approach of the bilinear model called BTV model has demonstrated a great ability to track markers based respiratory motion. A RLS algorithm with fixed forgetting factor that minimise one step ahead prediction error has been used to estimate online the model parameters. In order to predict a h_p steps ahead, the RLS algorithm was modified by minimising h_p steps ahead instead. The prediction starts after a training period of 1 min to allow the convergence of model parameters to the appropriate values. A fixed forgetting factor $\lambda = 0.99$ was used. The following second order BTV model has been chosen to model the respiratory motion:

$$y_k = -a_{1k}y_{k-h_p} - a_{2k}y_{k-h_p-1} + b_{1k}u_{k-h_p} + \eta_{1k}y_{k-h_p}u_{k-h_p} + d_k \tag{7.2.1}$$

The regression model can be expressed as

$$y_{k|k-h_p} = \varphi_{k|k-h_p}\theta_{k|k-h_p}, \tag{7.2.2}$$

where $\theta_{k|k-h_p} = [a_{1k}, a_{2k}, b_{1k}, \eta_{1k}, d_k]^T$. The regressor is given by

$$\varphi_{k|k-h_p} = [-y_{k-h_p}, -y_{k-h_p-1}, u_{k-h_p}, y_{k-h_p}u_{k-h_p}, 1] \tag{7.2.3}$$

It is important to note that the frequency of breathing must be known in advance, and hence the input signal can be generated. This assumption can be realised in practice by considering an audio or audio-video gating as it was done in [George et al. 2006]. Assuming that the position of the organ is acquired in real time by the measurement tool, the steps of modelling and prediction are given as follows:

Algorithm 3 Modelling and Prediction Algorithm for BTV Model

1: **for** $t = 1{:}N$ **do**
2: The h_p steps ahead prediction is : $\widehat{y}_{k|k-h_p} = \varphi_{k|k-h_p}\theta_{k|k-h_p}$.
3: The prediction error at step k is:

$$\varepsilon_{k|k-h_p}(\theta_{k|k-h_p}) = y_{k|k} - \widehat{y}_{k|k-h_p} = y_{k|k} - \varphi_{k|k-h_p}\theta_{k|k-h_p} \tag{7.2.4}$$

4: Estimate the parameters of the BTV model:

$$\theta^*_{k|k-h_p} = \underset{\theta}{\operatorname{argmin}}\{\varepsilon_{k|k-h_p}(\theta_{k|k-h_p})\}^2 \tag{7.2.5}$$

5: Use the actual model to predict h_p steps ahead.
6: **end for**

Illustrative examples of the motion prediction for h_p={0.2s, 0.4s, 0.5s} using the BTV model are shown in Figure 7.3. In Figure 7.3, the predicted position was compared against the real position and the performance of the predictor was assessed by means of two criteria namely RMSE and 95% CI. These two criteria were defined in Section 3.4. The 95% CI criterion is used here to specify the margins to accommodate for the prediction error. It was noticed from these simulations that the two adopted criteria increase by increasing h_p. It is clear from Figure 7.3 that the large prediction errors occur during the change in the motion direction. This was also observed in the rest of the prediction algorithms.

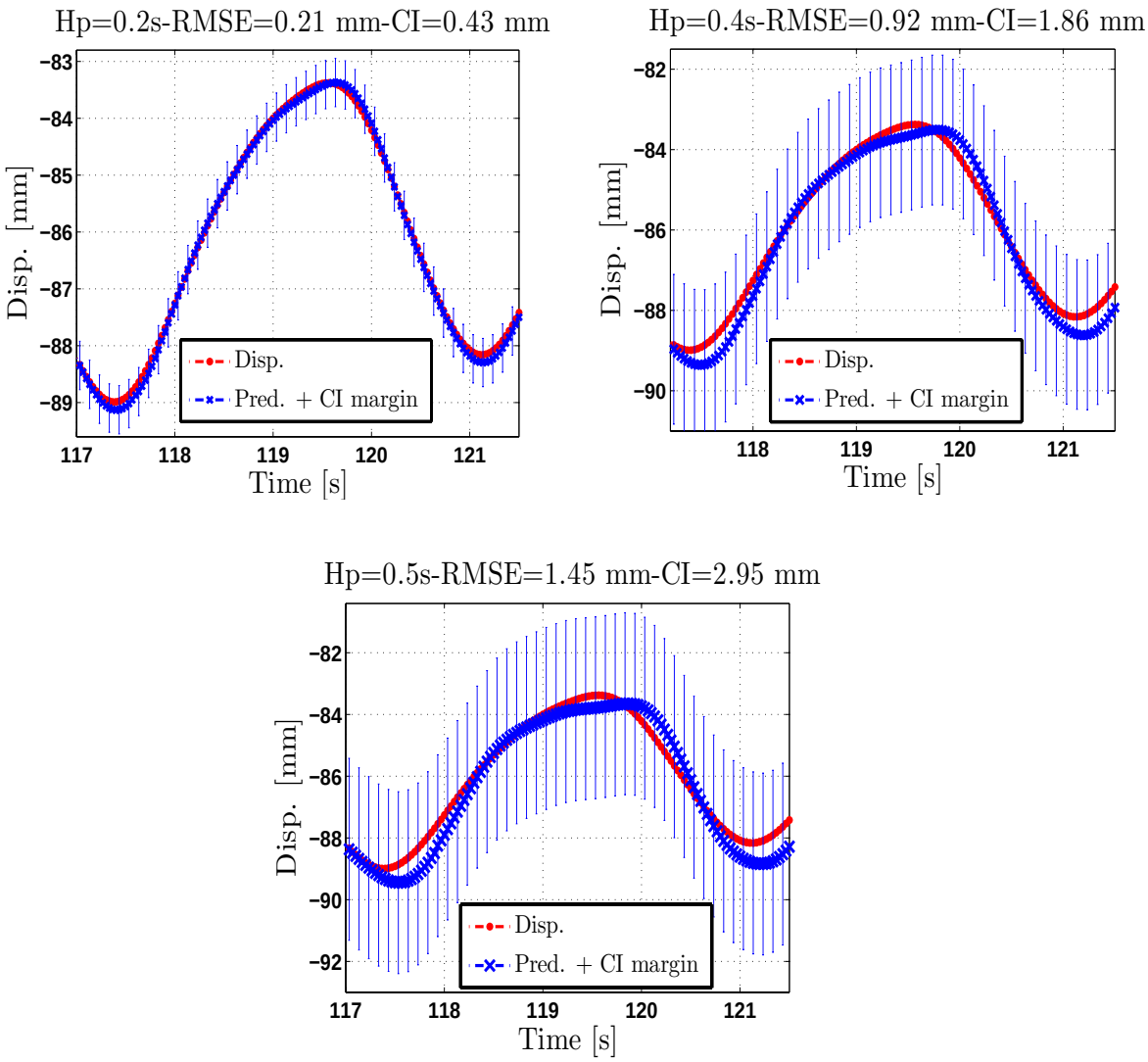

Fig. 7.3: Illustrating the prediction performance in term of 95% CI criterion as a margin to accommodate prediction errors of the BTV model using trajectory number 1 for different prediction horizons.

7.2.2 Polynomial model-based prediction

The second approach presented in this section to predict the respiratory motion online consists on a dynamic sliding window polynomial model. This technique was motivated by the satisfactory performance of the polynomial function to model respiratory cycles presented in Section 5.7. The adopted methodology for prediction was based on fitting the respiratory traces within a dynamic moving window and extract the fitting parameters of a 3^{th} order polynomial function at each sliding window position. The polynomial fitting was done by means of the LLS estimator. The size of the moving window is chosen to be the same as h_p. At each step, a polynomial function is fitted to the moving window and used then to predict in advance the required h_p.

An illustration of the motion prediction strategy for h_p=0.6s in different breathing phases is given in Figure 7.4. As shown in the latter, the polynomial prediction performs better in the linear phase compared to the phase of inhalation and exhalation. It is important to note that the first and second order polynomial function represent respectively the CV and CA models described in Appendix C.

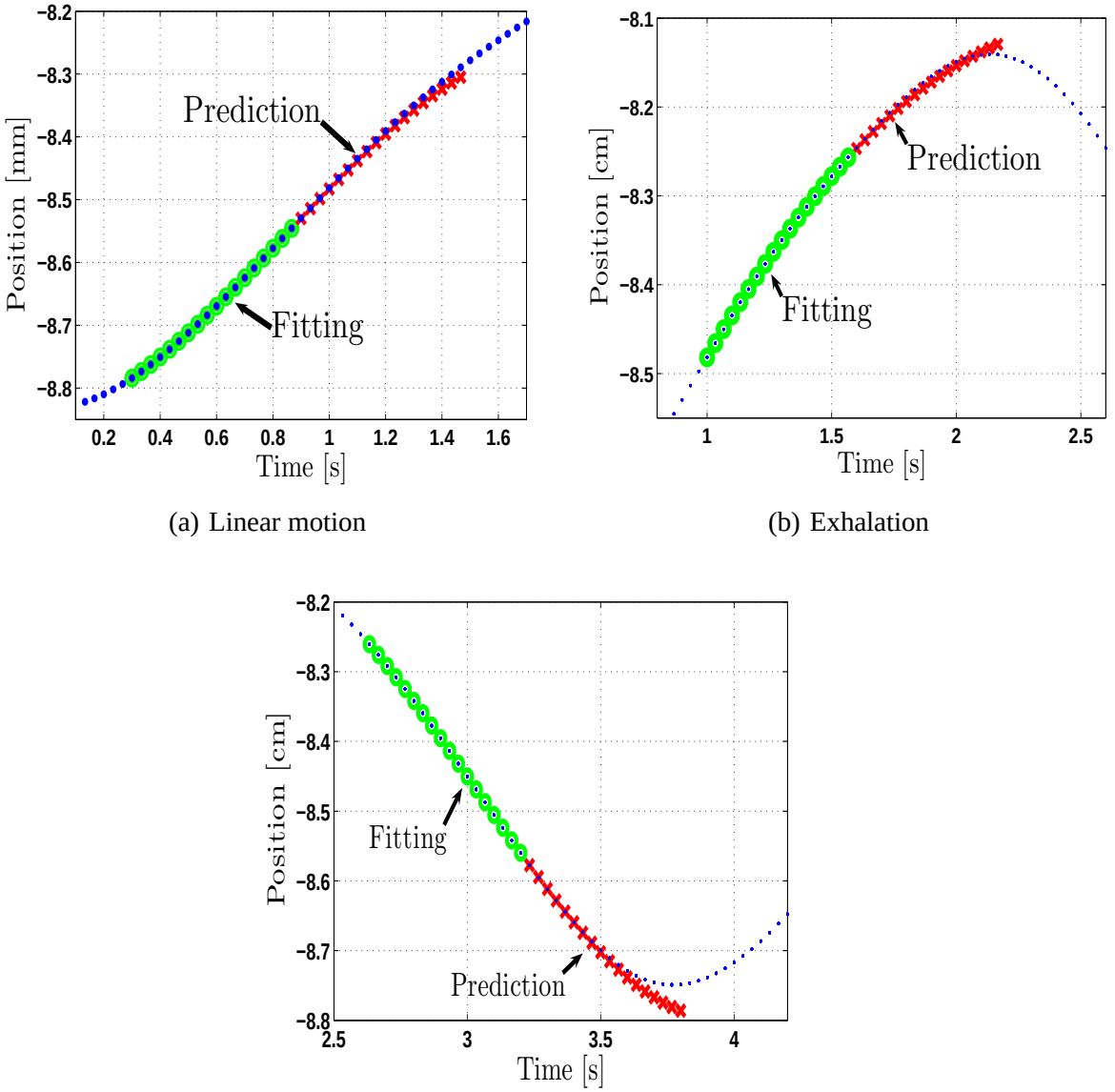

(a) Linear motion

(b) Exhalation

(c) Inhalation

Fig. 7.4: Illustrating motion prediction of 0.6s ahead for three different cases

The performance of the sliding polynomial model prediction for h_p=0.6s using different orders and sliding window sizes has been assessed on 100 respiratory traces and results are illustrated in Figure 7.5. The effect of the polynomial order has revealed that the $\overline{RMSE}$ criteria is smaller for the third and forth orders. Concerning the effect of the window size on prediction, it was concluded that the prediction error

increase with the increase of the moving window.

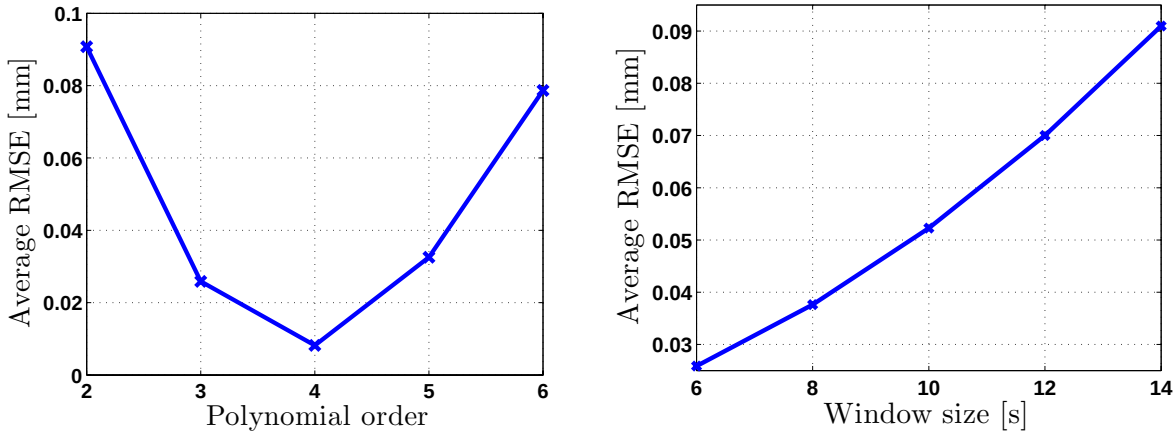

(a) The effect of the polynomial order (b) The effect of the window size

Fig. 7.5: The effect of the polynomial order and moving window size for 0.6s ahead prediction

7.2.3 Prediction comparison

In the literature, the difficulty associated with comparing the performance of several prediction algorithms is that they use either different data sets or different data within the same data set and restrict the applicability of their approaches to regular motion, which are in practice rarely achieved by patients. Further, the most widely used criterion to evaluate the performance of such prediction algorithms is the RMSE for each trajectory or the mean of the RMSE when more than one trajectory is considered. Such criteria do not, however, highlight algorithms that may fail for short periods of time and hence exhibit infrequent large errors. To account for large error, whilst at the same time preventing noise from the imaging equipment to interfere with the results, filtered measurements and predicted signals are used and then the maximum error is calculated. Moreover, in radiotherapy treatment and for safety reasons, it is very important to have a small maximum error, to avoid the radiation of healthy tissues. This has prompted the introduction of a new (in the context of ART) criteria to assess the performance of a given prediction algorithm. These criteria are based on the maximum error for each trajectory and the average of the maximum error for all trajectories.

The performance of the algorithms presented above has been assessed using the clinical data set from VCU. Results for h_p={0.2s,0.4s,0.5s,0.6s} are given in Table 7.1(a), 7.1(b), 7.1(c) and 7.1(d), respectively. The effectiveness of the algorithms is compared to the case of no prediction, i.e. the target is assumed to remain in the same position. This is equivalent to shifting the current trajectory by h_p steps ahead. Unlike the polynomial model, NNs schemes and the BTV, the Kalman CA, CV and IMM algo-

rithms require sampling the data at the same period as the prediction horizon h_p. It was found that all the predictors perform consistently, achieving a reduction of the RMSE compared to the case where no prediction is considered. In terms of RMSE criterion, the best prediction performance was achieved by the polynomial model for h_p=0.2s and the BTV model for h_p={0.4s,0.5s and 0.6s}. Similar results was found by comparing the standard deviation of the RMSE. Analysing the difference between the predicted trajectories and the actual marker position for the different predictors has highlighted that the largest errors occurred around the transition between the inhale and the exhale phases. However, significantly better accuracy could be achieved during the inhale and exhale phases. The use of prediction based NNs can result in a large prediction errors as shown in Table 7.1(a) and 7.1(b). Therefore, the algorithms based NNs were not considered in the comparison study for 0.4s and 0.6s ahead.

Tab. 7.1: Comparative study using 331 trajectories for 0.2s, 0.4s, 0.5s and 0.6s ahead prediction (the best results are indicated in bold).

(a) Prediction of 0.2s ahead

Prediction Methods	Prediction Error Criteria [mm]		
	$\overline{RMSE}$	Std. of RMSE	$\overline{\lvert e^{max}\rvert}$
No Predict.	1.29	0.51	3.00
Kalman CV	0.19	0.11	0.72
Kalman CA	0.34	0.17	1.05
IMM	0.30	0.15	0.94
BTV	0.14	0.07	0.67
Polynomial	**0.03**	**0.02**	**0.16**
CGBP	0.63	0.54	3.18
GRNN	0.77	0.16	5.25
LM	0.76	5.23	40.82
BR+CG	0.48	0.54	3.08

(b) Prediction of 0.4s ahead

Prediction Methods	Prediction Error Criteria [mm]		
	$\overline{RMSE}$	Std. of RMSE	$\overline{\lvert e^{max}\rvert}$
No Predict.	2.54	1.00	5.83
Kalman CV	0.78	0.44	2.84
Kalman CA	1.15	0.58	3.45
IMM	1.08	0.55	3.25
BTV	**0.51**	**0.23**	**2.36**
Polynomial	0.52	0.30	2.38
GRNN	1.69	0.50	4.35
CGBP	1.20	0.93	5.03
LM	1.61	8.40	66.56
BR+CG	0.97	0.78	5.66

(c) Prediction of 0.5s ahead

Prediction Methods	Prediction Error Criteria [mm]		
	$\overline{RMSE}$	Std. of RMSE	$\overline{\lvert e^{max}\rvert}$
No Predict.	3.13	1.22	7.14
Kalman CV	1.27	0.72	4.57
Kalman CA	1.70	0.87	5.04
IMM	1.62	0.82	4.80
BTV	**0.75**	**0.32**	**3.44**
Polynomial	1.19	0.68	5.29

(d) Prediction of 0.6s ahead

Prediction Methods	Prediction Error Criteria [mm]		
	$\overline{RMSE}$	Std. of RMSE	$\overline{\lvert e^{max}\rvert}$
No Predict.	3.70	1.44	8.37
Kalman CV	1.91	1.08	6.77
Kalman CA	2.35	1.19	6.81
IMM	2.25	1.14	6.55
BTV	**1.00**	**0.42**	**4.59**
Polynomial	2.28	1.31	9.81

7.2.4 Real-Time implementation of motion prediction

As the main objective of the project MAESTRO is to apply the newly proposed control strategy in clinical application, it was required to implement the PSS control system and the motion prediction in real-time. The implementation in real-time of the former was already carried out by MAESTRO co-workers, and is briefly described in [Skworcow 2008, Paluszczyszyn 2008]. This subsection will outline the real-time implementation of three motion predictors, namely Kalman CV, Kalman CA, and the IMM filter. After a brief research, it was found that an Embedded MATLAB function which is a block of Simulink environment can be utilized to generate embedded codes. The Embedded MATLAB function allows the creation of functions with a subset of MATLAB language. Once a Simulink model is simulated a function in an Embedded MATLAB Function block generates efficient *C* code. A Real-Time predictor block was built and added to the overall Simulink model of the PSS control strategy illustrated in Figure 7.1.

7.3 Model of the patient support system (PSS) movement

A short description of the PSS was given in Chapter 2. The aim of this section is to introduce a model of the PSS movement, which was built by the author through a new identification experiment carried out at the UHCW. It is important to recall that the PSS has four degrees of freedom: Forward-backward (Y-axis or longitudinal axis), left and right (X-axis or lateral axis), up and down (Z-axis or height axis) plus a rotation around Z-axis refereed to the Iso center. Note that only the motion along the three axes will be considered for modelling. There exist some PSS with built-in position controller, however, they are designed for pre-treatment patient positioning and not for patient repositioning during the treatment delivery [Brock et al. 2002]. This work will consider a standard PSS.

In practice, the PSS is operated manually using four one-degree-of-freedom ‘joysticks’ (one for each one-degree-of-freedom of the PSS), which are used to define a velocity set-point for each joint. All the joints are independently controlled by joint-level velocity servo loops, as it is classically done for industrial robots [Gangloff and de Mathelin 2003], thus it is assumed that the dynamics of separate axes are decoupled. However, there is kinematic coupling between longitudinal and vertical axes due to PSS deflection caused by finite rigidity of a table top [Skworcow 2008].

7.3.1 Data acquisition

Some models of the PSS have been developed by the MAESTRO team involving experiments where sine wave and steps stimuli were used [Haas et al. 2006]. In the experiment proposed by the author,

some usual test signals such as PRBS, RBS, and sine wave of amplitude ± 2 mm were used to excite the PSS system over its whole bandwidth (0-1 Hz). While, the amplitude of the first two signals was fixed, varying sine wave amplitude was used. The measurements were carried out at the UHCW on a PSS of an $Elekta^{®}$ Synergy^{TM} linear accelerator. A special hardware interface illustrated in Figure 7.6(a)) has been developed to enable communication between the PSS and a PC equipped with a dSPACE card and Matlab/Simulink software package. A special graphical platform was developed in the dSPACE control desk to enable the PC to send various input voltages to PSS and to measure output voltage from the potentiometer measuring the position of the PSS. The measurements were performed along the PSS longitudinal, lateral and vertical axes.

Previous measurements taken at the UHCW have revealed that the reading of the potentiometer installed in the clinical PSS required conversion from voltage units to millimetres. The relation between output of the PSS in voltage to position in millimetres was found by a MAESTRO co-worker to be linear with the conversion coefficient equal 0.0095. Furthermore, the experiment did take into account the patient's weight by using six weights of 13 kg each. The maximum load employed was thus similar to that proposed by [CAPCA 2005]. Three cases were assessed in this experiment: (i) PSS movement without load, (ii) PSS movement with 4 weights (52 kg), and (iii) PSS movement with 6 weights (72 kg).

(a) Connection set-up. (b) The PSS joystick.

Fig. 7.6: Illustrating the experiment connection set-up and the PSS joystick.

For each scenario the PSS was moved along its three axes with the help of the joystick depicted in Figure 7.6(b). An example of the PSS system input-output for the three axes and different simulated patient weight is given in Figure 7.7. Note that a constant offset value has been added to the amplitude values of each these signals to improve the clarity of the figures illustrated in Figure 7.7.

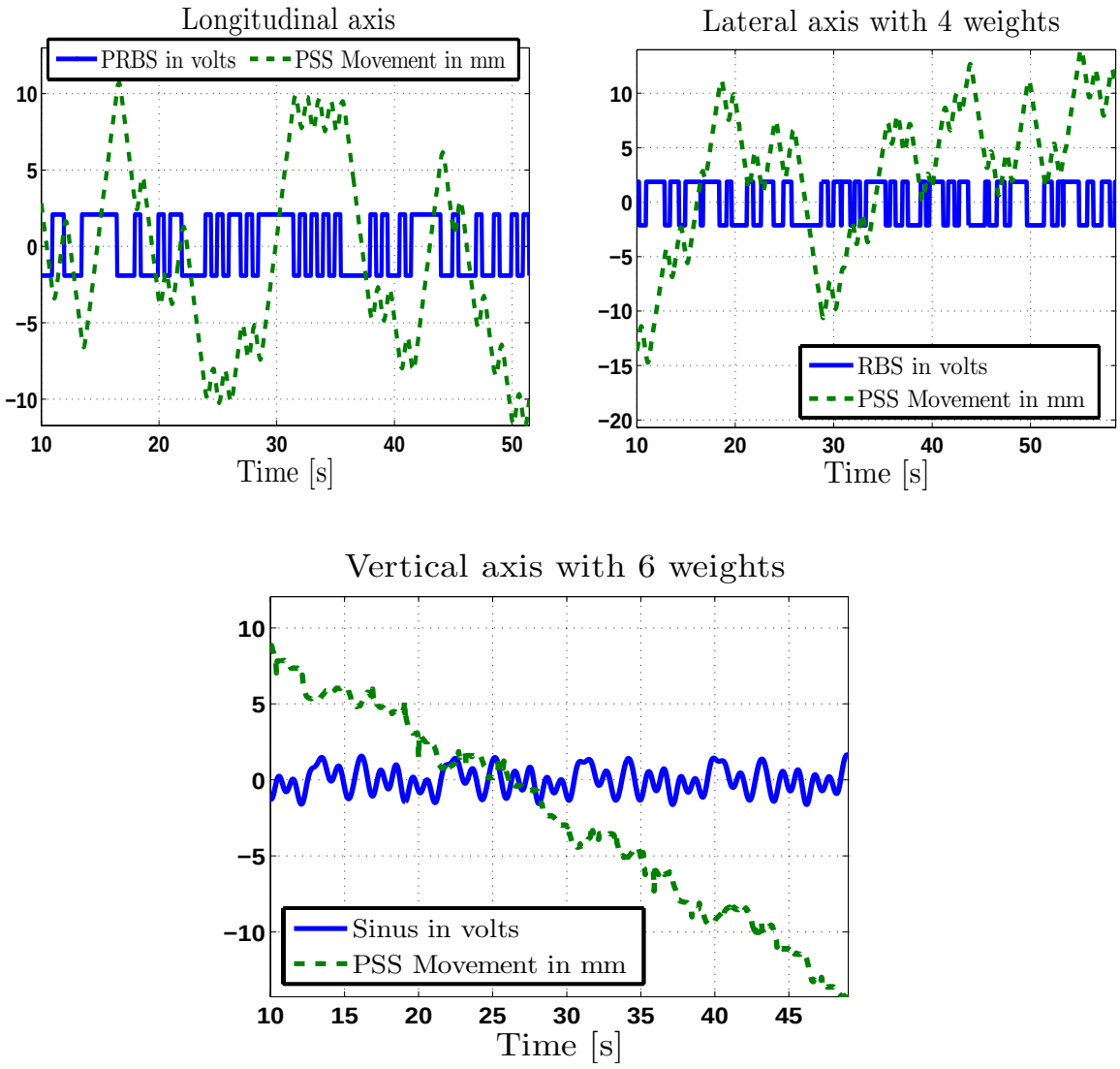

Fig. 7.7: Example of PSS input-output measurement data for different axis, inputs and weights.

7.3.2 Nonlinear autoregressive with exogenous variables (NARX) model

The data collected was then used to develop a simulation model of the PSS. The latter consists of a NARX model, in which the linear part represents the motor dynamics and the nonlinear components comprise logarithmic PSS input, a saturation, a dead zone, and friction. Note that the logarithmic input, dead zone and saturation are due to the joystick interface and the maximum speed achievable by the motors. The following NARX model structure was used:

$$y(t) = -a_1 y(t-1) - a_2 y(t-2) + bH(u(t-1)) + offset \tag{7.3.1}$$

where H is a nonlinear function of the input signal which consist of the following functions.

PSS logarithmic input

There was a logarithmic function at the level of the joystick, to enable better control at low velocity. This logarithmic function works such as when the input voltage of the PSS is increasing quickly the velocity of the PSS increase slowly. This was found to have the following model:

$$H_1(u) = \begin{cases} \log_{10}(u) & \text{if } u > 1 \\ -\log_{10}(-u) & \text{if } u < -1 \\ u/10 & \text{if } -1 < u < 1. \end{cases}$$

PSS saturation

Above a certain value, increasing the voltage input does not result in a speed increase. The saturation restricts the allowable voltage input to the specified saturation level (SL) $\pm 2V$. Assuming a symmetric saturation function, SL is a single parameter of the saturation. In our case the latter was fixed to 2V. The input signals were therefore limited to be between -2V and +2V such as not to infringe the saturation limits

PSS dead zone

The dead zone is used to prevent the PSS from reacting when subject to 'small' input signals. If the value of the input is inside the dead zone level then the actual input received by the PSS is zero. The dead zone was initially assumed to be symmetrical, warranting a single parameter Dz to model it. Note however that for some of the interface it was observed that the PSS started moving at voltages different to that used to stop and even different between positive and negative motion. Such behaviour was assumed to be due to stiction and friction as well as some hysteresis subsequently modelled as non symmetrical dead zone requiring two parameters Dzl and Dzh. The overall characteristic including a non symmetrical dead zone and symmetrical saturation is illustrated in Figure 7.8.

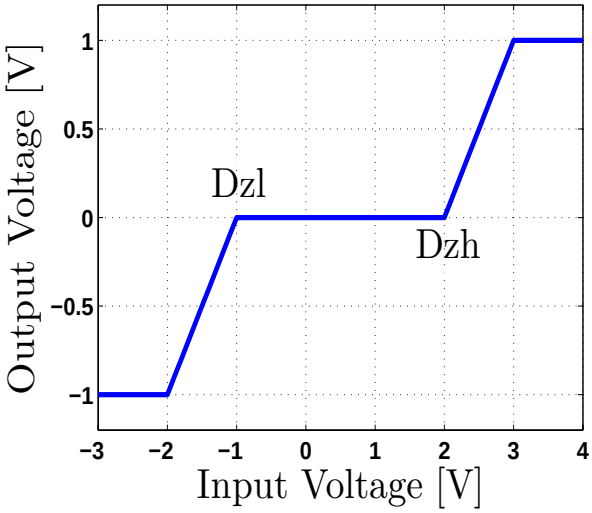

Fig. 7.8: Overall characteristic of a non symmetrical dead zone and symmetrical saturation.

In addition to the above-mentioned nonlinearities, there is also the friction force that opposes the motion of the PSS. The friction force depends mainly on the surface of motion and the PSS velocity. A mathematical description of the friction force can be found in [Putra 2004]. The friction force was omitted here for simplicity and therefore the values of the the friction component was given by the manufacturer.

The amount and combination of each of these nonlinearities are slightly different depending on the axis of motion. However, all these are present and thus a similar modelling framework was adopted for each axis. The parameters of these models are however different. The next part describes the system identification work done to estimate the parameters of the models for the longitudinal, lateral and vertical direction.

7.3.3 Simulation results

Simulation studies were carried out to determine the model of the PSS movement in the three axes. Firstly, the data collected in the experiment were divided into two sets, in order to use the first set for parameters estimation and the second one to validate the obtained models. The parameters estimation was performed using constrained nonlinear optimisation technique similar to the one described in the Subsection 5.4.1. The optimisation process was initialised by the least squares estimate for the linear part and an initial guess for the dead zone parameters (Dzl,Dzh). The PSS movement modelling and validation procedures are presented in the algorithm 4.

Algorithm 4 The PSS Movement Modelling and Validation Procedures

1: For a given PSS input-output signals $\{\mathbf{U}^N\}$ and $\{\mathbf{Y}^N\}$, where N is the number of samples considered.
2: Remove the mean value.
3: Apply the logarithmic function to the PSS input signal $\{\mathbf{U}^N\}$.
4: Separate data in two sets, the first set for modelling $\{\mathbf{U}_1, \mathbf{Y}_1\}$, and the other set of unseen data $\{\mathbf{U}_2, \mathbf{Y}_2\}$ to validate the model.
5: Apply the dead zone function and friction force to the PSS input signal $\{\mathbf{U}_1\}$
6: Estimate an initial vector parameter $\widehat{\boldsymbol{\theta}}_i$, for input-output observations $\{\mathbf{U}_1, \mathbf{Y}_1\}$, using linear least squares (LLS). This latter is then used to initialize the iterative optimization technique in the next step.
7: Estimate using a nonlinear optimization technique, the parameters of the model $\boldsymbol{\theta}$ iteratively by minimizing the MSSE, for input-output $\{\mathbf{U}_1, \mathbf{Y}_1\}$.
8: Use the input observations $\{\mathbf{U}_2\}$ and the model to simulate the estimated unseen data $\{\widehat{\mathbf{Y}}_2\}$.

The performance of the obtained three axes models were assessed for each input signal and different weights using the unseen data, see Table 7.2. Comparing the modelling performance in the case of the PRBS excitation, it was noticed that the longitudinal PSS movement model gives the lowest RMSE for the three different weights. For the RBS test, the best modelling performance for the 0, 52 and 78 kg was found to be the model of the PSS in the vertical, lateral and longitudinal respectively. Concerning the sine wave test, the lowest RMSE was given by the longitudinal model for 0 kg, and vertical model for both 52 and 78 kg weights. On can deduce from this comparison that the performance of the PSS movement model is weight and input signal independent. The largest RMSE has resulted from the validation of the lateral model of the PSS for the PRBS (0 kg) and RBS (78 kg).

Tab. 7.2: The evaluation of the PSS model in the three axes (the best results are indicated in bold).

Movement Axis		LONGITUDINAL								
Input Signal		PRBS			RBS			SINE WAVE		
Mass [kg]		0	52	78	0	52	78	0	52	78
RMSE [mm]	Mod.	**0.15**	**0.21**	**0.23**	1.17	0.36	**0.21**	**0.26**	0.31	0.39
	Val.	**0.53**	**0.22**	**0.70**	3.22	2.17	**1.21**	**0.71**	1.96	3.46
Movement Axis		LATERAL								
Input Signal		PRBS			RBS			SINE WAVE		
Mass [kg]		0	52	78	0	52	78	0	52	78
RMSE [mm]	Mod.	0.32	0.59	0.40	0.46	**0.35**	0.69	**0.26**	0.35	0.26
	Val.	15.36	2.80	3.57	2.98	**0.95**	7.56	4.87	3.96	4.64
Movement Axis		VERTICAL								
Input Signal		PRBS			RBS			SINE WAVE		
Mass [kg]		0	52	78	0	52	78	0	52	78
RMSE [mm]	Mod.	0.46	0.42	0.41	**0.18**	0.42	0.46	0.27	**0.23**	**0.24**
	Val.	1.20	3.44	1.06	**2.09**	4.72	1.69	3.75	**0.62**	**1.11**

Some good examples of the comparison between the simulated PSS model data and the measured data for each test signal and movement axis are depicted in Figures 7.9-7.11. Figure 7.9 illustrates the simulation results for the PRBS test. The obtained models in this case have performed the experimental data with a RMSE less than 0.6 mm. However, in the validation step, the lateral and vertical models of the PSS have achieved a RMSE bigger than 1 mm. This is mainly due to the fact that the adopted model of the PSS in the lateral and vertical axes does not cover all the PSS motion dynamics in the aforementioned axes. The simulation results for the RBS test are depicted in Figure 7.10. The model of the PSS in this case performs the validation set with a RMSE bigger than 1 mm in longitudinal and vertical axes. Finally, the simulation results in the case of the sine wave input signal are presented in Figure 7.11. The large simulation error was noticed in the lateral model of the PSS. As conclusion, some of the simulation models of the PSS movement show a good ability to replicate the PSS movement in the three axes. The large errors in the validation stage were mainly noticed for the vertical model of the PSS. This can be due to the fact that the adopted model does not cover all the PSS motion dynamics in the vertical axis. Therefore, the model of the vertical motion of the PSS has to be improved. The parameters of the obtained models are shown in Table 7.3. The estimated parameters depend on the movement axis and the input signal. The parameters a_1,a_2 and b_1 are slightly similar when comparing the longitudinal and lateral PSS response to the PRBS and RBS inputs for three cases (0,4 and 6 weights). The aforementioned parameters are dissimilar for the vertical movement. This is probably due to the complicated dynamic of the vertical movement of the PSS.

The NARX model was found to be a satisfactory simulation model of the PSS. However, as the MPC scheme requires the system model to be in linear state-space form, hence, model developed for control design purpose consider only the linear part of the SimMechnics mode, i.e. all nonlinearities are ignored (see [Skworcow 2008]). Some of the system nonlinearities were taken into account during the control design in the form of constraints.

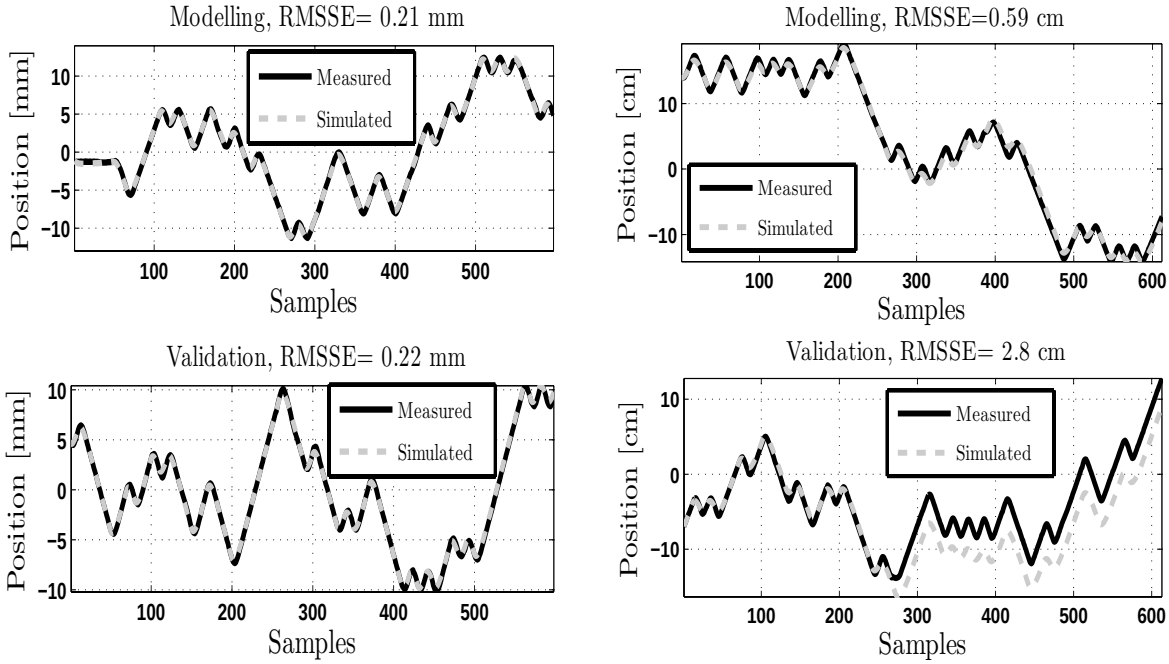

(a) (b)

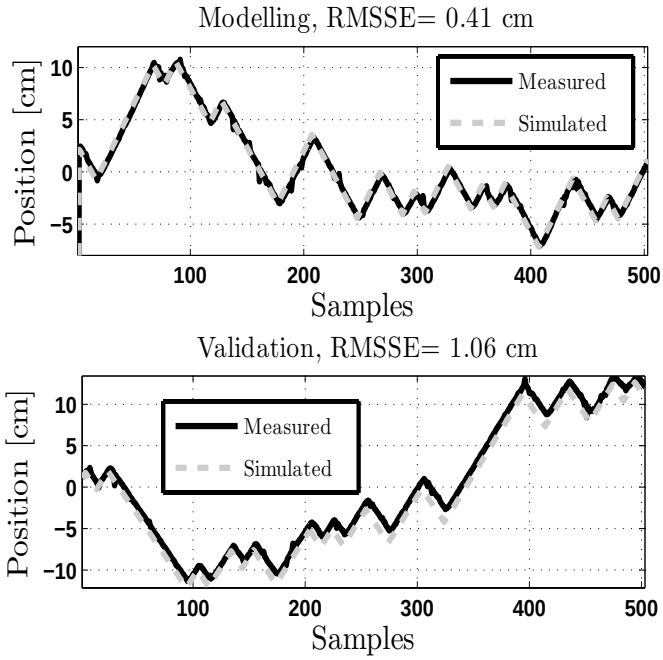

(c)

Fig. 7.9: Illustrating the PSS model evaluation for the PRBS excitation and for the three axes: longitudinal (a), lateral (b) and vertical (c).

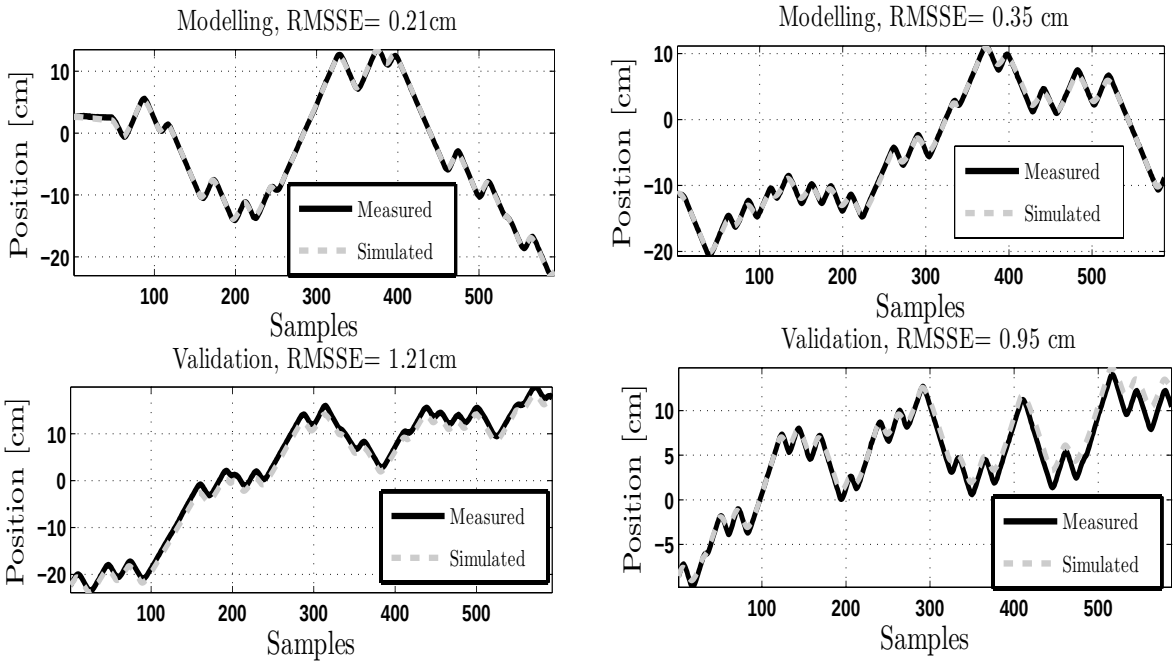

(a) (b)

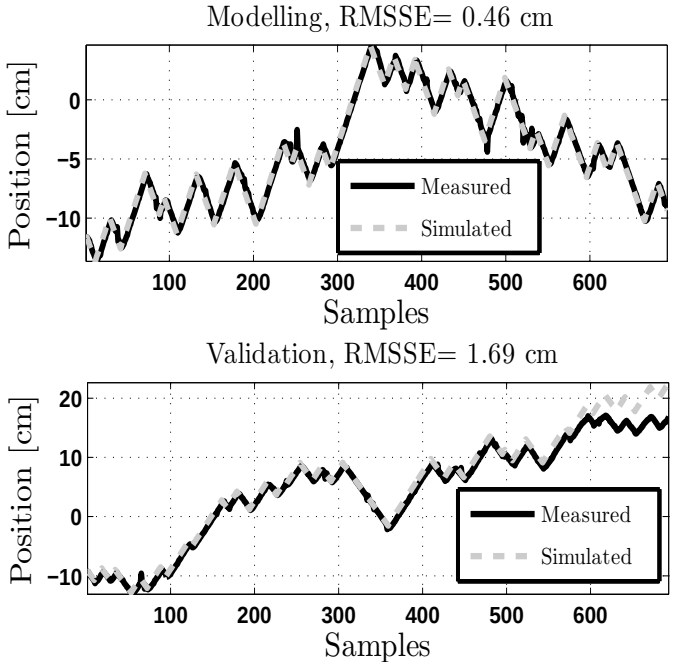

(c)

Fig. 7.10: Illustrating the PSS model evaluation for the RBS excitation and for the three axes: longitudinal (a), lateral (b) and vertical (c).

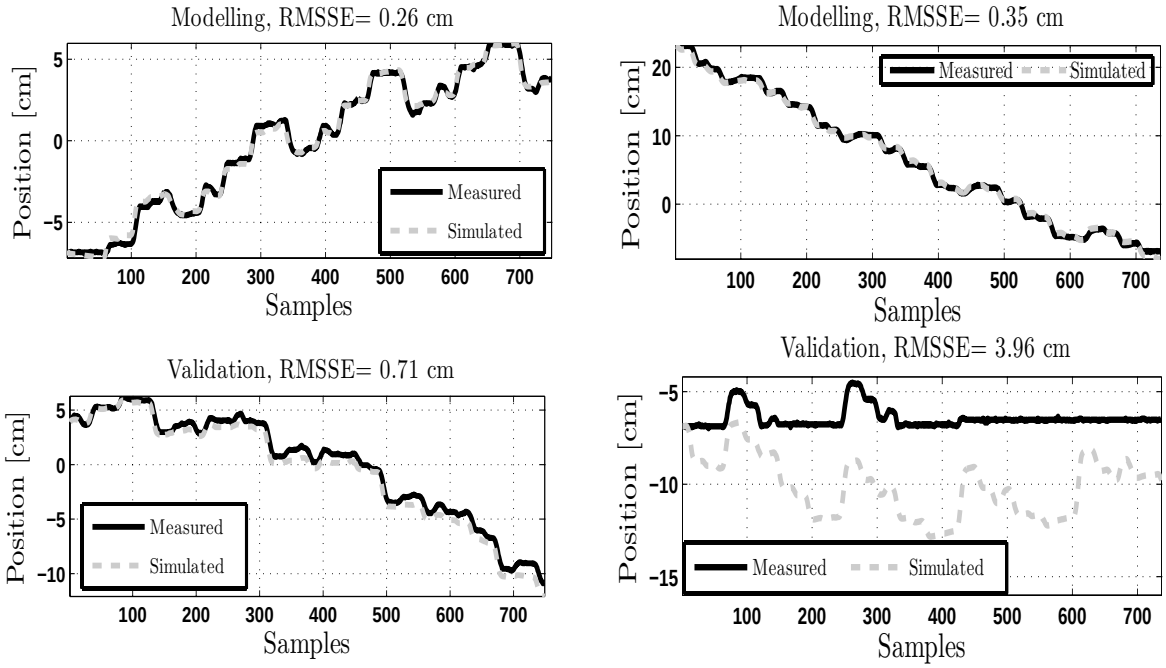

(a) (b)

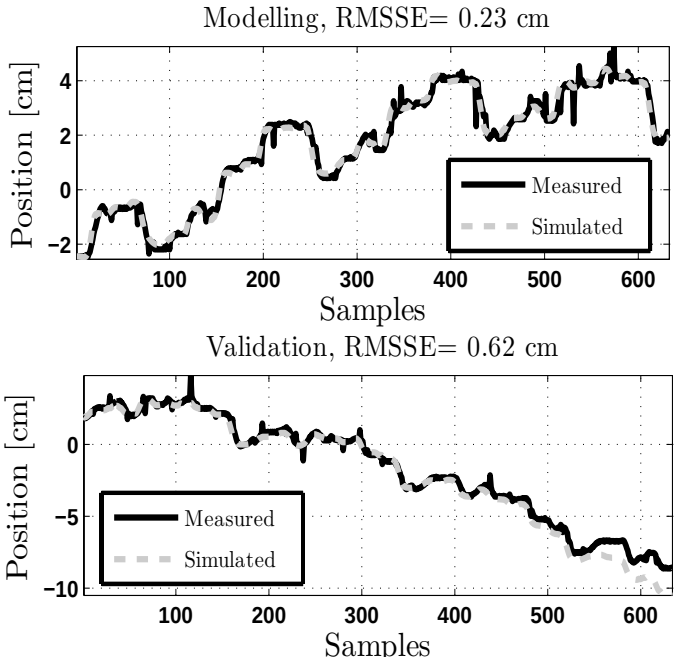

(c)

Fig. 7.11: Illustrating the PSS model evaluation for the sine wave excitation and for the three axes: longitudinal (a), lateral (b) and vertical (c).

Tab. 7.3: The estimated parameters of the PSS model in the three axes.

Movement Axis	LONGITUDINAL								
Input Signal	PRBS			RBS			SINE WAVE		
Weight	0	4	6	0	4	6	0	4	6
a_1	-1.7461	-1.7686	-1.7773	-1.7528	-1.7634	-1.7629	-1.3750	-1.2926	-1.3234
a_2	0.7461	0.7687	0.7773	0.7531	0.7635	0.7629	0.3745	0.2925	0.3236
b_1	0.283	0.2514	0.3358	0.2421	0.2380	0.2879	0.8894	0.5265	0.6486
Offset	-0.0001	0.0016	0.0039	0.0067	0.0102	-0.0034	0.0000	0.0215	0.0084
Dzh	0.0433	0.0122	0.1213	0.0000	0.0000	.0206	0.0543	0.0000	0.0052
Dzl	-0.0008	-0.0270	-0.0782	-0.0000	-0.0000	-0.0809	-0.0535	-0.0000	-0.0022
Movement Axis	LATERAL								
Input Signal	PRBS			RBS			SINE WAVE		
Weight	0	4	6	0	4	6	0	4	6
a_1	-1.7997	-1.8264	-1.8163	-1.8165	-1.8214	-1.8285	-1.4152	-1.5229	-1.4492
a_2	0.7997	0.8264	0.8164	0.8166	0.8214	0.8284	0.4155	0.5228	0.4492
b_1	0.2319	0.1895	0.1952	0.2311	0.1857	0.1885	0.5543	0.7969	0.7889
Offset	-0.0168	0.0011	0.0026	-0.0076	0.0051	0.0108	0.0033	0.0054	0.0034
Dzh	0.0255	0.0217	0.0111	0.0000	0.0108	0.0093	0.0102	0.0995	0.0561
Dzl	-0.0328	-0.0082	-0.0106	-0.1179	-0.0103	-0.0111	-0.0081	-0.0127	-0.0323
Movement Axis	VERTICAL								
Input Signal	PRBS			RBS			SINE WAVE		
Weight	0	4	6	0	4	6	0	4	6
a_1	-0.8351	-0.8149	-1.0015	-1.6751	-0.9319	-0.8556	-0.6442	-0.5937	-0.5615
a_2	-0.1647	-0.1860	0.0011	0.6751	-0.0686	-0.1446	-0.3554	-0.4082	-0.4390
b_1	0.8229	0.8684	0.7255	0.4707	0.7553	0.8094	1.1626	1.3654	1.7044
Offset	-0.0041	-0.0169	0.0040	-0.0323	0.0292	0.0357	-0.0179	-0.0007	0.0074
Dzh	0.0121	0.0164	0.0071	0.0649	0.0148	0.0072	0.0139	0.0381	0.1151
Dzl	-0.0123	-0.0218	-0.0184	-0.2486	-0.0002	-0.0058	-0.0179	-0.0262	-0.0000

7.4 Predictive bilinear feedforward model

In [D'Souza et al. 2005] some feasibility studies of PSS-based organ motion compensation was demonstrated. However, speed and frequency was four times slower than that necessary to track intra-fractional motion encountered in reality. In contrast, the first simulation considered in this section deals with actual SI motion data of a tumour collected during treatment [Shirato et al. 2000a]. This is used to generate the reference signal for the controller. The time response of the closed-loop PSS depends on controller gain, the load (patient mass) and variation in reference amplitude and frequency. For an average load of 70kg and a reference being the motion of an actual tumour, the time corresponding to the phase lag has been estimated to be 0.1s. The total latency due to respiratory monitoring and data processing leading to reference generation is estimated to be 0.2s.

The SimMechanics model introduced in [Skworcow 2008] was developed for the purpose of simulation and includes nonlinearities such as friction and stiction, quantization of measurements, backlash and input saturation. However, for the purpose of model-based controller design, nonlinearities are removed

resulting in a simplified linear model, which is considered to be realistic. In most commercial systems automated control of the PSS position is not currently available. To demonstrate the principle of PSS position control via a reference signal derived from organ motion, a proportional feedback controller implemented in Simulink was used. The predicted organ motion using the bilinear filter was taken as the reference signal.

Contrary to the previous methods, including KF, linear prediction and NN, which have been used to predict up to 1s ahead, a new approach represented here involves long term prediction i.e. one cycle in advance (three seconds for data acquired with 30 Hz) using a bilinear approach. This approach consists in building a predictive model for the exhalation and inhalations durations. This model assumed that the exhalation and inhalation durations are nearly constant with a small variation or error to allow the two parameters some fluctuation. Following the initial step of generating the input signal, the parameters of the bilinear model are estimated recursively using a weighted recursive least squares (WRLS) algorithm. To be able to predict next breathing cycle, a predicted input was generated by making use of mean values for the two half periods (noting the asymmetry). This is then fed into the bilinear model to obtain the prediction of the next cycle.

Assuming that the position of the organ is acquired in real time by the measurement tool, the steps of modelling and prediction are given as follows:

Algorithm 5 Modelling and Prediction Algorithm

1: **for** $t = 1{:}N$ **do**
2: Estimate Ymin (minimum value of system output).
3: Generate Umax (maximum value of system input).
4: Estimate $\theta_t = [a_t^1, a_t^2, b_t, \eta_t, d_t]^T$, by using optimization technique.
5: Estimate Ymax (maximum value of system output) $\Rightarrow$ T1 (time spent in exhale).
6: Switch to Umin (minimum value of system input).
7: Detect Ymin $\Rightarrow$ T2 (time spent in inhale).
8: Run KF to predict next T1 and T2.
9: Use the actual model to Predict k position ahead.
10: **end for**

During the training time of the bilinear model, the latter has satisfactorily replicated the motion with a RMSE of 0.41mm (see Figure 7.12(a)). The bilinear predictor is then set-up for prediction to generate the reference to be fed into the controller to ensure that the PSS is at the correct position at the desired time. The RMSE of the predicted unseen cycle is 1.1mm. Note, that motion of the PSS and the organ should be in opposite directions to aim towards organ immobilization. For the purpose of illustration, however, the organ and PSS motion is in the same direction. Figure 7.12(b) shows that the control strategy enables the PSS to compensate for organ motion by accurately following the desired trajectory, i.e. predicted organ position. The discrepancy between the predicted organ position and PSS position is 0.04mm RMSE,

while the discrepancy between the actual organ position and PSS position is 0.42mm RMSE.

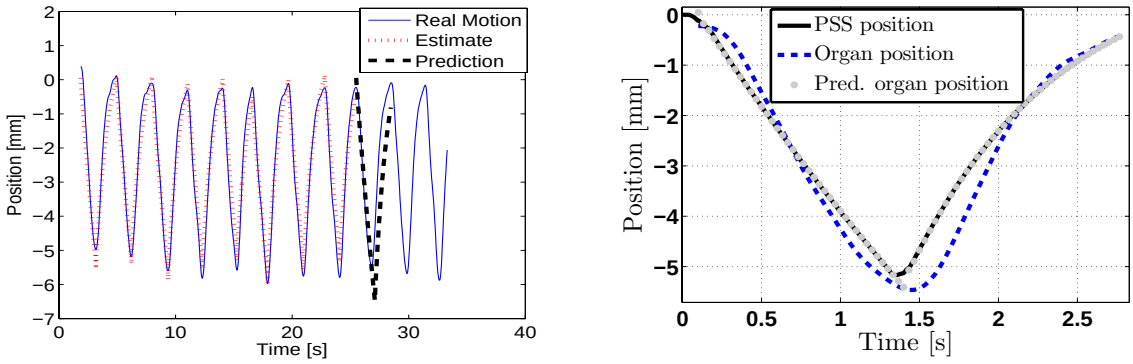

(a) Illustrating the effectiveness of bilinear filter approach to estimation and prediction of organ motion

(b) PSS position controlled by the predicted organ position.

Fig. 7.12: The bilinear prediction with the PSS control.

7.5 Clinical assessment of adaptive radiotherapy (ART) based patient support system (PSS) control

Some clinical experiments were carried out at the UHCW to assess the new ART strategy based on PSS control (see Appendix D), to accommodate for respiratory motion. This adaptive approach was the result of collaboration between CTAC and the UHCW, both involved in the MAESTRO project. The clinical tests were performed on an $Elekta^{®}$ Synergy^{TM} LINAC and involved a thorax phantom to simulate the tumour motion and the video camera tracking system developed to monitor the position of the markers placed on the phantom. An illustration of the experiments set-up is shown in Figure 7.13. The thorax phantom and its accompanying software used in the experiments were developed by the UHCW team in collaboration with CTAC (see [Land 2009]).

The new approach consisted in sending the acquired position by the video camera to the prediction block, which apply the Kalman CV algorithm to predict 28 samples in advance (equivalent to 0.56s for controller sampling time of 50 Hz). The latter was then sent to the PSS controller which moved the couch accordingly. Connection to the PSS was implemented using a special purpose interface designed at CTAC in collaboration with UHCW and $Elekta^{®}$. The aim of the strategy consisted on moving the PSS in the opposite direction to the movement of the target in the phantom, so that the latter is immobilized with respect to the treatment beam.

Fig. 7.13: Illustrating a typical set-up for experiments with the clinical PSS at UHCW.

The performance of the ART system was assessed for the longitudinal and vertical axes (corresponding to SI and AP tumour motion respectively), by comparing the motion generated by the phantom and the PSS response. The compensation for 2D motion (SI and AP) was successfully implemented in [Skworcow 2008]. Respiratory motion of the target within the lung of the thorax phantom was firstly produced by a regular signals such as sinewaves. Figure 7.14 shows the PSS positional response to a sinusoidal motion with a peak-to-peak amplitude of 14 mm and a frequency of 0.2 Hz generated by the phantom in longitudinal axis. The controlled PSS was able to follow the sinusoidal motion generated by the phantom with an accuracy less than 1 mm in terms of RMSE. To quantify the predictive tracking of compensation strategy in term of RMSE, maximum error and 95% CI the reference signal was compared the PSS response (see Figure 7.14). The compensation method has reduced the tracking error in term of RMSE, maximum error and the 95% CI by a factor of 10 to an error which could be easily accommodated by a slight increase of the treatment margin.

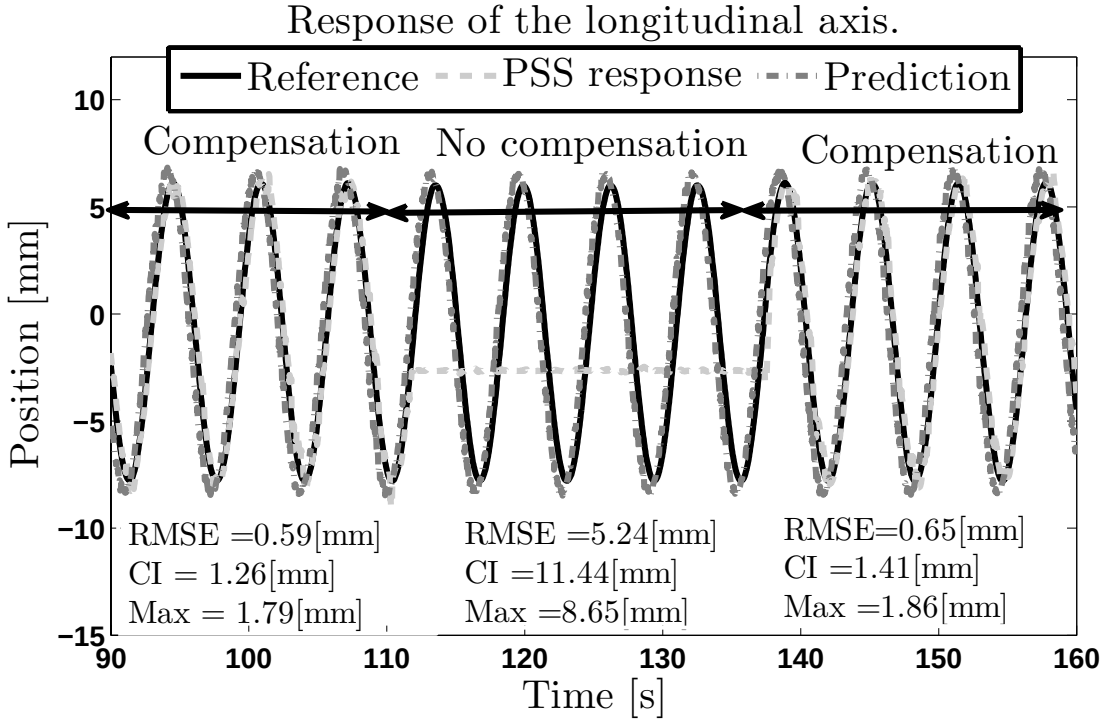

Fig. 7.14: Illustrating the interest of the compensation method.

7.6 Conclusions

Respiratory motion prediction was achieved in this chapter by means of two novel prediction algorithms, namely BTV and sliding window polynomial models. The effectiveness of these latter was assessed against some prediction algorithms developed by MAESTRO co-worker, including IMM, KF assuming CV and CA and two structures of NNs; a TSP MLP and GRNN, with four different training algorithms. It was found that all predictors can achieve a reduction of RMSE when compared to the case of no prediction is considered. The outcome of the comparison between the introduced predictors has shown that while the polynomial approach performs better for short time prediction horizon (0.2s), the BTV has achieved a better results for long time prediction (0.4s, 0.5s and 0.6s). The real-time implementation of three motion predictors, namely Kalman CV, Kalman CA, and the IMM filter has also been performed. The real-time implementation was useful for the clinical assessment of the developed compensation strategy. A model of each motion axis of the PSS was identified using experimental data collected at the UHCW. The developed models were shown to perform adequately being able to accommodate for most of the system's nonlinearities, leading to a RMSE of less than 1mm in most of the cases.

The new motion compensation strategy developed within the MAESTRO project was assessed clinically at the UHCW. This has involved a mechanical lung phantom, video camera tracking system, an MPC

controller and a motion predictor. The author has contributed to this practically significant outcome by implementing the initial KF predictor for use in dSPACE and the development of the video camera tracking system. The main outcome of this test was that the controlled PSS was able to follow the sinusoidal reference signals in longitudinal mode. Using such compensation strategy decreases the effect of target motion leading to a RMS compensation error of the order of 0.6. Such an error would warrant a margin of the order of 1.4mm to ensure a 95% coverage of the target.

Chapter 8

General conclusions and further research perspectives

This final chapter presents the overall conclusions that can be drawn from this research and suggests some of the future work that may follow-on from it.

8.1 General conclusions

The research, described in this thesis, considered the problem of delivering a radiation beam precisely to a tumour, when the tumour is in motion, caused by respiration, during the external beam radiotherapy process. Tumour motion is currently measured with the use of surrogate markers whose position is correlated to the actual tumour motion. In this work, it was assumed that the surrogate motion provides an accurate representation of the tumour motion. The main aim of this research was to model and derive the means to predict in advance the surrogate motion. Major efforts have been devoted to address the following objectives:

- Develop new surrogate motion models (chapter 5).
- Generate a set of realistic respiratory motion data sets (chapter 5).
- Develop new modelling and predictive tracking strategy based on flow measurement and external chest markers (chapter 6).
- Introduce new prediction algorithms (chapter 7).

To carry out the above objectives, both the theoretical and practical aspects have been considered. There are three types of contributions. The first relates to the surrogate motion models developed and their exploitation to derive a new set of benchmark data. The second involves the modification of the models developed to make them suitable for the purpose of motion prediction. The third involves experimental work and the demonstration of the algorithms developed on real time motion monitoring system. The outcomes and novelty of each part of this research is highlighted in the following paragraphs.

The success of this research was made possible with the most relevant clinical respiratory surrogate motion data provided by Virginia Commonwealth University (USA) and Hokkaido University-School of Medicine (Japan), representing respectively the anterior-posterior and superior-inferior movement of external and internal markers. This data was divided into four data sets; internal fiducial markers, free-breathing, audio instruction and audio-visual biofeedback. A time and frequency analysis of this data highlighted the different breathing irregularities and abnormalities that might affect the respiration together with measurement noise, baseline drift and heart beat. To derive average models, a subset of this data, referred as a 'good' data, was selected to build the respiratory model and provide the prior knowledge exploited in the derivation and tuning of respiratory motion model and prediction algorithms. By contrast to the respiratory motion parameterisation adopted in [Wu et al. 2004], the author has considered breathing as a succession of exhalation and inhalation, as this was found to be more appropriate with the modelling approach presented in chapter 4.

In addition to data from the literature, a new experiment presented in chapter 6 was designed and carried out by the author involving 13 healthy subjects. Three dimensional motion of external markers placed onto two different positions on the thorax were measured by the Polaris system and at the same time the breathing flow, lung volume, pressure and heart rate were measured by a spirometer. The aim of the experiment was to evaluate the applicability of using one of the physical signals from the spirometer as the input signal to drive a bilinear filter within the new model framework presented in chapter 5. This experiment is considered as a minor contribution, however it provided the means to validate the models and predictors developed using independent data as well as that of the literature.

The main contribution of this thesis in terms of modelling the respiratory surrogate motion is the motion modelling framework described in Section 5.4. The approach has presumed that the lung is approximated by a bilinear system, which responds to a square wave signal assumed to be generated by the nervous system. The novelty of the approach lies in the combination of the past and current motion data with an input signal correlated to the inhalation and exhalation phases. This framework can accommodate both linear and non linear motion models. The driving signal could be generated based on predicted inhalation and exhalation phases as well as measurement of other surrogate signals. Disturbances such as

drift, measurement noise and heartbeat as external signals were modelled separately and combined with the disturbance free model. Two methods based on a polynomial function and drift frequencies filtering were proposed to remove the drift signal. Both constrained and unconstrained nonlinear optimisation techniques were used to obtain the parameters of the models. The performance of this modelling approach was assessed using the 'good data' subset for both internal and external motion.

An average bilinear model was able to adequately replicate the validation set of the clinical data with an overall average root mean squared simulation error less than 1.5 mm for internal data and 2 mm for external data in the case of polynomial and pre-filtering drift removal methods respectively. However, an overall average maximum absolute simulation error was found to be larger than 3 mm in both cases, which was mainly due to some respiratory irregularities not considered in the modelling phase. A comparison between the modelling performance of the average bilinear model against the performance of the phase-based model presented in [Wu et al. 2004], both involving the internal fiducial markers data, was carried out. It was found that the overall average root mean squared simulation error criterion for the former is a slightly higher than the latter. It is believed, however, that the modelling framework presented can lead to more generalisable models able to cope with breathing period variability.

Moreover, the introduced model is based on a dynamic system with a fixed number of parameters. In contrast to the previous developed models that were evaluated on the same data that was used to build the models, the assessment of the introduced models in this work was evaluated on different data to that used to build the models. The constrained optimisation technique adopted to estimate the parameters of the models was able to reduce the simulation error. However, such a fixed parameter model can only partially replicate some of the variability of breathing motion. It was found however that varying the model parameters on line could produce significantly better model fit at the cost of varying parameters.

The second contribution in terms of respiratory cycles modelling was the use of polynomial fitting. This was performed online and compared to the widely used Lujan model, which was also implemented on-line. The polynomial model was able to reproduce more accurately the non-symmetrical breathing cycles compared to the Lujan model. In addition, the polynomial fitting is computationally faster as the model is linear in the parameters.

The third contribution, associated with the modelling work, was the generation of a set of benchmark data against which to assess motion prediction algorithms. The bilinear time-invariant model was found to provide an ideal platform to generate, for the research community, a new set of data representing a wide, as well as realistic, range of motion that could account for typical drift, heart beat and noise. The use of the bilinear time-invariant model to generate a new database of test signals is considered as another novelty of this work with great potential as there is currently no widely available database against which

the algorithms of various research groups may be compared. The generated test trajectories, presented in Section 5.8, exploit the statistical model of the period and duty cycle performed in chapter 4. The spectrum of the generated data has confirmed the existence of the expected respiratory frequencies as well as signal irregularities. These files are available from the MAESTRO website.

A final contribution in term of modelling was the experimental validation of the approach on the data obtained from the new experiment involving the spirometer and the Polaris. To illustrate the approach the breathing flow together with the external markers motion in the X direction were selected. It was found that ARX(2,2) was the 'best' model structure. The impact of using a square wave virtual input by contrast to physical input was shown to be able to improve the modelling performance in terms of mean absolute simulation error.

The main contribution in terms of motion prediction is the extension of the bilinear model for prediction. Recognising that patient motion changes regularly and that the model needs to be updated to cater for it, the bilinear model was modified to make it suitable to predict organ motion. The bilinear time-varying motion prediction model is considered as the second major contribution. A related contribution has been the demonstration of such novel online predictive tracking approach using flow rate as the input driving the bilinear time-varying model, which itself exploits position of external markers measured by a camera.

The second contribution in terms of motion prediction is the adaptation of the polynomial model developed in chapter 5 to be used within a sliding window to model and then extrapolate organ motion using polynomial approximation. The third contribution is the comparison between the prediction algorithms developed by the author and MAESTRO colleagues, particularly the interacting multiple model, Kalman filter assuming constant velocity and constant acceleration and two structures of neural networks; a time-series prediction multi-layer perceptron and generalised regression neural network, with four different training algorithms. It was concluded that the polynomial method is the best for the short time i.e. 0.2s and the bilinear time-varying method is appropriate for long time prediction up to 0.6s.

The combination of the predictive tracking and control to compensate for respiratory motion during the radiotherapy treatment was also considered. The motion prediction work was fed into a new compensation strategy has been developed by MAESTRO co-workers. The strategy was assessed in both simulation and in a clinical environment. In the former, a proportional control of the patient support system represented by a SimMechanics model and a predictive bilinear feedforward model has shown that the patient support system can follow the predicted organ motion with an accuracy of 0.04 mm. The developed approach was implemented in a clinical environment at the University Hospitals Coventry and Warwickshire.

In summary, a number of novel results have been contributed to the area of the external beam radiotherapy, which provide firm foundations to improve the treatment of moving tumours. It is hoped that the research, detailed in this thesis, will eventually lead to the successful and widespread use of the tumour motion models and compensation based patient support system control in radiotherapy treatment practice.

8.2 Further research perspectives

Based on the work presented in this thesis, the author believes that some research suggestions for further investigations can be made. These further research perspectives are described in the following paragraphs.

The bilinear modelling approach adopted in chapter 5 has considered only the breathing motion. It can be extended to a new model structure that involves the external signals such as measurement noise, drift and heart rate. However, the estimation of model parameters will not be an easy task as the estimation of some of these parameters can affect the others. This problem can be solved by considering a regularisation technique in order to make use of the a-prior-knowledge.

The polynomial drift removal used in chapter 5 was sensitive to the initial conditions. To overcome this problem a use of padding with the padded value being equal to the average of the signal over the first few cycles, alternatively the first few cycles and the last few should be extracted from the data and ignored in the analysis. Such an approach may also help reduce the order of the polynomial for the drift model.

In the experiment carried out in chapter 6 the delay between the input and the output signals was not taken into account. The developed models can be modified by introducing the delay as a parameter to be estimated. This can be adopted as an off-line practice to identify the delay as well as online in parallel with a predictor to define the time horizon to predict in advance. Indeed, it has been observed that the delay due to the video processing system used in the MAESTRO project changes over time.

Regarding the motion prediction, it might be useful to consider a new hybrid scheme where prediction based on neural network strategies, Kalman filter, polynomial and bilinear filter are merged together with signal pre-processing techniques such as wavelets, fast Fourier transform and noise filtering to give an accurate expected organ position, together with an estimate of the prediction accuracy. Moreover, some algorithms that have been used for tracking such as alpha-beta, alpha-beta-gamma filters, particle filter and Bayesian approaches can also be assessed.

Index

References

Aaltonen, P., Brahme, A., Lax, I., Levernes, S., Naslund, I., Reitan, J., and Turesson, I. (1997). Specification of dose delivery in radiation therapy. Recommendation by the Nordic Association of Clinical Physics (NACP). *Acta Oncologica*, 36(10):1–32.

Ahn, S., Yi, B., Suh, Y., Kim, J., Lee, S., Shin, S., Shin, S., and Choi, E. (2004a). A feasibility study on the prediction of tumour location in the lung from skin motion. *British Journal of Radiology*, 77(919):588.

Ahn, Y., Shimizu, S., Shirato, H., Hashimoto, T., Osaka, Y., Zhang, X., Abe, T., Hosokawa, M., and Miyasaka, K. (2004b). Application of real-time tumor-tracking and gated radiotherapy system for unresectable pancreatic cancer. *Yonsei Medical Journal*, 45(4):584–90.

Balter, J., Lam, K., McGinn, C., Lawrence, T., and Ten Haken, R. (1998). Improvement of CT-based treatment-planning models of abdominal targets using static exhale imaging. *International Journal of Radiation Oncology, Biology, Physics*, 41(4):939–43.

Balter, J., Lam, K., Sandler, H., Littles, J., and Bree, RL andTen Haken, R. (1995a). Automated localization of the prostate at the time of treatment using implantedradiopaque markers: Technical feasibility. *International Journal of Radiation Oncology, Biology, Physics*, 33(5):1281–6.

Balter, J., Sandler, H., Lam, K., Bree, R., and Lichter, AS andten Haken, R. (1995b). Measurement of prostate movement over the course of routine radiotherapyusing implanted markers. *International Journal of Radiation Oncology, Biology, Physics*, 31(1):113–8.

Balter, J., Ten Haken, R., Lawrence, T., Lam, K., and Robertson, J. (1996). Uncertainties in CT-based radiation therapy treatment planning associated with patient breathing. *International Journal of Radiation Oncology, Biology, Physics*, 36(1):167–74.

Barnes, E., Murray, B., Robinson, D., Underwood, L., Hanson, J., and Roa, W. (2001). Dosimetric evaluation of lung tumor immobilization using breath hold at deep inspiration. *International Journal of Radiation Oncology, Biology, Physics*, 50(4):1091–8.

Ben-Tal, A. (2006). Simplified models for gas exchange in the human lungs. *Journal of Theoretical Biology*, 238(2):474–495.

Benchetrit, G. (2000a). Brathing pattern in humans: diversity and individuality. *Respiration Physiology*, 122:123–129.

Benchetrit, G. (2000b). Breathing pattern in humans: diversity and individuality. *Respiration Physiology*, 122(2-3):123–129.

Berbeco, R., Jiang, S., Sharp, G., Chen, G., Mostafavi, H., and Shirato, H. (2004). Integrated radiotherapy imaging system(IRIS): design considerations of tumour tracking with linac gantry-mounted diagnostic x-ray systems with flat-panel detectors. *Physics in Medicine and Biology*, 49(2):243–255.

Berbeco, R., Mostafavi, H., Sharp, G., and Jiang, S. (2005). Towards fluoroscopic respiratory gating for lung tumours without radiopaquemarkers. *Physics in Medicine and Biology*, 50(19):4481–4490.

Biondi, E., Schmid, R., and Milan, I. (1972). Mathematical models and prostheses for sense organs. *Theory and Applications of Variable Structure Systems*, pages 183–212.

Bissett, R., Boyko, S., Leszczynski, K., Cosby, S., Dunscombe, P., and Lightfoot, N. (1995). Radiotherapy portal verification: an observer study. *British Journal of Radiology*, 68(806):165.

Blomgren, H., Lax, I., Naslund, I., and Svanstrom, R. (1995). Stereotactic high dose fraction radiation therapy of extracranial tumorsusing an accelerator. Clinical experience of the first thirty-one patients. *Acta Oncologica*, 34(6):861–70.

Booth, J. (2002). *Modelling the impact of treatment uncertainties in radiotherapy*. PhD thesis, Department of Physics and Mathematical Physics-University of Adelaide.

Bortfeld, T., Ullrich, R. S., De Neve, W., and Wazer, D. E. (2006). *Image-Guided IMRT*. Springer.

Bortfeld, T., van Herk, M., and Jiang, S. (2002). When should systematic patient positioning errors in radiotherapy be corrected. *Physics in Medicine and Biology*, 47(297):N302.

Boyer, A. and Strait, J. (1997). Delivery of intensity-modulated treatment with dynamic multileaf collimator. In *XII the international conference on the use of cpmputer in computer in radiationtherapy(ICCR)*, pages 13–15, Salt Lake city, Utah, USA.

Brewer, J., Betke, M., Gierga, D., and Chen, G. (2004). Real-Time 4D Tumor Tracking and Modeling from Internal and External Fiducials in Fluoroscopy. *Lecture notes in computer science*, pages 594–601.

Brock, K., McShan, D., and Balter, J. (2002). A comparison of computer-controlled versus manual on-line patient setup adjustment. *Journal of Applied Clinical Medical Physics*, 3(3):241–247.

Bronzino, J. (2000). *The biomedical engineering handbook*. Springer.

Bruce, E. (1996). Temporal variations in the pattern of breathing. *Journal of Applied Physiology*, 80(4):1079–1087.

Bruni, C., DiPillo, G., and Koch, G. (1974). Bilinear systems: An appealing class of" nearly linear" systems in theory and applications. *IEEE Trans. on Automatic and Control*, 19(4):334–348.

Butler, L., Forster, K., Stevens, C., Bloch, C., Liu, H., Tucker, S., Komaki, R., Liao, Z., and Starkschall, G. (2004). Dosimetric benefits of respiratory gating: a preliminary study. *Journal of Applied Clinical Medical Physics*, 5(1).

Caldwell, C., Mah, K., Ung, Y., Danjoux, C., Balogh, JM andGanguli, S., and Ehrlich, L. (2001). Observer variation in contouring gross tumor volume in patients with poorlydefined non-small-cell lung tumors on CT: the impact of 18FDG-hybrid PETfusion. *International Journal of Radiation Oncology, Biology, Physics*, 51(4):923–31.

CAPCA (2005). Quality Control Standards: Medical Linear Accelerators. Technical report, Canadian Association of Provincial Cancer Agencies.

Chen, G., Kung, J., and Beaudette, K. (2004). Artifacts in computed tomography scanning of moving objects. *Seminars in Radiation Oncology*, 14(1):19–26.

Chen, Q., Weinhous, M., Deibel, F., Ciezki, J., and Macklis, R. (2001). Fluoroscopic study of tumor motion due to breathing: Facilitating precise radiation therapy for lung cancer patients. *Medical Physics*, 28:1850.

Chetty, I., Rosu, M., McShan, D., Fraass, B., and andR.K.Ten Haken, J. B. (2004). Accounting for center-of-mass target motion using convolution methods inmontecarlo-based dose calculations of the lung. *Medical Physics*, 31(4):925–932.

Chetty, I., Rosu, M., Tyagi, N., Marsh, L., McShan, D., Balter, J., Fraass, B., and Ten Haken, R. (2003). A fluence convolution method to account for respiratory motion in three-dimensional dose calculations of the liver: A Monte Carlo study. *Medical Physics*, 30:1776.

Cohen, L. (1995). *Time-frequency analysis: theory and applications*. Prentice-Hall, Inc., Upper Saddle River, NJ, USA.

Cotes, J. (1993). *Lung Function: Assessment and Application in Medicine*. Blackwell Publishing.

Crooke, P., Hotchkiss, J., and Marini, J. (2002). Linear and nonlinear mathematical models for noninvasive ventilation. *Mathematical and computer modelling*, 35(11-12):1297–1313.

Daisne, J., Duprez, T., Weynand, B., Lonneux, M., Hamoir, M., Reychler, H., and Gregoire, V. (2004). Tumor Volume in Pharyngolaryngeal Squamous Cell Carcinoma: Comparison atCT, MR Imaging, and FDG PET and Validation with Surgical Specimen 1. *Radiology*, 233(1):93–100.

Davies, S., Hill, A., Holmes, R., Halliwell, M., and Jackson, P. (1994). Ultrasound quantitation of respiratory organ motion in the upper abdomen. *British Journal of Radiology*, 67(803):1096.

De Boer, H. and Heijmen, B. (2001). A protocol for the reduction of systematic patient setup errors with minimalportal imaging workload. *International Journal of Radiation Oncology, Biology, Physics*, 50(5):1350–65.

De Boer, H., van Sornsen de Koste, J., Senan, S., Visser, A., and Heijmen, B. (2001). Analysis and reduction of 3D systematic and random setup errors during the simulation and treatment of lung cancer patients with CT-based external beam radiotherapy dose planning. *International Journal of Radiation Oncology, Biology, Physics*, 49(3):857–68.

Della Biancia, C., Yorke, E., Chui, C., Giraud, P., Rosenzweig, K., Amols, H., Ling, C., and Mageras, G. (2005). Comparison of end normal inspiration and expiration for gated intensitymodulated radiation therapy (IMRT) of lung cancer. *Radiotherapy and Oncology*, 75(2):149–156.

DeSteene, J., Heuvel, F., and Bel, A. e. a. (1998). Electronic portal imaging with on-line correction of setup error in thoracicirradiation:clinicalevaluation. *International Journal of Radiation Oncology, Biology, Physics*, 40:967–976.

Di Yan, D. (2001). Organ/patient geometric variation in external beam radiotherapy and itseffects. *Medical Physics*, 28:593.

Díez, S., García, J., and Sendra, F. (2004). Analysis and evaluation of periodic physiological organ motion in radiotherapy treatments. *Radiotherapy and Oncology*, 73(3):325–329.

Digalakis, V. (1992). ML estimation of a stochastic linear systems with the EM algorithm anditsapplication to speech recognition. *IEEE Transactions on Speech and Audio Processing*, 1(4):431–442.

Disdell, K. (1995). *Bilinear Self-Tuning Control for Multivariable High Temperature Furnace Applications*. PhD thesis, PhD Thesis, Coventry University, Coventry, UK.

D'Souza, W., Naqvi, S., and Yu, C. (2005). Real-time intra-fraction-motion tracking using the treatment couch: a feasibility study. *Physics in Medicine and Biology*, 50(17):4021–4033.

Dunoyer, A. P. (1996). *Bilinear Self-tuning Control and Bilinearisation of Nonlinear Industrial Systems*. PhD thesis, Coventry University.

Ekberg, L., Holmberg, O., Wittgren, L., Bjelkengren, G., and Landberg, T. (1998). What margins should be added to the clinical target volume in radiotherapy treatment planning for lung cancer. *Radiotherapy and Oncology*, 48(1):71–77.

Engelsman, M., Damen, E., De Jaeger, K., van Ingen, K., and Mijnheer, B. (2001). The effect of breathing and set-up errors on the cumulative dose to a lung tumor. *Radiotherapy and Oncology*, 60(1):95–105.

Engelsman, M., Sharp, G., Bortfeld, T., Onimaru, R., and Shirato, H. (2005). How much margin reduction is possible through gating or breath hold? *Physics in Medicine and Biology*, 50(3):477–490.

Erridge, S., Seppenwoolde, Y., Muller, S., van Herk, M. andDe Jaeger, K., Belderbos, J., Boersma, L., and Lebesque, J. (2003). Portal imaging to assess set-up errors, tumor motion and tumor shrinkageduring conformal radiotherapy of non-small cell lung cancer. *Radiotherapy and Oncology*, 66(1):75–85.

Favoreel, W., De Moor, B., and Van Overschee, P. (1999). Subspace identification of bilinear systems subject to white inputs. *Automatic Control, IEEE Transactions on*, 44(6):1157–1165.

Figalli, G., La Cava, M., and Tomasi, L. (1984). An optimal feedback control for a bilinear model of induction motor drivesĘ. *International Journal of Control*, 39(5):1007–1016.

Fitzpatrick, M. J., Starkschall, G., Balter, P., andT.Guerrero, J. A. A., Nelson, C., Keall, P., and Mohan, A. (2005). A novel platform simulating irregular motion to enhance assessment of respiration-correlatedradiationtherapy procedures. *Journal of Applied Clinical Medical Physics*, 6(1).

Ford, E., Mageras, G., Yorke, E., Rosenzweig, K., Wagman, R., and Ling, C. (2002). Evaluation of respiratory movement during gated radiotherapy using film and electronic portal imaging. *International Journal of Radiation Oncology, Biology, Physics*, 52(2):522–531.

Gangloff, J. and de Mathelin, M. (2003). High-speed visual servoing of a 6-DOF manipulator using multivariable predictive control. *Advanced Robotics*, 17(10):993–1021.

George, R. (2005). *investigating the impact of audio instruction and audio- visual biofeedbackforlung cancer radiation therapy*. PhD thesis, Virginia Commonwealth University.

George, R., Chung, T., Vedam, S., Ramakrishnan, V., Mohan, R., Weiss, E., and Keall, P. (2006). Audio-visual biofeedback for respiratory-gated radiotherapy: Impact of audio instruction and audio-visual biofeedback on respiratory-gated radiotherapy. *International Journal of Radiation Oncology, Biology, Physics*, 65(3):924–933.

George, R., Vedam, S., Chung, T., Ramakrishnan, V., and Keall, P. (2005). The application of the sinusoidal model to lung cancer patient respiratory motion. *Medical Physics*, 32:2850.

Gibson, S., Wills, A., Ninness, B., Bros, L., and London, U. (2005). Maximum-likelihood parameter estimation of bilinear systems. *Automatic Control, IEEE Transactions on*, 50(10):1581–1596.

Gierga, D., Brewer, J., Sharp, G., Betke, M., Willett, C., and Chen, G. (2005). The correlation between internal and external markers for abdominal tumors: Implications for respiratory gating. *International Journal of Radiation Oncology, Biology, Physics*, 61(5):1551–1558.

Ginhoux, R., Gangloff, J., de Mathelin, M., Soler, L., Leroy, J., and Marescaux, J. (2003). Model predictive control for tracking of repetitive organ motions during teleoperated laparoscopic interventions. In *European Control Conference (ECC), Cambridge, Royaume-Uni, Sept*.

Giraud, P., De Rycke, Y., Dubray, B., Helfre, S., Voican, D., Guo, L., Rosenwald, J., Keraudy, K., Housset, M., Touboul, E., et al. (2001). Conformal radiotherapy (CRT) planning for lung cancer: analysis of intrathoracic organ motion during extreme phases of breathing. *International Journal of Radiation Oncology, Biology, Physics*, 51(4):1081–1092.

Goitein, M. (2004). Organ and tumor motion: an overview. *Seminars in Radiation Oncology*, 14(1):2–9.

Golla, F. and Antonovitch, S. (1929). The respiratory rhythm in its relation to the mechanism of thought. *Brain*, 52:491–509.

Goodband, J. and Haas, O. (2008). Artificial Neural Networks in Radiation Therapy. *Intelligent And Adaptive Systems in Medicine*.

Goodband, J. H. (2006). *Novel Applications Using Neural Networks And Liquid Meatls In Radiation-Therapy*. PhD thesis, Control Theory and applicatios Centre, Coventry University.

Grills, I., Yan, D., Martinez, A., Vicini, F., and Wong, J.W.and Kestin, L. (2003). Potential for reduced toxicity and dose escalation in the treatment of inoperablenon–small-cell lung cancer: A comparison of intensity-modulated radiationtherapy (imrt), 3d conformal radiation, and elective nodal irradiation. *International Journal of Radiation Oncology, Biology, Physics*, 57(3):875–890.

Haas, O., Skworcow, P., Burnham, K., and Mills, J. (2005). Deliverable Number D19 : Assessment of Gantry and PSS. Technical report, CTAC, Coventry University.

Haas, O., Skworcow, P., Putra, D., and Mills, J. (2006). Report on Radiotherapy Treatment Suite Simulator (RTSS). Technical report, MAESTRO.

Hagan, M., Demuth, H., and Beale, M. (1997). *Neural network design*. PWS Publishing Co. Boston, MA, USA.

Halperin, R., e. a. (1999). Setup reproducibility in radiation therapy for lung cancer: a comparisonbetweent-bar and expanded foam immobilization devices. *International Journal of Radiation Oncology, Biology, Physics*, 43:211–6.

Hanley, J., Debois, M., Mah, D., Mageras, G., Raben, A., Rosenzweig, K., Mychalczak, B., Schwartz, L., Gloeggler, P., Lutz, W., et al. (1999). Deep inspiration breath-hold technique for lung tumors: the potential value of target immobilization and reduced lung density in dose escalation. *International Journal of Radiation Oncology, Biology, Physics*, 45(3):603–611.

Harada, T., Shirato, H., Ogura, S., Oizumi, S., Yamazaki, K., Shimizu, S., Onimaru, R., Miyasaka, K., Nishimura, M., and Dosaka-Akita, H. (2002). Real-time tumor-tracking radiation therapy for lung carcinoma by the aid of insertion of a gold marker using bronchofiberscopy. *Cancer*, 95(8):1720–1727.

Herk, M. (2004). Errors and margins in radiotherapy. *Seminars in Radiation Oncology*, 14(1):52–64.

Herk, M., Remeijer, P., Rasch, C., and Lebesque, J. (2000). The probability of correct target dosage: dose-population histograms for deriving treatment margins in radiotherapy. *International Journal of Radiation Oncology, Biology, Physics*, 47(4):1121–1135.

Herk, M., Witte, M., van der Geer, J., Schneider, C., and Lebesque, J. (2003). Biologic and physical fractionation effects of random geometric errors. *International Journal of Radiation Oncology, Biology, Physics*, 57(5):1460–1471.

Herman, M. (2005). Clinical use of electronic portal imaging. *Seminars in Radiation Oncology*, 15:157–167.

Hoisak, J., Sixel, K., Tirona, R., Cheung, P., and Pignol, J. (2004). Correlation of lung tumor motion with external surrogate indicators of respiration. *International Journal of Radiation Oncology, Biology, Physics*, 60(4):1298–1306.

Hoisak, J., Sixel, K., Tirona, R., Cheung, P., and Pignol, J. (2006). Prediction of lung tumour position based on spirometry and on abdominaldisplacement: Accuracy and reproducibility. *Radiotherapy and Oncology*, 78(3):339–346.

Hugo, G., Agazaryan, N., and Solberg, T. (2002). An evaluation of gating window size, delivery method, and composite field dosimetry of respiratory-gated IMRT. *Medical Physics*, 29:2517.

Hugo, G., Agazaryan, N., and Solberg, T. (2003). The effects of tumor motion on planning and delivery of respiratory-gated IMRT. *Medical Physics*, 30:1052.

Hummel, J., Figl, M., Kollmann, C., Bergmann, H., and Birkfellner, W. (2002). Evaluation of a miniature electromagnetic position tracker. *Medical Physics*, 29:2205.

Huntzinger, C. (2004). Image Guided Radiation Therapy. Technical report, varian.mediaroom.

Hurkmans, C., Remeijer, P., Lebesque, J., and Mijnheer, B. (2001). Set-up verification using portal imaging; review of current clinical practice. *Radiotherapy and Oncology*, 58(2):105–120.

ICRU (1987). Use of computer in externel beam radiotherapy procedures with high-energyphotonsand electrons. ICRU Report, 42. Bethesda, MD: ICRU Publications.

ICRU (1994). Prescribing, recording and reporting photon beam radiotherapy. ICRU Report, 50. Bethesda, MD: ICRU Publications.

ICRU (2000). Prescribing, recording and reporting photon beam radiotherapy (supplimentto icru report 50). ICRU Report, 62. Bethesda, MD: ICRU Publications.

Ionascu, D., Jiang, S., Nishioka, S., Shirato, H., and Berbeco, R. (2007). Internal-external correlation investigations of respiratory induced motion of lung tumors. *Medical Physics*, 34:3893.

Isaksson, M., Jalden, J., and Murphy, M. (2005a). On using an adaptive neural network to predict lung tumor motion during respiration for radiotherapy applications. *Medical Physics*, 32:3801.

Isaksson, M., Jalden, J., and Murphy, M. (2005b). On using an adaptive neural network to predict lung tumour motion duringrespiration for radiotherapy applications. *Medical Physics*, 32:3801–3809.

Jaffray, D. (2005). Emergent technologies for 3-dimensional image-guided radiation delivery. *Seminars in Radiation Oncology*, 15(3):208–16.

Jaldén, J. and Isaksson, M. (2001). Temporal Prediction and Spatial Correlation of Breathing Motion by Adaptive Filtering. Technical report, Tech. rep., Stanford University, Stanford, CA.

Jeremić, B. and Aaronson, N. (2005). *Advances in radiation oncology in lung cancer*. Springer Verlag.

Jiang, S. (2006a). Radiotherapy of mobile tumors. *Seminars in Radiation Oncology*, 16:239–48.

Jiang, S. (2006b). Technical aspects of image-guided respiration-gated radiation therapy. *Medical Dosimetry*, 31(2):141–151.

Jin, J. and Yin, F. (2005). Time delay measurement for linac based treatment delivery in synchronize-drespiratory gating radiotherapy. *Medical Physics*, 32:1293.

Kakar, M., Nystrom, H., Aarup, L., Nottrup, T., and Olsen, D. (2005). Respiratory motion prediction by using the adaptive neuro fuzzy inference system (ANFIS). *Physics in Medicine and Biology*, 50:4721–4728.

Kalman, R. (1960). A new approach to linear filtering and prediction problems. *Journal of Basic Engineering*, 82(1):35–45.

Kanae, S., Muramatsu, K., Yang, Z., and Wada, K. (2004). Modeling of respiration and estimation of pulmonary elastance. In *Control Conference, 2004. 5th Asian*, volume 1.

Keall, P. (2004). 4-dimensional computed tomography imaging and treatment planning. *Seminars in Radiation Oncology*, 14(1):81–90.

Keall, P., Cattell, H., Pokhrel, D., Dieterich, S., Wong, K., Murphy, M., Vedam, S., Wijesooriya, K., and Mohan, R. (2006a). Geometric accuracy of a real-time target tracking system with dynamic multileaf collimator tracking system. *International Journal of Radiation Oncology, Biology, Physics*, 65(5):1579–1584.

Keall, P., Joshi, S., Vedam, S., Siebers, J., and Kini, V.R.and Mohan, R. (2005). Four-dimensional radiotherapy planning for DMLC-based respiratory motiontracking. *Medical Physics*, 32(4):942–951.

Keall, P., Kini, V., Vedam, S., and Mohan, R. (2001). Motion adaptive x-ray therapy: a feasibility study. *Physics in Medicine and Biology*, 46(1):1–10.

Keall, P., Kini, V., Vedam, S., and Mohan, R. (2002). Potential radiotherapy improvements with respiratory gating. *Australas Phys Eng Sci Med*, 25(1):1–6.

Keall, P., Mageras, G., Balter, J., Emery, R., Forster, K., Jiang, S., Kapatoes, J., Low, D., Murphy, M.J.and Murray, B., et al. (2006b). The management of respiratory motion in radiation oncology report of AAPMTask Group 76. Technical report, AAPM.

Keall, P., Siebers, J., Joshi, S., and Mohan, R. (2004a). Monte Carlo as a four-dimensional radiotherapy treatment-planning tool to account for respiratory motion. *Physics in Medicine and Biology*, 49(16):3639–3648.

Keall, P., Starkschall, G., Shukla, H., Forster, K., Ortiz, V., Stevens, C., Vedam, S., George, R., Guerrero, T., and Mohan, R. (2004b). Acquiring 4 D thoracic CT scans using a multislice helical method. *Physics in Medicine and Biology*, 49(10):2053–2067.

Kenney, J. and Keeping, E. (1962). *Mathematics of Statistics*. Van Nostrand, 3 edition.

Kenyon, C., Cala, S., Yan, S., Aliverti, A., Scano, G., Duranti, R., Pedotti, A., and Macklem, P. (1997). Rib cage mechanics during quiet breathing and exercise in humans. *Journal of Applied Physiology*, 83(4):1242–1255.

Ketting, C., Austin-Seymour, M., Kalet, I., Unger, J., Hummel, S., and Jacky, J. (1997). Consistency of three-dimensional planning target volumes across physicians and institutions. *International Journal of Radiation Oncology, Biology, Physics*, 37(2):445–53.

Kim, D., Murray, B., Halperin, R., and Roa, W. (2001). Held-breath self-gating technique for radiotherapy of non-small-cell lungcancer: A feasibility study. *International Journal of Radiation Oncology, Biology, Physics*, 49(1):43–9.

Kini, V., Vedam, S., Keall, P., Patil, S., Chen, C., and Mohan, R. (2003). Patient training in respiratory-gated radiotherapy. *Medical Dosimetry*, 28(1):7–11.

Kini, V. R., Keall, P. J., Vedam, S. S., Arthur, D. W., Kavanagh, B. D., Cardinale, R. M., and Mohan, R. (2000). Preliminary results from a study of a respiratory motion tracking system:underestimation of target volume with conventional ct simulation. *International Journal of Radiation Oncology, Biology, Physics*, 48:164.

Kitamura, K., Shirato, H., Seppenwoolde, Y., Onimaru, R., Fujita, M. O., Shimizu, H., Shinohara, N., Harabayashi, T., and K.Miyasaka (2002). three-dimensional intrafractional movement of prostate measured during real-timetumor-trackingradiotherapy in supine and prone treatment positions. *International Journal of Radiation Oncology, Biology, Physics*, 53(5):1117–1123.

Korin, H., Ehman, R., Riederer, S., Felmlee, J., and Grimm, R. (1992). Respiratory kinematics of the upper abdominal organs: a quantitative study. *Magn Reson Med*, 23(1):172–8.

Krell, G., Michaelis, B., and Gademann, G. (1999). Using pre-treatment images for evaluation of on-line data in radiotherapywith neural networks. In *European Medical and Biological Engineering Conference EMBEC*, Vienna.

Kruse, J., Herman, M., Hagness, C., Davis, B., Garces, YI andHaddock, M., Olivier, K., Stafford, S., and Pisansky, T. (2002). Electronic and film portal images: a comparison of landmark visibility andreview accuracy. *International Journal of Radiation Oncology, Biology, Physics*, 54(2):584–91.

Kubo, H. and Hill, B. (1996). Respiration gated radiotherapy treatment: a technical study. *Physics in Medicine and Biology*, 41(1):83–91.

Kubo, H., Len, P., Minohara, S., and Mostafavi, H. (2000). Breathing-synchronized radiotherapy program at the University of California Davis Cancer Center. *Medical Physics*, 27:346.

Kubo, H. and Wang, L. (2002). Introduction of audio gating to further reduce organ motion in breathingsynchronized radiotherapy. *Medical Physics*, 29:345.

Kutcher, G., Coia, L., Gillin, M., Hanson, W., Leibel, S., Morton, R., Palta, J., Purdy, J., Reinstein, L., Svensson, G., et al. (1994). Comprehensive QA for radiation oncology: Report of AAPM radiation therapy committee task group 40. *Medical physics*, 21:581.

Lagarias, J., Reeds, J., Wright, M., and Wright, P. (1998). Convergence properties of the Nelder-Mead simplex method in low dimensions. *SIAM Journal on Optimization*, 9(1):112–147.

Land, I. (2006). The delivery limitations of adaptive radiotherapy systems. Technical report, University of Warwick.

Land, I. (2009). *The Delivery Limitations of Adaptive Radiotherapy Systems*. PhD thesis, University of Warwick.

Langen, K., Jones, D., et al. (2001). Organ motion and its management. *International Journal of Radiation Oncology, Biology, Physics*, 50(1):265–78.

Le rest, C., Couturier, O., Turzo, A., and Bizais, Y. (2000). Post-synchronization of dynamic images of periodically moving organs. *Nuclear Medicine Communications*, 21(7):677.

Leontief, W. (1970). The dynamic inverse. *Proceedings of the Fourth International Conference on Input-Output Techniques, Geneva, 8-12 January 1968: Published in Honor of Wassily Leontief*.

Levitzky, M. (2002). *Pulmonary Physiology*. McGraw-Hill.

Links, J., II, L., Subramaniam, B., Rubin, M., Hennessey, J., and Reiss, A. (1998). Edge Complexity and Partial Volume Effects. *Journal of Computer Assisted Tomography*, 22(3):450.

Liu, H., Yu, Y., OŠDell, W., and Schell, M. (2003). A prospective tracking algorithm for motion compensation radiotherapy. In *American Association of Physicists in Medicine: Annual meeting, San Diego*.

Ljung, L. (1999). *System Identification: Theory for the User (ed.)*. Prentice-Hall, Englewood Cliffs, NJ.

Low, D., Parikh, P., Lu, W., Dempsey, J., Wahab, S., Hubenschmidt, J., Nystrom, M., Handoko, M., and Bradley, J. (2005). Novel breathing motion model for radiotherapy. *International Journal of Radiation Oncology, Biology, Physics*, 63(3):921–929.

Lujan, A., Larsen, E., Balter, J., and Ten Haken, R. (1999). A method for incorporating organ motion due to breathing into 3D dose calculations. *Medical Physics*, 26:715.

Mageras, G. (2005). Introduction: management of target localization uncertainties in external-beamtherapy. *Seminars in Radiation Oncology*, 15(3):133–5.

Mageras, G., Pevsner, A., Yorke, E., Rosenzweig, K., Ford, E., Hertanto, A., Larson, S., Lovelock, D., Erdi, Y.E.and Nehmeh, S., et al. (2004). Measurement of lung tumor motion using respiration-correlated CT. *International Journal of Radiation Oncology, Biology, Physics*, 60(3):933–941.

Mageras, G. and Yorke, E. (2004). Deep inspiration breath hold and respiratory gating strategies for reducing organ motion in radiation treatment. *Seminars in Radiation Oncology*, 14(1):65–75.

Mageras, G., Yorke, E., Rosenzweig, K., Braban, L., Keatley, E., Ford, E., Leibel, S., and Ling, C. (2001). Fluoroscopic evaluation of diaphragmatic motion reduction with a respiratory gated radiotherapy system. *J Appl Clin Med Phys*, 2(4):191–200.

Mah, D., Hanley, J., Rosenzweig, K., Yorke, E., Braban, L., Ling, C., Leibel, S., and Mageras, G. (2000). Technical aspects of the deep inspiration breath-hold technique in the treatment of thoracic cancer. *International Journal of Radiation Oncology, Biology, Physics*, 48(4):1175–1185.

MathWorks (2006). *Signal Processing Toolbox: For Use with MATLAB*. The MathWorks Inc.

McCall, K. and Jeraj, R. (2007). Dual-component model of respiratory motion based on the periodic autoregressive moving average (periodic ARMA) method. *Physics in Medicine and Biology*, 52(12):3455–3466.

McKenzie, A. (2000). How should breathing motion be combined with other errors when drawing margins around clinical target volumes? *British Journal of Radiology*, 73(873):973.

Mead, J. and Loring, S. (1982). Analysis of volume displacement and length changes of the diaphragm duringbreathing. *Journal of Applied Physiology*, 53(3):750–755.

Meyer, J. (2001). *Accommodation Practical Constraints For Intensity Modulated Radiation Therapy-Bymeans of compensators*. PhD thesis, Control Theory and applications Centre, Coventry University.

Minohara, S., Kanai, T., Endo, M., Noda, K., and Kanazawa, M. (2000). Respiratory gated irradiation system for heavy-ion radiotherapy. *International Journal of Radiation Oncology, Biology, Physics*, 47(4):1097–103.

Mohler, R. (1970). Natural Bilinear Control Processes. *Systems Science and Cybernetics, IEEE Transactions on*, 6(3):192–197.

Mohler, R. (1971). A Common Model in Socio-Economics, Ecology and Physiology. *Proc. Int. Conf. on Systems, Man and Cybernetics, Anaheim, California, October*.

Mohler, R. (1972). Bilinear Structures and Man. *Theory and Applications of Variable Structure Systems (Mohler, RR, and Ruberti, A., ed.), Academic Press, New York*, pages 169–181.

Mohler, R. and Kolodziej, W. (1980). An overview of bilinear system theory and applications. *IEEE Transactions on Systems, Man and Cybernetics*, 10(10):683–688.

Mohler, R. R. (1973a). Bilinear control processes. *Mathematics in science and engineering*, 106.

Mohler, R. R. (1973b). *Bilinear Control Processes: With Applications to Engineering, Ecology, and Medicine*. New York: Academic Press. ISBN 0-12-504140-3.

Mohler, R. R., Khapalov, A. Y., Rajkumar, V., and Zakrzewski, R. R. (1996). On bilinear control methodology. In *Proceedings of the IFAC* 13^{th} *Triennal World Congress*, pages 365–370, San Francisco, USA.

Munro, P. (1995). Portal imaging technology: Past, present, and future. *Seminars in Radiation Oncology*, 5(2):115–133.

Murphy, M. (2002). Fiducial-based targeting accuracy for external-beam radiotherapy. *Medical Physics*, 29:334.

Murphy, M. (2004). Tracking moving organs in real time. *Seminars in Radiation Oncology*, 14(1):91–100.

Murphy, M., Chang, S., Gibbs, I., Le, Q., Hai, J. andKim, D., Martin, D., and Adler, J. (2003). Patterns of patient movement during frameless image-guided radiosurgery. *International Journal of Radiation Oncology, Biology, Physics*, 55(5):1400–1408.

Murphy, M. and Dieterich, S. (2006). Comparative performance of linear and nonlinear neural networks to predict irregular breathing. *Physics in Medicine and Biology*, 51:5903–14.

Murphy, M., Jalden, J., and Isaksson, M. (2002a). Adaptive filtering to predict lung tumor breathing motion during image guided radiation therapy. In *Proc. 16th Int. Conf. on Computer Assisted Radiology (CARS 2002)*.

Murphy, M., Martin, D., Whyte, R., Hai, J., Ozhasoglu, C., and Le, Q. (2002b). The effectiveness of breath-holding to stabilize lung and pancreas tumors during radiosurgery. *International Journal of Radiation Oncology, Biology, Physics*, 53(2):475–82.

Nederveen, A., Dehnad, H., van der Heide, U., van Moorselaar, RJand Hofman, P., and Lagendijk, J. (2003). Comparison of megavoltage position verification for prostate irradiationbased on bony anatomy and implanted fiducials. *Radiotherapy and Oncology*, 68(1):81–8.

Neicu, T., Berbeco, R., Wolfgang, J., and Jiang, S. (2006). Synchronized moving aperture radiation therapy (SMART): improvement of breathing pattern reproducibility using respiratory coaching. *Physics in Medicine and Biology*, 51(3):617–636.

Neicu, T., Shirato, H., Seppenwoolde, Y., and Jiang, S. (2003). Synchronized moving aperture radiation therapy(SMART): Average tumour trajectoryfor lung patients. *Physics in Medicine and Biology*, 48(5):587–598.

Nioutsikou, E., Symonds-Tayler, R., et al. (2006). Experimental quantification of respiratory motion effects during lung radiotherapy. *Physics in Medicine and Biology*, 51:3359–3374.

Ohara, K., Okumura, T., Akisada, M., Inada, T., Mori, T., Yokotaand, H., and Calguas, M. (1989). Irradiation synchronized with respiration gate. *International Journal of Radiation Oncology, Biology, Physics*, 17(4):853–857.

Onimaru, R., Shirato, H., Fujino, M., Suzuki, K., Yamazaki, K., Nishimura, M., Dosaka-Akita, H., and Miyasaka, K. (2005). The effect of tumor location and respiratory function on tumor movement estimated by real-time tracking radiotherapy (RTRT) system. *International Journal of Radiation Oncology, Biology, Physics*, 63(1):164–169.

Overschee, P. V. and De Moor, B. (1996). *Subspace Identification for Linear Systems. Theory, Implementation, Applications*. Kluwer Academic Publishers. ISBN 0-7923-9717-7.

Ozhasoglu, C. and Murphy, M. (2002). Issues in respiratory motion compensation during external-beam radiotherapy. *International Journal of Radiation Oncology, Biology, Physics*, 52(5):1389–1399.

Ozhasoglu, C., Murphy, M., Glosser, G., Bodduluri, M., Schweikard, A., Forster, K., Martin, D., and Adler, J. (2000). Real-time tracking of the tumor volume in precision radiotherapy and bodyradiosurgery–a novel approach to compensate for respiratory motion. *Computer Assisted Radiology and Surgery (San Francisco*, pages 691–6.

Paluszczyszyn, D. (2008). Real-time implementation of a new control system utilising the model predictive control and the Kalman filter predictor for the radiotherapy patient support system. Master's thesis, Coventry University, Faculty of Engineering and Computing, Control Theory and Application Centre.

Plathow, C., Ley, S., Fink, C., and et al. (2004). Evaluation of chest motion and volumetry during the breathing cycle bydynamicmri in healthy subjects. *Invest. Radiol.*, 39:202–209.

Pollock, D. et al. (1999). *A Handbook of Time-series Analysis, Signal Processing and Dynamics*. Academic Press.

Priban, I. (1963). An analysis of some short-term patterns of breathing in man at rest. *The Journal of Physiology*, 166(3):425.

Putra, D. (2004). *Control of Limit Cycling in Frictional Mechanical Systems*. PhD thesis, Technische Universiteit Eindhoven.

Putra, D., Haas, O., Mills, J., and Bumham, K. (2006). Prediction of Tumour Motion using Interacting Multiple Model Filter. In *Advances in Medical, Signal and Information Processing, 2006. MEDSIP 2006. IET 3rd International Conference On*, pages 1–4.

Putra, D., Haas, O., Mills, J., and Burnham, K. (2008). A multiple model approach to respiratory motion prediction for real-time IGRT. *Physics in Medicine and Biology*, 53(6):1651–1663.

Putra, D., Skworcow, P., Young, K., Haas, O., Mills, J., and Burnham, K. (2007). Margin to accommodate inherent errors of tracking-based radiation delivery system. In Bissonnette, J.-P., editor, *XVth International Conference on the Use of Computers in Radiation Therapy, Toronto, Canada*, pages 190–194.

Quetelet, A. (1842). A Treatise on Man and the Development of His Faculties. *Edinburgh: W. andR. Chambers*, 82.

Ramsey, C., Cordrey, I., and Oliver, A. (1999). A comparison of beam characteristics for gated and nongated clinical x-ray beams. *Medical Physics*, 26:2086.

Rasch, C., Barillot, I., Remeijer, P., Touw, A., van Herk, M., and Lebesque, J. (1999). Definition of the prostate in CT and MRI: a multi-observer study. *International Journal of Radiation Oncology, Biology, Physics*, 43(1):57–66.

Remouchamps, V., Letts, N., Vicini, F., Sharpe, M., Kestin, L., Chen, P., Martinez, A., and Wong, J. (2003a). Initial clinical experience with moderate deep-inspiration breath holdusing an active breathing control device in the treatment of patients withleft-sided breast cancer using external beam radiation therapy. *International Journal of Radiation Oncology, Biology, Physics*, 56(3):704–715.

Remouchamps, V., Letts, N., Yan, D., Vicini, F., Moreau, M., Zielinski, J., Liang, J., Kestin, L., and Martinez, A.A.and Wong, J. (2003b). Three-dimensional evaluation of intra-and interfraction immobilizationof lung and chest wall using active breathing control: A reproducibilitystudy with breast cancer patients. *International Journal of Radiation Oncology, Biology, Physics*, 57(4):968–978.

Ritchie, C., Hsieh, J., Gard, M., Godwin, J., and Kim, Y.andCrawford, C. (1994). Predictive respiratory gating: a new method to reduce motion artifacts onctscans. *Radiology*, 190:847–852.

Rosenzweig, K., Hanley, J., Mah, D., Mageras, G., Hunt, M.and Toner, S., Burman, C., Ling, C., Mychalczak, B., Fuks, Z., et al. (2000). The deep inspiration breath-hold technique in the treatment of inoperablenon-small-cell lung cancer. *International Journal of Radiation Oncology, Biology, Physics*, 48(1):81–87.

Ross, C., Hussey, D., Pennington, E., Stanford, W., and Doornbos, J. (1990). Analysis of movement of intrathoracic neoplasms using ultrafast computerized tomography. *International Journal of Radiation Oncology, Biology, Physics*, 18(3):671–677.

Ruan, D., Fessler, J., and Balter, J. (2007). Real-time prediction of respiratory motion based on local regression methods. *Physics in Medicine and Biology*, 52(23):7137–7152.

Ruan, D., Fessler, J., Balter, J., and Sonke, J. (2006). Exploring breathing pattern irregularity with projection-based method. *Medical Physics*, 33:2491.

Sahih, A., Haas, O., Burnham, K., and Mills, J. (2005). Organ motion modelling and prediction for adaptive radiotherapy. In *Proc. CD-ROM of IAR Annual Meeting 2005, Mulhouse, France*, volume 2, pages 211–216.

Sahih, A., Haas, O., Goodband, J., Putra, D., Mills, J., and Burnham, K. (2006). Respiratory Motion Prediction For Adaptive Radiotherapy. In *Proc. CD-ROM of IAR Annual Meeting 2006, Nancy, France*.

Sahih, A., Haas, O., Mills, J., and Burnham, K. (2007). A new bilinear model for respiratory motion. In *XVth International Conference. on the use of Computers in Radiation Therapy*.

Samson, M., van Sornsen de Koste, J., de Boer, H., Tankink, H.and Verstraate, M., Essers, M., Visser, A., and Senan, S. (1999). An analysis of anatomic landmark mobility and setup deviations in radiotherapyfor lung cancer. *International Journal of Radiation Oncology, Biology, Physics*, 43(4):827–32.

Sawada, A., Yoda, K., Kokubo, M., Kunieda, T., and Nagata, Y. andHiraoka, M. (2004). A technique for noninvasive respiratory gated radiation treatment systembased on a real time 3D ultrasound image correlation: A phantom study. *Medical Physics*, 31:245.

Schwartz, L., Richaud, J., Buffat, L., Touboul, E., and Schlienger, M. (1994). Kidney mobility during respiration. *Radiotherapy and Oncology*, 32(1):84–6.

Schwarz, H., Ingenbleek, R., and Jelali, M. (1996). Application of bilinear system models and design methods to hydrostatic drives. *Proc. 13: thTriennial World Congress of IFAC, San Francisco, USA*.

Schweikard, A., Glosser, G., Bodduluri, M., Murphy, M., and Adler, J. (2000). Robotic Motion Compensation for Respiratory Movement duringRadiosurgery. *Computer Aided Surgery*, 5:263–277.

Schweikard, A., Shiomi, H., and Adler, J. (2004). Respiration tracking in radiosurgery. *Medical Physics*, 31(10):2738–41.

Seiler, P., Blattmann, H., Kirsch, S., Muench, R., and Schilling, C. (2000). A novel tracking technique for the continuous precise measurement of tumour positions in conformal radiotherapy. *Physics in Medicine and Biology*, 45(9):103.

Seppenwoolde, Y., Engelsman, M., De Jaeger, K., Muller, SH andBaas, P., McShan, D., Fraass, B., Kessler, M., Belderbos, JSand Boersma, L., et al. (2002a). Optimizing radiation treatment plans for lung cancer using lung perfusioninformation. *Radiotherapy and Oncology*, 63(2):165–77.

Seppenwoolde, Y., Shirato, H., Kitamura, K., Shimizu, S., van Herk, M., Lebesque, J., and Miyasaka, K. (2002b). Precise and real-time measurement of 3D tumor motion in lung due to breathing and heartbeat, measured during radiotherapy. *International Journal of Radiation Oncology, Biology, Physics*, 53(4):822–834.

Sharp, G., Jiang, S., Shimizu, S., and Shirato, H. (2004). Prediction of respiratory tumour motion for real-time image-guided radiotherapy. *Physics in Medicine and Biology*, 49(3):425–440.

Sharp, G., LU, H., Trofimov, A., Tang, X., Jiang, S., Turcotte, J., Gierga, D., Chen, G., and Hong, T. (2007). Assessing Residual Motion for Gated Proton-Beam Radiotherapy. *Journal of Radiation Research*, 48(Suppl. A):55–59.

Shea, S. and Guz, A. (1992). Personnalite ventilatoire–an overview. *Respiration Physiology*, 87(3):275–291.

Shenoi, B. and Wiley, J. (2006). *Introduction to Digital Signal Processing and Filter Design*. Wiley-Interscience.

Shimizu, S., Shirato, H., Aoyama, H., Hashimoto, S., Nishioka, T., Yamazaki, A., Kagei, K., and Miyasaka, K. (2000a). High-speed magnetic resonance imaging for four-dimensional treatment planningof conformal radiotherapy of moving body tumors. *International Journal of Radiation Oncology, Biology, Physics*, 48(2):471–4.

Shimizu, S., Shirato, H., Kagei, K., Nishioka, T., Bo, X., Dosaka-Akita, H., Hashimoto, S., Aoyama, H., Tsuchiya, K., and Miyasaka, K. (2000b). Impact of respiratory movement on the computed tomographic images of small lung tumors in three-dimensional (3D) radiotherapy. *International Journal of Radiation Oncology, Biology, Physics*, 46(5):1127–33.

Shimizu, S., Shirato, H., Kitamura, K., Ogura, S., Akita-Dosaka, H., Tateishi, U., Watanabe, Y., Fujita, K., and Shimizu, T. andMiyasaka, K. (2000c). Fluoroscopic real-time tumor-tracking radiation treatment (rtrt) can reduceinternal margin (im) and set-up margin (sm) of planning target volume (ptv)for lung tumors. *International Journal of Radiation Oncology, Biology, Physics*, 48:166–167.

Shimizu, S., Shirato, H., Kitamura, K., Shinohara, N., Harabayashi, T., Tsukamoto, T., Koyanagi, T., and Miyasaka, K. (2000d). Use of an implanted marker and real-time tracking of the marker for the positioning of prostate and bladder cancers. *International Journal of Radiation Oncology, Biology, Physics*, 48(5):1591–1597.

Shimizu, S., Shirato, H., Ogura, S., Akita-Dosaka, H., Kitamura, K., Nishioka, T., Kagei, K., Nishimura, M., and Miyasaka, K. (2001). Detection of lung tumor movement in real-time tumor-tracking radiotherapy. *International Journal of Radiation Oncology, Biology, Physics*, 51(2):304–310.

Shirato, H., Harada, T., Harabayashi, T., Hida, K., Endo, H., Kitamura, K., Onimaru, R., Yamazaki, K., Kurauchi, N., Shimizu, T., et al. (2003). Feasibility of insertion/implantation of 2.0-mm-diameter gold internal fiducial markers for precise setup and real-time tumor tracking in radiotherapy. *International Journal of Radiation Oncology, Biology, Physics*, 56(1):240–247.

Shirato, H., Oita, M., Fujita, K., Shimizu, S., Onimaru, R., Uegaki, S., Watanabe, Y., Kato, N., and Miyasaka, K. (2004a). Three-dimensional conformal setup (3D-CSU) of patients using the coordinate system provided by three internal fiducial markers and two orthogonal diagnostic X-ray systems in the treatment room. *International Journal of Radiation Oncology, Biology, Physics*, 60(2):607–612.

Shirato, H., Seppenwoolde, Y., Kitamura, K., Onimura, R., and Shimizu, S. (2004b). Intrafractional tumor motion: lung and liver. *Seminars in Radiation Oncology*, 14(1):10–18.

Shirato, H., Shimizu, S., and Kitamura, K. (2000a). Four dimensional treatment planning and fluoroscopic real time tumor trackingradiotherapyfor moving tumor. *International Journal of Radiation Oncology, Biology, Physics*, 48(2):435–442.

Shirato, H., Shimizu, S., Kitamura, K., and Onimaru, R. (2007). Organ motion in image-guided radiotherapy: lessons from real-time tumor-tracking radiotherapy. *International Journal of Clinical Oncology*, 12(1):8–16.

Shirato, H., Shimizu, S., Kunieda, T., Kitamura, K., van Herk, M., Kagei, K., Nishioka, T., Hashimoto, S., Fujita, K. andAoyama, H., et al. (2000b). Physical aspects of a real-time tumor-tracking system for gated radiotherapy. *International Journal of Radiation Oncology, Biology, Physics*, 48(4):1187–95.

Shirato, H., Shimizu, S., Shimizu, T., Nishioka, T., and Miyasaka, K. (1999). Real-time tumour-tracking radiotherapy. *Lancet*, 353(9161):1331–2.

Shirato, H., Suzuki, K., Sharp, G., Fujita, K., Onimaru, R., Fujino, M., Kato, N., Osaka, Y., Kinoshita, R., Taguchi, H., et al. (2006). Speed and amplitude of lung tumor motion precisely detected in four-dimensional setup and in real-time tumor-tracking radiotherapy. *International Journal of Radiation Oncology, Biology, Physics*, 64(4):1229–1236.

Sixel, K., Ruschin, M., Tirona, R., and Cheung, P. (2003). Digital fluoroscopy to quantify lung tumor motion: potential for patient-specificplanning target volumes. *International Journal of Radiation Oncology, Biology, Physics*, 57(3):717–723.

Skworcow, P. (2008). *Modelling and predictive control of radiotherapy treatment machines.* PhD thesis, Coventry University.

Skworcow, P., Putra, D., Sahih, A., Goodband, J. ., Haas, O.C.L.and Burnham, K., and Mills, J. (2007). Predictive tracking for respiratory induced motion compensation in adaptive radiotherapy. *Measurement + Control*, 40(1). The Journal of the Institute of Measurement and Control.

Solberg, T. (2000). Development and modification of a virtual source model for monte carlo based imrt verification. In *World Congress of Medical Physics and the AAPM Annual Congress.*

Sontag, M., Lai, Z., McRoy, B., and Waters, R. (1996). Characterization of Respiratory Motion for Pedriatic Conformal 3D Therapy. *Medical Physics*, 23:1082.

Stevens, C., Munden, R., Forster, K., Kelly, J., Liao, Z., Starkschall, G., Tucker, S., and Komaki, R. (2001). Respiratory-driven lung tumor motion is independent of tumor size, tumorlocation, and pulmonary function. *International Journal of Radiation Oncology, Biology, Physics*, 51(1):62–68.

Stromberg, J., Sharpe, M., Kim, L., Kini, V., Jaffray, D. andMartinez, A., and Wong, J. (2000). Active breathing control (abc) for hodgkinŠs disease: reduction in normaltissue irradiation with deep inspiration and implications for treatment. *International Journal of Radiation Oncology, Biology, Physics*, 43(3):797Ű–806.

Suramo, I., Paivansalo, M., and Myllyla, V. (1984). Cranio-caudal movements of the liver, pancreas and kidneys in respiration. *Acta Radiol Diagn (Stockh)*, 25(2):129–31.

Tada, T. (1998). Lung cancer: intermittent irradiation synchronized with respiratory motion–resultsof a pilot study. *Radiology*, 207(3):779–783.

Tiddens, H., Hofhuis, W., Bogaard, J., Hop, W., de Bruin, H., Willems, L., and de Jongste, J. (1999). Compliance, Hysteresis, and Collapsibility of Human Small Airways. *American Journal of Respiratory and Critical Care Medicine*, 160(4):1110–1118.

Tobin, M. (1983). Breathing patterns. 1. Normal subjects. *Chest*, 84(2):202–205.

Tsunashima, Y., Sakae, T., Shioyama, Y., Kagei, K., Terunuma, T., Nohtomi, A., and Akine, Y. (2004). Correlation between the respiratory waveform measured using a respiratory sensor and 3D tumor motion in gated radiotherapy. *International Journal of Radiation Oncology, Biology, Physics*, 60(3):951–958.

Vaseghi, S. (2006). *Advanced Digital Signal Processing and Noise Reduction*. John Wiley & Sons.

Vedam, S., Docef, A., Fix, M., Murphy, M., and Keall, P. (2005). Dosimetric impact of geometric errors due to respiratory motion prediction on dynamic multileaf collimator-based four-dimensional radiation delivery. *Medical Physics*, 32:1607.

Vedam, S., Keall, P., Docef, A., Todor, D., Kini, V., and Mohan, R. (2004). Predicting respiratory motion for four-dimensional radiotherapy. *Medical Physics*, 31:2274.

Vedam, S., Keall, P., Kini, V., and Mohan, R. (2001). Determining parameters for respiration-gated radiotherapy. *Medical Physics*, 28:2139.

Vedam, S., Keall, P., Kini, V., Mostafavi, H., Shukla, H., and Mohan, R. (2003a). Acquiring a four-dimensional computed tomography dataset using an external respiratory signal. *Physics in Medicine and Biology*, 48(1):45–62.

Vedam, S., Kini, V., Keall, P., Ramakrishnan, V., Mostafavi, H., and Mohan, R. (2003b). Quantifying the predictability of diaphragm motion during respiration with a noninvasive external marker. *Medical Physics*, 30:505.

Verdult, V. and Verhaegen, M. (1999). Subspace-based identification of mimo bilinear systems. *Proceedings of the European Control Conference (Karlsruhe, Germany)*.

Vijlbrief, R., de Goede J., P., R., van Herk M., and LebesqueJ. (1998). Development and evaluation of a verification procedure for setup correctionsof lung cancer patients. In *Proceedings of the 5th international workshop on electronic portal imaging*.

Wade, O. (1954). Movements of the thoracic cage and diaphragm in respiration. *The Journal of Physiology*, 124(2):193.

Webb, S. (2001). *Intensity-Modulated Radiation Therapy*. Taylor & Francis.

Webb, S. (2005a). Limitations of a simple technique for movement compensation via movement-modifiedfluence profiles. *Physics in Medicine and Biology*, 50(155):N155–N161.

Webb, S. (2005b). The effect on IMRT conformality of elastic tissue movement and a practicalsuggestion for movement compensation via the modified dynamic multileafcollimator(dMLC) technique. *Physics in Medicine and Biology*, 50(6):1163–1190.

Webb, S. (2006). Quantification of the fluence error in the motion-compensated dynamic MLC (DMLC) technique for delivering intensity-modulated radiotherapy (IMRT). *Physics in Medicine and Biology*, 51:L17–L21.

Webb, S. and Nahum, A. (1993). A model for calculating tumour control probability in radiotherapy including the effects of inhomogeneous distributions of dose and clonogenic cell density. *Physics in medicine and biology*, 38:653–653.

Weeb, A. C., Burnham, K. J., James, D. J. G., and Williams, R. A. (1996). Modelling and simulation of a road vehhicle bump/rebound stop: a bilinear approach. In *11th Int. Conf. on Systems Engineering*, pages 224–229, Las Vegas.

Weiss, P., Baker, J., and Potchen, E. (1972). Assessment of Hepatic Respiratory Excursion. *Journal of Nuclear Medicine*, 13(10):758.

Wijesooriya, K., Bartee, C., Siebers, J., Vedam, S., and Keall, P. (2005). Determination of maximum leaf velocity and acceleration of a dynamic multileafcollimator: Implications for 4D radiotherapy. *Medical Physics*, 32:932.

Wiles, A., Thompson, D., and Frantz, D. (2004). Accuracy assessment and interpretation for optical tracking systems. In *Proc. SPIE*, volume 5367, pages 421–32.

Wilson, E. (2006). Accuracy analysis of electromagnetic tracking within medical environments. Technical report, Georgetown University.

Wong, J., Sharpe, M., Jaffray, D., Kini, V., Robertson, J., Stromberg, J., and Martinez, A. (1999). The use of active breathing control (ABC) to reduce margin for breathingmotion. *International Journal of Radiation Oncology, Biology, Physics*, 44(4):911–919.

Wu, H., Sharp, G., Salzberg, B., Kaeli, D., and Shirato, H. andJiang, S. (2004). A finite state model for respiratory motion analysis in image guided radiationtherapy. *Physics in Medicine and Biology*, 49(23):5357–5372.

Wu, H., Sharp, G., Zhao, Q., Shirato, H., and Jiang, S. (2007). Statistical analysis and correlation discovery of tumor respiratory motion. *Physics in Medicine and Biology*, 52(16):4761–4774.

Xing, L., Thorndyke, B., Schreibmann, E., Yang, Y., Li, T.F.and Kim, G., Luxton, G., and Koong, A. (2006). Overview of image-guided radiation therapy. *Medical Dosimetry*, 31(2):91–112.

Yan, D. (2004). Adaptive radiotherapy: what is it and what can it become ? *ESTRO*.

Yan, D., Jaffray, D., and Wong, J. (1997a). Accounting for deformation of organs in dose/volume evaluation. *Medical Physics*, 24(6):1021.

Yan, D., Vicini, F., Wong, J., and Martinez, A. (1997b). Adaptive radiation therapy. *Physics in Medicine and Biology*, 42(1):123–32.

Yan, H., Yin, F., Zhu, G., Ajlouni, M., and Kim, J. (2006). Adaptive prediction of internal target motion using external marker motion:a technical study. *Physics in Medicine and Biology*, 51(1):31–44.

Yu, Y., Anderson, L., Li, Z., Mellenberg, D., Nath, R. andSchell, M., Waterman, F., Wu, A., and Blasko, J. (1999). Permanent prostate seed implant brachytherapy: Report of the American Associationof Physicists in Medicine Task Group No. 64. *Medical Physics*, 26:2054.

Zhang, T., Keller, H., O'Brien, M., Mackie, T., and Paliwal, B. (2003). Application of the spirometer in respiratory gated radiotherapy. *Medical Physics*, 30:3165.

Zhou, T., Tang, J., Dieterich, S., and Cleary, K. (2004). A robotic 3-D motion simulator for enhanced accuracy in CyberKnife stereotactic radiosurgery. In *International Congress Series*, volume 1268, pages 323–328. Elsevier.

Appendix A

The Methods and advanced equipment for simulation and treatment in radiation oncology (MAESTRO) project

The research work described in this Thesis is part of the European project entitled methods and advanced equipment for simulation and treatment in radiation oncology (MAESTRO). The project which started in May 2004 and finished in October 2009, has involved 25 partners (research institutes, oncology centers and manufactures) from 14 European countries. The project was organised in four scientific specific work packages (WPs), one WP on dissemination and one WP on management.

The work described in this Thesis is part of WP1 that involves the CTAC at Coventry University, the UHCW, the University of East Anglia, and the University Castilla-La Mancha in Spain. WP1 deals with ART that includes the assessment of the geometrical accuracy of PSS and gantry systems, the development of a dynamic phantom, the evaluation of methods to track in real-time ROI from medical images and the development of a couch-based motion compensation system.

The main achievement of the WP1 was the development of a new couch-based motion compensation strategy demonstrated in a clinical environment at the University Hospitals Coventry and Warwickshire (UHCW). The WP 1 demonstrated the ability to detect the surrogate motion and to compensate for its motion in real-time using a standard Elekta PSS. A new model predictive control MPC system was combined with a video tracker and a Kalman filter motion predictor to detect surrogate motion and move the PSS to compensate for the detected motion taking into account the software delays as well as the PSS dynamics.

CTAC and UHCW (Coventry, UK) developed a ‘breathing’ thorax phantom to facilitate the clinical validation of the ’breathing couch’ developed. The phantoms as well as other simpler electromechanical devices were positioned onto the PSS. Their motion was computer controlled to replicate realistic external as well as internal organ motion. The motion detection was performed using external markers monitored by video cameras or infrared tracking systems (e.g. Polaris). The control algorithms exploited the measured and predicted position to calculate the control action required to move the PSS in real time to enable it to compensate for target movements in such a way that the markers remain as motionless with respect to the room coordinate system and the treatment beam (i.e. the target does not move with respect to the beam).

Kalman filter based predictors were compared to neural networks, polynomial and bilinear filters. The effect of motion prediction was assessed and a typical prediction horizon of 0.3s selected as the most appropriate to perform motion compensation with a standard Elekta PSS. The effect of motion prediction was experimentally demonstrated and it was shown to clearly improve the overall motion compensation.

The role of the author in the WP1 was to build a model of the respiratory motion in order to generate a set of realistic respiratory motion that can be replicated by the lung phantom. Moreover, the author has also investigated different prediction algorithms and performed a comparative study between the ’in house’ developed prediction algorithms. During the MAESTRO project the author has co-supervised with Dr. Haas the placement students: Mr Amir Mekherbeche, Mr Hugues Kode, Ms Audrey Rizzo, Ms Myriam Clesse. In addition, the author has co-supervised with Dr Haas the MSc project of Mr George Koustoumpardis.

Coventry MAESTRO Members:

- Dr O.C. Haas (MAESTRO Coordinator - CTAC)
- Dr J. A. Mills (Project Supervisor - UHCW)
- Prof K.J. Burnham (Project Supervisor - CTAC)
- Dr D. Putra (Former Research Assistant - CTAC)
- Dr P. Skworcow (Former MAESTRO PhD student - CTAC)
- Dr I. Land (Former MAESTRO PhD student - UHCW)
- Dr J. Goodband (Former PhD student - CTAC)
- Mr D. Paluszcyszyn (Former Research Assistant - CTAC)

Appendix B

Breathing experiment approval

B.1 Full research proposal

Introduction

Adaptive radiation therapy and image guided radiation therapy are novel techniques that aim to improve the precision of the prescribed dose delivery to the tumour target whilst avoiding the surrounding healthy tissues by compensating for target motion. One of the predominant cause of such motion is breathing. A variety of motion compensation and cancelation techniques have been developed including margin expansion (to account for changes in organ motion and geometry), breath-holding, respiratory gating and beam-tracking [Keall et al. 2006b]. With the exception of breath-holding, all these techniques require real-time organ position tracking (RTOPT). To date, RTOPT has been achieved either by monitoring external motion signal using video imaging system [George et al. 2006] or Spirometer [Hoisak et al. 2006], which is correlated with internal motion [Ahn et al. 2004a], or more accurately by inserting gold markers into or near the tumour [Shimizu et al. 2000d, Seppenwoolde et al. 2002b]. These two techniques are complicated, expensive and/or time consuming to set up and difficult to assess from a quality assurance perspective.

Whilst several models have been proposed to describe the respiratory motion [Wu et al. 2004, Lujan et al. 1999, Brewer et al. 2004], a good generalisable model remains an open question.

Methods and materials

This experiment is part of a project aimed to improve the delivery of radiation by tracking the patient motion during treatment. The experiment aims to collect data to build a model of respiratory motion combining biological signals with geometrical information.

The model will be used to track and predict motion as well as explain the relation between biological signals and geometrical information. A Spirometer will measure breathing flow, lung volume and pressure as well as an electrical recording of the heart or electrocardiogram (ECG). A three dimensional tracking system (Polaris^{TM}) will be used to measure real-time position and orientation of optical markers affixed to wireless tools which will be positioned onto the thorax with elastic band. The Polaris system is not able to take picture of the volunteer and can only detect specifically designed markers. The experiment will not involve any drugs and is not part of a clinical trial.

The correlation between external markers and biological signals will be investigated in order to find a model that can deduce the external motion when only biological signal is given or vice versa. A new technique of modelling will be used to model the lung function which is based on input-output signals. Having reviewed different models of the lung, it has been found that the main variables are pressure and volume of the lung [Crooke et al. 2002]. In our case, the pressure will be considered as input and volume as output. The heart beat signal, will be used to quantify its influence in breathing and will be included in the model.

To ensure the good progress of the experiment, two physiologists will take part in this experiment as advisors on physiological measurement as well as a first aider from the department. The staff operating the equipment have been trained appropriately to deal with Spirometer and Polaris. All the equipment will be electrically isolated.

Data analysis

The geometrical as well as biological data collected will be analysed using system modelling technique [Ljung 1999]. The aim of the analysis will be to identify the signals that are necessary to provide an accurate representation of the lung chest motion.

Procedures

1. (Time t from start of experiment = 0 min) On arrival, we will explain to the participant the aim of the research and procedures that will be followed during the experiment. The participant will be asked if he/she has any serious problem, e.g. lung, heart, joints, neck and back. If they do have medical problems, explecitly chest, skin infection and heart condition they will be excluded. He/she will be asked if he/she has any allergy, specifically to the antibacterial product used to clean the Spirometer flow head.

2. (Time t = 10 min) The queries of the participants will be answered.

3. (Time t = 15 min) If the participant agreed with the explanations and do not have any objections, he/she will be asked to sign the consent form and healthy declaration, so that we can proceed with the experiment.

4. (Time t = 20 min) Having seen the equipment, the participant will be asked to remove his/her coat and heavy jumpers, but be able to keep light piece of clothing and he/she will be asked to lie down on a table in a comfortable position, with your head on a pillow, slightly tilted. To measure ECG signals it will be necessary to stick the electrodes (which will be isolated from the main power supply) to your skin. The procedure involves cleaning with water and soft tissue these small areas of 4cm*4cm (a bit more than a square inch) in the left and right clavicle and under the thorax. He/she will have the possibility to opt out of this procedure if he/she does not want electrodes in contact with his/her skin. The position of three different points on the thorax will be monitored by the 3D tracking system. To do so, three reflective markers will be positioned onto his/her T-shirt using flexible elastic bands specially designed by the University Hospitals Coventry and Warwickshire NHS Trust.

5. (Time t = 20min) Once the participant feel at ease, he/she will be given a Spirometer head flow which will have been cleaned with antibacterial surface spray before each session. In pre-test the participant will be asked to breath normally for 30 seconds, and then asked to sit down. If he/she feel any discomfort the experiment will be stopped.

6. (Time t= 25 min) If the participant feel comfortable and agree to continue, then he/she will be asked to lie down and breath normally into the Spirometer flow head for two sessions of 4 min separated by 5 min break. He/she will have the possibility to stop the experiment at any time if he/she feel uncomfortable. The participant should bearing in mind that the electrodes connected to the Spirometer are safely removed before stepping out of the table top.

7. (Time t= 40 min) Once the data have been collected, the participant will be asked to remove the electrodes and given any assistance to do so if you require it.

8. (Time t= 45 min) Approximately 45 minutes after you have entered the room, the experiment will be completed and participant will be free to leave the room.

Recruitment of participants

An e-mail will be sent to university researchers, staff and students explaining the aim and purpose of the experiment. Only healthy adults who do not have any serious medical problem will be asked to take part in this survey after signing health declaration.

Confidentiality

Confidentiality of participants information including medical records and personal research data gathered in connection with this study, will be annonymised and maintained in password protected computer. The data will be used for modelling purpose. Some models have already been been developed and will be tested and improved using the data from this experiment. Although results of this research may be presented at meeting or in publications, identifiable personal information pertaining to participants will not be disclosed.

B.2 Participant information sheet

Participant Information Sheet

Version 2.0 22 November 2005

You are being invited to take part in a research study. Before you decide it is important for you to understand why the research is being done and what it will involve. Please take time to read the following information carefully. Talk to others about the study if you wish.

- Part 1 tells you the purpose of this study and what will happen to you if you take part.
- Part 2 gives you more detailed information about the conduct of the study.

Ask us if there is anything that is not clear or if you would like more information. Take time to decide whether or not you wish to take part.

You will be given a copy of this information sheet and a signed consent form to keep.

Part 1

1. **Study title**

   Respiratory motion experiment

2. **What is the purpose of the study ?**

   This experiment is part of a project aimed to improve the delivery of radiation by tracking the patient motion during treatment. The experiment aims to collect data to create a computer model of chest motion by combining biological signals with geometrical information. A spirometer will measure breathing flow, lung volume and pressure as well as an electrical recording of the heart or electrocardiogram (ECG). A three dimensional improved tracking system ($dSPACE^{©}$) will be used to measure real-time position and orientation of optical markers affixed to wireless tools which will be positioned onto the thorax with elastic band. The Polaris system is not able to take picture of the volunteer and can only detect specifically designed markers. No images of the volunteers' body will thus be collected. The experiment will not involve any drugs and is not part of a clinical trial.

3. **Why have I been chosen ?**

   The research requires the participation up to 100 healthy university researchers, student and staff. The call for volunteer will be via e-mails, phones and invitations. The volunteers need to have no previous problems with lung and heart or any illness that can be influenced by the experiment.

4. **Do I have to take part ?**

   No, it is up to you to decide whether or not to take part. If you do, you will be given this information sheet to keep and be asked to sign a consent form. You are still free to withdraw at any time and without giving a reason. A decision to withdraw at any time, or a decision not to take part, will not affect the standard of care you receive.

5. **What will happen to me if I take part ?**

   (a) (Time t from start of experiment = 0 min)

   On arrival, we will explain to you the aim of the research and procedures that will be followed during the experiment. To be able to carry out the experiment you will be asked to remove your coat and heavy jumpers, but be able to keep light piece of clothing. You will be asked if you have any allergy, specifically to the antibacterial product used to clean the spirometer flow head. We will use a spirometer (on loan from the University Hospitals Coventry and Warwickshire NHS Trust) to measure your breathing flow, lung volume and pressure as well

as ECG. A three-dimensional infrared video tracking system (the Polaris) will be used to determine real-time position and orientation of optical markers attached to a flexible elastic band. Note that this camera is only able to track specially designed markers, and can thus not be used to take any picture of yourself.

(b) (Time t = 10 min)

If you have any queries we will answer them.

(c) (Time t = 15 min)

If you feel happy with the explanations and do not have any objections, you will be asked to sign the consent form and health declaration so that we can proceed with the experiment.

(d) (Time t = 20 min)

Having seen the equipment, you will be asked to lie down on a table in a comfortable position, with your head on a pillow, slightly tilted. To measure ECG signals it will be necessary to stick the electrodes (isolated from the main power supply) to your skin. The procedure involves cleaning with water and soft tissue these small areas of 4cm*4cm (a bit more than a square inch) in the left and right clavicle and under the thorax. You will have the possibility to opt out of this procedure if you do not want electrodes in contact with your skin. The position of three different points on the thorax will be monitored by the 3D tracking system. To do so, three reflective markers will be positioned onto your T-shirt using flexible elastic bands specially designed by the University Hospitals Coventry and Warwickshire NHS Trust.

(e) (Time t = 20min)

Once you feel at ease, you will be given a spirometer head flow which will have been cleaned with antibacterial surface spray before each session. In pre-test you will be asked to breath normally for 30 seconds, and then asked to sit down. If you feel any discomfort the experiment will be stopped.

(f) (Time t= 25 min)

If you feel comfortable and agree to continue, then you be asked to lie down and breath normally into the spirometer flow head for two sessions of 4 min separated by 5 min break. You will have the possibility to stop the experiment at any time if you feel uncomfortable. You should bearing mind that the electrodes connected to the spirometer are safely removed before stepping out of the table top.

(g) (Time t= 40 min)

Once the data have been collected, you will be asked to remove the electrodes and given any assistance to do so if you require it.

(h) (Time t= 45 min)

Approximately 45 minutes after you have entered the room, the experiment will be completed and you will be free to leave the room.

6. **Expenses and payments:**

   You will not receive any expenses or payment to take part in this study.

7. **What do I have to do ?**

   You will only have to lay down on your back and breath normally for an initial 30s followed by two 4 minutes sessions.

8. **What are the side effects of any treatment received when taking part ?**

   You will not receive any treatment and as much there will not be any associated side effect.

9. **What are the other possible disadvantages and risks of taking part ?**

   A 30 seconds pre-test is planned to see whether if the participant is comfortable or not. If not he can stop the experiment

10. **What are the possible benefits of taking part ?**

    We cannot promise the study will help you but the information will be used to develop better computer model of the chest, and hence will indirectly help improve the treatment of people with (lung cancer).

11. **What if there is a problem ?**

    Any complaint about the way you have been dealt with during the study or any possible harm you might suffer will be addressed. The detailed information on this is given in Part 2.

    Should the complaint relate directly to the research, you are requested to inform the research team who will try to resolve the matter. Failing this, you may wish to contact the Coventry University Ethics Committee chair, Dr Ray Carson, in writing at JS347, Coventry University, Priory Street, Coventry CV1 5FB, or by telephone on 024 7688 7688."

12. **Will my taking part in the study be kept confidential ?**

    Yes. All the information about your participation in this study will be kept confidential in password computer. The details are included in Part 2'

    The markers position information collected by the Polaris and biological signals recorded by the spirometer during the initial 30 second period as well as the two four minutes period will be sent to a PC directly connected to the Spirometer and the Polaris. The PC will not be connected to the

internet. Once the data have been collected, they will be saved onto CDs and USB data storage and the PC with password.

13. **Contact Details:**

Abdelhamid Sahih,
Control Theory and Applications Centre
Faculty of Engineering & Computing-Coventry University
Armstrong Siddeley Building-Priory Street, Coventry CV1 5ED, United Kingdom.
Tel: +44-(0)24 7688 8972
Mob: +44-(0)7854111756
Email: a.sahih@coventry.ac.uk
Or
Dr Olivier Haas, MIEEE
Reader in Applied Control Systems
Control Theory and Applications Centre
Systems Engineering Department
Faculty of Engineering and Computing
Coventry University, Coventry, CV1 5ED, UK
Tel: 024 7688 7658, Tel (Lab) 024 7688 8972

This completes Part 1 of the Information Sheet. If the information in Part 1 has interested you and you are considering participation, please continue to read the additional information in Part 2 before making any decision.

Part 2

14. **What if relevant new information becomes available ?**

No clinical information is expected to arise from this experiment (which is not a clinical trial). If the computer model is successful, it will be published, however no volunteer information will be revealed.

15. **What if there is a problem ?**

We don't expect that there will be any problems linked to medication or diagnosis as this study involves neither. We will be particularly careful with the equipment used to monitor the various

information that we require to ensure that no harm can come from them.

16. **Harm:**

    In the event that something does go wrong and you are harmed during the research study there are no special compensation arrangements. If you are harmed and this is due to someone's negligence then you may have grounds for a legal action for compensation against (Coventry University) but you may have to pay your legal costs.

17. **Will my taking part in this study be kept confidential ?**

    Any data/ results from your participation in the study will be used by **ABDELHAMID SAHIH** as part of his project work. The data will also be available to maestro team supervised by **DR OLIVIER HAAS**. It may also be published in scientific works, but your name or identity will not be revealed.

    Data that is stored electronically and subject codes will be used in place of names such that individuals cannot be identified.

    If you have any questions or queries, **ABDELHAMID SAHIH** will be happy to answer them. If he cannot help you can speak to **DR OLIVIER HAAS**

18. **What will happen to the results of the research study ?**

    The markers position information collected by the Polaris and biological signals recorded by the spirometer during the initial 30 second period as well as the two four minutes period will be used to find the parameters of models able to replicate the motion of the chest. The research will investigate if what signals (amongst breathing flow, lung volume and pressure, electrocardiogram (ECG) and marker motion) are key to being able to model the chest motion. The ultimate aim is to minimize the number of signals to be collected from the patient during radiotherapy treatment. The results will be published in conference and journal papers. The volunteers will not be identified in any report/publication.

19. **Who is organising and funding the research ?**

    The collection of information is funded by MAESTRO research project.

20. **Who has reviewed the study?**

    This study was reviewed and given a favorable ethical opinion for conduct in Coventry University by the Coventry University Ethics Committee chair, Dr Ray Carson, JS347, Coventry University, Priory Street, Coventry CV1 5FB, or by telephone on 024 7688 7688."

B.3 Consent form

Centre Number:

Study Number:

Patient Identification Number for this trial:

CONSENT FORM

Title of Project: Respiratory Motion Experiment.

Name of Researcher: **Abdelhamid Sahih**

Please initial box

1. I confirm that I have read and understand the information sheet dated (Version 2.0) for the above study. I have had the opportunity to consider the information, ask questions and have had these answered satisfactorily. ☐

2. I understand that my participation is voluntary and that I am free to withdraw at any time, without giving any reason, without my medical care or legal rights being affected. ☐

3. I agree to take part in the above study. ☐

_____	_____	_____
Name of Participant	Date	Signature
_____	_____	_____
Name of Person taking consent (if different from researcher)	Date	Signature
_____	_____	_____
Researcher	Date	Signature

When completed, 1 for participant; 1 for researcher site file; 1 (original) to be kept in medical notes.

B.4 Health declaration

Health Declaration Participant No:

Name:

Height:	Weight:	Age:	BMI:

Do you have any health problems with your heart or breathing? YES/NO

Do you have any health problems with your joints, neck or back? YES/NO

Are you currently taking any medication, prescribed or un-prescribed? YES/NO

Have you taken any illicit drugs in the last 72 hours? YES/NO

Any other health issues which you feel may be relevant? YES/NO

Signature:	Date:

Appendix C

Respiratory motion prediction for adaptive radiotherapy (ART)

Appendix D

Predictive tracking for respiratory induced motion compensation in adaptive radiotherapy (ART).